

THE UNIVERSITY OF HULL

**VISCOELASTICALLY PRESTRESSED
COMPOSITES: TOWARDS PROCESS
OPTIMISATION AND APPLICATION TO
MORPHING STRUCTURES**

being a Thesis submitted for the Degree of

Doctor of Philosophy

in the

School of Engineering, University of Hull

by

Bing Wang

BSc, BBA, MSc

July 2016

Dedicated

to

my parents

Mrs Heying Li and Mr Xinfu Wang

brother Jian Wang and lovely niece

ABSTRACT

This thesis covers research that focuses on facilitating the industrial application of viscoelastically prestressed polymeric matrix composites (VPPMCs). With nylon 6,6 fibre as the reinforcement and polyester resin as the matrix material, unidirectional prestressed composite samples were produced and investigated, to expand the knowledge of existing VPPMC technology, and identify the potential application of viscoelastic fibre prestressing to morphing (shape-changing) structures.

To produce a VPPMC, a tensile load is applied to polymeric fibre yarns to induce viscoelastically prestress; following load removal, the yarns are cut and moulded into a matrix. Previous research has shown that by using viscoelastic fibre prestressing within a composite, mechanical properties, such as tensile strength, flexural modulus and impact toughness can be increased by up to 50%. To further understand the underlying prestress mechanisms, the viscoelastic performance of nylon 6,6 fibre was investigated in terms of creep, recovery and recovery force measurement. By using various creep loading conditions, the viscoelastic behaviour of the fibre also provided the basis for investigations into the optimisation of load-time conditions for producing prestress. This provides the first step towards facilitating the production of VPPMCs for industrial application. Since there are increasing demands for using composites within morphing technology, the application of VPPMC principles to morphing structures was studied through both experimental and numerical investigations.

The viscoelastic behaviour of nylon 6,6 fibre showed approximately linear viscoelasticity under 24 h creep conditions with up to 590 MPa stress. This was further verified through use of the time-stress superposition principle: instead of a nonlinear relationship as predicted by the well-known WLF equation, a linear relationship between the applied creep stress and the stress shift factor was found. By approaching the maximum creep potential of the fibre material, impact benefits from the prestressing effect were further improved by ~75% (at ~4.0% creep strain level). Charpy impact testing and recovery force measurement demonstrated that there was an optimum level of viscoelastic fibre

prestressing to maximise the mechanical benefits. A viscoelastic deformation mechanism based on the three-phase microstructural model and latch-based mechanical model was then proposed.

It was found that the fibre processing time for viscoelastically generated prestress could be significantly reduced from 24 h to tens of minutes. By employing the time-temperature superposition principle, the impact benefits from viscoelastically generated prestress under the standard 330 MPa, 24 h creep (at ~3.4% creep strain level), was found broadly to be the same as subjecting the yarns to 590 MPa for 37 min creep. Hence, there was no deterioration in prestress benefits from VPPMC samples produced under both creep conditions to an equivalent of 20,000 years at a constant 20°C. Two viscoelastic creep strain levels (i.e. ~3.4% and ~4.0%) were evaluated through Charpy impact testing, the relationships between applied creep stress and the corresponding fibre processing time followed a logarithmic trend. This suggested that the fibre processing time for prestress could be reduced further, subjecting to avoiding fibre damage. The effects from increasing creep time were found to compare with increasing stress in terms of optimum VPPMC performance.

Finally, the principle of viscoelastic fibre prestressing was successfully used to produce a bistable composite structure, which could snap from one stable cylindrical shape to another when subjected to external loading. The bistable structure was produced by bonding four prestressed strips to the sides of a thin, flexible resin-impregnated fibre-glass sheet. Here, bistability was achieved through pairs of strips orientated to give opposing cylindrical configurations within the sheet. Snap-through behaviour of the bistable structure was investigated through both experimental and numerical simulation; a snap-through mechanism was subsequently proposed based on these observations.

ACKNOWLEDGEMENTS

I would like to express my sincere and heartfelt gratitude to my principle supervisor, Dr Kevin Fancey, for his continuing support and guidance, as well as his patience, enthusiasm and immense knowledge throughout my PhD research. He has inspired me with helpful advice and many discussions, and always encouraged me whenever I meet difficulties in my research. With all his dedicated supervision, wisdom and kindness, I could complete this PhD thesis smoothly. I also wish to thank my second supervisor, Professor Xudong Zhao, for valuable discussions and encouragement throughout my research.

I greatly appreciate the Chinese Scholarship Council (CSC) and the University of Hull (UoH) for awarding the CSC-UoH joint scholarship to support my three years PhD research financially.

I would also like to thank the staff from the School of Engineering and Graduate School for their support and assistance throughout my studies. Technical support is highly appreciated, including: Mr Garry Robinson for his advice and assistance on using optical and scanning electron microscopy; Dr Tung Lee for his support on the universal test machine; Dr Grazia Francesconi for X-ray diffraction testing. Special thanks go to Dr Adnan Fazal (University of Southampton) for helping in the initial stages of my PhD research; Mr Chao Ge (Beijing Institute of Technology) for facilitating my understanding of finite element method; Dr Moona Hope for commenting and proofreading the draft of this thesis; Dr Fuli Zheng for constructive ideas and sharing knowledge on writing skills.

Last but not least, I would like to thank my colleagues and friends for all the useful discussions and pleasant memories during the last three years, including Associate Prof. Peng Xu, Dr Dongyue Tan, Dr Wei Zhang, Dr Jia Chuan Khong, Dr Chuangnan Wang, Miss Yuchen Guo, Miss Lu Wang, Miss Shanshan Hu, Mr Xiaofeng Zhang, Mr Bingyong Guo, Mr Zhen Yu, Mr Kai Wang, Mr Wei Zhang Mr Wenjia Du and Mr Yang Qin.

LIST OF CONTENTS

Chapter 1	INTRODUCTION.....	1
1.1	INTRODUCTION	2
1.2	AIM AND OBJECTIVES.....	3
1.3	MOTIVATION	4
1.4	THESIS OVERVIEW	4
1.5	WORK DISSEMINATION	7
Chapter 2	GENERAL LITERATURE REVIEW.....	9
2.1	INTRODUCTION	10
2.2	MICROMECHANICS OF COMPOSITE STIFFNESS	11
2.3	PRESTRESSED COMPOSITES	14
2.4	ELASTICALLY PRESTRESSED COMPOSITES.....	15
2.4.1	Elastic fibre prestressing	15
2.4.2	Development of EPPMCs	16
2.4.3	Elastic fibre prestressing methods.....	25
2.5	VISCOELASTICALLY PRESTRESSED COMPOSITES.....	26
2.5.1	Viscoelastic fibre prestressing	26
2.5.2	Development of VPPMCs.....	27
2.6	PRESTRESS MECHANISMS	31
2.7	SEMI-CRYSTALLINE FIBRE MICROSTRUCTURES	33
2.7.1	Two-phase microfibrillar model	36
2.7.2	Three-phase ‘Swiss-cheese’ model	37
2.7.3	Viscoelastic deformation.....	38
2.8	MORPHING STRUCTURES.....	40
2.8.1	Un-symmetric morphing structures	40
2.8.2	Symmetric morphing structures	46

Chapter 3	MATERIALS, EVALUATION PRINCIPLES AND EXPERIMENTAL PROCEDURES	49
3.1	MATERIALS.....	50
3.1.1	Nylon 6,6 fibre	50
3.1.2	Unsaturated polyester resin	51
3.2	FIBRE EVALUATION PRINCIPLES.....	53
3.2.1	Annealing effect on nylon 6,6 fibre	54
3.2.2	Creep and recovery	56
3.2.3	Recovery force	57
3.2.4	X-ray diffraction.....	58
3.3	MECHANICAL EVALUATION OF COMPOSITES - PRINCIPLES	67
3.3.1	Charpy impact testing	68
3.3.2	Three-point bending test	69
3.4	FIBRE PROCESSING AND EVALUATION PROCEDURES	70
3.4.1	Fibre annealing.....	70
3.4.2	Creep and recovery	71
3.4.3	Recovery force measurement.....	72
3.4.4	Scanning electron microscopy	73
3.4.5	Wide-angle X-ray diffraction.....	74
3.5	COMPOSITE PRODUCTION AND EVALUATION PROCUDURES	75
3.5.1	Composite production	75
3.5.2	Charpy impact testing	77
3.5.3	Three-point bending test	78
3.5.4	Optical microscopy	79
Chapter 4	PRELIMINARY WORK AND INVESTIGATIONS.....	80
4.1	STRETCHING RIG CALIBRATION.....	81
4.1.1	Small stretching rig calibration	82
4.1.2	Large stretching rig calibration	83
4.1.3	Effectiveness of stress generated from the stretching rigs.....	84
4.2	NYLON FIBRE EVALUATION	86
4.2.1	SEM topography	86
4.2.2	X-ray diffraction.....	88

4.2.3	Creep and recovery	91
4.2.4	Recovery force	92
4.3	RESIN SELECTION FOR VPPMC PRODUCTION	94
4.3.1	Resin curing characteristics.....	94
4.3.2	Charpy impact testing	99
4.3.3	Resin selection	101
4.4	CONCLUSIONS.....	103
Chapter 5	VISCOELASTIC BEHAVIOUR OF NYLON 6,6 FIBRE AND ITS EFFECT ON VPPMCS	105
5.1	INTRODUCTION	106
5.2	BACKGROUND	107
5.2.1	Viscoelastic behaviour	107
5.2.2	Time-stress superposition principle	109
5.2.3	Elastic modulus	111
5.3	EXPERIMENTAL PROCEDURES	112
5.3.1	Creep and recovery	112
5.3.2	Viscoelastic recovery force	112
5.3.3	Wide-angle X-ray diffraction.....	113
5.3.4	Production and evaluation of composite samples	113
5.4	RESULTS AND DISCUSSION	114
5.4.1	Fibre topography	114
5.4.2	Fibre creep and recovery characteristics	115
5.4.3	Stress rupture testing	117
5.4.4	Predicting the ‘true’ elastic modulus	118
5.4.5	Linear viscoelasticity	119
5.4.6	Long-term viscoelastic behaviour	125
5.4.7	Effect of viscoelastic creep strain on VPPMC performance.....	127
5.4.8	Recovery force	129
5.4.9	X-ray diffraction.....	130
5.4.10	Viscoelastic deformation mechanisms in nylon 6,6 fibre	133
5.4.11	Viscoelastic prestress mechanisms within VPPMCs	135
5.5	CONCLUSIONS.....	137

Chapter 6	TOWARDS OPTIMISATION OF LOAD-TIME CONDITIONS FOR PRODUCING VPPMCS	140
6.1	INTRODUCTION	141
6.2	PRINCIPLES	142
6.2.1	Creep time reduction	142
6.2.2	Time-temperature superposition principle	143
6.3	EXPERIMENTAL PROCEDURES	146
6.3.1	Creep and recovery	146
6.3.2	Preparation and evaluation of composite samples	147
6.3.3	Viscoelastic recovery force	148
6.4	RESULTS AND DISCUSSION	149
6.4.1	Creep and recovery characteristics.....	149
6.4.2	Recovery force	152
6.4.3	Short-term impact performance	154
6.4.4	Long-term impact performance.....	158
6.4.5	Aging effects and the time-temperature boundary.....	159
6.4.6	Towards optimisation of load-time conditions	161
6.4.7	Further optimisation	163
6.4.8	Prestress mechanisms.....	166
6.5	CONCLUSIONS.....	168
Chapter 7	MORPHING (BISTABLE) COMPOSITES BASED ON VISCOELASTICALLY GENERATED PRESTRESS	170
7.1	INTRODUCTION	171
7.2	PRINCIPLE	171
7.3	EXPERIMENTAL PROCEDURES	174
7.3.1	Production of VPPMC strips.....	174
7.3.2	Production of the bistable composite structure	174
7.3.3	Evaluation of the bistable composite assembly	175
7.3.4	Evaluation of beam deflection	176
7.4	FINITE ELEMENT METHOD	177
7.4.1	Principle	177
7.4.2	Material properties	178
7.4.3	FE model	180

7.5	RESULTS AND DISCUSSION	182
7.5.1	Static evaluation of the bistable structure	182
7.5.2	Static evaluation of the beam structures.....	184
7.5.3	Dynamic (snap-through) testing details	185
7.5.4	Effect of test speed on the snap-through characteristics	187
7.5.5	Effect of indenter geometry on the snap-through characteristics.....	189
7.5.6	Effect of sample age on the snap-through characteristics.....	191
7.5.7	FE analysis	193
7.5.8	Bistability mechanisms	201
7.6	CONCLUSIONS.....	203
 Chapter 8 OVERALL FINDINGS, FUTURE WORK AND CONCLUSIONS		205
8.1	OVERALL FINDINGS	206
8.1.1	Preliminary investigations.....	206
8.1.2	Viscoelasticity of nylon 6,6 fibre and its effect on VPPMCs	207
8.1.3	Towards process optimisation for VPPMC production	208
8.1.4	Application of VPPMCs to morphing structures	210
8.2	FUTURE WORK.....	211
8.2.1	Investigation into fibre-matrix interfaces.....	211
8.2.2	Fibre stretching apparatus	212
8.2.3	Morphing composite structures.....	212
8.3	CONCLUSIONS.....	213
 REFERENCES.....		214
 APPENDIX		230
APPENDIX-A EXPERIMENTAL DATA FOR CHAPTER 4		231
APPENDIX-B EXPERIMENTAL DATA FOR CHAPTER 5.....		238
APPENDIX-C EXPERIMENTAL DATA FOR CHAPTER 6.....		239

LIST OF FIGURES

Figure 2-1	Bounds on stiffness for a two-phase composite. HS refers to the Hashin-Shtrikman bounds for isotropic composites.	13
Figure 2-2	Schematic representation showing the utilisation of elastic fibre prestressing to produce EPPMCs: (a) applying tension to polymeric fibre; (b) stresses generated following the matrix curing process, as the fibre remains in tension; (c) releasing of the tensile load, and compressive stresses induced within a EPPMC.....	16
Figure 2-3	Elastic fibre prestressing method adopted by Zhigun [47].	25
Figure 2-4	Schematic representation of utilising the viscoelastic fibre prestressing principle for a PMC: (a) applying tension to polymeric fibre; (b) moulding process followed tensile load removal; (c) residual stresses within a VPPMC.	27
Figure 2-5	Polariscope image of nylon 6,6 monofilament embedded in polyester resin samples [11].	28
Figure 2-6	Schematic representation of highly ordered crystal and amorphous structures: (a) highly ordered crystal; (b) tangled amorphous; (c) lamellae; (d) spherulitic semi-crystalline structure.....	34
Figure 2-7	Schematic representation of the microfibrillar model for the fibre structure: A is interfibrillar tie molecule; B is intrafibrillar tie molecule; the fibre axis is vertical. Redrawn from [108].	37
Figure 2-8	Schematic representation of ‘Swiss-cheese’ model of the fibre structure. Crystallites are periodically arranged to form microfibrils and are surrounded by the amorphous phase. Redrawn from [107].	38
Figure 2-9	Schematic representation of a mechanical spring-dashpot model: (a) deformation under tensile loading; (b) recovery following load removal.	39
Figure 2-10	Basic shapes of laminates: (a) reference state at stress-free temperature; (b) a saddle shape at room temperature; (c) a cylindrical shape with curvature in y -direction; (d) alternative cylindrical shape with curvature in x -direction.	42
Figure 2-11	Size effect on the room-temperature shapes of un-symmetric laminates.	45
Figure 3-1	Formula to produce nylon 6,6 and its repeating unit.	50

Figure 3-2	Schematic representation of micro-structures of nylon 6,6 fibre and intermolecular hydrogen bonding formed between carbonyl oxygen and amide hydrogen within the polyamide chains.....	51
Figure 3-3	Schematic representation of cross-linking reaction within a resin curing system. A and B are repeating units within an unsaturated polyester resin; S is a cross-linking agent, e.g. styrene.	53
Figure 3-4	Schematic representation of annealing effect on molecular structure in oriented nylon 6,6 fibre: (a) oriented molecules; (b) molecular chain folding after annealing. The dots represent a polymer repeat period or some of the hydrogen bond positions. Redrawn from [150].	55
Figure 3-5	Schematic of the polymeric fibre creep-recovery strain cycle.....	57
Figure 3-6	Schematic representation of the polymeric fibre recovery force-time characteristics generated from a creep-recovery cycle.	58
Figure 3-7	Schematic representation of experimental set-up for X-ray diffraction....	59
Figure 3-8	Incident X-ray striking a periodic crystalline solid, as represented by a series of planes with an equal inter-planar distance d	60
Figure 3-9	Schematic representation of crystal phase structures for: (a) basic triclinic unit cell; (b) α -crystal; (c) β -crystal. Solid lines in (b) and (c) represent sheets of molecules seen from an edgewise view.	61
Figure 3-10	Example of profile analysis of an equatorial diffraction pattern from nylon 6,6 fibre used in this work.....	63
Figure 3-11	Schematic representation of the α -form molecular unit cell structure in nylon 6,6 fibre, showing the associated diffractive crystalline planes...	65
Figure 3-12	Schematic representation of the principle for flatwise Charpy impact testing: (a) basic set-up of a impact tester; (b) sample arrangement during impact test.	69
Figure 3-13	Schematic representation of the principle for the three-point bending test.	70
Figure 3-14	Fan-assisted oven used for fibre annealing. Inner view shows the yarns were placed in aluminium trays to ensure uniform heat treatment and prevent movement from air flow.....	70
Figure 3-15	Schematic representation of the bespoke stretching rigs (not to scale): (a) small stretching rig, mainly used for creep and recovery strain tests; (b) large stretching rig, used to provide greater amounts of stretched fibre to produce composite samples with higher fibre volume fractions.....	71
Figure 3-16	Schematic representation of recovery force measurement apparatus. The lower bobbin was height-adjustable, allowing the loose fibre yarn to contract to a fixed strain. The cradle on the top, positioned on the force	

	sensor, enabled the contraction forces generated from yarn recovery to exert compression on the sensor. Redrawn from [99].....	73
Figure 3-17	Equipment used for scanning electron microscopy: (a) SEM operation system; (b) sputter gold coater.	74
Figure 3-18	Experimental set-up for the X-ray diffraction analysis. Inset shows a typical WAXD sample mounted with nylon 6,6 yarns.	75
Figure 3-19	Flowchart of the composite sample production and evaluation process...	76
Figure 3-20	Aluminium open moulds used for composite production. Test and control counterparts were moulded simultaneously to ensure no differences between samples other than fibre prestressing.....	77
Figure 3-21	Experimental set-up for Charpy impact testing: (a) impact testing rig; (b) sample arrangement with schematic representation of impact direction, i.e. fibre-rich region facing away from the pendulum.	78
Figure 3-22	Experimental set-up of the three-point bending test to determine the elastic modulus of a beam sample.....	79
Figure 4-1	Schematic diagram for calibration of the stretching rigs: (a) SSR calibration; (b) LSR calibration.	82
Figure 4-2	Mean calibration results from the small stretching rig. Solid line is from a linear fit, and the corresponding equation is shown. Calibration data are presented in Appendix-A, Table A-1.....	83
Figure 4-3	Mean calibration data from the large stretching rig. Solid line is from the linear fit, and the corresponding equation is also shown. Calibration data are presented in Appendix-A, Table A-2.	84
Figure 4-4	SEM micrographs of the nylon 6,6 fibres: (a) as-received new yarn (ARN); (b) annealed new yarn (ANN); (c) as-received old yarn (ARO); (d) annealed old yarn (ANO). Micrographs were taken ~212 h after the annealing. ...	87
Figure 4-5	Diameters of the nylon 6,6 fibre of both new and old yarn before and after annealing; error bars are standard errors. Measured diameter results are presented in Appendix-A, Table A-5.	88
Figure 4-6	X-ray diffraction patterns of both fibre materials before and after annealing. Samples were tested ~45 h after annealing.....	89
Figure 4-7	Creep and recovery strain-time data for the annealed new and old yarns. Line-fits and parameters were obtained from the Weibull based model [96] using <i>CurveExpert 1.4</i> ; r is the corresponding correlation coefficient.	92
Figure 4-8	Viscoelastic recovery force from both new and old nylon 6,6 yarns. The force output data of the old yarn is from [99].....	93

Figure 4-9	Schematic illustration of experimental set-up for resin exothermic tests.	95
Figure 4-10	Curing process for the general purpose resin, mixed with 2% catalyst. Ambient temperature range was 20.1° to 21.9°C.	96
Figure 4-11	Curing process for the polylite 32032-00 resin, mixed with 2% catalyst. Ambient temperature range was 20.2° to 21.3°C.	97
Figure 4-12	Curing process for the DSM synolite 0382-A-1 resin, mixed with 2% catalyst. Ambient temperature range was 20.2° to 21.6°C.	97
Figure 4-13	Curing process for the S-70361TA-isophthalic polyester laminating resin, mixed with 2% catalyst. Ambient temperature range was 20.6° to 21.6°C.	98
Figure 4-14	Curing process for the CFS casting resin, mixed with 2% catalyst. Ambient temperature range was 20.1° to 21.5°C.	98
Figure 4-15	Comparison of resin properties with peak curing temperature. Data points are from Tables 4-3 and 4-4. Dashed line is from a linear fit; the corresponding equation is also shown.	100
Figure 4-16	Plot of increase in impact energy absorption of VPPMC samples against the impact toughness of resin only samples. The triangle data point is from Ref [92]; the round circle data point is from Ref [12]. Dashed line is from a linear fit, together with the corresponding equation.	101
Figure 5-1	Schematic of the creep and recovery characteristics of a polymeric material: (a) creep and recovery behaviour under constant stress; (b) creep and recovery cycle following load removal at t_c , and subsequent recovery (through stress) at a fixed strain.	108
Figure 5-2	Schematic of stress-strain behaviour for elastic and viscoelastic materials at two values of elapsed time t' and t'' . Redrawn from [16].	109
Figure 5-3	SEM micrographs of the nylon 6,6 fibres, showing test (24 h creep at 590 MPa) and control (no creep) samples. Both fibres were annealed simultaneously. While the test sample was subjected to creep, the control sample was positioned nearby to ensure the same ambient conditions. Micrographs were taken 72 h (to allow for sample preparation) after creep load removal for the test sample.	114
Figure 5-4	Strain-time data for (a) 24 h creep and (b) recovery at the five stress values with curve-fits from Equations 3-1 and 3-2.	115
Figure 5-5	Plot of instantaneous strain ϵ_i and elastic recovery strain ϵ_e values at each creep condition. These values are obtained from Equations 3-1 and 3-2.	116

Figure 5-6	Strain-time data from nylon 6,6 fibre under 665 MPa creep stress. Dashed line shows the development of Stage III in creep behaviour, which quickly leads to fibre failure.	118
Figure 5-7	Plot of elastic strain ϵ_e , predicted from Equation 3-1, versus creep stress σ values. A linear regression was applied, indicating that the modulus value of nylon 6,6 fibre is 4.61 GPa. Dashed lines show a ‘worst case’ gradient on both sides of the best linear fit with intercepts set as zero, indicating the uncertainty in the modulus result.	119
Figure 5-8	Creep strain isochrones of nylon 6,6 fibre at 1 min, 1 h and 24 h respectively. Linear regression shows the trends.	120
Figure 5-9	Shift factor α_c for each creep stress value; data points are from Table 5-2 (330 MPa creep stress is set as the reference).	121
Figure 5-10	Strain-time relationships normalised to the 330 MPa creep condition through shift factors α_c from Table 5-2.	122
Figure 5-11	Shift factor α_r for each recovery curve; data points are from Table 5-3 (recovery strain from 330 MPa creep is set as the reference).	124
Figure 5-12	Strain-time relationships after normalising to the 330 MPa recovery condition through shift factors α_r , as shown in Table 5-3.	124
Figure 5-13	Master curve for creep strain versus time in nylon 6,6 fibre, obtained from TSSP, using data from Figure 5-4 (a).	125
Figure 5-14	Plot of the time-stress shift factor, α_σ , as a function of stress difference. Reference creep stress is 330 MPa. The line and equation are from linear regression, r is the correlation coefficient.	126
Figure 5-15	Recovery master curve obtained from TSSP using data from Figure 5-4 (b) plotted against time. Applied shift factor values are the same as shown in Figure 5-14, but in a reversed order.	127
Figure 5-16	Charpy impact test results from Table 5-4; error bars represent the standard error.	129
Figure 5-17	Viscoelastic recovery force generated from the three creep conditions. Data for the 330 MPa, 24 h creep condition are from Section 4.2.4.	130
Figure 5-18	Comparison of WAXD patterns for the nylon 6,6 fibre under the three creep conditions. Sample age (following load removal) was 20 h for 330 MPa, 44 h for 460 MPa and 68 h for 590 MPa.	131
Figure 5-19	Changes (%) in microstructural parameters with creep stress in terms of crystallinity, apparent crystal size (ACS), index of crystalline perfection (ICP) and amorphous peak position ($2\theta_a$).	132

Figure 5-20	Schematic representation of creep deformation within nylon 6,6 fibre. Solid lines in crystalline regions represent both molecular chains and sheets; dashed lines represent TTMs.	134
Figure 6-1	Reducing the fibre creep time from 24 h to t_n by equalising the creep strain from a higher stress, $\varepsilon_c(t_n)$, with $\varepsilon_c(24)_{std}$	142
Figure 6-2	Plot to determine the time-temperature shift factor a_T using published data for creep [193] and stress relaxation [201] in nylon 6,6 fibre. Reference temperature was 25°C where $\log a_T = 0$; the solid line and the equation shows the linear regression, and r is the correlation coefficient. Redrawn from [98].	145
Figure 6-3	Arrangements of samples within a tray (a) before and (b) after being subjected to the accelerated aging. T stands for test sample, and C is the control (non-prestressed) counterpart.	147
Figure 6-4	Strain-time data for (a) 24 h creep and (b) recovery at the three stress values with curve-fits from Equations 3-1 and 3-2. Redrawn from Figure 5-4.	149
Figure 6-5	Plots of creep strain to values of t_n for 460 MPa and 590 MPa, and the corresponding recovery strain-time data. Curve-fits and associated parameters are from Equations 3-1 and 3-2, as shown in Section 3.2.2.	150
Figure 6-6	Recovery curves from Figures 6-4 and 6-5, using Equation 3-2, plotted on common axes to show their offsets.	151
Figure 6-7	Recovery force measurements from nylon 6,6 fibre after being subjected to the standard creep condition (data from Figure 4-16) and the 590 MPa 37 min condition.	153
Figure 6-8	Charpy impact test results from Table 6-2; error bars represent the standard error.	156
Figure 6-9	Representative test and control samples following Charpy impact testing, showing similar debonding and fracture characteristics from the three creep conditions; note the larger area of fibre-matrix debonding in the test samples.	156
Figure 6-10	Increase in impact energy against time for VPPMC samples produced under the two creep conditions. Data are collected from Tables 6-2, 6-3 and 6-4.	159
Figure 6-11	Time-temperature boundary established in accordance with Figure 6-2 to an equivalent of 20,000 years at 20°C, showing the reduction in known life with increasing ambient temperature. Redrawn from [98].	160
Figure 6-12	Plot showing the relationship between applied creep stress σ and required t_n for loading. Round data points are calculated using the basic principle as	

	shown in Figure 6-1; the square point predicts the creep stress requirement for a stretching period of 20 minutes.	161
Figure 6-13	Charpy impact test results from Table 6-6; the three creep conditions are equivalent in terms of final viscoelastic creep strain for $\varepsilon_c(24)$ at 460 MPa, i.e. ~4.0%; error bars represent the standard error.	164
Figure 6-14	Plot showing relationship between applied creep stress σ and required t_n for loading to a level of ~4.0% viscoelastic creep strain ε_c , i.e. yarns were stretched under 460 MPa for 24 h. Data points were calculated using the basic principle as shown in Figure 6-1.....	165
Figure 6-15	Summary of increase in impact energy from samples tested at 336 h (two weeks), a creep stress of 590 MPa was adopted for all runs. Various creep strain levels were achieved through longer exposure to creep loading; i.e. 37 min for ~3.4%, 134 min for ~4.0% and 24 h for 4.8%. Data were collected from Tables 5-4, 6-2, and 6-6.	167
Figure 7-1	Schematic representation of bistable VPPMC principles, showing the VPPMC assembled structure in both states (Shapes I and II) and also the prestress-generated deflection δ in accordance with Equation 7-2.....	173
Figure 7-2	Schematic three point bending set-up used to evaluate the snap-through characteristics of the VPPMC-based test samples: (a) is the point-force indenter; (b) is the short-length indenter.....	176
Figure 7-3	Effective modulus of glass fibre mat reinforced polyester resin composite as a function of fibre volume fraction. The dashed line was from Equation 7-4 with $k = 3/8$; the black solid lines were fitted with the ‘rule of mixtures’ relationships (Section 2.2).....	179
Figure 7-4	Boundary and loading conditions on the plate: (a) constraints applied in Step-1; (b) constraints applied in Step-2.....	180
Figure 7-5	An assembled VPPMC-based bistable sample (test), compared with the equivalent control (non-prestressed) sample.....	182
Figure 7-6	Static deflection of the three bistable samples with age. The insert shows the deflection position; the dashed curve shows the trend.....	183
Figure 7-7	Representative cross-sectional view of a VPPMC strip attached to fibreglass-resin sheet, with estimated location of the nylon fibre centroid... ..	184
Figure 7-8	Static deflection of VPPMC strip bonded to fibreglass sheet impregnated with the same resin compared with an equivalent control (no prestress) beam sample, ~350 h after manufacture.	185

Figure 7-9	Experimental set-up for point-force snap-through tests. Shape I indicates the first cylindrical stable shape before the test; Shape II is the second cylindrical stable shape after the test.	186
Figure 7-10	Experimental set-up for short-length indenter snap-through tests. The direction of the short-length indenter is perpendicular to the initial cylindrical shape direction (Shape I).....	186
Figure 7-11	Snap-through load response of bistable composite assembly in both directions for 6 mm/min (a, b) and 60 mm/min (c, d).....	188
Figure 7-12	Snap-through from small ripple effect at 60 mm/min.....	189
Figure 7-13	Snap-through load response of bistable composite assembly with short-length indenter loading at 60 mm/min test speed.....	190
Figure 7-14	Short-length snap-through test and typical sample performance before (a) and after (b) the snap-through moment.	190
Figure 7-15	Point-force snap-through loading response of bistable composite assembly at 60 mm/min test speed with sample age of ~4000 h.	192
Figure 7-16	Snap-through tests for the three VPPMC-based bistable assemblies using the point-force indenter at 60 mm/min. Hollow symbols represent the tests at ~500 h; filled symbols at ~4000 h.....	192
Figure 7-17	Loading history for the FE model: (a) temperature change during the simulation process; (b) displacement change of the indenter throughout the modelling period.	194
Figure 7-18	Relationship between predefined temperature change ΔT and deflection of the bistable structure from the FE model during Step-1.	195
Figure 7-19	Simulated stable shape in y -direction generated after Step-1: (a) stress distribution within the whole bistable structure; (b) stress distribution within the mid-fibreglass layer.....	195
Figure 7-20	Snap-through process of the bistable structure through FEA: (a) original plate; (b) first stable cylindrical shape in y -direction; (c) second stable cylindrical shape in x -direction.	196
Figure 7-21	Reaction force versus indenter displacement within the snap-through process for FE simulation, compared to the experimental curves from Section 7.5.4.....	196
Figure 7-22	Development of the snap-through process for a bistable structure panel with pre-defined deflections. Dashed lines show the change in maximum load and critical displacement for snap-through behaviour; inserted figures show the corresponding deformation before (a) and after (b) the critical moment of each feature.	198

- Figure 7-23 FE results for load-displacement curves of bistable structures with different modulus ratios; dashed line shows trend in maximum load.200
- Figure 7-24 FE results of the modulus ratio effect on peak load, critical displacement and model deflection; dashed lines show the trends.201

LIST OF TABLES

Table 2-1	Summary of research into elastic fibre prestressing.	21
Table 2-2	Summary of research into viscoelastic fibre prestressing.	30
Table 3-1	Crystal phase unit cells and dimensions for nylon 6,6 fibre. Note c is along the fibre axis. Data from [143].	62
Table 3-2	Refined α -crystal phase unit cells and dimensions for nylon 6,6 fibre at room temperature. Note c is along the fibre axis. Data from [188].	67
Table 4-1	Charpy impact test results from VPPMC samples fabricated with different stretching rigs and polyester resins. Tests were performed two weeks after sample moulding; SE is the standard error. Individual sample results are presented in Appendix-A, Tables A-3 and A-4.	85
Table 4-2	Microstructural parameters of both materials before and after annealing.	91
Table 4-3	Summary of the resin exothermic tests, data are from Figures 4-10 to 4-14.	96
Table 4-4	Charpy impact test results for resin only and composite samples produced with various resins. Individual test data are presented in Appendix-A, Tables A-6 and A-7.	99
Table 5-1	Summary of the creep and recovery parameter values from data in Figure 5-4 using Equations 3-1 and 3-2; r is the correlation coefficient	117
Table 5-2	Shift factor (α_c) values determined from Equation 5-5, as calculated from the average of five selected creep strain values on the fitting curves at each creep condition, relative to 330 MPa. SE is the standard error.	121
Table 5-3	Shift factor (α_r) values determined from Equation 5-6, as calculated from the average of five selected recovery strain values on the fitting curves at each creep condition, relative to 330 MPa. SE is the standard error.	123
Table 5-4	Charpy impact test results relative to each 24 h creep condition. Samples were tested 336 h after moulding. Individual test data are presented in Appendix-B, Table B-1.	128
Table 5-5	Microstructural parameters for the nylon 6,6 fibre after creep process. .	131

Table 6-1	Summary of the recovery force parameter values from data in Figure 6-7 using Equation 3-3; r is the correlation coefficient.....	154
Table 6-2	Summary of Charpy impact results, tested at 336 h (two weeks) after manufacture. Five sample batches were tested for each prestressing condition (5 test and 5 control samples in each batch); SE is the standard error. Individual test data are presented in Appendix-C, Table C-1.	155
Table 6-3	Summary of Charpy impact results, tested at 4392 h (0.5 years) after manufacture. Five sample batches (5 test and 5 control samples in each batch) were tested for each prestressing condition; SE is the standard error. Individual test data are presented in Appendix-C, Table C-2.....	157
Table 6-4	Summary of Charpy impact results. Samples were subjected to accelerated aging to an equivalent of 20,000 years at 20°C. Each prestressing condition is represented by three batches, with 5 test and 5 control samples in each batch; SE is the standard error. Individual test data are presented in Appendix-C, Table C-3.....	158
Table 6-5	Charpy impact results for VPPMC samples produced with the creep condition of 665 MPa for 20 min; testing was performed at 336 h after manufacture; SE is the standard error. Individual test data are presented in Appendix-C, Table C-4.....	162
Table 6-6	Summary of Charpy impact results, tested at 336 h (two weeks) after manufacture. Five sample batches were tested for each prestressing condition with 5 test and 5 control samples in each batch; SE is the standard error. Individual test data are presented in Appendix-C, Table C-4.	163
Table 6-7	Charpy impact results. Fibre yarns were subjected to 590 MPa for 134 min, and tested at 4392 h after fabrication; SE is the standard error. Individual test data are presented in Appendix-C, Table C-2.	165
Table 7-1	Mechanical properties of the materials involved in the bistable assembly.	178
Table 7-2	Point-force loading snap-through test results from two different loading speeds, 6 mm/min and 60 mm/min.	189
Table 7-3	Snap-through test results for short-length indenter loading at 60 mm/min.	191
Table A-1	Stretching rig calibration data for the SSR as shown in Figure 4-2. SE is the standard error.....	231
Table A-2	Stretching rig calibration data for the LSR as shown in Figure 4-3. SE is the standard error.....	232

Table A-3	Charpy impact test data to evaluate the effectiveness of prestress generated from the stretching rigs, with GPR as the matrix, as presented in Table 4-1. T and C represent prestressed (test) and non-prestressed (control) counterparts, respectively; SE is the standard error.	233
Table A-4	Charpy impact test data to evaluate the effectiveness of prestress generated from the stretching rigs, with SLT as the matrix, presented in Table 4-1. T and C represent prestressed (test) and non-prestressed (control) counterparts, respectively; SE is the standard error.	234
Table A-5	Diameter measurement data for fibre yarn samples. Fibre single filaments were selected from each yarn sample, and three readings were taken from three different locations on each filament. Mean results are presented in Figure 4-5; SE is the standard error.	235
Table A-6	Charpy impact test data for resin only samples, tested at 336 h (two weeks) after moulding. Mean results are shown in Table 4-4; SE is the standard error.	236
Table A-7	Charpy impact test data for nylon-based composite samples (2% V_f), tested at 336 h (two weeks) after moulding. Mean results are shown in Table 4-4; SE is the standard error.	237
Table B-1	Charpy impact test data for nylon-based composite samples, produced under 24 h creep conditions (2% V_f). Samples were tested 336 h (two weeks) after moulding. Mean results are shown in Table 5-4; SE is the standard error.	238
Table C-1	Charpy impact test data for nylon-based composite samples, produced under two creep conditions (2% V_f). Samples were tested 336 h (two weeks) after moulding. Mean results are shown in Table 6-2; SE is the standard error.	239
Table C-2	Charpy impact test data for nylon-based composite samples, produced under various creep conditions (2% V_f). Samples were tested at 4392 h (0.5 years). Mean results are shown in Tables 6-3 and 6-7; SE is the standard error.	240
Table C-3	Charpy impact test data for nylon-based composite samples, produced under two creep conditions (2% V_f). Samples were subjected to accelerated aging to an equivalent of 20,000 years at 20°C before testing. Mean results are shown in Table 6-4; SE is the standard error.	241
Table C-4	Charpy impact test data for nylon-based composite samples, produced under different creep conditions (2% V_f). Samples were tested at 336 h (two weeks) after moulding. Mean results are shown in Tables 6-5 and 6-6; SE is the standard error.	242

ABBREVIATIONS

ANN	Annealed New Yarn
ANO	Annealed Old Yarn
ARN	As-received New Yarn
ARO	As-received Old Yarn
ASTM	American Society for Testing and Materials
BPO	Benzoyl Peroxide
CFRP	Carbon Fibre-reinforced Composite
CFS	CFS Casting Resin
CLT	Classical Lamination Theory
EEST	Elastic Energy Storage Site
EPPMC	Elastically Prestressed Polymeric Matrix Composite
FMR	Force Measurement Rig
GFRP	Glass Fibre-reinforced Composite
GPR	General Purpose Resin
HDPE	High Density Polyethylene
HMW-HDPE	High Molecular Weight-High Density Polyethylene
HS	Hashin-Shtrikman bound
LSR	Large Stretching Rig
MEKP	Methyl Ethyl Ketone Peroxide
PA	Polyamide
PE	Polyethylene
PET	Polyethylene Terephthalate
PLT	Polylite 32032-00 Resin
PMC	Polymeric Matrix Composite
PP	Polypropylene
PSL	Parallel Strand Lumber
SAXD	Small-angle X-ray Diffraction
SEM	Scanning Electron Microscopy
SLT	DSM Synolit 0382-A-1 Resin

SSR	Small Stretching Rig
STA	S-70361TA-isophthalic Polyester Laminating Resin
TSSP	Time-stress Superposition Principle
TTM	Taut-tie Molecule
TTSP	Time-temperature Superposition Principle
UHMWPE	Ultra-high Molecular Weight Polyethylene
UPS	Unsaturated Polyester Resin
UV	Ultraviolet
VEST	Viscoelastic Energy Storage Site
VIRALL	Vinyon-reinforced Aluminium Laminate
VPPMC	Viscoelastically Prestressed Polymeric Matrix Composite
VR	Voigt-Reuss bound
WAXD	Wide-angle X-ray Diffraction
WLF	Williams-Landel-Ferry
XRD	X-ray Diffraction

SYMBOLS

A	Area
ACS	Apparent Crystal Size
AR_{tr}	Aspect Ratio at the Bifurcation Point
CI	Crystallinity Index
d_{hkl}	Inter-planar Distance of the (hkl) Crystalline Plane
E	Elastic Modulus
e	Distance between Beam and Fibre Centroids
F	Applied Force
f	Fractional Free Volume
$FWHM$	Full-width-half-maximum
G	Shear Modulus
ICP	Index of Crystalline Perfection
K	Bulk Modulus
L	Edge Length of the Square Laminate
M_T	Mechanical Properties of Test Sample Mean
M_C	Mechanical Properties of Control Sample Mean
P	Force generated from the Prestress
R_E	Elastic Modulus Ratio
ΔT	Change in Temperature
t	Single Ply Thickness
V_{GF}	Fibreglass Volume Fraction
V_f	Fibre Volume Fraction
α	Thermal Expansion Coefficient
α_ε	Strain Shift Factor
α_σ	Creep Stress Shift Factor
α_T	Temperature Shift Factor
α_c	Creep Strain Shift Factor
α_r	Recovery Strain Shift Factor
β	Shape Parameter

δ	Deflection
ε	Strain
η	Characteristic Life Parameter
θ	X-ray Diffraction Angle
λ	Wavelength of the X-rays
μ	Poisson's Ratio
ν_c	Cross-link Density
ρ	Density
σ	Tensile Stress
σ_v	Viscoelastic Recovery generated Stress
Γ	Impact Absorbed Energy

Chapter 1

INTRODUCTION

SUMMARY

This chapter is prelude to the whole thesis. The aim and objectives of the work are listed, and motivation behind the project is provided. This is followed by an overview of each chapter. Briefly, the thesis is focused on the investigation into facilitating the future industrial application of viscoelastically prestressed polymeric matrix composite (VPPMC) technology. VPPMCs are produced by stretching polymeric fibres to induce tensile creep; the stretching load is then released before the strained fibres are moulded into a resin matrix. Following matrix curing, the viscoelastically recovering fibres created prestressing effects, which can improve mechanical properties. By considering the first steps towards process optimisation of load-time conditions, the fibre stretching period is significantly reduced, thereby facilitating the manufacture of VPPMCs. Moreover, since there is increasing interest in shape-adaptive structures using composite materials, the potential application of VPPMC technology to morphing structures is also investigated. This could open new opportunities for VPPMCs in industrial applications.

This work has been driven mainly through the use of comprehensive experimental investigations; however, a feasibility study is also carried out on the applicability of finite element analysis to model the snap-through behaviour of a bistable morphing structure.

1.1 INTRODUCTION

Viscoelastically prestressed polymeric matrix composites (VPPMCs) are produced by applying a tensile load to polymeric fibres to induce tensile creep; then the load is released and the strained fibres are embedded into a matrix. Once the matrix has cured, the viscoelastically recovering fibres impart compressive stresses to the surrounding matrix (balanced by residual tension in the fibres). The prestress effect can improve mechanical properties, especially impact toughness and flexural stiffness [1, 2], and it has been successfully demonstrated with nylon 6,6 fibres and UHMWPE fibres [3, 4]. This is a novel method for improving mechanical properties, which can avoid the need to increase composite mass or sectional thickness. It also overcomes the potential drawbacks that exist in more conventional elastically prestressed polymeric matrix composites, i.e. restrictive processing methods and possible longer term deterioration of prestress effects. Therefore, there are considerable opportunities for VPPMCs to replace other materials in industrial applications that need superior mechanical properties [2, 5].

Previous studies have demonstrated the basic VPPMC performance characteristics relating to tensile, flexural and Charpy impact behaviour [1, 5-7]. Initially, studies were based on nylon fibre VPPMCs, though other mechanically superior polymeric fibres have been subsequently under investigation, i.e. UHMWPE fibres and nylon commingled with aramid fibres [3, 4, 8]. A basic understanding of the prestress mechanisms has been obtained but there are growing needs to investigate further the processing of VPPMCs and their potential applications. This can be facilitated by research into process optimisation of load-time conditions for viscoelastic fibre prestressing, and their application to morphing composites. This should improve confidence in the ability of VPPMCs to perform successfully in future industrial applications. It is these considerations which justify the nature of this research.

1.2 AIM AND OBJECTIVES

The aim of this research is to facilitate the industrial application of VPPMCs. This is expected to be achieved through several objectives. Briefly, investigation into the viscoelastic behaviour of nylon 6,6 fibre can provide an understanding of viscoelastic deformation mechanisms within the fibre material, and further promote the identification of prestress mechanisms within a VPPMC. In addition, this also provides the basis for research into process optimisation of load-time conditions for VPPMC production. An additional consideration focuses on the potential application of VPPMCs to morphing structures. Therefore, the specific objectives are as follows:

(i) Viscoelastic behaviour of nylon 6,6 fibre

Investigate the viscoelastic behaviour of nylon 6,6 fibre under various creep conditions and its effect on the mechanical performance of VPPMCs, to offer a further understanding of viscoelastic mechanisms within a VPPMC.

(ii) Towards optimisation of load-time conditions for producing VPPMCs

Investigate the effect of fibre creep load-time conditions on the mechanical properties of VPPMCs to optimise the force output for viscoelastic fibre prestressing; also to facilitate opportunities for the future industrial production of VPPMCs.

(iii) Application to morphing structures

Investigate the potential application of VPPMCs to morphing structures, i.e. a bistable composite structure, which can snap from one stable shape to another under external stimulation. This could be useful for aerofoil applications, e.g. aircraft, wind turbine blades.

1.3 MOTIVATION

The concept of the VPPMC was invented by Dr Kevin Fancey at the University of Hull in the 1997 [9]. There is a well-developed understanding of prestress mechanisms within a VPPMC from the scientific point of view; however, more research needs to be considered towards the industrial application of VPPMC technology. To date, for viscoelastic fibre prestressing, all previous research on VPPMCs has utilised a creep loading period of 24 h [1-8, 10-12] with ~330 MPa stress. Though it is a convenient period for laboratory research, such a lengthy duration would be less practical for VPPMC production in a commercial environment; i.e. it is both time consuming and unlikely to be economically viable. Therefore, this project considers the first steps towards process optimisation of load-time conditions to facilitate the production of VPPMCs for industrial applications. Moreover, a feasibility study on the potential application of VPPMCs as morphing structures is also conducted; this is expected to open new opportunities for VPPMC technology.

1.4 THESIS OVERVIEW

This section provides an overview of the main content in each chapter, to offer a quick index for finding information of specific interest. It should be noted that to facilitate understanding, each chapter is essentially ‘self-contained’. Therefore, although Chapter 2 is a general literature review, more specific review details are provided where appropriate in subsequent chapters. Similarly, for clarity, some chapters (after Chapter 3) include sections on experimental procedures, where specific testing methods and sample preparation details relevant to those chapters are provided.

Chapter 2-General literature review

Chapter 2 provides a general review of previously published literature that relates to this research. This includes an introduction on composite materials and mechanical theory of composite stiffness, followed by the principles and developments of prestressed

composites in terms of elastically and viscoelastically generated prestress. The main reasons for mechanical benefits from fibre prestressing are summarised in a prestress mechanisms section, and this is categorised by four aspects. Viscoelastic mechanisms within a polymeric fibre are reviewed in terms of microstructural and mechanical models. Finally, the development of morphing composite structures produced by utilising thermal residual stresses and elastic fibre prestressing is given.

Chapter 3-Materials, evaluation principles and experimental procedures

Chapter 3 gives an overview of the materials and evaluation techniques involved in this research. General information on the fibre and matrix materials used is given, followed by a summary of the basic principles and theoretical analysis that is involved in this research. Experimental procedures and evaluation techniques are provided in terms of (i) fibre processing and (ii) composite production.

Chapter 4-Preliminary work and investigations

Chapter 4 focuses on preliminary studies that were required to support the main research project. In addition to the need to become familiar with the equipment and experimental procedures, the following work was required. First, the stretching rigs used to induce viscoelastic creep into the polymeric fibres were re-calibrated to reduce system errors; second, newly obtained nylon 6,6 yarn was evaluated and compared to the previously used (old) yarn in several aspects to determine possible structural differences; finally, a replacement resin for the production of VPPMCs was required and selection was based on measurement of the resin exothermic curing characteristics and impact energy absorption properties.

Chapter 5-Viscoelastic behaviour of nylon 6,6 fibre and its effect on VPPMCs

Chapter 5 investigates the viscoelastic behaviour of nylon 6,6 fibre and its effect on the impact behaviour of VPPMCs. Large creep stresses varying from 330 MPa to 590 MPa were applied to the fibre yarns to determine creep strain-time performances, and corresponding recovery strain was monitored in situ. The yield properties of the fibre

were determined from creep rupture tests where a stress of 665 MPa was applied. A latch-based Weibull model, as previously adopted, enabled prediction of the ‘true’ elastic modulus through purely elastic deformation from the creep-recovery data. The time-stress superposition principle was applied to predict the long-term performance of the material. Finally, the effect of viscoelastic creep strain level on the impact behaviour of VPPMCs was evaluated through Charpy impact testing.

Chapter 6-Towards optimisation of load-time conditions for producing VPPMCs

Chapter 6 presents the optimisation of load-time conditions for producing VPPMCs. This is based on the viscoelastic behaviour of nylon 6,6 fibre as discussed in Chapter 5. The Weibull-based model allows prediction of the viscoelastic creep strain at each creep condition, which offers opportunities to reduce processing time for fibre stretching. Since prestress benefits within a VPPMC are determined by the viscoelastic recovery of polymeric fibres, the prestress levels could be represented by the magnitude of viscoelastic creep strain. Therefore, the same creep strain level could be attained by employing higher creep stress over a shorter term, enabling the standard 24 h creep condition to be reduced to tens of minutes. The effectiveness of the basic principle was verified through Charpy impact testing, and further consideration was focused on the optimisation of load-time conditions for VPPMC production.

Chapter 7-Morphing (bistable) composites based on viscoelastically generated prestress

Chapter 7 outlines the experimental and numerical investigations into the application of VPPMCs to morphing structures. A novel form of shape-changing bistable structure has been successfully developed through the use of viscoelastically generated prestress. Bistability was achieved through pairs of deflecting VPPMC strips, which were orientated to give opposing cylindrical configurations within a thin, flexible resin-impregnated fibreglass sheet. This arrangement enabled the structure to ‘snap through’ between one of the two states from external stimulation. Snap-through behaviour of the bistable structure was investigated both experimentally and through modelling. The effects of loading speed, loading geometry, and sample-age on the snap-through properties were presented through experimental evaluation. A feasibility study of finite element analysis

was then carried out to investigate the development of bistability, and the influence of modulus ratio on the snap-through characteristics. Experimental and numerical simulation results showed good agreement with the snap-through behaviour of the bistable structure. From this, a possible snap-through mechanism was proposed.

Chapter 8-Overall findings, future work and conclusions

Chapter 8 summarises overall findings from the work in this thesis; this is followed by potential paths for future work and finally, the conclusions are presented.

1.5 WORK DISSEMINATION

This section lists the peer-reviewed journal publications and conference presentations completed as part of the work outlined in this thesis.

Award

A CIMComp Travel Grant awarded by EPSRC Centre for Innovative Manufacturing in Composites (CIMComp). Financial support was provided towards the travel, registration and subsistence costs to attend the ‘10th International Conference on Composite Science and Technology (ICCST/10)’ held on 2-4th September, 2015, Portugal.

Papers for journal publication (peer-reviewed)

- (i) **Bing Wang** and Kevin S. Fancey. Towards optimisation of load-time conditions for producing viscoelastically prestressed polymeric matrix composites. *Composites Part B-Engineering*, 2016, 87: 336-342.

- (ii) **Bing Wang**, Chao Ge, Kevin S Fancey. Snap-through behaviour of a bistable structure based on viscoelastically generated prestress. *Composites Part B-Engineering* (Accepted), 2016.
- (iii) **Bing Wang** and Kevin S Fancey. A bistable morphing composite using viscoelastically generated prestress. *Materials Letters*, 2015, 158: 108-110.
- (iv) **Bing Wang** and Kevin S Fancey. Application of time-stress superposition to viscoelastic behavior of nylon 6,6 fiber and its ‘true’ elastic modulus. (Submitted).
- (v) **Bing Wang** and Kevin S Fancey. Effect of creep strain level on the impact performance of viscoelastically prestressed polymeric matrix composites. (Drafted).
- (vi) Chao Ge, **Bing Wang**, Kevin S. Fancey. An evaluation of the scanning electron microscope mirror effect to study viscoelastically prestressed polymeric matrix composites. (Submitted).

Papers for conference proceedings

- (vii) **Bing Wang** and Kevin S Fancey. Shape-changing (bistable) composites based on viscoelastically generated prestress. *10th International Conference on Composite Science and Technology Proceeding (ICCST/10)*. 2015, Portugal. Doi: 10.13140/RG.2.1.1735.6249.
- (viii) Chao Ge, **Bing Wang**, Kevin S Fancey. Techniques to investigate viscoelastically generated prestress in polymeric composites. *10th International Conference on Composite Science and Technology Proceeding (ICCST/10)*. 2015, Portugal. Doi: 10.13140/RG.2.1.2784.2004.

Chapter 2

GENERAL LITERATURE REVIEW

SUMMARY

This chapter provides a review of relevant previous research into prestressed composites and morphing structures. Following the basic introduction to composite materials and mechanical theory of composite stiffness, the principles and developments of prestressed composites in terms of elastically and viscoelastically generated prestress are given. Prestress mechanisms are categorised into four aspects, which are considered to form the main reasons for mechanical benefits from fibre prestressing. To promote the understanding of viscoelastic mechanisms within a polymeric material, previously developed microstructural and mechanical models of semi-crystalline fibres are summarised. Finally, morphing composite structures are reviewed in terms of the development of un-symmetric and symmetric morphing structures.

2.1 INTRODUCTION

A composite material is a three-dimensional combination of at least two chemically or physically different materials, and usually possesses superior properties over the single constituent material [13]. Normally, composite materials are composed of two phases: a strong and stiff component is present, termed as reinforcement, which is embedded in a softer constituent, named as matrix. The reinforcement is in the form of fibre, fabric or particles; the matrix can be metal, ceramic or polymer material. There is considerable scope for tailoring their structures to suit various conditions. Therefore, they have been used in a wide variety of applications [14]. Polymeric matrix composites (PMCs) which are produced with polymeric matrices, i.e. thermosets and thermoplastics, are the most established engineering composite materials to date. Continuous fibre reinforced PMCs have been used in the aircraft industry since the 1950s [15], and have seen a rapid growth during the last seventy years, especially fibre reinforced thermoset resin composites. Fibres can provide strength and stiffness to the composite, while thermoset resins protect fibres from chemicals and moisture. Owing to their advantages of low weight, corrosion resistance, high fatigue strength, faster assembly and outstanding damping properties, PMCs are becoming an essential part of materials that are extensively used within aircraft structures, electronic packaging, automotive industries and medical equipment.

The PMCs involved in this thesis use thermoset resins as the matrix materials. PMCs can be manufactured using a wide variety of processing techniques, including hand lay-up, hot-pressing, vacuum bagging, pressure bagging, resin transfer moulding, filament winding, pultrusion, extrusion and autoclave moulding techniques [16, 17]. Here, to facilitate the composite manufacture, hand lay-up using open-cast moulding was adopted throughout the thesis. The mechanical performance of composite materials is determined by the individual properties of reinforcements and matrix materials that are used, as well as the processing methods. This results in composites having a significant advantage over traditional homogeneous engineering materials, in that there can be considerable control over the structure during composite production, hence they can be manufactured with the desired properties [18].

2.2 MICROMECHANICS OF COMPOSITE STIFFNESS

The properties of composites are greatly dependent on microstructure [18]. It is well-known that for a two-phase composite with known fibre volume fraction (V_f), the simplest model to predict the effective modulus is the rule of mixtures, which is represented by the Voigt-Reuss (VR) bounds [19-23]. The Voigt upper bound assumes the fibre reinforcement and matrix are arranged in parallel and subject to the same stress; this is known as the iso-strain rule of mixtures. In the Reuss lower bound, the applied stress is perpendicular to the fibres and constituents of the composite undergo the same stress; this is known as the iso-stress rule of mixtures. The upper bound E_{VR}^u and lower bound E_{VR}^l can be represented through:

$$E_{VR}^u = E_f V_f + E_m V_m \quad (2-1)$$

$$E_{VR}^l = \left[\frac{V_f}{E_f} + \frac{V_m}{E_m} \right]^{-1} \quad (2-2)$$

where E_f and E_m are the elastic modulus of reinforcement and matrix, separately; V_m is the volume fraction of matrix; the superscripts ‘ u ’ and ‘ l ’ correspond to the upper and lower bounds, respectively. Hill [24] noted that none of the iso-strain or iso-stress assumptions are realistic compared to the real materials. In the Voigt condition (Equation 2-1), the tractions at the interfaces are not in equilibrium status, and it is only valid when the Poisson’s ratio of the components of the composites are the same; while in the case of the Reuss condition (Equation 2-2), the two phases no longer remain bounded, and the fact that the phase with the higher elastic modulus usually undergoes higher stress makes the Reuss conditions unrealistic [25, 26].

Since the Voigt-Reuss bounds are too unrealistic to be useful [27], modifications made through incorporating additional information and principles have accordingly been

proposed [26-34]. One of the best known is the Hashin-Shtrikman (HS) bounds model [18, 28, 30] derived to evaluate transversely isotropic composites with arbitrary phase geometry. It gives good estimation when the ratio of modulus values between different phases are not too large. The upper and lower bounds of the bulk modulus K and shear modulus G of the composite follow:

$$K_{\text{HS}}^u = K_f + \frac{V_m}{\frac{1}{(K_m - K_f)} + \frac{3V_f}{(3K_f + 4G_f)}} \quad (2-3)$$

$$K_{\text{HS}}^l = K_m + \frac{V_f}{\frac{1}{(K_f - K_m)} + \frac{3V_2}{(3K_m + 4G_m)}} \quad (2-4)$$

$$G_{\text{HS}}^u = G_f + \frac{V_m}{\frac{1}{(G_m - G_f)} + \frac{6V_f(K_f + 2G_f)}{5G_f(3K_f + 4G_f)}} \quad (2-5)$$

$$G_{\text{HS}}^l = G_m + \frac{V_f}{\frac{1}{(G_f - G_m)} + \frac{6V_m(K_2 + 2G_m)}{5G_m(3K_m + 4G_m)}} \quad (2-6)$$

The HS upper and lower bounds for the effective modulus of the composite can be described as:

$$E_{\text{HS}}^u = \frac{9K_{\text{HS}}^u G_{\text{HS}}^u}{3K_{\text{HS}}^u + G_{\text{HS}}^u} \quad (2-7)$$

$$E_{HS}^l = \frac{9K_{HS}^l G_{HS}^l}{3K_{HS}^l + G_{HS}^l} \quad (2-8)$$

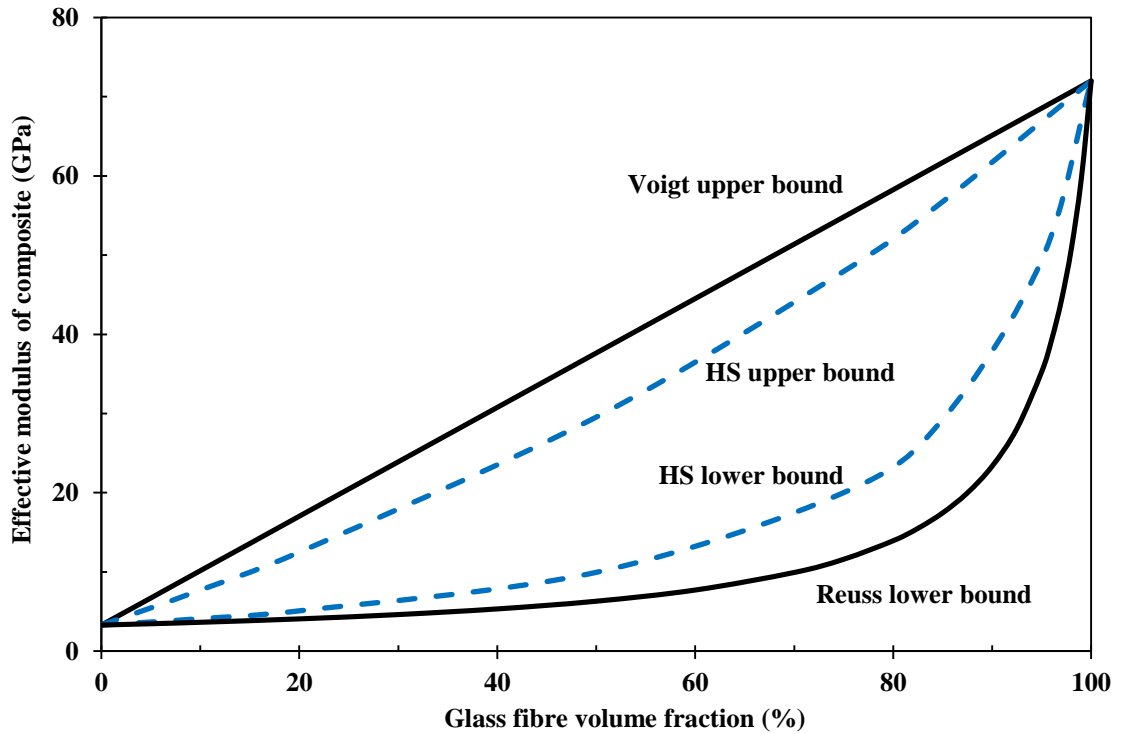


Figure 2-1 Bounds on stiffness for a two-phase composite. HS refers to the Hashin-Shtrikman bounds for isotropic composites.

An example would be glass fibre reinforced polyester resin composite (referred to in Chapter 7), with $E_f = 72$ GPa [35], $E_m = 3.3$ GPa [1]; plots for the effective modulus of the composite versus volume percentage of glass fibre are presented in Figure 2-1. The HS bounds lie within the Voigt-Reuss bounds with narrower range for the effective modulus, which can be calculated from [21]:

$$E_{HS}^u = E_f \frac{5E_m + 3V_f(E_f - E_m)}{5E_f - 2V_f(E_f - E_m)} \quad (2-9)$$

$$E_{\text{HS}}^l = E_m \frac{3E_m + 2E_f + 3V_f(E_f - E_m)}{3E_m + 2E_f - 2V_f(E_f - E_m)} \quad (2-10)$$

where, E_{HS}^u and E_{HS}^l are the HS upper and lower bounds of the effective modulus, respectively.

2.3 PRESTRESSED COMPOSITES

Substantial residual stresses can be developed within continuous-fibre reinforced composites during the cooldown process of manufacture. These stresses are generated from (i) shrinkage of the polymeric matrix during curing, and (ii) thermal expansion mismatch between fibre and matrix material [17, 36, 37]. For (i), the curing process of matrix systems usually leads to shrinkage due to the polymerisation reaction, and forms cross-linked networks [38]; for (ii), the mismatch in thermal expansion coefficients of the constituent fibre and matrix materials could induce internal stresses in the interface regions upon cooling down from cure to room temperature. Although residual stresses can occasionally be beneficial, they are usually detrimental [14]. Depending on the fibre and matrix combinations, as well as the laminate stacking sequences, the accumulation of residual stresses can lead to fibre waviness [39], laminate warping, buckling or matrix cracking [40, 41], which can significantly affect the mechanical performance of composite products [42], or even lead to premature fracture of a composite structure [36]. Therefore, there are significant demands on reducing the residual stresses within a PMC. The relevant techniques include: heat treatment after the curing process [43]; addition of nanoparticles to the matrix to reduce the mismatch in mechanical properties of the constituents [44, 45]; exploiting partial relaxation of residual stresses, which is possible due to the viscoelastic behaviour of polymeric matrix materials [46].

Prestressed composites were first developed to reduce or completely eliminate the residual stresses from manufacture. Zhigun [47] and Tuttle [48] were amongst the earliest

investigators to utilise the prestressing principle, which is adapted from prestressed concrete. As a well-known concept, prestressed concrete can be produced by applying tension to steel rods, embedded in liquid concrete. On solidification of the concrete, the tensile load is released. Owing to the attempted contraction of the reinforcing rods, a compressive prestress is generated within the concrete matrix, and corresponding tensile prestress within the rods, hence the overall mechanical properties of the reinforced concrete are improved. To date however, it has been demonstrated by many investigators that this concept can offer advantages when used in continuous fibre reinforced PMCs. For typical polymeric fibres, prestress can cause (instantaneous) elastic creep strain and (delayed) viscoelastic creep strain, followed by elastic recovery and viscoelastic recovery. Thus, the prestressing principle can be used to produce either elastically prestressed or viscoelastically prestressed PMCs. It has been demonstrated that both fibre prestressing methods can be used to enhance the mechanical properties of PMCs without the need to increase mass or product dimensions. Although the application of prestressing to structural materials such as concrete is a well-known concept, an awareness of possible benefits from making fibre-reinforced PMCs with some residual level of (compressive) prestress seems to be comparatively recent [49].

2.4 ELASTICALLY PRESTRESSED COMPOSITES

2.4.1 Elastic fibre prestressing

As stated earlier, elastically prestressed PMCs (EPPMCs) are based on prestressed concrete principles [48]. Figure 2-2 schematically illustrates the general procedures to produce an EPPMC and generated prestress effects. A tensile load is applied to fibres and maintained throughout the curing cycle; the prestress load is removed after the matrix is solidified and (if heating is required for curing) cooled down to room temperature. Owing to contraction of the fibres from elastic strain, compressive stresses can be induced in the matrix. Since residual thermal stresses generated during the curing process would induce tensile stresses in the matrix, together with compressive stresses in the fibres, the

compressive stresses generated from elastic fibre prestressing could significantly change the residual stresses within an EPPMC.

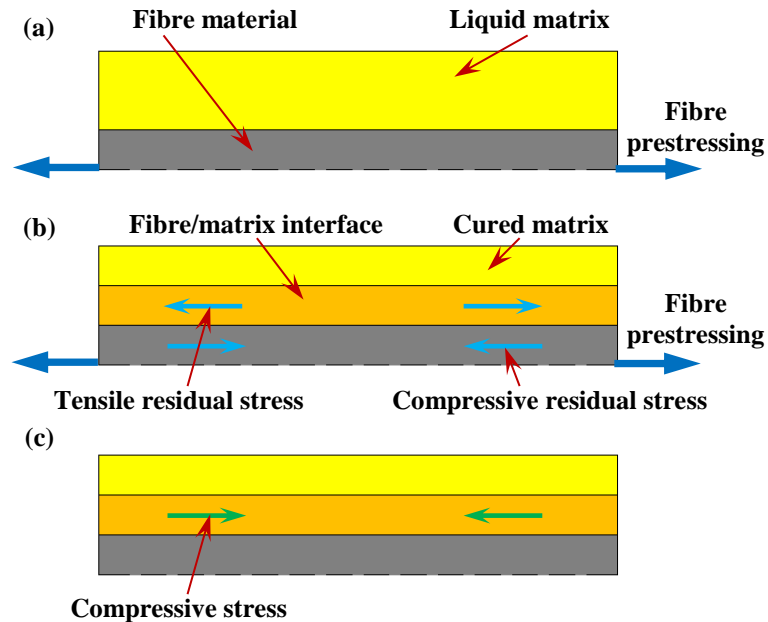


Figure 2-2 Schematic representation showing the utilisation of elastic fibre prestressing to produce EPPMCs: (a) applying tension to polymeric fibre; (b) stresses generated following the matrix curing process, as the fibre remains in tension; (c) releasing of the tensile load, and compressive stresses induced within a EPPMC.

2.4.2 Development of EPPMCs

In the past few decades, researchers have investigated the theoretical and experimental aspects of prestressed composites. To the best of the author's knowledge, elastic fibre prestressing was first applied to PMCs by Zhigun [47] in 1968. He applied prestress on oriented glass fibre-reinforced composite laminates (GFRP), in which plain-weave glass was used as the reinforcement and phenol-formaldehyde resin as the matrix. Mechanical benefits in terms of the elastic modulus were observed, and this was mainly attributed to the reduction from risks of distortion within the woven fabric through prestressing. From 1973 to 1984, developments in prestressed composites were mainly focused on reducing the weak fibres, leading to improved mechanical properties. Mills and Dauksys [50] adopted fibre prestressing to boron/epoxy composites, and found that the pre-breaking of the weaker proportion of boron fibres could increase the average fibre strength, concurrent with a reduced standard deviation. By embedding these previously stretched

(prestressed) boron fibres into an epoxy matrix, the composite strength was increased by ~20% with 50% V_f . Brown [51] conducted the prestressing on graphite fibres. Again, breakage in weak filaments was considered to increase the tensile strength by 32%, angle ply tension by 15%, and unidirectional short beam shear by 5%; a reduction in dispersion was also obtained compared to their composites with untreated fibres. Similar effects were also observed by Chi and Chou [52] through their study on prestressed carbon fibre-reinforced composites (CFRPs).

Though mechanical benefits were observed through weak fibre breakage as demonstrated above, there was a lack of understanding the basic mechanisms from the effects of fibre prestressing. In 1983, Manders and Chou [53] proposed a theoretical analysis based on a 'Chain-of-Bundles' model in which a composite was represented by a chain of short bundles loaded in series [54]. The mechanical benefits from fibre prestressing could be explained by the reinforcing fibres having a distribution of strengths, i.e. a statistical strength distribution of filaments. When a PMC is under load, stresses concentrated on weaker yarns lead to initial fibre breakage. This releases the stored energy within a single yarn, which causes a stress wave to propagate outwards, and in turn gives rise to an oscillatory overstress on neighbouring fibres [55]. Further accumulation of groups of adjacent fibre breaks would ultimately generate fracture of composites. Therefore, fibre prestressing offered an opportunity to increase the strength of a composite by pre-fracture of the weak fibres [53]. This was considered to be the main reason for strength enhancement by fibre prestressing. Since prestressing of fibre materials would also weaken the fibre properties when overstressed, an optimum level of prestress was required to obtain the appropriate prestress benefits. This was subsequently observed in Refs [6, 17, 56-62].

In 1988, interest in elastically generated prestress within PMCs, as previously demonstrated by Zhigun [47] returned. Tuttle [48] found that fibre prestressing could be utilised to reduce or eliminate the tensile residual stresses within a PMC laminate; appropriately controlled pretension of fibres could induce compressive stresses into a matrix, impeding the propagation of cracks, hence enhancing the mechanical properties of the composites. Tuttle proposed a micromechanics model to predict the effect of fibre prestress on residual stresses in composites [48]. The model was based on the rule of

mixtures and classical lamination theory; the assumptions were: (i) perfect bonding between fibre and matrix; (ii) constituents are isotropic materials with linear elasticity; (iii) properties of composites are independent of temperature. Therefore, the final residual strain in the matrix ϵ_m in the fibre direction could be represented by:

$$\epsilon_m = \frac{-\sigma_f^P V_f}{E_{11}} + \Delta T \cdot \alpha_{11} \quad (2-11)$$

where, σ_f^P is the applied fibre prestress level; ΔT is the temperature difference during the cooling down process; E_{11} and α_{11} are the Young's modulus and thermal expansion coefficient of the composite in the fibre direction, respectively. The model successfully predicted that residual thermal stresses could be significantly reduced or completely eliminated by applying fibre prestressing. Experimental investigations verified this prediction: by employing a multi-ply unidirectional graphite/epoxy composite laminate with $[0/\pm 45/90]$ lay-up, a fibre prestress under 1.4 GPa was found to reduce the residual tensile stresses to negligible levels.

Hadi and Ashton [63] further developed Tuttle's model to predict the tensile strength (σ_C^P) of a unidirectional EPPMC, which follows:

$$\sigma_C^P = \sigma_f V_f + \sigma_m (1 - V_f) + \sigma_f^P V_f \quad (2-12)$$

where σ_f and σ_m are the fibre and matrix tensile strength respectively, valid when $\sigma_f > \sigma_f^P$. Hence, fibre prestressing increased the tensile strength and elastic modulus. This increase was a function of prestress level and V_f . It gave good agreement with experimental work when a unidirectional E-glass fibre reinforced epoxy composite was investigated. Improvements of up to ~45% in tensile modulus and up to ~20% in tensile strength were observed.

Schulte and Marissen [64] studied the influence of prestressing on hybrid carbon/aramid/epoxy cross-ply [0/90/90/0] laminates, with fibre prestressing on 0° plies. Upon load release when cooled to room temperature, compressive residual stresses were stored in the 0° plies and tensile residual stresses in the 90° plies. Interaction between plies resulted in compressive stresses in 90° plies, and development of transverse cracks when subjected to tensile loading was delayed and shifted to higher strain and load values, hence improving the first-ply failure stress (the stress required to cause matrix cracking in the 90° plies) by 60%.

The effect of elastic fibre prestressing on the first-ply failure problem was also investigated by Rose and Whitney [65]. They examined the benefits of prestressing through theoretical and experimental techniques. A theoretical model was constructed, based on the concentric cylinder model [66] and classical lamination theory. The model predicted that application of sufficient prestressing would suppress the first-ply failure completely. Experimental analysis was based on graphite/epoxy composites, and indicated that prestressed composite samples possessed superior capability to withstand first-ply failure compared to its conventional specimens, and first-ply failure strength was increased by 50%. Sui et al [67, 68] evaluated the effect of elastic prestress on vinylon-reinforced aluminium laminate (VIRALL). Vinylon fibre was prestressed and subsequently bonded on aluminium sheets with epoxy resin adhesive, and preload was maintained throughout the curing process. Prestressing was considered to modify or recreate the internal ply stress states of VIRALL, and induced a tensile strengthening effect to the vinylon fibres; hence prestressed VIRALL had superior properties in terms of initial modulus, elastic limit, yield strength, failure strength and fatigue properties.

In 1996, Tuttle et al [40] introduced a new concept, in that elastic fibre prestressing could be used to generate morphing structures. By considering the prestressing effects, they modified the un-symmetric laminate theory developed by Hyer [69]. Though it predicted that curvatures in laminates could be reduced with increasing prestress level, it theoretically predicted that fibre prestressing could be adopted to produce morphing structures for the first time. Morphing structures utilising fibre prestressing were subsequently demonstrated in Refs [70-73]. Hence this opened up a new vision for fibre prestressing. This is further discussed in Section 2.8.2. In addition, Tuttle [40] employed

a hydraulic system to apply fibre prestressing to produce $[0^P/90]_T$ laminates, and found that thermal warpage of un-symmetric laminates was reduced through prestressing; tensile testing results also indicated a reduction in residual tensile stresses.

To promote environmentally friendly composite production with superior mechanical properties, employing elastic fibre prestressing on nature fibres was conducted by Bekampienė et al [74] in 2011. They applied fibre prestressing to glass and cotton plain-weave woven fabrics separately, with unsaturated polyester resin as the matrix material. A single-layer laminate was produced through a pressure forming technique with pre-tensioned fabrics. Mechanical improvements to the cotton fabric reinforced composites are highlighted here: tensile strength at break was increased by 12% in the warp direction, 58% in the weft direction and 39% in the bias direction. Širvaitienė et al [75] investigated the prestress effects on flax and cotton fibre reinforced biodegradable poly(lactic acid) composites. Improvements in tensile strength and flexural stress were observed, and an optimum prestress level was found for maximum prestress benefits to be obtained. Similar improvements in tensile strength and modulus through fibre prestressing were also reported by Zaidi et al [76], through their studies on prestressed flax fibre reinforced composites. These mechanical benefits (from natural fibre prestressing) were mainly attributed to the improvement in fibre orientation and bulk integrity, causing fibre straightening, and inducing compressive stresses in the matrix.

Various methods of elastic fibre prestressing have been developed and these have been found to improve mechanical properties mainly by counteracting the thermal residual stresses. Thus EPPMCs possess superior mechanical performance compared with non-prestressed counterparts. This has been demonstrated by many through tests on tensile strength and stiffness, impact toughness, and flexural stiffness. Table 2-1 summarises previous studies on elastic fibre prestressing since 1968; this is arranged in chronological order. The composite constituents, prestress method (Section 2.4.3) and main effects from elastic fibre prestressing are included.

Table 2-1 Summary of research into elastic fibre prestressing.

Year	Investigator	Composite constituents	Prestress method	Prestress effects
1968	Zhigun [47]	Woven glass fibre (49% V_f) Phenol-formaldehyde resin	Applied by tightening nuts on tension rods	Improved elastic modulus by up to ~30%; prestressing reduced the fabric distortion.
1973	Mills and Dauksys [50]	Boron fibre (50% V_f) Epoxy prepreg tape	Prebending the prepreg tape	Increased tensile strength in both fibre material and its composites. Prestressing induced weak fibre breakage.
1976	Brown [51]	Graphite Epoxy prepreg tape	Prebending the prepreg tape	Increased tensile strength and reduced strength dispersion. Prestressing induced weak fibre breakage.
1983	Manders and Chou [53]	Theoretical analysis	N/A	Proposed mechanisms of mechanical benefits from fibre prestressing.
1983	Chi and Chou [52]	Carbon multifilament yarn Epoxy resin	Prebending the fibres	Increased tensile strength up to 20%; reduced failure probability of manufacturing.
1988	Tuttle [48]	Graphite fibre (66% V_f) Epoxy resin & Theoretical analysis	Not provided	Reduction or elimination of the tensile residual stresses, or even induced compressive stresses into matrix; experimental studies verified this prediction.
1990	Jorge et al [59]	E-glass fibre(56% V_f) Unsaturated polyester resin	Dead weight	Increased tensile strength and modulus up to a given prestress level; beyond this level, these properties became stabilised.
1992	Schulte and Marissen [64]	Hybrid cross-ply lay-up with carbon and aramid fibre Epoxy resin	V-slot notched bar	Induced compressive stresses into the laminate which delayed the formation of transverse cracks, these being shifted to higher strain and load values; increased first ply failure strength by 60%.
1992	Scherf and Wagner [77]	Single Carbon fibre (9.9 μm in diameter) Epoxy resin	Dead weight	Increased interfacial shear stress.
1993	Rose and Whitney [65]	Graphite fibre Epoxy resin	Filament winding	Improved first ply failure problem.
1995	Sui et al [67]	Vynylon fibre bonded on aluminium, with epoxy resin as adhesive	Not provided	Modified or recreated the internal ply stress states; induced tensile strengthening effect to the vynylon fibres, hence prestressed VIRALL had superior properties in initial modulus, elastic limit, yield strength, and strength at failure.

1996	Sui et al [68]	Vinyon fibre bonded on aluminium, with epoxy resin as adhesive	Not provided	Fatigue strength was increased with increasing prestrain.
1996	Tuttle et al [40]	Graphite fibre (60% V_f) Epoxy resin & Theoretical analysis	Hydraulic cylinder (hot pressing)	Reduced thermal warpage of composite; predicted the feasibility of creating morphing structures.
1997	Motahhari and Cameron [78]	E-glass fibre (40% V_f) Epoxy resin	Horizontal tensiometer machine	Prestress had two opposite effects on composites: (i) improved strength by impeding crack propagation; (ii) higher residual shear stresses weakened the bonding in interface region, thus reduced the strength at the same time.
1998	Hadi and Ashton [63]	E-glass fibre (30, 45 and 60% V_f) Epoxy resin	Filament winding	Increased tensile strength and modulus; the increase was a function of prestress level and V_f .
1998	Zhao and Cameron [58]	Glass fibre (40% V_f) Polypropylene resin	Fibre-stretching frame	Prestress increased tensile, flexural and interlaminar shear properties; an optimum prestress level existed to maximise the prestress benefits.
1998	Motahhari and Cameron [56]	E-glass fibre (40% V_f) Epoxy resin	Horizontal tensiometer machine	Increased impact strength by up to 33%; an optimum prestress level (~30 MPa) existed to maximise the flexural properties; beyond this level, prestress benefits started to decrease.
1999	Motahhari and Cameron [57]	E-glass fibre (40% V_f) Epoxy resin	Horizontal tensometer machine	Increased flexural strength and modulus by up to 33%; an optimum prestress level (~60 MPa) existed to maximise the impact strength; beyond this level, prestress benefits started to decrease.
2000	Dvorak and Suvorov [79]	S-glass fibre (50% V_f) Epoxy resin	Not provided	Reduced tensile residual stresses in the matrix; increased resistance to first-ply failure; minimised fibre waviness.
2001	Suvorov and Dvorak [80]	Carbon fibre (61% V_f) Kevlar (60% V_f) Epoxy resin Al_2O_3 ceramic	Not provided	Induced compressive stresses to enhance dynamic compressive strength of laminate/ceramic plate; optimal design was carried out through theoretical analysis; stress relaxation effect due to temperature changes and matrix creep was minor.

2001	Suvorov and Dvorak [81]	S-glass fibre (50% V_f) Epoxy resin	Not provided	Optimised fibre prestress distribution in individual plies of the laminate created residual stresses that suppress both damage development in the interior of the laminate and inter-laminar delamination at the free edges.
2004	Jevons [82]	E-glass fibre (56% V_f) Epoxy resin	Biaxial loading frame	Increased resistance to delamination by up to 25% when subjected to low-velocity impacts however, prestressing had no discernible effect on high-velocity impact performance.
2006	Krishnamurthy [17]	E-glass fibre (58% V_f) Epoxy resin	Flat-bed loading frame	Improved fibre alignment, hence improved mechanical properties; an optimum level of prestressing existed for maximum benefits.
2006	Cao and Cameron [60]	E-glass fibre (20% and 30% V_f) Silica particle Epoxy resin	Hounsfield tensiometer	Improved flexural properties and shear modulus of composites (without silica particles); an optimum prestressing level existed to maximise the mechanical benefits; addition of silica particles enhanced the fibre-matrix bonding, and promoted prestress benefits.
2006	Cao and Cameron [83]	E-glass fibre (20% and 29% V_f) Silica particle Epoxy resin	Hounsfield tensiometer	Improved impact properties of composites (without silica particles); an optimum prestressing level existed for impact benefits and a more significant improvement was observed with silica particle modified prestressed composites.
2010	Schlichting et al [84]	S-glass fibre (12% V_f) Quixfil and adoro resin	Dead weight	Increased deflection for initial bending failure and flexural strength of composites, with limited effects on the flexural modulus.
2011	Bekampienė et al [74]	E-glass fibre fabrics (27% V_f) Cotton fibre fabrics (32% V_f) Unsaturated polyester resin	Pressure forming	With cotton reinforced composites, tensile strength at break was increased by 12% in warp direction, 58% in weft direction and 39% in bias direction; for E-glass fibre reinforced composites, improvement in tensile strength at break was 135% in bias direction.
2013	Jie et al [85]	Finite element analysis	N/A	Prestressed composite was advantageous in stress distribution and lower principal stress value during a three-point bending test.

2013	Širvaitienė et al [75]	Flax (68 tex) and cotton (70 tex) twisted yarn Biodegradable polylactic acid resin	Not provided	Prestressing increased fibre orientation and bulk integrity, hence enhanced tensile and flexural strength.
2013	Graczykowski et al [86]	E-glass fabric (48% V_f) Epoxy resin	Applied by loading screw on the plane stand	Increased maximum flexural deflection by 25% compared to non-prestressed counterparts.
2014	Nishi et al [87]	Carbon fibre (50% V_f) Epoxy resin	Dead weight	Improved impact energy by 30% at optimum (17.6 MPa) prestress level.
2015	Hassan and Abdullah [61]	Carbon fibre (50% V_f) Epoxy resin	Horizontal tensiometer	Improved tensile strength and tensile modulus by up to 114.9% and 85.1% respectively compared to non-prestressed counterparts; an optimum value of prestress level was observed to maximise the prestress benefits.
2015	Zaidi et al [76]	Flex fibre spun yarn (46%-49% V_f) Unsaturated polyester resin	Screw tensioning frame	Increased fibre packing density, caused fibre straightening, and reduction in fibre obliquity, hence enhanced mechanical properties of composite samples.
2015	Mostafa et al [88]	E-glass fabric (~11% V_f) Unsaturated polyester resin	Biaxial loading frame	Increased flexural strength by ~15% and modulus by ~16% at the optimum prestress level of 50 MPa; prestress benefits reduced with increasing fabric orientation angle towards the bias direction; prestress benefits decreased with time due to localised matrix creep.
2016	Graczykowski et al [89]	E-glass fabric (~23% V_f) Epoxy resin	Applied by loading screw on the plane stand	Prestressed composite had lower V_f due to fibre stretching; numerical simulation showed prestressed composites would benefit from stress and strain distribution in particular plies, resulting in improved mechanical properties.
2016	Mostafa et al [90]	E-glass fabric (~11% V_f) Unsaturated polyester resin	Biaxial loading frame	Increased fatigue life by up to 43% compared with non-prestressed counterparts; prestress benefits decreased with increasing off-axis fabric orientation angle from 0 to 45° relative to warp direction.

2016	Krishnamurthy et al [91]	E-glass fibre Epoxy resin	Flat-bed loading frame	Embedded sensors to monitor the residual strain within composites; by applying prestress level of 108 MPa to a unidirectional $[0]_{16}$ laminate, the residual strain was measured to be reduced to a negligible level.
2016	Mostafa et al [62]	E-glass fabric (~11% V_f) Unsaturated polyester resin	Biaxial loading frame	Enhanced elastic modulus and critical stress at first matrix fracture of the composite by 10-20%; an optimum prestress level for these benefits was obtained.

2.4.3 Elastic fibre prestressing methods

In order to employ elastic fibre prestressing, suitable equipment is needed to provide preloading to the polymeric fibres during the curing process of a matrix. Since the prestressing method is critical to the mechanical performance of an EPPMC, researchers have developed various prestressing methods for different tasks, mainly focused on providing prestressing on fabrics or continuous fibres.

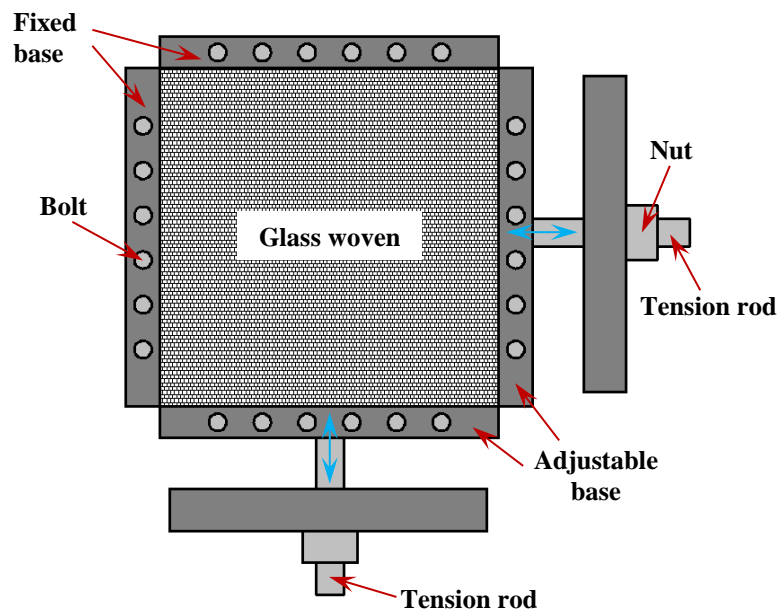


Figure 2-3 Elastic fibre prestressing method adopted by Zhigun [47].

As stated in Section 2.4.2, it is believed that Zhigun [47] did the first attempt at prestress on oriented GFRP laminate, in which plain-weave glass fabric was used as the reinforcement and phenol-formaldehyde resin as the matrix. A bespoke prestressing

apparatus was developed and Figure 2-3 schematically shows the basic arrangement. Prestressing was achieved by tightening nuts on the ends of the tension rods, and two layers were allowed to be stretched simultaneously. A dynamometer was used to monitor the prestress level. Mechanical benefits in terms of elastic modulus were observed. This was mainly attributed to the reduction of risks of distortion within the fabric woven through prestressing. Subsequent elastic fibre prestressing methods have been developed mainly by utilising: dead-weight; V-slot notched bar; filament winding; hydraulic cylinder; pressure forming; horizontal tensiometer; flat-bed loading frame and biaxial loading frame. Since the development of the existing prestressing methods and their advantages and limitations have been discussed in details, in Refs [17, 92, 93], they are not elaborated here. However, the corresponding fibre prestressing methods, listed with the available studies as shown in Table 2-1, provide a suitable outline into the development of elastic fibre prestressing methods.

2.5 VISCOELASTICALLY PRESTRESSED COMPOSITES

2.5.1 Viscoelastic fibre prestressing

Viscoelastically prestressed PMCs (VPPMCs) are produced by applying tension to polymeric fibres, then the tensile load is released before moulding the fibres into a polymeric matrix. As discussed in Section 2.4.1, the contraction of fibres is produced through the locked elastic strain within EPPMCs; however, for VPPMCs, the compressive stresses are generated from viscoelastic recovery of polymeric fibres. Figure 2-4 schematically shows the general principles for producing a VPPMC and the resulting prestress effects. Following tensile load release, fibres start to shrink due to viscoelastic recovery. When embedded into a matrix, tensile residual stresses generated from the curing process are counterbalanced by viscoelastic recovery of fibres, hence compressive stresses are induced into the matrix as shown in Figure 2-4 (c). Research on VPPMCs indicate that this viscoelastic fibre prestressing can improve mechanical properties, especially impact toughness, flexural stiffness and tensile strength. Investigations into

VPPMCs to date have involved nylon 6,6 fibres [1, 2, 5-8, 10-12], ultra-high molecular weight polyethylene fibre (UHMWPE) [3, 4] and bamboo slivers [94].

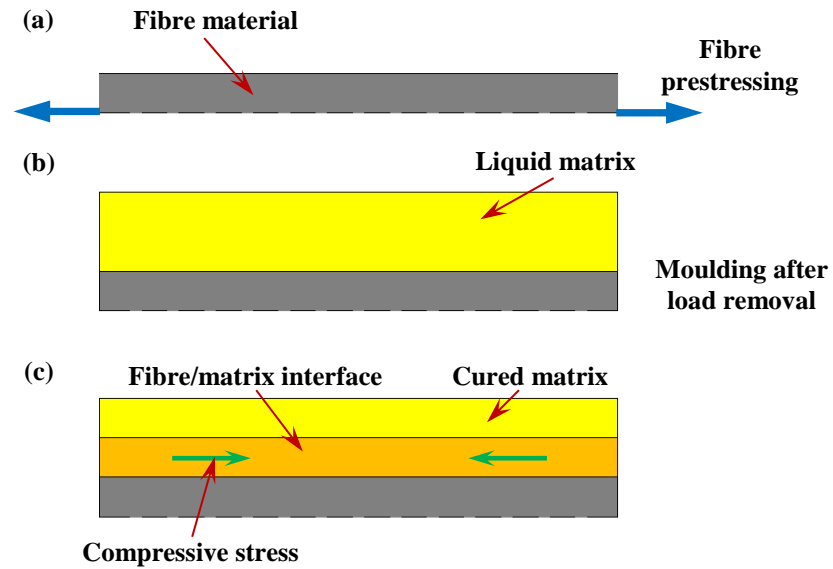


Figure 2-4 Schematic representation of utilising the viscoelastic fibre prestressing principle for a PMC: (a) applying tension to polymeric fibre; (b) moulding process followed tensile load removal; (c) residual stresses within a VPPMC.

2.5.2 Development of VPPMCs

Exploiting viscoelastic fibre prestressing in a PMC is comparatively recent [95]. Fancy was the first investigator into VPPMCs, in 2000 [11, 12]. By employing photo-elasticity principles, Figure 2-5 shows the visual evidence of viscoelastically induced stresses within a VPPMC. Nylon 6,6 monofilament was stretched first, and then an appropriate length was cut and embedded into polyester resin, which was transparent after being cured. ‘Test’ and ‘control’ samples were made simultaneously to ensure there were no differences other than from fibre prestressing. In contrast with the (non-prestressed) control sample, evidence of residual stresses surrounding the filament in the test sample can be clearly seen as the white region in Figure 2-5.

To produce a VPPMC, the reinforcement material needs to have appropriate viscoelastic behaviour. Nylon 6,6 fibre, as a low cost and high strength polymeric fibre, was the first material adopted to examine the feasibility of viscoelastically generated prestress in PMCs [11, 12]. Viscoelastic performance of the fibre was investigated in terms of creep

and recovery [11]. It was found that the viscoelastic recovery of nylon 6,6 fibre exhibited long-term behaviour, even when subjected to creep over a short-period (24 h). Later, Fancey [96, 97] presented a latch-based Weibull model to represent the viscoelastic behaviour of polymeric fibres. It was well fitted to describe the creep and recovery performance of nylon 6,6 fibre. Furthermore, the time-temperature superposition principle was used to investigate the long-term viscoelastic recovery of nylon 6,6 fibres previously subjected to 24 h creep. It indicated that viscous flow effects were predicted to be less than $10^{-4}\%$ after exposure to a period equivalent to 100 years at 20°C . Hence, the viscoelastic prestressing mechanism would not be limited by the eventual onset of viscous flow [10].

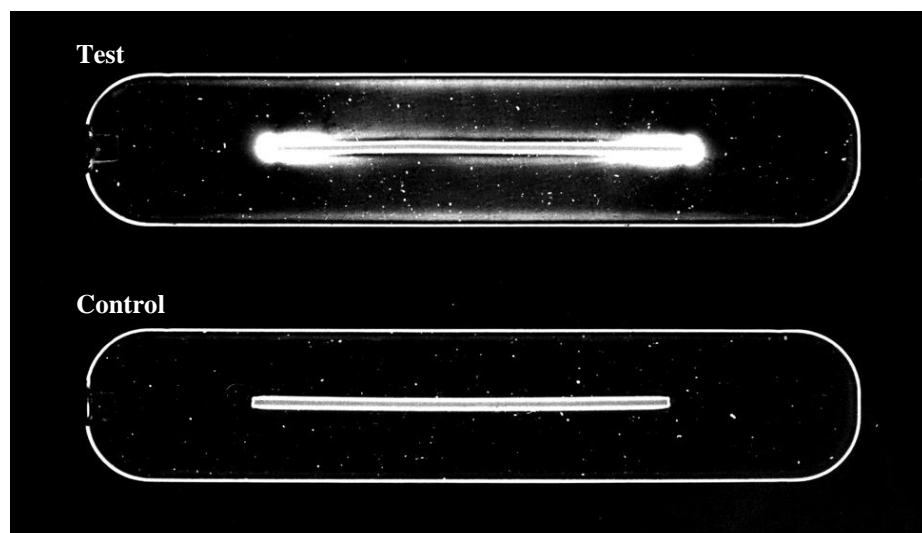


Figure 2-5 Polariscope image of nylon 6,6 monofilament embedded in polyester resin samples [11].

In order to evaluate the effect of viscoelastic fibre prestressing in PMCs, mechanical properties, i.e. tensile strength, bending stiffness and impact toughness, were evaluated to compare the test (prestressed) with control (non-prestress) samples. By adopting nylon 6,6 fibre, an increase in impact energy absorption was observed for VPPMC samples by up to 25% (compared to their control counterparts) [2, 11, 12]. Accelerated aging showed there was no deterioration in increased impact energy absorption after ~ 25 years at a constant 50°C ambient temperature [98]. Pang and Fancey [6] performed tensile tests on individual nylon 6,6 fibre and reinforced VPPMCs. They found viscoelastically induced prestressing could increase the tensile strength, modulus and toughness by 15%, 30%, 40% respectively, and the effects being V_f -dependent. Flexural properties were evaluated

through three-point bending tests. With an L/h ratio of ~ 30 , nylon-based VPPMCs (8-16% V_f) gave an increase of $\sim 50\%$ in both elastic modulus and short-term creep flexural modulus due to prestress effects; also, accelerated aging of samples to an equivalent of 100 years at 20°C , demonstrated no significant change in increased flexural modulus from the prestressed samples [1].

When the previously stretched fibres are embedded into a polymeric resin, a certain amount of viscoelastic strain within the fibres will be locked inside the matrix. Thus a recovery force will be generated as the fibres attempt to contract. In 2008, recovery force measurement apparatus was first developed by Pang et al [99]. Results indicated that by subjecting nylon 6,6 yarn to a 320 MPa, 24 h tensile creep stress, recovery forces at a fixed strain gave a contraction stress up to 10.9 MPa over a 2700 h period. The force-time behaviour could be fitted to a four parameter Weibull-model. This provided further evidence of prestress benefits from viscoelastic fibre prestressing.

Research into the influence of fibre prestressing on UHMWPE fibre-based VPPMCs was carried out by Fazal and Fancey [3, 4]. By applying a 1.3 GPa creep stress for 24 hours, the UHMWPE fibre gave a creep strain of 5.4%. After releasing the creep load, compressive stresses generated from viscoelastic recovery started to grow within 8 h to a maximum value of 23 MPa, and then decreased with time. Equilibrium was reached after ~ 3000 h and gave 13 MPa of stress [3, 4]. When the prestressed UHMWPE fibres were embedded into polyester resin, test samples with 3.6% V_f (compared with unstressed counterparts) showed a 40% increase in flexural stiffness; while 7.2% V_f samples gave 23% increase [4]. In Charpy impact testing, prestressed samples demonstrated a $\sim 20\%$ increase in absorbed impact energy [3].

Cui et al [94] adopted the viscoelastic fibre prestressing technique to bamboo slivers to reinforce parallel strand lumber (PSL). They found the viscoelastic deformation induced prestress could enhance the flexural properties of PSL, in which modulus of rupture and modulus of elasticity of pre-tensioned samples were increased by 7.84% and 11.76%, respectively. Table 2-2 summarises previous studies on VPPMC research in chronological order.

Table 2-2 Summary of research into viscoelastic fibre prestressing.

Year	Investigator	Composite constituents	Prestress method	Prestress effects
2000	Fancey [12]	Nylon 6,6 fibre (3-4% V_f) Unsaturated polyester resin	Vertical stretching rig	There was no deterioration in prestress benefits up to 3552 h in real time.
2000	Fancey [11]	Nylon 6,6 fibre (3-4% V_f) Unsaturated polyester resin	Vertical stretching rig	Evidence of viscoelastic recovery-induced compressive stresses; increased impact energy absorption by up to 25% compared to equivalent non-prestressed counterparts.
2001	Fancey [96]	Nylon 6,6 fibre	Vertical stretching rig	Creep and recovery behaviour of nylon 6,6 fibre were well fitted to a Weibull-based time-dependent latch element model.
2005	Fancey [2]	Nylon 6,6 fibre (3-4% V_f) Unsaturated polyester resin	Vertical stretching rig	Accelerated aging indicated that there was no deterioration in impact performance of VPPMCs up to ~10 years at 20°C.
2006	Pang and Fancey [10]	Nylon 6,6 fibre (3-4% V_f) Unsaturated polyester resin	Vertical stretching rig	Prestressed nylon 6,6 fibre was subjected to accelerated aging for an equivalent of 100 years at 20°C, the viscoelastic recovery was still active; this corresponded with results from long-term impact performance in that no deterioration was observed.
2008	Pang and Fancey [6]	Nylon 6,6 fibre (16, 28, 41, 53% V_f) Epoxy resin	Vertical stretching rig	Increases in tensile strength, modulus and energy absorbed by up to 15%, 30% and 40% respectively; optimum V_f level for nylon-based VPPMCs in tensile testing was 35-40%.
2008	Pang et al [99]	Nylon 6,6 fibre	Vertical stretching rig	A recovery force measurement rig was developed to monitor the force generated within a viscoelastically recovering polymeric fibre.
2009	Pang and Fancey [1]	Nylon 6,6 fibre (8, 12, 16% V_f) Epoxy resin Unsaturated polyester resin	Vertical stretching rig	Elastic and short-term flexural modulus were increased by up to ~50%; there was no deterioration in flexural benefits from viscoelastic fibre prestressing when subjected to accelerated aging to 100 years at 20°C.
2010	Fancey [5]	Nylon 6,6 fibre (2-3% V_f) Unsaturated polyester resin	Vertical stretching rig	Increase in impact energy absorption by ~30%; no significant decrease in impact benefits was detected through accelerated aging to 20 years at 40°C.

2012	Cui et al [94]	Bamboo slivers mixed with poplar veneer strands at weight ratio of 1:4 (75% V_f) Phenol formaldehyde resin	Not provided	Reinforced modulus of rupture and modulus of elasticity by 7.84% and 11.76 respectively; flexural toughness was increased by 27.55%.
2013	Fazal and Fancey [7]	Nylon 6,6 fibre (3.3, 10.0, 16.6% V_f) Unsaturated polyester resin	Vertical stretching rig	Prestress benefits in impact properties depended mainly on shear stress-induced fibre-matrix debonding; i.e. the prestress benefit decreased with increasing Charpy test span.
2013	Fazal and Fancey [4]	UHMWPE fibre (3.6 and 7.2% V_f) Unsaturated polyester resin	Vertical stretching rig	Increase in flexural modulus by up to 40%, and benefits showed no deterioration over ~2000 h in real time.
2014	Fazal and Fancey [8]	Hybrid nylon 6,6 and Kevlar fibres (3.3% V_f in nylon and 1.2% V_f in Kevlar) Unsaturated polyester resin	Vertical stretching rig	Absorbed impact energy was increased by up to 33% for nylon and Kevlar hybrid composite sample, and flexural modulus was increased by ~40%.
2014	Fazal and Fancey [3]	UHMWPE fibre (3.6 and 7.2% V_f) Unsaturated polyester resin	Vertical stretching rig	Increase in impact absorbed energy by up to 40%; debonding at the skin-core interface within the fibres was observed as a significant energy absorbing factor.
2015	Fancey and Fazal [98]	Nylon 6,6 fibre (2.2% V_f) Unsaturated polyester resin	Vertical stretching rig	Increase in impact energy was ~40%; time-temperature boundary was extended to ~25 years at 50°C, and no deterioration in impact benefits was observed.

2.6 PRESTRESS MECHANISMS

Research into EPPMCs and VPPMCs has demonstrated enhanced mechanical performance of composites in tensile, flexural, and impact properties as discussed in Sections 2.4 and 2.5. These investigations have led to proposed prestress mechanisms within a prestressed composite. This section summarises these mechanisms. The mechanical benefits from fibre prestressing effects being mainly attributed to [5, 6]: (i) impeding crack propagation; (ii) attenuating dynamic overstress effects; (iii) effective and collective responses to external loads; (iv) promoting energy absorption through residual shear stresses.

(i) Impeding crack propagation

For both EPPMCs and VPPMCs, fibre prestressing is considered to impart compressive stresses into the composites. When the prestressed composite samples are subjected to mechanical testing, i.e. tensile [6] or flexural [57] or impact tests [11, 12, 56], the compressive stresses impede crack propagation, which results in delaying or preventing the formation of cracks within the samples, hence improving the mechanical properties.

(ii) Attenuating dynamic overstress effects

This mechanism was first proposed in Ref [53], and further considered by Pang and Fancey [5, 6]. Reinforcing fibres have a distribution of strengths. When a non-prestressed composite sample is under loading, stresses would concentrate on weaker fibres and further lead to fibre breakage. This premature fibre breakage would release stored energy, generating a stress wave to propagate outwards. Accumulation of the dynamic stresses results in overstressing of neighbouring fibres, which can promote fracture within the composite. By subjecting the fibre to either elastic or viscoelastic prestressing, the induced compressive stresses may decrease stress wave propagation within the composite. Hence, dynamic overstress effects could be attenuated, reducing the probability of collective fibre failure, and improving the mechanical properties.

(iii) Effective and collective responses to external loads

Fibre prestressing (either elastic or viscoelastic) results in taut and straightened fibre yarns within a prestressed composite. Hence, responses from fibre yarns can be expected to be more effective and more collective when subjected to external loads. This could contribute to improve the flexural modulus [57], tensile strength, and reduce sample displacement during the fibre fracture process [6].

(iv) Promoting energy absorption through residual shear stresses

Impact tests on elastically and viscoelastically prestressed composites both showed the impact toughness was increased through de-bonding within the fibre-matrix interfaces [2, 5, 7, 12, 56]. Residual stresses generated from prestressing are expected to make the fibre-matrix interface vulnerable to external loads. Subjected to impact loads, fibre-matrix debonding occurs in preference to breaking the fibres. Fancey [5, 12] found that the prestress could reduce the shear stresses responsible for initial debonding. Hence, debonding tends to be promoted over transverse fibre fracture.

Though elastic fibre prestressing can provide similar mechanical property improvements to those offered by viscoelastic fibre prestressing, there are notable advantages to VPPMCs over EPPMCs [2, 6]. Since fibre prestressing and moulding processes are decoupled for VPPMC production, there is total flexibility in terms of product geometry [7]; however, to produce an EPPMC, the tension load needs to be maintained throughout the matrix curing process, which could restrict product geometry [2]. Also, equipment designs for simultaneously stretching and moulding can be technically challenging [17, 71]. A further advantage is longevity aspect. Although viscoelastic activity is temperature sensitive, by subjecting the nylon-based VPPMC samples to accelerated aging (time-temperature superposition), impact results have demonstrated that there is no deterioration in increased energy absorption over a duration equivalent to ~25 years at 50°C [98]. Therefore, any potential prestress deterioration through localised matrix creep would be offset by activity from longer term viscoelastic recovery mechanisms within the polymeric fibres [2]. For EPPMCs however, elastically generated prestress would deteriorate with time due to localised matrix creep as proposed by Fancey [2, 49], and subsequently observed by Mostafa [88] through natural aging experiments.

2.7 SEMI-CRYSTALLINE FIBRE MICROSTRUCTURES

To produce VPPMCs with superior mechanical performance, fibre materials need to have appropriate viscoelastic properties. Since most of the research into VPPMCs has involved using semi-crystalline fibres, i.e. nylon 6,6 and UHMWPE fibres (Section

2.5.1), it is vital to look into the microstructures of these types of fibre materials. This section summarises the development of understanding semi-crystalline fibre microstructures, aiming to provide further insight into fibre microstructural deformation mechanisms.

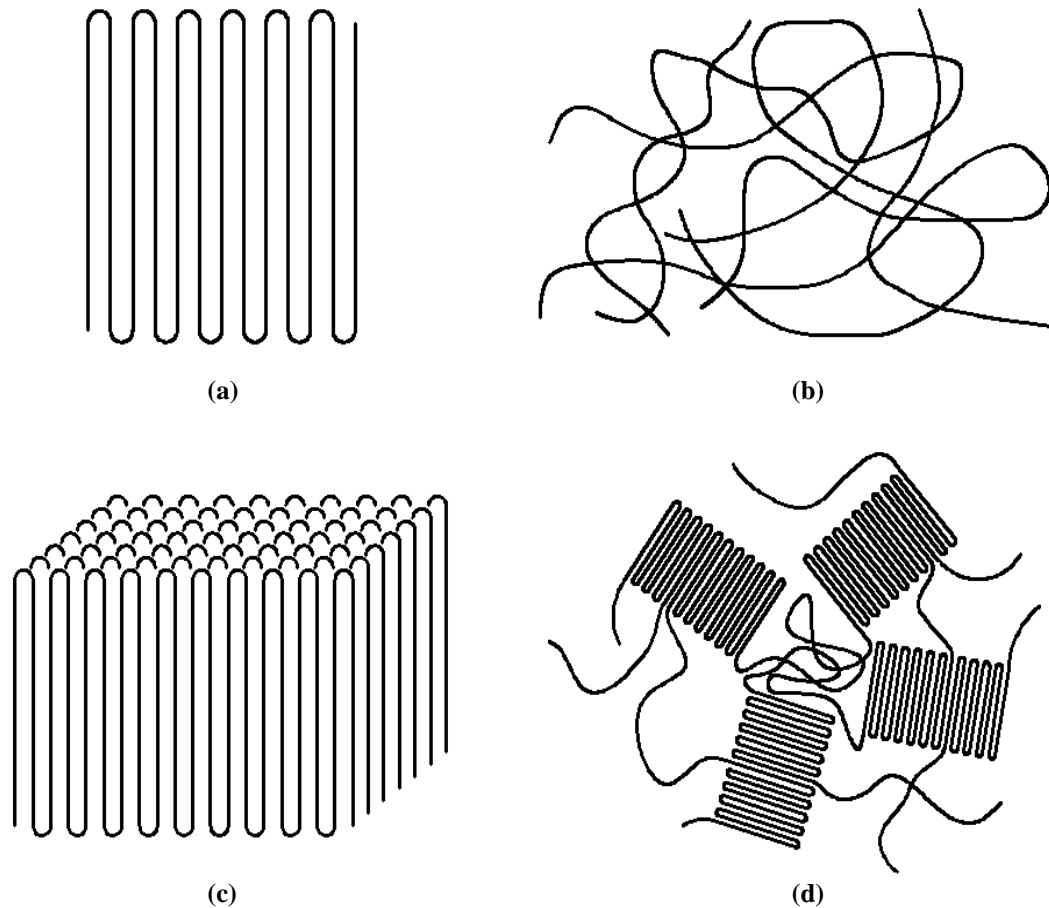


Figure 2-6 Schematic representation of highly ordered crystal and amorphous structures: (a) highly ordered crystal; (b) tangled amorphous; (c) lamellae; (d) spherulitic semi-crystalline structure.

Semi-crystalline polymeric fibres are increasingly used in a wide range of structural applications subjected to thermal and mechanical loadings, thus it is essential to consider their microstructures. Crystals are developed when molecules are arranged in a highly ordered microscopic structure or pattern as illustrated in Figure 2-6 (a). Comparatively, if there is no order, the polymer chains form a large tangled mass and are commonly defined as being amorphous, as shown in Figure 2-6 (b). The ordered chains within a crystal are not only folded as in Figure 2-6 (a), but also stacked to form lamellae as represented in Figure 2-6 (c). However, only a few polymers can form purely crystalline

materials; most polymeric fibres are semi-crystalline polymers that consist of both crystalline and amorphous domains.

With synthetic fibres, the initial material used to produce fibres consists of broad, thin crystalline lamellae as shown in Figure 2-6 (c), surrounded by amorphous layers. The lamellae are developed from a central nucleus and are radially oriented, leading to the formation of spherulitic structures [100, 101] as exemplified in Figure 2-6 (d). The drawing process could induce plastic deformation and structural changes in both crystallographic texture and morphology: Hiss et al [101] employed a video-controlled tensile testing machine to study the uniaxial drawing of polyethylene and ethylene-vinylacetate copolymers, simultaneously. The related texture changes were revealed through wide-angle X-ray diffraction (XRD) patterns. Butler et al [102] investigated the plastic deformation of unoriented linear polyethylenes (PE) using the simultaneous small-angle XRD (SAXD) and wide-angle XRD (WAXD) techniques. They observed that the uniaxial tension during the cold-drawing process of high-density PE (HDPE), high molecular weight-HDPE (HMW-HDPE) and UHMWPE would gradually destroy the lamellae and form microfibrils. A similar transition in fibre morphology was also reported by Bartczak et al [103]. They explored the deformational properties of linear HDPE in simple shear to large strains. By using SAXD, WAXD and transmission electron microscopy, they found that the crystallographic deformation was active throughout the strain history; further deformation in bands could destroy the crystalline lamellae and form microfibrils at certain strain rate.

Many studies have been carried out to investigate the interdependence of structure and properties from both academic and technological view-points [104-110]. Several microstructural models have been proposed to describe the morphological architecture of semi-crystalline fibres; however, two microfibrillar models have been commonly recognised to offer interpretations to link structure and properties: the two-phase microfibrillar model by Peterlin [105, 106, 108] and the three-phase 'Swiss-cheese' model by Prevorsek [104, 107]. The widely spread opinion is that the three-phase 'Swiss-cheese' model is applicable in all cases of PA6 fibre, i.e. either in the case of high-tenacity PA6 or standard melt-spun processed PA6, in which, oriented amorphous interfibrillar phase controls the stiffness and tenacity [104, 111].

2.7.1 Two-phase microfibrillar model

The microfibrillar model [105, 106, 108, 112] as illustrated in Figure 2-7 is a well-defined two-phase model, where crystallite and amorphous phases are arranged in series. It is been used to describe and explain certain properties and modifications of polymeric fibres during mechanical processing or in manufacture. Plastic deformation of semi-crystalline polymeric fibres undergoes three stages during the cold-drawing process [108]: (i) plastic deformation of the parallel lamellae structure of raw materials before the onset of necking; (ii) formation of micro-fibrils through micro-necking; (iii) plastic deformation of the fibre structure. Most raw materials required to produce semi-crystalline fibres consist of stacks of parallel lamellae. The rotation and sliding of lamellae cause phase changes and twinning of the crystal lattice. Microfibrils of 100-300 Å in width are formed during drawing, which stack into small bundles of long, thin fibrils. The chains bridging the gaps are partially unfolded as shown in Figure 2-7. These are connected with microfibrils in the axial direction and develop into intrafibrillar tie molecules which are mostly located on the outside of microfibrils and are fully stretched and taut. In accordance with intrafibrillar tie molecules, the intermicrofibrillar tie molecules between microfibrils form a layer to connect adjacent microfibrils. Therefore, crystallites are connected by intramicrofibrillar tie molecules and form microfibrils; intermicrofibrillar tie molecules link the microfibrils, thus transforming the raw material into a continuous fibre structure.

The microfibrillar model is well suited to explain the cold-drawing and necking process, e.g. for PE and polypropylene (PP), and it also applies (with some limitations) to hot drawing without a neck [108]. Appropriate explanations have been developed for the more-than-linear increase of elastic modulus with draw ratio, and it can be concluded that the best parameter for characterisation of the fibrous structure is the fraction, orientation, and tautness of (both intra and inter) tie molecules [105].

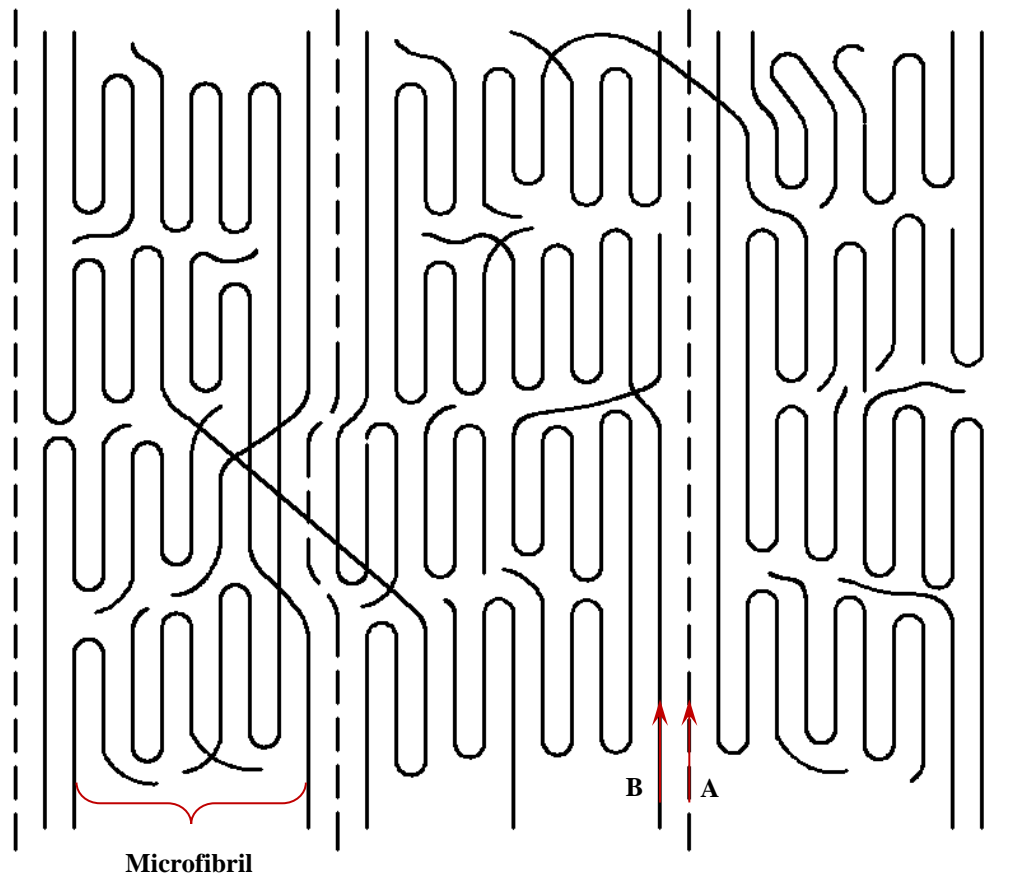


Figure 2-7 Schematic representation of the microfibrillar model for the fibre structure: A is interfibrillar tie molecule; B is intrafibrillar tie molecule; the fibre axis is vertical. Redrawn from [108].

2.7.2 Three-phase ‘Swiss-cheese’ model

Unlike the microfibrillar model described above, the ‘Swiss-cheese’ model [104, 107] is based on three phases, i.e. the crystalline phase, isotropic amorphous phase and oriented amorphous interfibrillar phase as represented in Figure 2-8. It is mainly established to explain the properties of polyamide (PA) and polyethylene terephthalate (PET) fibres [104]. Similar to the microfibrillar model, the cold-drawing process would also transfer the initial structure into a microfibrillar structure; however, intrafibrillar tie molecules are distributed more or less uniformly inside microfibrils. Crystalline microfibrils are surrounded by amorphous domains, and comparatively larger amounts of interfibrillar tie molecules in the amorphous region are stretched during the drawing process, to become oriented taut-tie molecules (TTMs) and these form the third phase; i.e. the oriented amorphous regions which control the mechanical properties of polymeric fibres [104, 111].

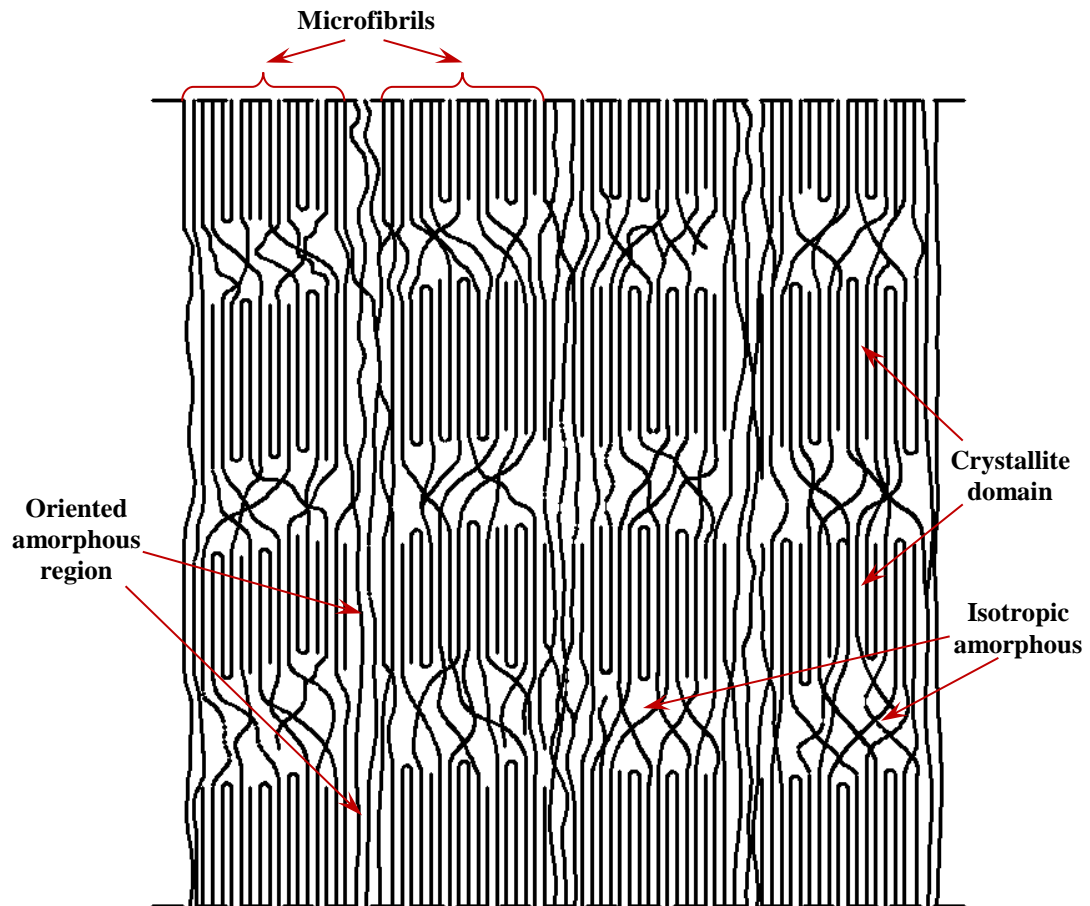


Figure 2-8 Schematic representation of ‘Swiss-cheese’ model of the fibre structure. Crystallites are periodically arranged to form microfibrils and are surrounded by the amorphous phase. Redrawn from [107].

The two-phase microfibrillar model (Section 2.7.1) was developed from the investigations of drawing PE and PP [108], and not suited to PA and PET fibres; however, the Swiss-cheese model is well developed to be capable of these [107]. The major difference between the Swiss-cheese model and the microfibrillar model is the interpretation regarding the role played by the microfibril structure and the matrix in determining the fibre mechanical properties. Certainly the microstructure is not limited to current models and there is a need for further development.

2.7.3 Viscoelastic deformation

As stated above, the mechanical properties of semi-crystalline polymeric fibres depend not only on their chemical composition, but also on the fibre forming process. For a semi-

crystalline polymer, the instantaneous response to an external mechanical loading, as well as its load-bearing ability, is mainly determined by the crystallised chains; while time-dependent effects such as the development of viscoelastic strains are caused by the amorphous regions [113]. The time-dependent viscoelastic behaviour can be represented by a simple mechanical spring-dashpot model as schematically shown in Figure 2-9; however, deformation behaviour of the real fibre material may consist of a number of spring-dashpot elements connected in series with a broad distribution of spring stiffnesses and dashpot viscosities [97, 114].

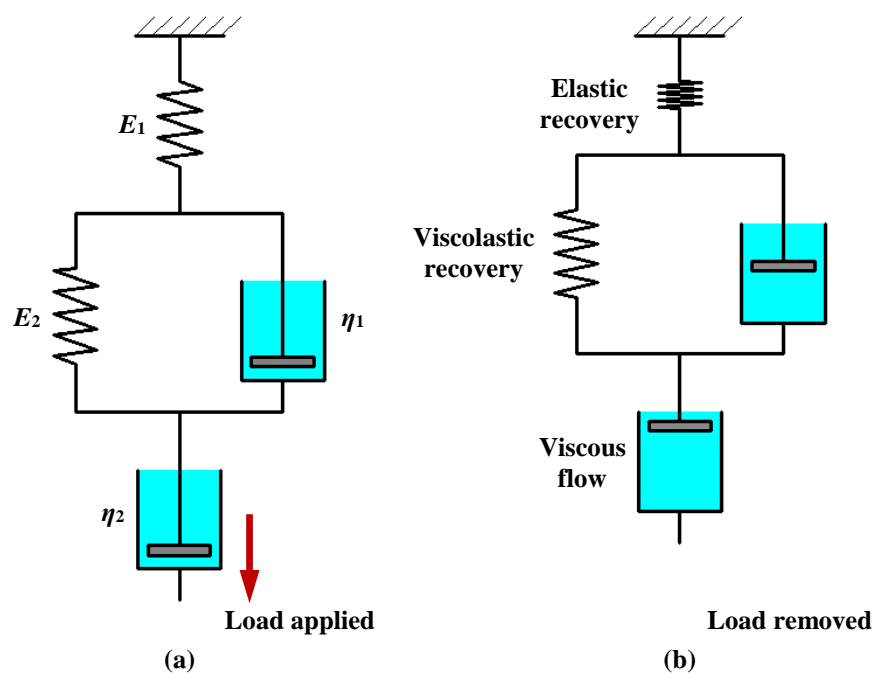


Figure 2-9 Schematic representation of a mechanical spring-dashpot model: (a) deformation under tensile loading; (b) recovery following load removal.

When subject to a tensile stress (below the ultimate tensile stress), as shown in Figure 2-9 (a), the spring with stiffness E_1 represents elastic deformation that occurs in the crystalline regions, and recovers instantaneously following load removal in Figure 2-9 (b). The stability of the crystallites under mechanical loading is determined by intermolecular forces and degrees of orientation [110]. The spring with stiffness E_2 together with the dashpot with viscosity η_1 connected in parallel, represent the time-dependent deformation behaviour. The deformation of this unit is usually accompanied with extensive molecular rearrangement [114]. The dashpot designated η_2 represents viscous flow, which is non-

recoverable after load removal; this may be due to the displacements (jumps) of molecules under loading [97].

2.8 MORPHING STRUCTURES

Since VPPMC technology offers the capability for producing morphing structures, this section reviews the development of morphing composites. Morphing technology have received increasing interest in recent years in aircraft aerofoils [115-117], automobile structures [118], and wind turbine blades [119]. Morphing structures can provide several benefits over conventional mechanical approaches in terms of cost, aerodynamic efficiency, complexity, weight and shape adaptivity. Morphing structures generated from utilising the deformation of PMCs have been developed since the 1980s [69, 120, 121]. Similar to smart materials, they are able to change shape due to external stimulation, i.e. piezoelectric patches [122], piezocomposite actuators [123] or pressure [71, 124].

To date, morphing composite structures have been generally produced through: (i) thermally induced un-symmetric laminates and (ii) elastic fibre prestress-induced symmetric laminates. For (i) extensive research has been carried out by many investigators (Section 2.8.1), and it was found that the residual stresses generated from thermal expansion mismatch could be expected. For (ii), the method for utilising prestress has received progressive interest.

2.8.1 Un-symmetric morphing structures

It is known that un-symmetric laminates exhibit twisted or deformed shapes. This deformation is due to the mismatch in thermal expansion coefficients of the reinforcement fibre (α_f) and matrix materials (α_m). Substantial thermal residual stresses can be developed within continuous-fibre reinforced polymeric matrix composite laminates during cool-down from curing process (Section 2.3). These effects can lead to laminate warping, buckling or matrix cracking, depending on the fibre and matrix combination and laminate stacking sequence used [40]. For many years, these deformed shapes were

regarded as undesirable, and were often compensated by adding extra layers to make the laminate symmetrical [121, 125]. More recently (since the 1980s), these properties have been exploited to create the deflections for morphing structures [69, 121, 126, 127].

Thermal residual stresses within un-symmetric laminates have been widely studied during the past few decades [69, 120, 121, 125-133]. Here, geometrical non-linearity and residual stresses can be exploited to generate large out-of-plane displacements to give bistable or multistable behaviour [118, 120, 121]. It is well-known that the response of composite laminates can be analysed using classical lamination theory (CLT), which is based on several assumptions:

- (i) The displacements are continuous throughout the laminates;
- (ii) The Kirchhoff hypothesis is assumed to be valid;
- (iii) The strain-displacement relationship is linear;
- (iv) The material is linearly elastic;
- (v) The through-the-thickness stresses are small in comparison to the in-plane stresses.

CLT theory integrates constitutive equations through the thickness of the laminate to give overall properties defined by in-plane, coupling, and flexural stiffness matrices. It is capable of accurately predicting static deflections, natural vibration frequencies and mode shapes, buckling loads and mode shapes, and thermal expansion coefficients of laminates. However, there are situations when CLT fails to present the correct materials behaviour. As for all un-symmetric laminates, CLT predicts their room temperature shapes to be an unstable saddle shape [23, 69, 121] as shown in Figure 2-10 (b); while Hyer [121] observed from experiments that some un-symmetric laminates exhibited two stable room-temperature configurations which were both cylindrical and possessed a ‘snap-through’ phenomenon; i.e. a loading force could make it ‘snap’ from one stable cylindrical shape to another. Hyer [69] pointed out that there are two limitations to the CLT which result in its failure to predict the correct answer:

- (i) Inability to predict the response of thicker laminates;
- (ii) Inability to explain the behaviour of laminates near edges.

For (i), Whitney et al [134, 135] performed corrections to the CLT and satisfactory results were then obtained for thicker laminates; Hyer [121] found that 100×100 mm and 150×150 mm $[0_2/90_2]_T$ graphite/epoxy laminates produced cylindrical shapes at room temperature.

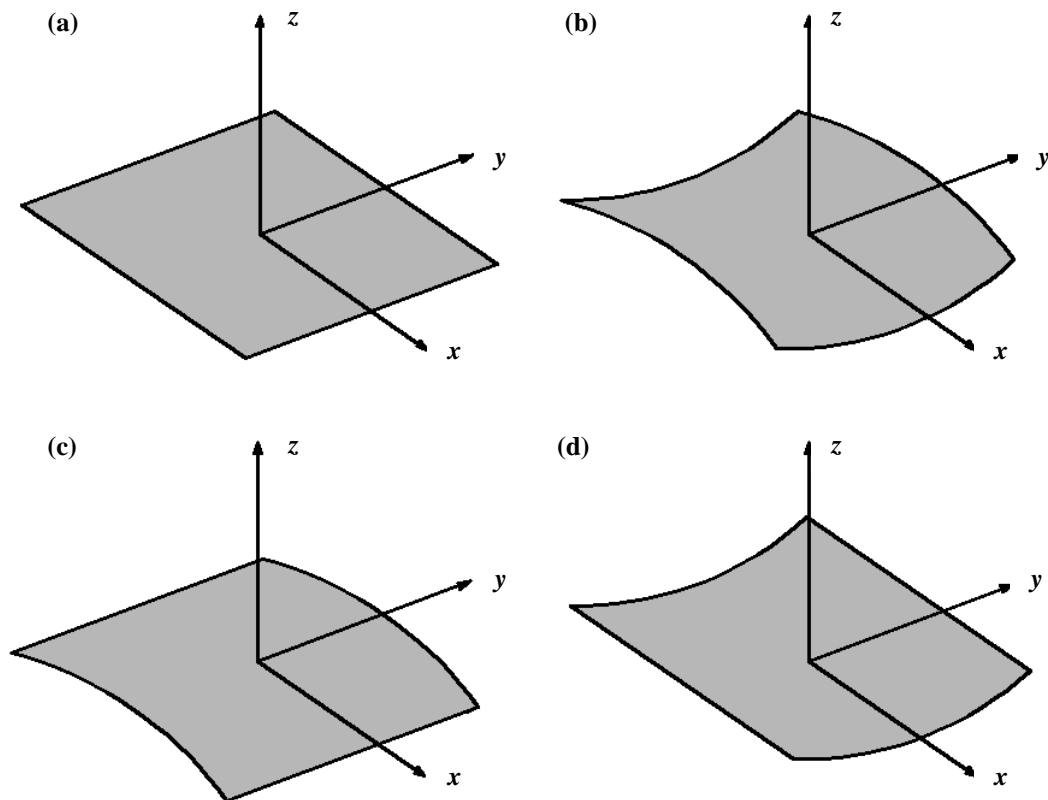


Figure 2-10 Basic shapes of laminates: (a) reference state at stress-free temperature; (b) a saddle shape at room temperature; (c) a cylindrical shape with curvature in y -direction; (d) alternative cylindrical shape with curvature in x -direction.

For (ii), which is known as the free-edge effect, has been observed and investigated by many researchers during the past few decades. There have been numerous studies to analyse the highly concentrated inter-laminar stresses near and at the free edges of composite laminates both experimentally and numerically. Since these have been fully reviewed by Mittelstedt and Becker [136, 137], Kant and Swaminathan [138], it is not elaborated in this section.

Hyer [69] made the first attempt to model the un-symmetric laminate behaviour. Since a uncured prepreg laminate is flat at the elevated curing temperature as illustrated in Figure 2-10 (a), it was assumed that during the cooling process, the out-of-plane deflection developed only from the differences in thermal expansion of the individual lamina. Upon cooling, the laminate deformed into either a saddle shape or a cylindrical shape as shown in Figure 2-10 (b), (c) and (d). The actual shape depended on the minimum of the total potential energy. Since geometric non-linearity was essential for out-of-plane deflection development, the following strain-displacement relationships were extended from the CLT:

$$\varepsilon_x^0 = \frac{\partial u^0}{\partial x} + \frac{1}{2} \left(\frac{\partial w}{\partial x} \right)^2 \quad (2-13)$$

$$\varepsilon_y^0 = \frac{\partial v^0}{\partial y} + \frac{1}{2} \left(\frac{\partial w}{\partial y} \right)^2 \quad (2-14)$$

$$\varepsilon_{xy}^0 = \frac{1}{2} \left(\frac{\partial u^0}{\partial y} + \frac{\partial v^0}{\partial x} + \frac{\partial w}{\partial x} \frac{\partial w}{\partial y} \right) \quad (2-15)$$

where, ε_x^0 , ε_y^0 , ε_{xy}^0 are midplane strains; u^0 , v^0 and w are the laminate mid-plane displacements in the x -, y - and z -directions, respectively.

Then the approximate solution for the laminate midplane displacements were obtained based on two assumptions: (i) the midplane elongation strains do not vary significantly from the linear prediction, i.e. ε_x^0 and ε_y^0 are independent of x and y , respectively; (ii) the mid-plane shear strain is negligible, i.e. $\varepsilon_{xy}^0 = 0$. Thus:

$$u^0(x, y) = cx - \frac{a^2 x^3}{6} - \frac{abxy^4}{4} \quad (2-16)$$

$$v^0(x, y) = dy - \frac{b^2 y^3}{6} - \frac{abx^2 y}{4} \quad (2-17)$$

$$w(x, y) = \frac{1}{2}(ax^2 + by^2) \quad (2-18)$$

in which, a , b , c , and d are constants.

From Equations 2-16 to 2-18, the saddle shape, as in Figure 2-10 (b), can be obtained when $a = -b$, conforming to the CLT; and either of the two cylindrical shapes can be produced as $a \neq 0$ and $b = 0$, in Figure 2-10 (c), or $a = 0$ and $b \neq 0$ in Figure 2-10 (d). This theory successfully predicted the disappearance of the saddle shape, and the two stable equilibrium states observed from graphite-epoxy thin $[0_n/90_n]_T$ un-symmetric laminates [69, 120, 121], but clearly there needs to be more experimental work. However, since the above theory is based on one-term Rayleigh-Ritz solution, it is over-constrained. Thus Hyer [120] developed it further by considering more stacking sequences on four-ply un-symmetric laminates.

It was also noticed by investigators that there is a size effect in un-symmetric laminates, as described by Hyer [121]. The thickness-to-length ratio and width-to-length ratios of the laminate govern whether the laminate would be cured into a saddle shape or a cylindrical shape. Figure 2-11 shows the edge length to thickness ratio effect on the room-temperature shapes of un-symmetric laminates. As the ratio moves along segment AB, the room-temperature shapes of the laminates are predicted to form a saddle, and the curvatures become smaller. When it reaches the critical value r_c , there is a bifurcation point B. Beyond this point, the laminates follow three possible shapes, as denoted by BC, BD and BE. BC represents a continuation of the saddle shape which is unstable; BD and BE correspond to a stable cylindrical shape in x - and y -direction, respectively.

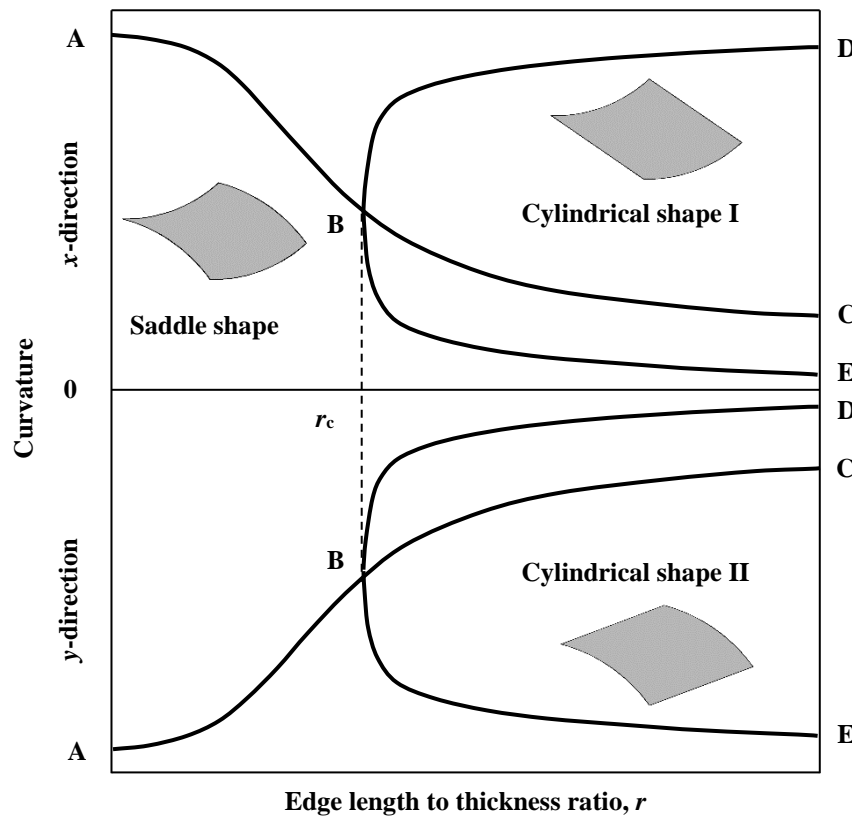


Figure 2-11 Size effect on the room-temperature shapes of un-symmetric laminates.

As demonstrated in Figure 2-11, the amount of curvature gives a non-linear function with the aspect ratio. A similar trend was also demonstrated by Hufenbach et al [132]. They considered the effect of edge length on the curvature of CFRP and GFRP based multistable un-symmetric laminates. An optimisation procedure was developed to determine the stable stationary points of the strain energy. The bifurcation point analogous to point B in Figure 2-11 was also demonstrated, this being a critical edge length to indicate the possibility of bistability for a given laminate.

Gigliotti et al [133] investigated the bifurcation point of thin [0/90] unsymmetric composite laminates using the finite element analysis method. The length-to-width aspect ratio was found to be crucial in determining the existence and stability of the cylindrical shapes. Their observations were based on the following non-dimensional quantities:

$$a^* = \frac{\alpha L^2}{t}, \quad b^* = \frac{b L^2}{t}, \quad L^* = \frac{\alpha \Delta T L^2}{t^2} \quad (2-19)$$

where, a^* and b^* are the non-dimensional curvatures; L is the edge length of the square laminates; L^* is the non-dimensional edge length; t is the single ply thickness; α is the difference between the transverse and longitudinal coefficients of thermal expansion. Then the following relationships regarding to the bifurcation point were established through the predictions from ABAQUS and Rayleigh-Ritz models:

$$\text{constant} = L_A^* (t_0/t_{90})^3 \quad (i) \quad (2-20)$$

$$\text{constant} = L^* / (AR_{tr}) \quad (ii)$$

where, L_A^* is the minimum edge length for a square laminate with aspect ratio of t_0/t_{90} to behave with bistability; AR_{tr} is the aspect ratio at the bifurcation point. Equation 2-20 (i) shows that the critical edge length for bistability of square laminate decreases as the ratio of ply thicknesses increases. Equation 2-20 (ii) allows the establishment of transition from saddle to stable cylindrical shapes from known reference values. Experimental investigation in Ref [133] was also conducted on rectangular laminates with an aspect ratio of 10, and good agreement with numerical simulations was found.

2.8.2 Symmetric morphing structures

As discussed above, morphing structures generated from thermal residual stress within the composite have been mainly $[0_n/90_n]$ un-symmetric laminates since the 1980s; however, the technique to produce symmetric laminates are comparatively new and have been developed since 2004. Here, Potter et al realised the morphing laminates do not necessarily need to be un-symmetric [71, 131]. By inserting narrower 90° carbon fibre

prepreg into 0° unidirectional glass fibre prepreg, a multistable structure was derived with symmetric layup across the mid-plane. The interaction from different thermal expansion responses during the curing process generated out-of-plane distortion, and the laminate exhibited four stable states with the snap-through phenomenon. As investigated by Tuttle [48], prestressing fibres could generate compressive stresses within the composite and induce out-of-plane deflections. This was investigated further by Potter et al [131] and Daynes et al [70, 71]. They reported that independent control of elastic prestress levels from different directions of unidirectional fibre layers could produce bistable or multistable structures. To adopt elastic fibre prestressing into the production of symmetric bistable laminates, they applied prestrain to selected fibres from outside 0° fibre layer for both CFRP and GFRP $[0/90/90/0]$ laminates prior to resin curing. It was found that bistability could be achieved by careful manipulation of fibre prestressing along the width. Numerical analysis showed that the lowest critical buckling prestress occurred when the width ratio b_1/b was in the region of 0.5-0.8 for 0.15% prestrained CFRP and 0.40% prestrained GFRP laminates, which correlated well with experimental results [70].

Later, Daynes et al [71] applied the prestressing to selected fibre plies prior to resin curing and produced prestressed symmetric laminates. The layup of laminates included $[0^P/90/90^P/0]_T$ and $[0^P/90/90/90^P/90^P/0]_T$, with superscript P referring to prestressing in fibres. Bistability was derived from geometrically un-symmetric fibre prestressing. Finite element results indicated that abilities for larger load-carrying capability and tailored snap-through loads and curvatures could be achieved. Lachenal et al [72] investigated the application of prestressed composites on twisting structures. A bistable twisting I-beam was produced by combining two prestressed CFRP flanges on GFRP web geometry. Prestress was achieved by flattening the curved flanges. It could snap-through from one stable shape to another when an external moment was applied, and demonstrated a non-linear torsional stiffness relationship with twist angle. Similar structures were reported in Ref [73], to produce a multistable twisting structure.

Morphing structures utilising elastic fibre prestressing offer benefits over those exploiting residual thermal stresses. These include: (i) since residual stresses are induced by thermal curing of the matrix, thermal stresses generated in morphing structures can be highly susceptible to hygrothermal variability [132, 133, 139-141], while this has very limited

effects on elastically prestressed morphing composites [70, 71]; (ii) residual thermal stresses generated in laminates possess low snap-through loads [130], but snap-through loads and curvatures of prestressed symmetric laminates can be designed from independent control of prestress levels within unidirectional composites, which make it possible for them to sustain significant external loading [71].

Chapter 3

MATERIALS, EVALUATION PRINCIPLES AND EXPERIMENTAL PROCEDURES

SUMMARY

This chapter presents an overview of materials and evaluation techniques involved in this research. General information on the fibre and matrix materials used in this work is given. To facilitate understanding of the thesis, a summary of the basic principles and theoretical analysis involved in later chapters is also provided. Experimental procedures and evaluation techniques are provided in terms of (i) fibre processing and (ii) composite production. For (i), the fibres were subjected to annealing first, and their viscoelastic characteristics were evaluated through measurement of creep, recovery, and recovery force. Additionally, details on fibre analysis methods using scanning electron microscopy and X-ray diffraction are given, to provide information at the microstructural level. For (ii), composite production procedures are described, followed by mechanical evaluation methods; i.e. Charpy impact testing and the three-point bending test; optical microscopy was used to evaluate the fibre distribution within a composite.

3.1 MATERIALS

3.1.1 Nylon 6,6 fibre

Nylon (polyamide) 6,6 is synthesised through the polycondensation of hexamethylene diamine and adipic acid. This was pioneered by Carothers in the early 1930s [142]. The formula and repeating unit are shown in Figure 3-1. The repeat distance for nylon 6,6 along the fibre axis gives approximately 17.2 Å [143]. Inter-chain hydrogen bonds between the C=O groups of one molecule and the N-H groups of the adjacent chain gives nylon 6,6 a relatively high melting temperature of 265°C [144]. It also has a high water absorption capacity, which can significantly affect other physical and mechanical properties. Today it has attained considerable commercial importance, particular in fibre form, and has already been used in a wide range of industrial applications.

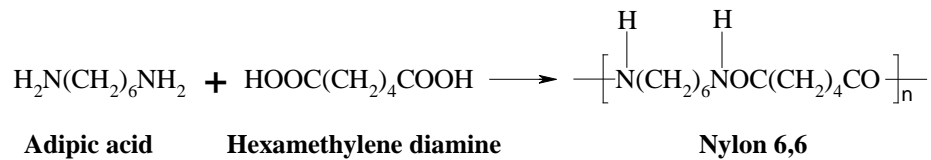


Figure 3-1 Formula to produce nylon 6,6 and its repeating unit.

Nylon 6,6 fibre is a semi-crystalline multi-filament polymeric fibre with crystalline domains, isotropic amorphous regions, and oriented amorphous regions [111]. The filaments are melt spun through spinnerets and orientation occurs during the cold-drawing process. The drawn filaments have a density of 1.14 g/cm³, a moderately high degree of elasticity, and a high moisture absorption capability (8 wt% equilibrium) [142, 145]. The crystal structure results from the conformation of the macromolecules and their lateral packing. Appropriate distances are maintained due to the intermolecular forces, i.e. hydrogen and van der Waals bonds [146]. The amide group in the repeating unit provides intermolecular hydrogen bonding between polyamide chains as illustrated in Figure 3-2. Adjacent molecule chains are then linked to form sheets. Simple stacking of these sheets control the size and shape of the crystal unit cell, which are connected through van der

Waals interactions. This ensures the nylon 6,6 has high strength, low friction coefficient, and good chemical and abrasion resistance. Details of the crystalline structure within nylon 6,6 fibre are discussed further in Section 3.2.4.

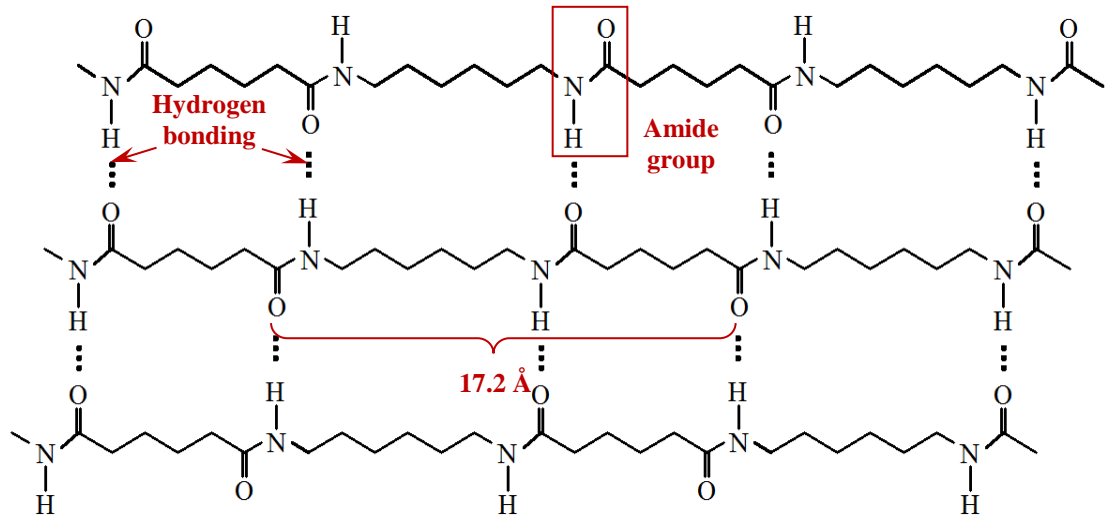


Figure 3-2 Schematic representation of micro-structures of nylon 6,6 fibre and intermolecular hydrogen bonding formed between carbonyl oxygen and amide hydrogen within the polyamide chains.

In this study, a continuous untwisted multifilament nylon 6,6 yarn supplied by an industrial supplier, i.e. Ogden Fibres Ltd, UK, was used. Nylon fibre used in previous work, was supplied by Goodfellow Cambridge Ltd., UK [1, 2, 5-7, 10, 98, 99]. Though they were both specified to be 94 tex yarn, with 140 filaments of 26 μm filament diameter, the evaluation of the new fibre, compared to the previously used material was required to determine possible differences in physical and mechanical properties. This is presented in Chapter 4, using various techniques outlined in Section 3.4.

3.1.2 Unsaturated polyester resin

Polyester resins are one of the most versatile synthetic copolymers [147]. They have received significant attention since they were synthesised by Carothers [148] through his study on step-growth polymerizations in 1929. Today, thermosetting polyester products have been widely used for commercial and industrial purposes. The term ‘polyester resin’ is applied to the condensation reaction products of diacids and diols; i.e. the esterification reaction between COOH and OH groups to form the carboxylate ester functional group.

The choice of raw material available to formulate polyester resins is vast and determines the final cured properties of the material. Thus polyester resins can be tailored to suit a wide variety of structural applications [149]. This versatility depends upon the structure of diacids, diols, cross-linking agents, initiators and other additives. These can influence resin properties such as weather resistance and ultraviolet (UV) aging. From this point of view, polyester resins can be characterised as either ‘saturated polyester resin’, synthesised from saturated monomers or ‘unsaturated polyester resin’. The latter has an unsaturated component in the macromolecules which enables further reaction.

Unsaturated polyester resin (UPS) is one of the most commonly used thermosetting resins. It is generally used as solutions with additives, such as poly-functional monomers or oligomers, and cross-linking agents (e.g. styrene) to reduce viscosity of the resin to facilitate the moulding process. The styrene also performs a vital function, as it serves as a co-monomer, capable of reacting with the polymer chains. The curing process of the liquid UPS is induced through addition of suitable initiators (also known as catalysts) which are generally organic peroxides, such as benzoyl peroxide (BPO) or methyl ethyl ketone peroxide (MEKP). These compounds can decompose into free radicals under appropriate conditions (heating, UV radiation). At the initial curing stage, the free radicals start to act on the unsaturated bonds of monomer molecular chains, which in turn produce more radicals. The reaction at the initial stage occurs slowly, the resin system maintains low viscosity, allowing good flow and impregnation for the moulding process. Further reaction between monomers release heat, which accelerates the movement of free radicals, propagating a chain reaction of the resin system. Meanwhile, the branching and cross-linking reactions between styrene and polyester chains produce a three-dimensional network of covalently bonded chains, which are insoluble and infusible [38]. Depending on the stability and structure of the unsaturated bonds of the raw materials, the resin can be cured within a time frame ranging from less than a minute to the order of an hour.

Figure 3-3 schematically represents the cross-linking between styrene and the strictly alternating polyester chains. Cross-linking imparts the resin rigidity, high strength, solvent resistance, good thermal and oxidative stability. The cured resin properties are directly related to the cross-link density (ν_c) and the chain molecular weight between cross-links (M_c) [38]. A higher ν_c value results in a greater matrix rigidity or higher elastic

modulus, while an increase in the M_c value would provide better impact resistance, and superior fracture toughness.

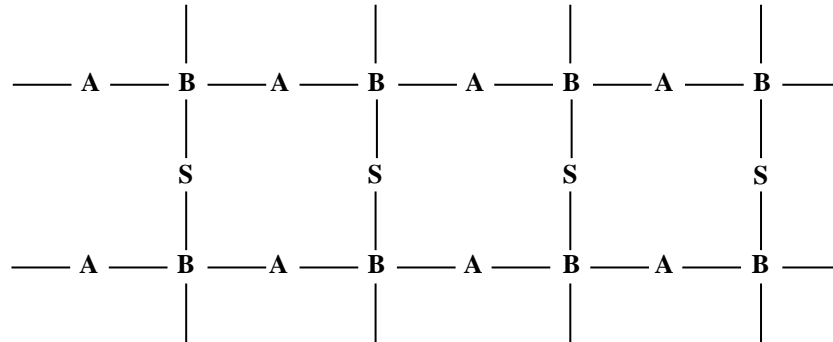


Figure 3-3 Schematic representation of cross-linking reaction within a resin curing system. A and B are repeating units within an unsaturated polyester resin; S is a cross-linking agent, e.g. styrene.

As UPS has been the most common resin used in VPPMC studies, the matrix materials involved in this research also fall into this category. Due to resin supply problems, an alternative resin had to be selected for the future investigations. This is covered in Chapter 4.

3.2 FIBRE EVALUATION PRINCIPLES

To better understand prestress characteristics within a prestressed composite, the viscoelastic behaviour of annealed polymeric fibre was investigated through measurement of creep strain, recovery strain, and viscoelastic recovery force. Detailed investigations on creep and recovery behaviour of nylon 6,6 fibres under various creep conditions are presented in Chapters 5 and 6. The loading period varied from tens of minutes to 24 h for different objectives. This section summarises the basic principles and theoretical analysis of the adopted evaluation methods.

3.2.1 Annealing effect on nylon 6,6 fibre

Thermomechanical history can influence the ability of polymeric materials to undergo plastic deformation. Annealing effects on polymers, such as nylon, have been previously reported [105, 144, 150-156]. The annealing process can perfect the crystal structure, increase boundary definition between crystals and amorphous regions [152], increase the number of regular chain folds [150, 151], and cause molecular relaxation in amorphous regions [105] which often leads to sample shrinkage. At a microstructural level, it has been recognised that for polymeric materials, there is chain rearrangement due to hydrogen bond rupture, which is subject to elevated thermal effects, and relaxation of the load bearing TTMs (Section 2.7.2). More significantly, chain motion in amorphous regions produce chain folding or recrystallization, leading to further increases in crystallinity. Owing to the contribution from shrinkage to chain relaxation, molecular level changes are maximized when the fibre is free, and minimized when the fibre is constrained [144, 151].

For nylon 6,6, it is known that heating causes recrystallization in localized areas within the fibre [105, 150, 151]. Dismore and Statton [150] proposed a model to interpret the annealing effect on this fibre material. As shown in Figure 3-4 (a), the oriented molecules in a drawn fibre are highly extended and essentially parallel to each other, with comparatively few chain folds. These molecules are connected with a distribution of intermolecular bond energies through hydrogen or van der Waals bonding. When subject to heating, the intermolecular bonds, with relatively low energy, break or 'melt'. This makes the molecular chains free to move and become randomised. The molecular mobility enables chain folding, as illustrated in Figure 3-4 (b), leading to an increase in crystallinity. The remaining un-melted intermolecular bonds maintain fibre orientation. Chain folding after annealing results in fewer TTMs to carry loads which in turn, may cause premature breakage of fibres [150]. Matsuoka [154] found the excess entropy would decrease when a polymeric solid is annealed; i.e. the potential energy of the structure is reduced further. They also suggested that a well-annealed sample tended to be stiffer and more brittle. Research on annealing of drawn nylon 6,6 fibre from Dumbleton and Buchanan [153] agreed generally with the findings Dismore and Statton [150] as represented in Figure 3-4. The main difference was the observation of

disorientation at higher annealing temperatures, which may be caused by the relaxation of molecular chains in non-crystalline regions within the fibre. Similar conclusions were also obtained by Statton [151] through SAXD and WAXD. Higher temperature annealing of drawn nylon 6,6 fibre would cause increases in local ordering, number of regular chain folds, fraction of movable molecular chains, and recrystallization in localised areas.

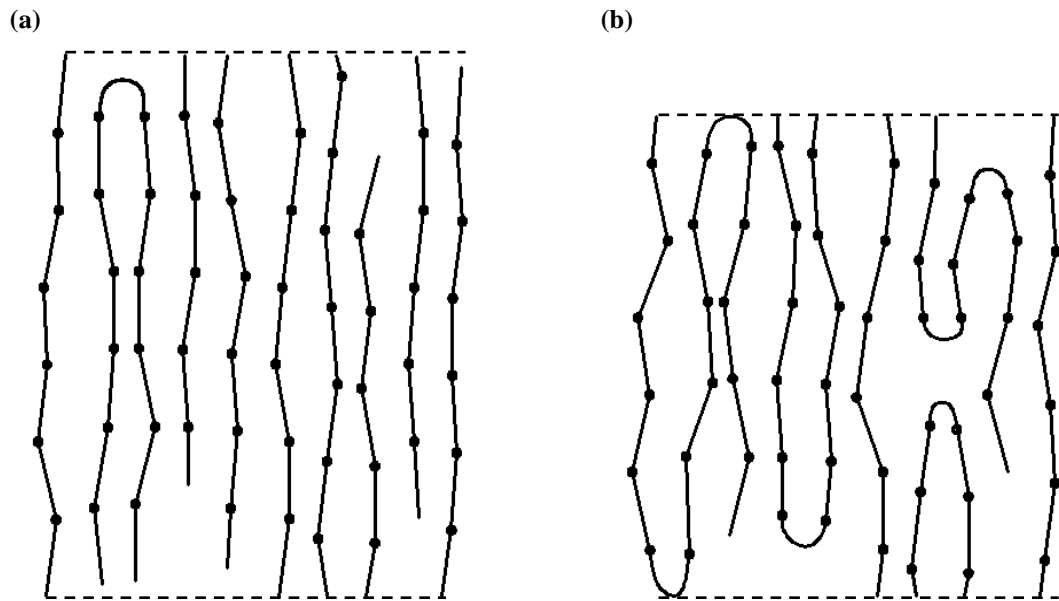


Figure 3-4 Schematic representation of annealing effect on molecular structure in oriented nylon 6,6 fibre: (a) oriented molecules; (b) molecular chain folding after annealing. The dots represent a polymer repeat period or some of the hydrogen bond positions. Redrawn from [150].

As pointed out by Peterlin [105], the relaxation of molecules, especially the oriented TTMs, may be detrimental to the mechanical properties of polymers. Since crystal and isotropic amorphous regions are connected through oriented amorphous chains, the slackened TTM chains are unable to efficiently transmit axial forces between crystallites through the intervening amorphous layers, which in turn could reduce the elastic modulus of some polymers, i.e. PE [157]. Therefore, the balance of molecular relaxation and recrystallization on material properties should be considered during annealing. Babatope and Isaac [144] suggested that for nylon 6,6, the optimisation of chain packing and reduced randomisation in the amorphous phase was reached at an annealing temperature of 150°C. Above this temperature, a non-uniform weakening due to thermal fluctuation and chain degradation occurred. Their experiments on annealing of unconstrained nylon

have shown that up to the annealing temperature of 150°C, tensile modulus, and to a lesser extent, the yield strength, increase with annealing time.

Investigations into the viscoelastic recovery of nylon 6,6 yarn have shown that a higher residual strain is observed in the annealed yarn, compared to the non-annealed fibre in terms of both creep and recovery [2, 11]. The ability to store more mechanical energy through viscoelasticity from fibre stretching is an important issue. Therefore, by considering the above points, unconstrained annealing of nylon 6,6 fibre at 150°C for 0.5 h was conducted in this research, to obtain long-term viscoelastic recovery and remove manufacturing-induced residual stresses [5, 10, 144].

3.2.2 Creep and recovery

When a polymeric fibre is subjected to a creep load, the material will undergo both elastic and plastic deformation. Conventionally, the viscoelastic component of creep and recovery can be represented by a number of Voigt elements connected in series [18]. Figure 3-5 schematically shows the strain-time characteristics of a polymeric creep-recovery cycle, with time-dependent components represented by functions based on the Weibull or Kohlrausch-Williams-Watts function [96]. For creep, $\varepsilon_{\text{tot}}(t)$ is the total strain at time t , under an applied constant stress and it can be represented by:

$$\varepsilon_{\text{tot}}(t) = \varepsilon_i + \varepsilon_c \left[1 - \exp\left(-\left(\frac{t}{\eta_c}\right)^{\beta_c}\right) \right] \quad (3-1)$$

here, ε_i is the instantaneous strain from initial application of the stress which is independent of time; ε_c function is the time dependent creep strain where η_c is the characteristic life and β_c is the shape parameter. Following removal of the creep load, the elastic deformation is (effectively) recovered, as represented by ε_e in Figure 3-5, and the remaining recovery strain $\varepsilon_{\text{vis}}(t)$ is:

$$\varepsilon_{\text{rvis}}(t) = \varepsilon_r \left[\exp \left(- \left(\frac{t}{\eta_r} \right)^{\beta_r} \right) \right] + \varepsilon_f \quad (3-2)$$

The ε_f function is the time dependent recovery strain with η_r and β_r being the Weibull parameters analogous to those in Equation 3-1. The (non-recoverable) strain from viscous flow is represented by ε_f in Figure 3-5.

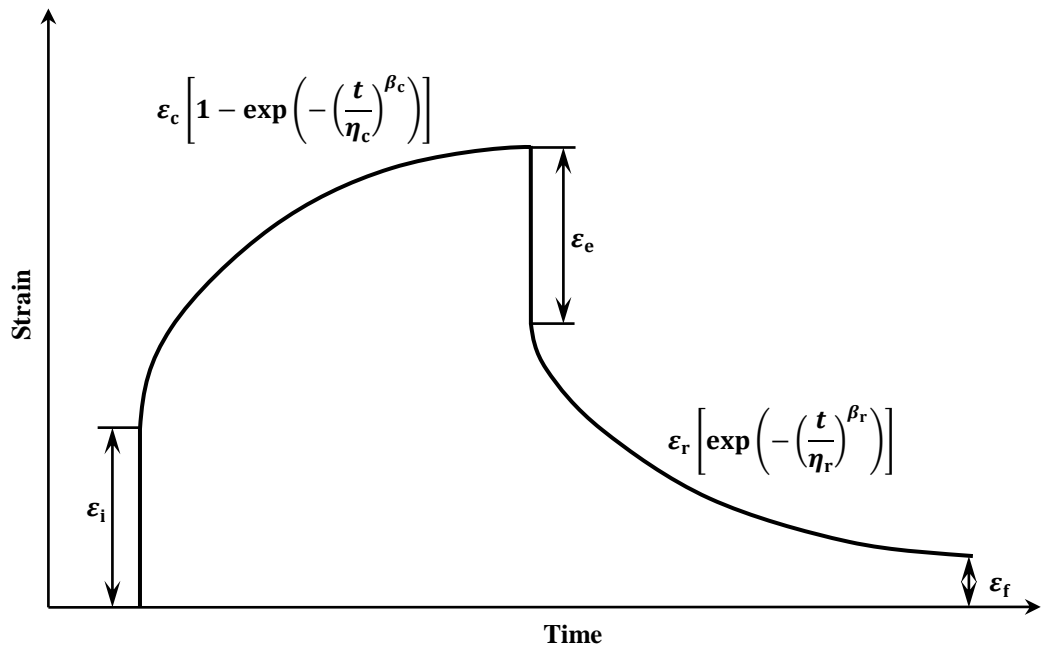


Figure 3-5 Schematic of the polymeric fibre creep-recovery strain cycle.

3.2.3 Recovery force

The viscoelastic recovery, following creep load removal, should be capable of producing a force. By fixing the yarn at a constant strain, the continuing contraction effect from the fibres will generate a force [99]. Figure 3-6 shows schematically, the recovery force-time characteristics generated from a creep-recovery test cycle. As discussed in Section 3.2.2, the elastic recovery is recovered instantaneously after creep load removal. Since viscoelastic recovery is time dependent, the stress generated from viscoelastic recovery follows [99]:

$$\sigma(t) = \sigma_v \left[\exp\left(-\left(\frac{\Delta t}{\eta}\right)^\beta\right) - \exp\left(-\left(\frac{t}{\eta}\right)^\beta\right) \right] \quad (3-3)$$

where, the σ_v function represents time-dependent viscoelastically generated stress, as determined by the characteristic life η and shape β parameters; Δt is the time delay between releasing the load and the start of force measurement, as shown in Figure 3-6. It should be noted that the yarn is in a loose state during Δt .

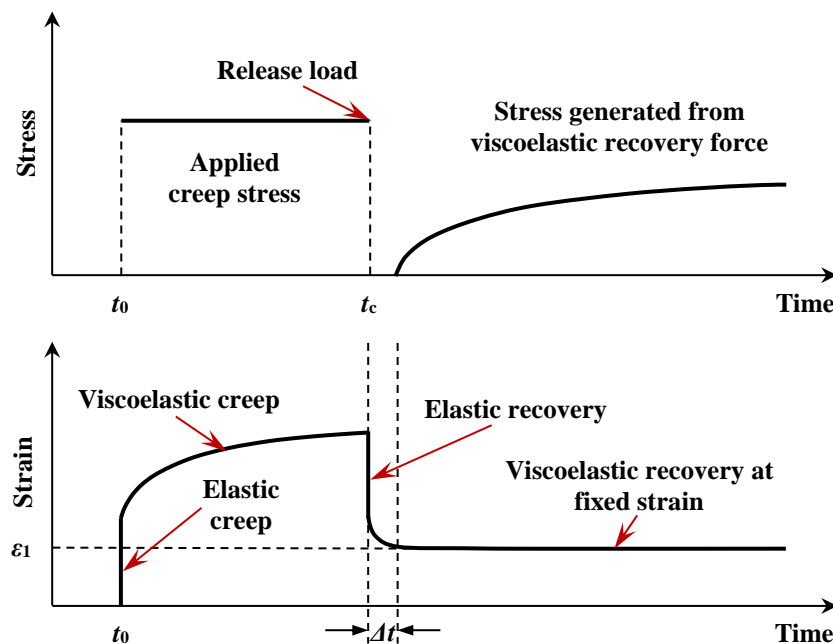


Figure 3-6 Schematic representation of the polymeric fibre recovery force-time characteristics generated from a creep-recovery cycle.

3.2.4 X-ray diffraction

3.2.4.1 Brief history and principle

In 1895, Wilhelm Röntgen discovered X-rays. At a time when Röntgen was investigating the range of cathode rays in air from different types of evacuated glass tubes, he noticed that while the rays were being produced, a screen coated in fluorescent barium platinocyanide would glow. As the screen was too far from the tube to be affected by the cathode rays, he assumed there were unknown rays being emitted from the walls of the

tube which resulted in them being named as X-rays. In 1912, Max von Laue proposed the hypothesis that crystalline substances act as 3D diffraction gratings for X-rays, based on following assumptions: (i) the atomic lattice of a crystal is regular and periodic; (ii) X-rays are electromagnetic radiation; (iii) the interatomic distances of a crystal are the same order of magnitude as X-rays. Laue's prediction was confirmed by Walter Friedrich and Paul Knipping. They successfully photographed the X-ray diffraction pattern of crystalline $\text{CuSO}_4 \cdot 5\text{H}_2\text{O}$. After the discovery of the diffraction of X-rays by crystals in 1912, William L. Bragg [158, 159] developed Bragg's law, which relates the wavelength of X-rays to the glancing angle of reflection. The birth of X-ray diffraction (XRD), was in 1913; William H. Bragg built the first X-ray spectrometer, which was used to study X-ray spectral distributions.

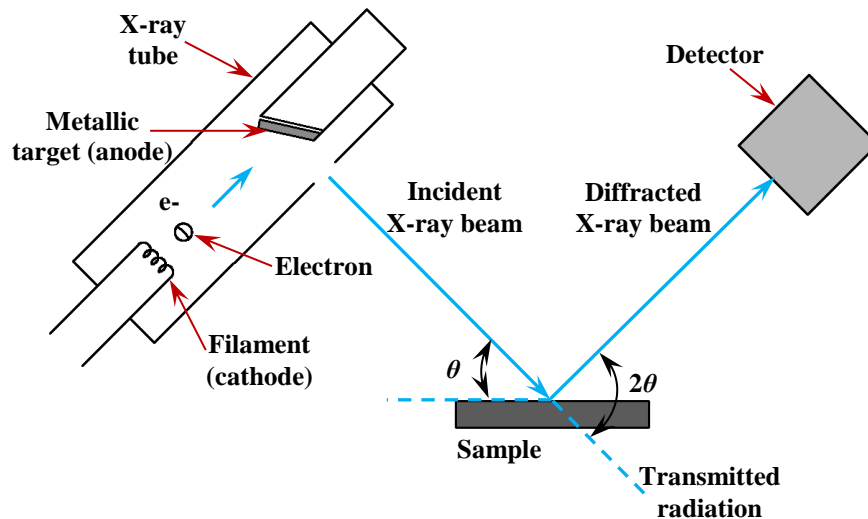


Figure 3-7 Schematic representation of experimental set-up for X-ray diffraction.

The commonly used source of X-rays in an XRD instrument is the X-ray tube as illustrated in Figure 3-7. A bias voltage of 30-50 kV is applied between the filament and metallic target in an evacuated X-ray tube, causing electrons emitted from the filament to collide with the metallic target at a high speed and radiate X-rays. The wavelengths of the X-rays are about 0.5-2.5 Å, and depends on the metallic target material. The most commonly used metal is copper, which can emit strong X-rays with a wavelength of 1.54 Å. A crystalline solid can be considered as a series of planes with an equal inter-planar distance d , as shown in Figure 3-8. Diffraction occurs when the X-ray beam (with a wavelength of λ) strikes the surface of a crystal. As the X-ray beam line (Y, Z) hits the

surface of the crystal at an angle θ , some of the beam is diffracted away at the same angle (Y'), some travels into the crystal and interacts with the second plane (Z'), and the remainder travels deeper into the crystal. This process is repeated at many planes in the solid material. The diffracted X-rays (Y' , Z') travel different path lengths, so that when they meet in the detector (Figure 3-7), there will be constructive and destructive interference. The constructive interference only occurs if the path length difference ($EF+EH$) is equal to an integer number n of X-ray wavelengths; in this case:

$$2d \sin \theta = n\lambda \quad (3-4)$$

The above equation is known as Bragg's law [160, 161]. With semi-crystalline materials, the X-rays will be scattered in certain directions when they hit the lattice planes, and form high intensity diffraction peaks. For amorphous regions, X-rays will be scattered in many directions and develop into a continuum distributed over a wide range of detector positions. Moreover, the internal stress in a crystal and its composition variation can shift diffraction peaks due to changes in inter-planar distances [161]. Therefore, the resulting diffraction patterns can be used to characterise the crystal structure, crystal size, degree of crystallinity, orientation, internal stress and composition.

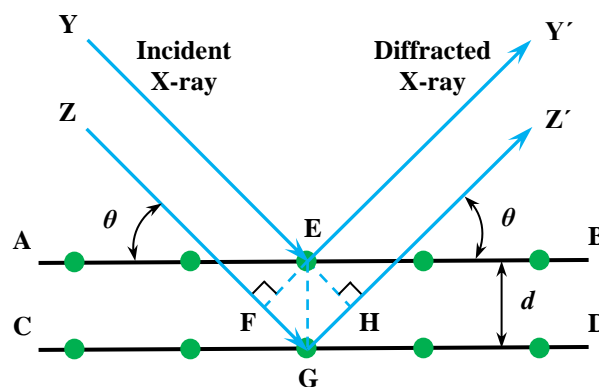


Figure 3-8 Incident X-ray striking a periodic crystalline solid, as represented by a series of planes with an equal inter-planar distance d .

3.2.4.2 Phase identification of nylon 6,6 fibre

Semicrystalline nylon has a spherulitic structure at room temperature, as proposed by Bunn and Garner [143]. Two forms of α and β triclinic crystals are oriented in nylon 6,6, and their dimensions are listed in Table 3-1. The α form of unit cell contains one well-extended chemical repeat unit; while the β form has a two-molecule triclinic cell. Figure 3-9 shows the schematic representation of the triclinic unit cell and the two crystal forms. The main difference between the two crystals is that successive layers within the α -form crystal are displaced in the same direction by a fixed distance; whereas in the β form, adjacent layers are displaced alternately up and down by the same distance. The α -crystals give reflections from $(hk0)$ planes, and the spots from β -crystals have (usually with small proportion) low intensities corresponding to $(00l)$ crystalline planes [162]. In addition to the equilibrium of α and β crystals phases, a pseudo-hexagonal γ phase was also observed by Brill [163], which occurs at elevated temperature. As a nylon 6,6 sample is heated, the α and β crystal unit cells gradually merge and transfer into the γ phase, which occurs at the Brill transition temperature. The Brill transition in nylon 6,6 has been intensively investigated in Refs [164-169]. The transformation between the phases may occur upon drawing of nylon, annealing [151], hydration [170], and under mechanical stresses [171]. Therefore, a particular nylon 6,6 XRD pattern may reveal partial levels of the α , β , γ phases, depending on the conformation and packing of the polymer chains during crystallization [172].

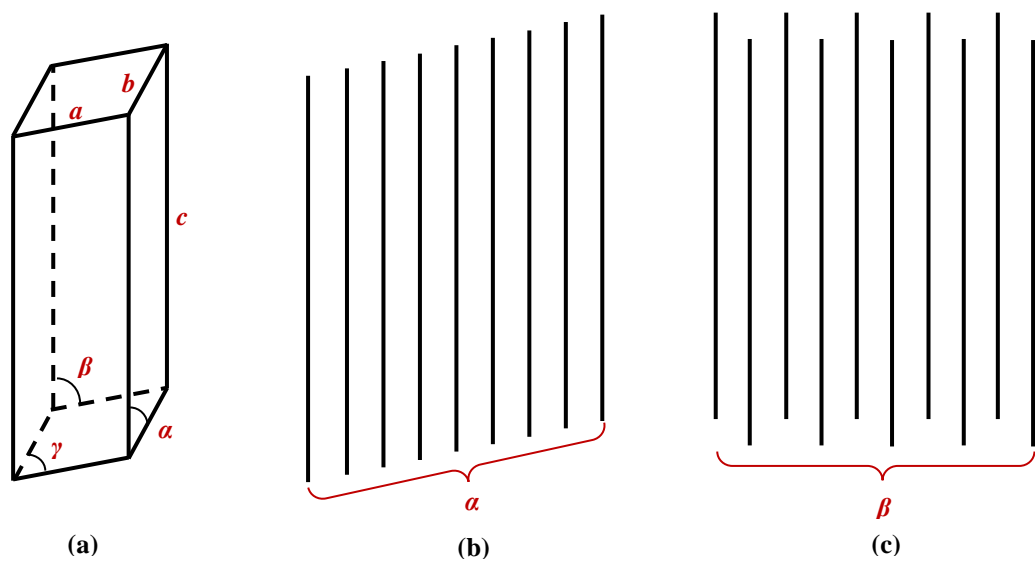


Figure 3-9 Schematic representation of crystal phase structures for: (a) basic triclinic unit cell; (b) α -crystal; (c) β -crystal. Solid lines in (b) and (c) represent sheets of molecules seen from an edgewise view.

Table 3-1 Crystal phase unit cells and dimensions for nylon 6,6 fibre. Note *c* is along the fibre axis. Data from [143].

Phase	Unit cell	<i>a</i> (Å)	<i>b</i> (Å)	<i>c</i> (Å)	<i>α</i> (°)	<i>β</i> (°)	<i>γ</i> (°)
<i>α</i> -crystal	Triclinic	4.9	5.4	17.2	48.5	77	63.5
<i>β</i> -crystal	Triclinic	4.95	5.4	22.4	49	76.5	63.2

3.2.4.3 Crystallinity

A typical semi-crystalline nylon 6,6 material is usually regarded as a two-phase structural model, which consists of crystalline regions embedded in an amorphous matrix [173, 174]. The molecules within the crystalline regions are arranged periodically in three-dimensional space which can produce constructive interference from X-ray diffraction according to the Bragg's law [160, 161]; thus a sharp peak would occur. The amorphous regions however, are isotropic with no periodicity, and this generates a broad amorphous halo in the pattern. Therefore, the XRD scan of semi-crystalline nylon consists of a broad amorphous halo, superimposed with sharp peaks from the crystalline regions [172]. Diffraction patterns can be fitted to the sum of a base line and a number of bell-shaped curves. The general profile fitting formula follows [175, 176]:

$$I = B + \sum_{i=1}^n f_i(2\theta) \quad (3-5)$$

where, *I* is the intensity; *θ* is the diffraction angle; *B* is the background function which can be linear [175] or polynomial [176]; the *f*(2*θ*) function represents the symmetrical bell-shaped curve, and *n* is the number of bell-shaped curves. For the *f*(2*θ*) function, Gaussian [176, 177], Lorentzian (Cauchy) [178], Logistic [175], and Pearson VII [111, 179, 180] have been commonly used, and can be represented by:

Gaussian $f(2\theta) = I_0 2^{-4z^2}$ (3-6)

Lorentzian (Cauchy) $f(2\theta) = \frac{I_0}{1 + 4z^2}$ (3-7)

Logistic $f(2\theta) = \frac{4I_0(17 - 12\sqrt{2})^z}{[1 + (17 - 12\sqrt{2})^z]^2}$ (3-8)

Pearson VII $f(2\theta) = \frac{I_0}{[1 + 4z^2(2^{1/m} - 1)]^m}$ (3-9)

where, $z = (2\theta - X_0)/FWHM$; I_0 and X_0 represent the intensity and position of the peak centre; $FWHM$ is the full-width at half-maximum; m is the shape factor in the Pearson VII function, and yields the Lorentzian function when $m = 1$.

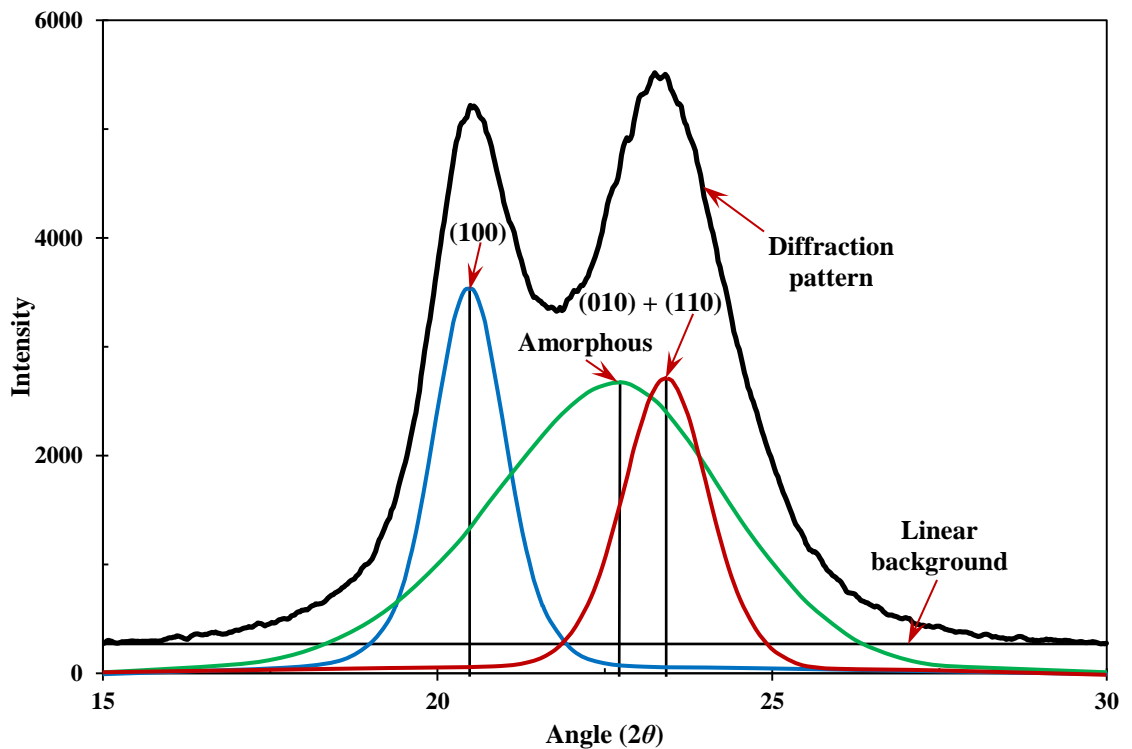


Figure 3-10 Example of profile analysis of an equatorial diffraction pattern from nylon 6,6 fibre used in this work.

The crystal structures of nylon 6,6 have been intensively studied and well understood through WAXD [111, 162, 181-184]. Figure 3-10 shows an example of profile analysis of an equatorial diffraction pattern of semi-crystalline nylon 6,6 fibre used in this research, and there is no detectable proportion of β crystals. As represented in Figure 3-11, for the triclinic Bravais cell structure, three reflexions appear when Bragg planes pass through the axes of nearest neighbour chains [174], and the spacing given from a (100) reflection is 4.39 Å, the (010) reflection corresponds to 3.73 Å, and the (110) reflection gives 3.66 Å [168]. Usually the latter two reflections join together. Therefore, a unique X-ray fingerprint for nylon 6,6 is obtained. The ideal α -crystal has two strong equatorial diffraction peaks: the (100) peak at 2θ value of $\sim 20.3^\circ$, with a distance of ~ 4.4 Å, corresponds to the inter-chain distance within the hydrogen-bonded sheet; the joint (010, 110) peak at 2θ of $\sim 23.3^\circ$, with a distance of ~ 3.7 Å, represents the inter-sheet distance [185, 186]. The normalized area of the crystalline peaks, as shown in Figure 3-10, can be used to obtain an absolute degree of crystallinity of the polymer. A relative measure of crystallinity, in the form of a crystallinity index (CI), is commonly obtained from [146]:

$$CI \% = \frac{A_c \times 100}{A_c + A_a} \quad (3-10)$$

where, A_c is the integrated area underneath the crystalline peaks and A_a is the integrated area of the amorphous halo.

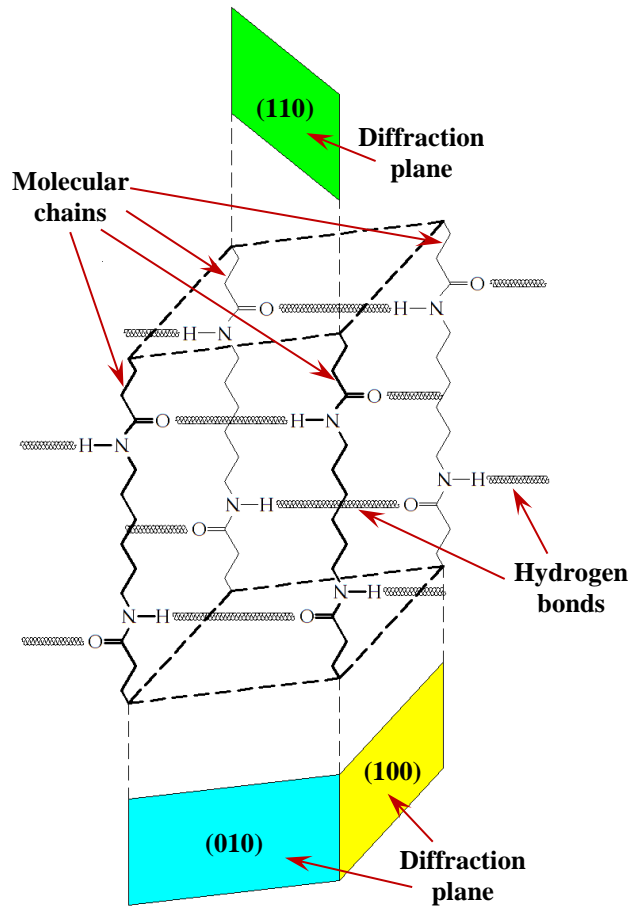


Figure 3-11 Schematic representation of the α -form molecular unit cell structure in nylon 6,6 fibre, showing the associated diffractive crystalline planes.

3.2.4.4 Apparent crystallite size

The width of the crystalline peak is inversely related to the size of the crystals. The crystalline reflections of fibres are broadened additionally by the considerable defects and disorder in the crystal lattice after drawing. Therefore, the ‘apparent crystallite size’ ACS_{hkl} , rather than the actual crystallite size, is yielded from profile analysis of equatorial scans using the Scherrer equation [146, 172]:

$$ACS_{hkl} = \frac{0.9\lambda}{\Delta\theta_{hkl} \cos \theta_{hkl}} \quad (3-11)$$

where, λ is the wavelength of the X-rays, in angstroms; θ_{hkl} is the peak position of the (hkl) crystalline plane, in radians; $\Delta\theta_{hkl}$ is the full-width-half-maximum (*FWHM*) of the (hkl) crystalline peak, in radians.

3.2.4.5 Index of crystalline perfection

Profile analysis of the equatorial pattern can also be used to calculate the index of crystalline perfection (*ICP*), which is based on the shift in crystalline peak position compared to the crystalline features of well-crystallized nylon 6,6 fibre, as first proposed by Bunn and Garner [143]. It is routinely used to monitor small changes in the unit cell volume in chain-axis projection and follows [150]:

$$ICP(\%) = \frac{d_{(100)}/d_{(010,110)} - 1}{0.189} \times 100 \quad (3-12)$$

where, $d_{(100)}$ is the inter-planar spacing of the (100) planes; $d_{(010, 110)}$ is the inter-planar spacing of the (010, 100) planes; 0.189 is the numerator calculated from a well-crystallized nylon 6,6 structure given by Bunn and Garner [143] with $d_{(100)}=4.4 \text{ \AA}$ and $d_{(010, 110)}=3.7 \text{ \AA}$ (Section 3.2.4.3); this being regarded as ‘perfect’.

Since each reflection represents an average lattice spacing, the *ICP* is also a measure of the density of the chains in the equatorial plane [187]. The α phase defined in Section 3.2.4.2 is the major phase in nylon 6,6 material; Haberkorn and Simak [188] refined the α unit cell into α_I and α_{II} phases with slightly varied crystallographic parameters as shown in Table 3-2. The α_I phase is more highly ordered than the α_{II} phase, with densities of 1.213 and 1.173 g/cm³ respectively [169]. The density of completely amorphous nylon 6,6 is 1.069 g/cm³ [189].

Table 3-2 Refined α -crystal phase unit cells and dimensions for nylon 6,6 fibre at room temperature. Note c is along the fibre axis. Data from [188].

Phase	Unit cell	a (Å)	b (Å)	c (Å)	α (°)	β (°)	γ (°)
α_I -crystal	Triclinic	4.97	5.47	17.29	48.35	76.6	62.5
α_{II} -crystal	Triclinic	4.95	5.45	17.12	51.8	79.9	63.3

A key part of this research involved fibre annealing, followed by stretching, to induce viscoelastic creep and recovery. There has been significant research into annealing effects on nylon fibre (Section 3.2.1); however, investigations into microstructural changes from creep after fibre annealing is rare. Therefore, a microstructural study of fibre creep effects is an important requirement. In addition to inter-planar distance, it is reported that the internal stress in a crystal could shift X-ray diffraction peaks [161]. Thus WAXD was utilised in this work to address this issue. The equatorial scans can provide various parameters relating to the crystalline domains.

3.3 MECHANICAL EVALUATION OF COMPOSITES - PRINCIPLES

As stated earlier, the mechanical performance of VPPMCs was mainly evaluated in terms of Charpy impact testing and three-point bending tests. Prestress effects were determined by comparing the test (prestressed) and control (non-prestressed) sample means. Hence, the mechanical improvements from fibre prestressing can be calculated from:

$$\text{Increase (\%)} = \frac{M_T - M_C}{M_C} \times 100 \quad (3-13)$$

where, M_T and M_C represent mechanical properties of test and control sample means, respectively. Below provides the evaluation principles of Charpy impact testing and the three-point bending test.

3.3.1 Charpy impact testing

Charpy impact testing has been used for many years to determine the impact toughness of various materials. Figure 3-12 shows the principle of the Charpy impact test. Sample support consists of two rigidly mounted anvils, with adjustable span. The specimen is placed on the supports along the longitudinal axis with no constraint as shown in Figure 3-12 (b), and the striking face of the sample is parallel to the striking edge of the pendulum hammer. The pendulum is raised to a height h_0 and allowed to fall. As the pendulum swings, the energy absorbed by the specimen reduces the final maximum height of the pendulum to a value of h_i , thus the total absorbed energy, Γ , of the sample from fracture follows [190]:

$$\Gamma = mg(h_0 - h_i) \quad (3-14)$$

where, m is the mass of the pendulum; g is the gravitational acceleration. Furthermore, the Charpy impact strength (kJ/m^2) of a un-notched specimen with width b (mm), and thickness h (mm), can be determined from [191]:

$$\text{Impact strength} = \frac{\Gamma}{h \cdot b} \times 10^3 \quad (3-15)$$

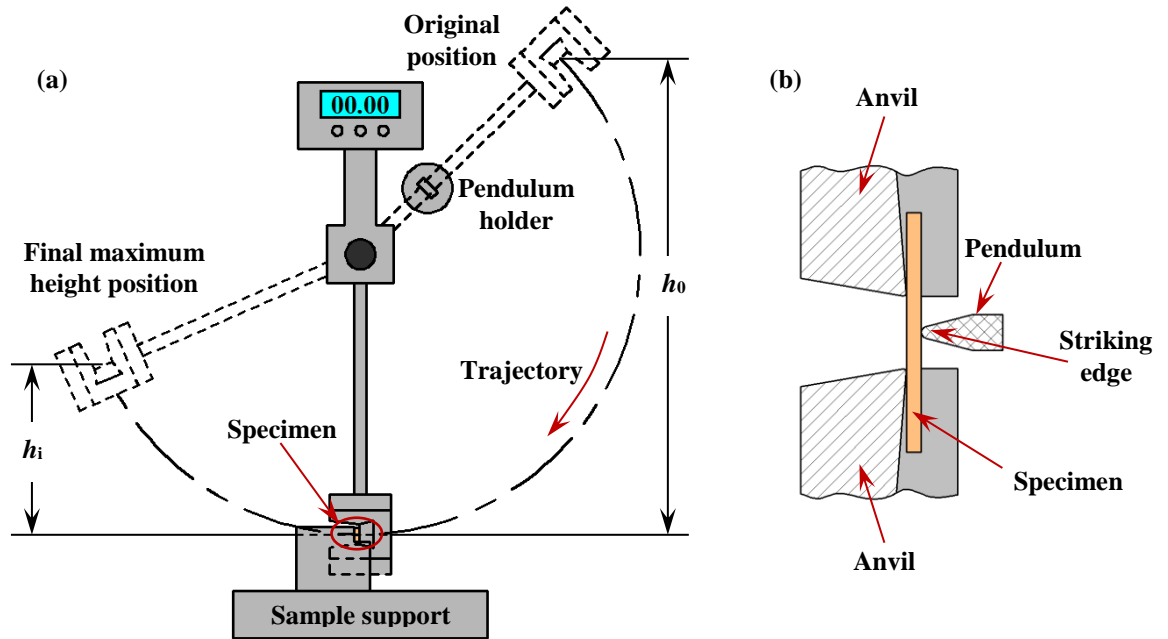


Figure 3-12 Schematic representation of the principle for flatwise Charpy impact testing: (a) basic set-up of an impact tester; (b) sample arrangement during impact test.

3.3.2 Three-point bending test

The three-point bending test is a common material test method to determine the flexural modulus. Rectangular beam specimens without notches are generally used, and Figure 3-13 shows the basic principle. The sample is positioned on two supports with no other constraints, and a freely suspended mass is applied at the centre. By measuring the deflection $\delta(t)$ at the midpoint, the time-dependent flexural modulus can be determined from elementary beam theory [192]:

$$E(t) = \frac{FL^3}{48\delta(t)I} \quad (3-16)$$

where, $E(t)$ is the elastic modulus determined from deflection $\delta(t)$ at the centre of the beam at time t ; F is the applied load; L is the span; I is the second moment of area which is equal to $(bh^3/12)$ for a rectangular sample of width b and thickness h .

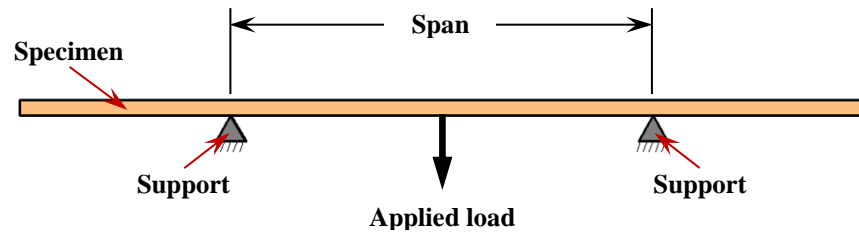


Figure 3-13 Schematic representation of the principle for the three-point bending test.

3.4 FIBRE PROCESSING AND EVALUATION PROCEDURES

3.4.1 Fibre annealing

In accordance with previous nylon fibre-based VPPMC studies [1, 2, 6, 10-12], annealing followed the same procedure to ensure the same heat treatment for future comparison. To facilitate the heat treatment, a (calibrated) Carbolite fan-assisted oven was adopted to provide uniform heat distribution and large capacity. Figure 3-14 shows the equipment and yarn arrangement during annealing. The oven was preheated to 150°C and allowed to stabilise for at least 30 min prior to the annealing process (Section 3.2.1). Designated lengths of continuous fibre samples were cut, placed (unconstrained) in preheated aluminium trays to ensure uniform heat treatment and prevent (unwanted) fibre movement from air flow. Then the trays were placed in the oven for 30 min.



Figure 3-14 Fan-assisted oven used for fibre annealing. Inner view shows the yarns were placed in aluminium trays to ensure uniform heat treatment and prevent movement from air flow.

3.4.2 Creep and recovery

To produce a VPPMC, annealed yarn samples were subjected to stretching to induce viscoelastic creep strain prior to embedding the fibres into a matrix. As illustrated in Figure 3-15, two bespoke rigs were adopted to stretch polymeric yarn. Based on the loads that could be applied, they were designated as the small stretching rig (SSR) and large stretching rig (LSR). Since only a small amount of fibre was needed for the creep tests, the SSR was employed mainly for creep and recovery evaluation. The LSR was designed to provide a factor of ~8 higher load relative to the applied load, through a pulley system. Thus multiple yarns could be stretched to produce prestressed composite samples with higher fibre volume fractions.

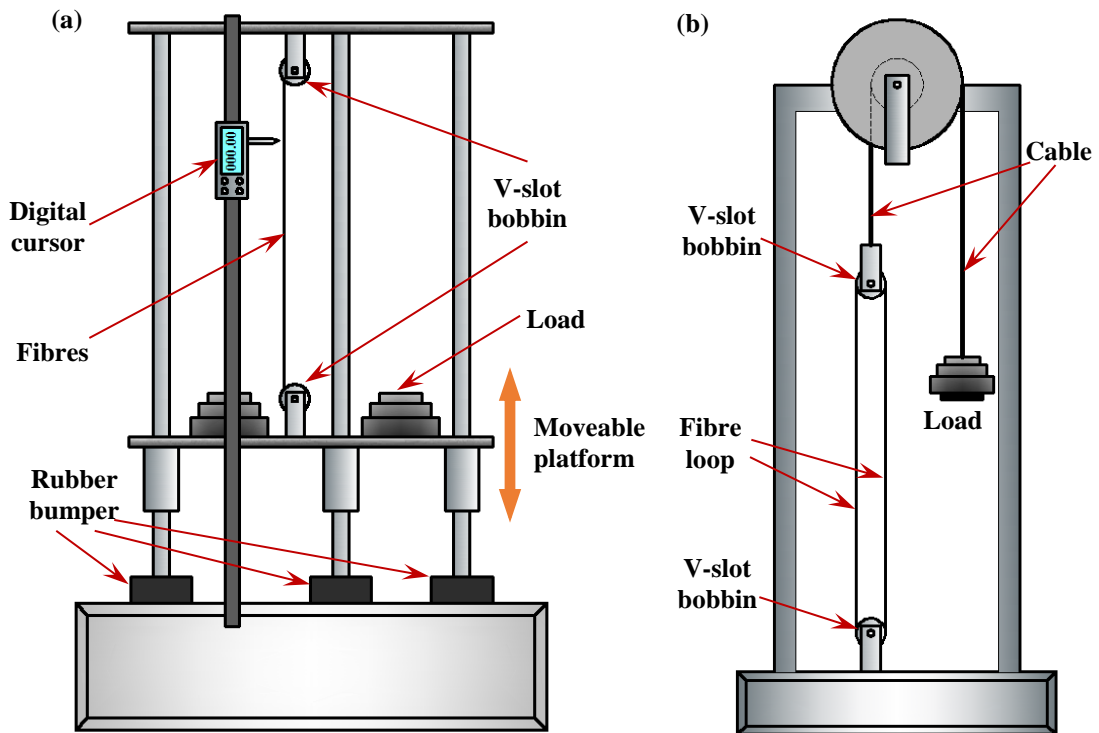


Figure 3-15 Schematic representation of the bespoke stretching rigs (not to scale): (a) small stretching rig, mainly used for creep and recovery strain tests; (b) large stretching rig, used to provide greater amounts of stretched fibre to produce composite samples with higher fibre volume fractions.

Creep and recovery measurement follows previously described procedures [10-12]. Following annealing (Section 3.4.1), at least 0.5 h was allowed to elapse for the yarns to regain equilibrium moisture content before performing the creep tests. A length of ~1300

mm of nylon yarn was cut, folded and attached to the SSR as shown in Figure 3-15 (a). Both ends were clamped to the upper and lower V-slot bobbins separately; the lower bobbin was fixed to a counterbalanced platform on which dead weights could be supported for applying creep stress. Creep tests were carried out by applying a constant load and measuring the distance between two inked marks on the yarn (typically 300-400 mm apart). The tensile load divided by the initial cross sectional area of the yarn was defined as the stress. Following load release, recovery was monitored in-situ. A digital cursor with a precision of ± 0.01 mm was used for all strain measurements and ambient conditions were controlled to be 20.0-21.5°C and 30-40% RH.

3.4.3 Recovery force measurement

The procedures for recovery force measurement followed those previously published [4, 99]. A bespoke force measurement rig (FMR) was used as illustrated in Figure 3-16, and the V-slot bobbins were compatible with the SSR (Figure 3-15 a). A fibre loop was annealed (Section 3.4.1) and then attached to the bobbins. Creep was applied with the SSR following the same procedures in Section 3.4.2. Upon releasing the load, the loop was removed from the SSR and transferred to the FMR, where it was progressively tightened to a fixed strain. Since the fibre loop was in a loose state during the transfer, elastic strain component immediately recovered upon creep load removal, thus the strain locked on the FMR was time-dependent viscoelastic strain. The force was monitored through voltage output from the force sensor located at top of the rig (Figure 3-16). All readings were recorded with ambient conditions of 20.0-21.0°C and 30-40% RH.

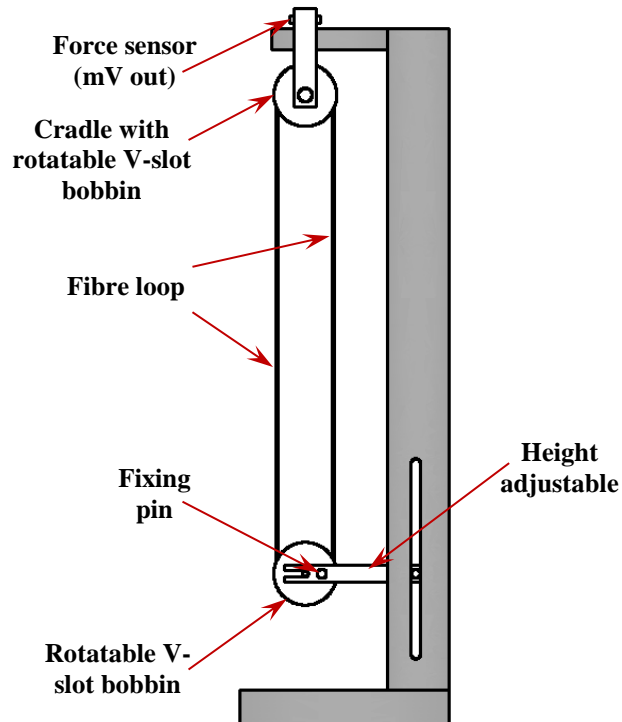


Figure 3-16 Schematic representation of recovery force measurement apparatus. The lower bobbin was height-adjustable, allowing the loose fibre yarn to contract to a fixed strain. The cradle on the top, positioned on the force sensor, enabled the contraction forces generated from yarn recovery to exert compression on the sensor. Redrawn from [99].

3.4.4 Scanning electron microscopy

Scanning electron microscopy (SEM) was employed in this research to examine the fibre topography as reported in Chapters 4 and 5. A Stereoscan 360 was used, supplied by Cambridge Instruments, UK, shown in Figure 3-17. An Edwards S150B sputter coater was adopted for gold coating. To perform SEM analysis, the material sample was mounted on an aluminium stub using a colloidal silver adhesive. The stub was subsequently coated with gold to enhance sample conductivity, which in turn increased the contrast of the topography. The stub was then positioned in the sample chamber, ready for SEM analysis.



Figure 3-17 Equipment used for scanning electron microscopy: (a) SEM operation system; (b) sputter gold coater.

3.4.5 Wide-angle X-ray diffraction

WAXD was carried out to evaluate the microstructural changes of fibres when subjected to tensile creep. An Empyrean X-ray diffractometer from PANalytical UK Ltd. was adopted, using Cu-K α radiation with wavelength $\lambda=1.5406 \text{ \AA}$. Detection was provided by a PIXcel^{1D} detector. Figure 3-18 shows the experimental set-up. Wide-angle equatorial scans were performed at 40 kV and 30 mA for a 2θ range of $15\text{-}30^\circ$, and the scanning rate was $0.04^\circ/\text{s}$. The transmission mode was used with automatic slit settings and the samples could rotate 360° in their own plane. To produce a WAXD specimen, multifilament nylon 6,6 yarns (Section 3.1.1) were cut and folded into 6 parallel yarns, then brushed into a flat ribbon with $\sim 100 \text{ mm}$ in length and $\sim 10 \text{ mm}$ in width. The flat fibre ribbon was mounted on a WAXD sample holder, and yarns were kept as parallel as possible; the insert in Figure 3-18 shows a typical specimen. Any overlap effects were minimised by ensuring the yarns had the same width, i.e. $\sim 10 \text{ mm}$.

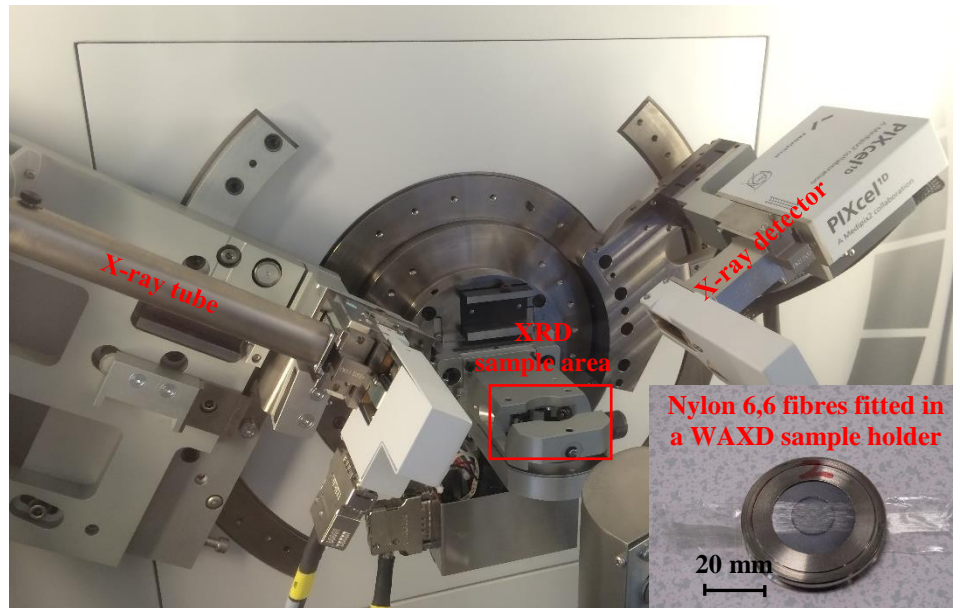


Figure 3-18 Experimental set-up for the X-ray diffraction analysis. Inset shows a typical WAXD sample mounted with nylon 6,6 yarns.

3.5 COMPOSITE PRODUCTION AND EVALUATION PROCEDURES

3.5.1 Composite production

Figure 3-19 shows a flowchart to produce composite samples and variations in composite production involved in each Chapter. The procedures follow the previous studies on VPPMCs [1, 2, 98]. To produce one batch of composite samples, two fibre yarns with similar length were subjected to simultaneous annealing and designated as ‘test’ and ‘control’ separately. The test yarns were subjected to creep loading, following the procedure outlined in Section 3.4.2, whilst the control yarns were kept under the same ambient conditions (20.0-21.5°C and 30-40% RH) close to the test yarns. On releasing the creep load, both yarns were folded, cut and brushed into flat ribbons ~10 mm wide, to ensure an appropriate fibre distribution, ready for moulding. To induce creep stretching, both the SSR and LSR (shown in Figure 3-15) were adopted in Chapter 4. Since larger variations in mechanical properties were detected in samples produced by the SSR (as discussed in Section 4.1.3), the LSR was mainly used to provide fibre creep in Chapters 5, 6 and 7.

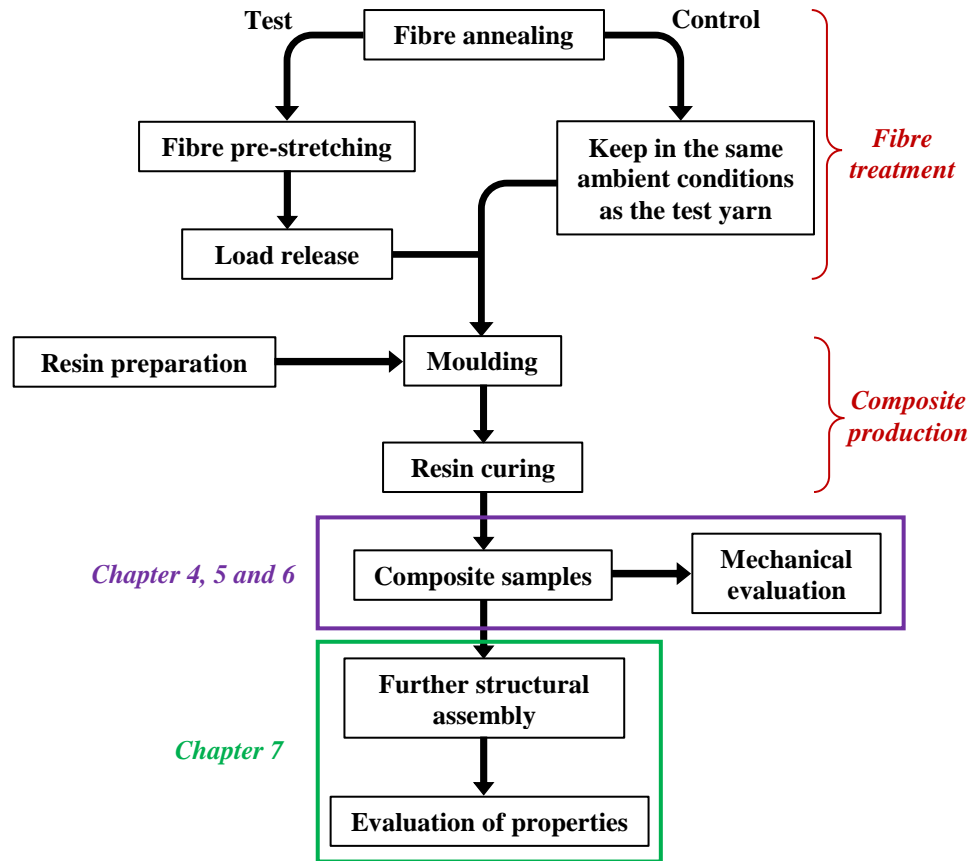


Figure 3-19 Flowchart of the composite sample production and evaluation process.

The composite samples were manufactured by open-casting, in which two identical aluminium open moulds were used, each with a polished channel of 450 mm length, 10 mm width and 3 mm depth, as shown in Figure 3-20. This enabled the test and control counterparts to be moulded simultaneously with the same resin mix, so that no differences between the samples would be expected other than effects from the polymeric fibre creep process. The matrix materials used in this research were polyester based resin systems, with MEKP as the initiator. The resin was pre-prepared prior to creep load removal. Following the preparation of fibre yarns into flat ribbons, the MEKP was added to the resin, then the mixture was stirred slowly and thoroughly for two minutes to keep a minimum bubble content. Though the moulding period was varied slightly between the different resin systems, casting had to be completed before the initial curing stage, i.e. resin gelling (Section 3.1.2). Demoulding took place, 2 to 4 h later, depending on the resin systems used. For Charpy impact tests, each of the two composite strips was cut into five 80 mm lengths to provide a batch of five test and five control samples, the sample dimensions being $80 \times 10 \times 3.2$ mm. All samples were held under a weighted plate for

~24 h to prevent any distortion from residual stresses, and then sealed in polyethylene bags and stored at room temperature ($20 \pm 2^\circ\text{C}$) for future evaluation. The composite samples reported in Chapters 4, 5 and 6 had a fibre volume fraction V_f , of ~2.0%, while other sample dimensions and V_f values were adopted and explained in Chapter 7.

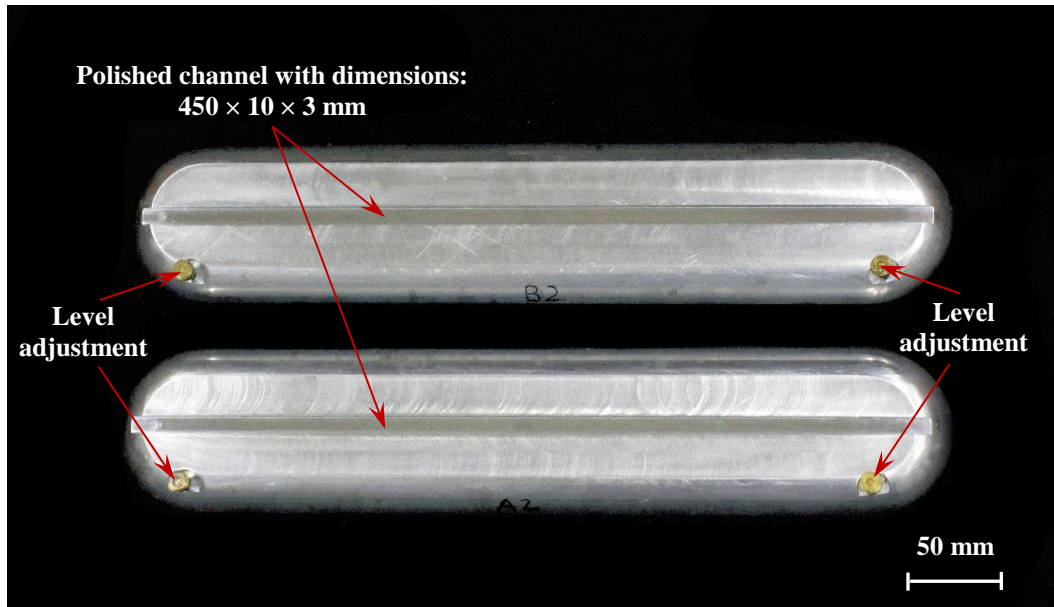


Figure 3-20 Aluminium open moulds used for composite production. Test and control counterparts were moulded simultaneously to ensure no differences between samples other than fibre prestressing.

3.5.2 Charpy impact testing

In this work, low velocity impact tests were adopted to evaluate the properties of VPPMC samples produced with various fibre prestressing conditions. These were performed on a Ceast Resil 25 Charpy machine, using a 7.5 Joule hammer at a velocity of 3.8 m/s. Figure 3-21 shows the facility and experimental set-up. In accordance with earlier Charpy-based studies on low V_f nylon 6,6 fibre composite samples [2, 5, 10-12], a 24 mm span was adopted in this research, and tests were operated in accordance with the BS EN ISO 179 standard [191]. Since open-casting was adopted for composite sample production (Section 3.5), previous research on low V_f open-cast prestressed composite samples showed that the fibres tended to settle towards the bottom of the mould before the matrix had cured [2-5, 7, 8, 10-12]. Therefore, samples were positioned with the fibre-rich side facing away from the pendulum hammer to maximise prestress effects [12],

as shown in Figure 3-21 (b). This set-up also enables comparisons to be made with previous findings.

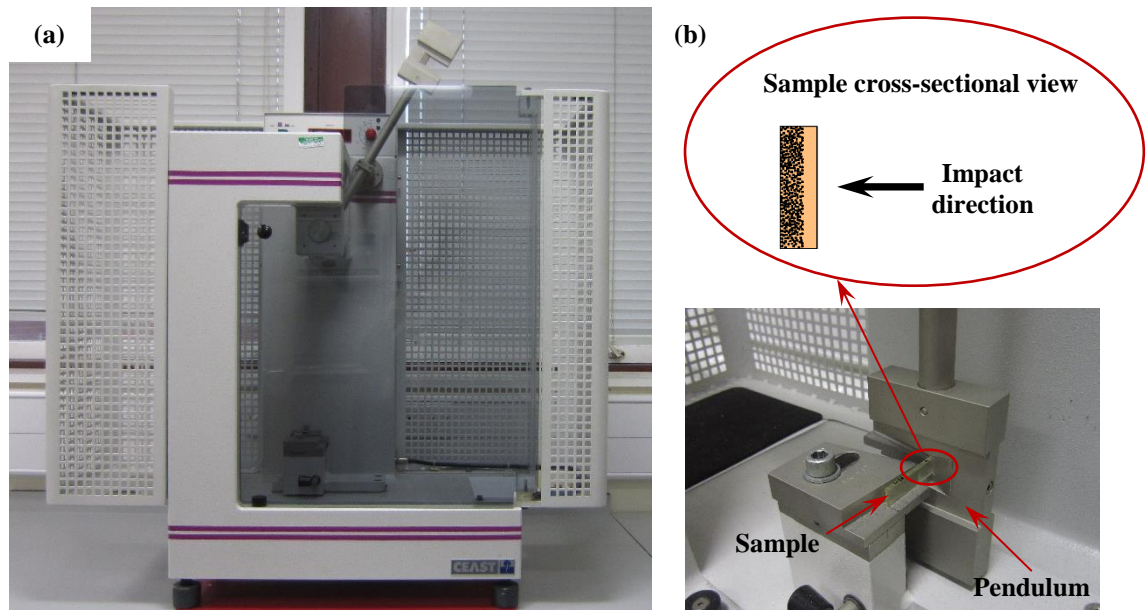


Figure 3-21 Experimental set-up for Charpy impact testing: (a) impact testing rig; (b) sample arrangement with schematic representation of impact direction, i.e. fibre-rich region facing away from the pendulum.

3.5.3 Three-point bending test

Three-point bending tests were carried out in Chapter 7 to determine the modulus of beam structures utilised in the morphing composites. Procedures were similar to those performed with composite samples based on nylon fibre [1] and UHMWPE fibre [4]. Tests were operated in accordance with the ASTM D-790M standard recommendations in terms of span-to-sample thickness ratio, and the freely rotatable central pin. Figure 3-22 shows the experimental set-up. By measuring $\delta(t)$ at $t = 5$ s, the result for $E(t)$ from a rectangular beam with $h \ll L$, is close to the true elastic modulus [1, 4]. A bending test on each sample was performed only once, and a video recording of the deflection in progress was made to improve measurement accuracy. All the deflections were performed at 20-21°C.

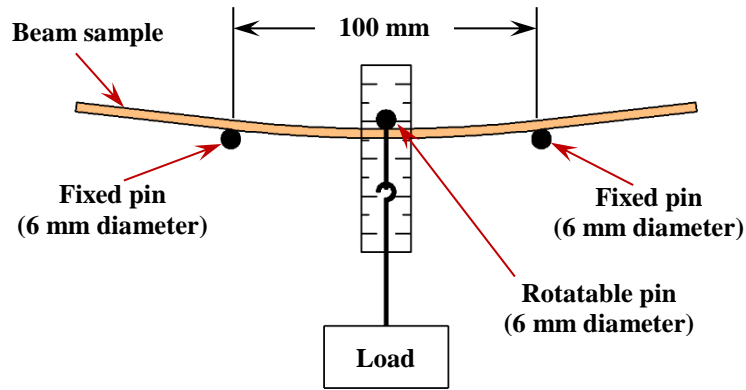


Figure 3-22 Experimental set-up of the three-point bending test to determine the elastic modulus of a beam sample.

3.5.4 Optical microscopy

Optical microscopy was undertaken using a Nikon SMZ-2T stereo optical microscope to evaluate the cross-sectional area of the composite samples, as demonstrated in Chapter 7. The microscope was fitted with a light source, and a Q-imaging MicroPublisher 3.3 RTV digital camera was mounted on the top. To capture a micrograph, a computer with Media Cybernetics Image Pro-Plus software was adopted. Specimen was made by casting the sample into epoxy resin. Following resin curing, the specimen was progressively ground using P240, P1200 and P2500 grit silicon carbide (SiC) abrasive paper. Further polishing of the specimen was carried out with 6 micron grade diamond paste. After cleaning with ethanol, the specimen was dried in a desiccator at room temperature, prior to microscopy work. To enhance the appearance of the fibre-matrix boundary, the specimen could be coated in gold, with an Edwards S150B sputter coater which is shown in Figure 3-17 (b).

Chapter 4

PRELIMINARY WORK AND INVESTIGATIONS

SUMMARY

This chapter focuses on preliminary studies that were required to support the main research project. First, the stretching rigs used to induce viscoelastic creep into the polymeric fibres were re-calibrated to reduce system errors. Second, the newly obtained nylon 6,6 yarn was evaluated and compared to the previously used (old) yarn in several aspects to determine possible structural differences. Finally, a replacement resin for the production of VPPMCs was required and selection was based on measurement of the exothermic curing characteristics and impact energy absorption properties.

From these studies, re-calibration of stretching rigs enabled the same viscoelastic creep strain to be achieved with the same loadings used in previous (published) work, thus allowing direct comparison to be made. Investigation of both the new and old nylon 6,6 fibre suggested slight differences exist at the microstructural level; i.e. higher crystallinity was observed for the old yarn. This difference was considered to result in the relatively lower creep strain and viscoelastic recovery force achieved with the old yarn. In addition, a replacement polyester resin was selected as a suitable matrix material to produce composite samples. It gave comparatively low viscosity, low curing temperature, good transparency after curing, and enabled the viscoelastic prestress effect to be successfully demonstrated.

4.1 STRETCHING RIG CALIBRATION

To ensure minimal system errors, re-calibration of stretching rigs was carried out first. The two bespoke stretching rigs were used in this study for various purposes, i.e. the SSR and LSR (Section 3.4.2). The SSR was mainly used for creep and recovery strain-time studies, while the LSR was primarily used to stretch larger amounts of fibres to produce composite samples. Re-calibration was achieved by attaching a standard digital scale with a precision of ± 0.01 kg on one side of the rig, and applying dead weights at the other side, as shown in Figure 4-1 (a) and (b). To simulate the same stress conditions as the nylon 6,6 fibre creep tests, multiple nylon yarns were used to attach the standard digital scale to measure the output load applied. Thus, for consistency, a typical distance of ~ 350 mm between the top and bottom bobbins of the SSR was used with both the calibration and creep stretching, while a length of ~ 1.5 m was adopted for the LSR. For calibration, ten readings for each load condition were recorded. This was achieved by returning the digital scale to 0.00 kg load, and then reloading. Each reading was taken ~ 5 seconds after the scale was stabilised.

In the simplest case (ignoring friction effects), the stress applied to the fibres can be calculated through the following equation:

$$\sigma = \frac{mg}{A_f} \quad (4-1)$$

where m is the dead weight applied to the fibres; g is the gravitational acceleration; A_f is the cross-sectional area of the yarns prior to stretching.

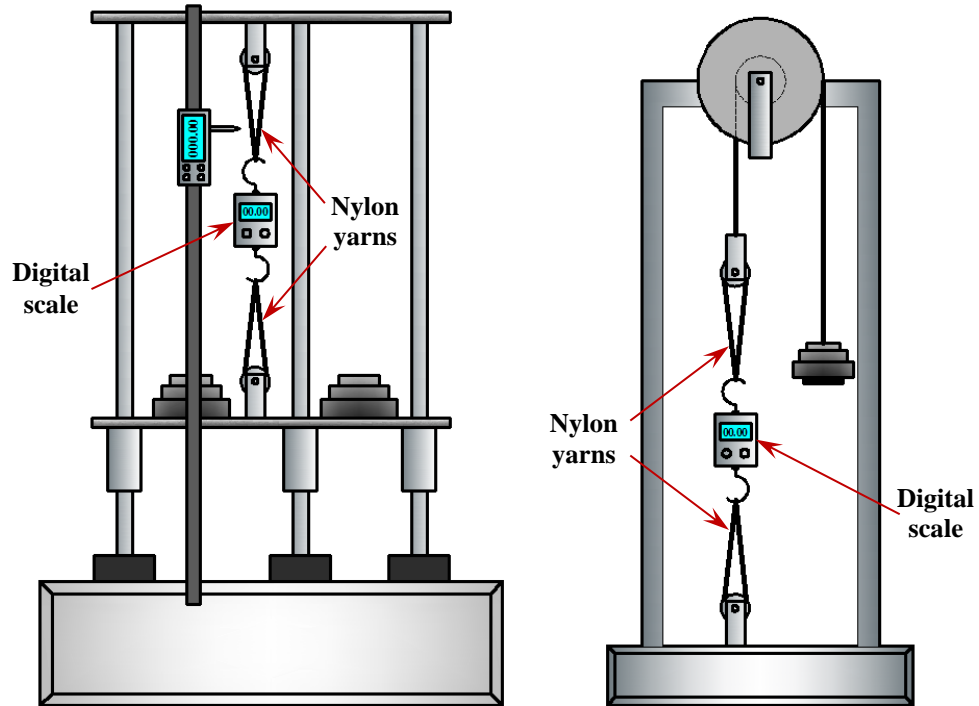


Figure 4-1 Schematic diagram for calibration of the stretching rigs: (a) SSR calibration; (b) LSR calibration.

4.1.1 Small stretching rig calibration

Calibration of the SSR was performed by applying various weights in the range 5 kg to 24 kg, and the resulting mean digital scale readings are presented in Figure 4-2. The corresponding standard errors (Appendix-A, Table A-1) are too small to be shown in Figure 4-2. A linear trend was fitted to the measurement data to give the calibration equation shown in the figure. By combining the calibration equation with Equation 4-1, the stress applied on the fibre with a dead weight m using the SSR can be obtained from:

$$\sigma_{\text{SSR}} = \frac{(1.01 m_{\text{applied}} - 0.07)g}{A_f} \quad (4-2)$$

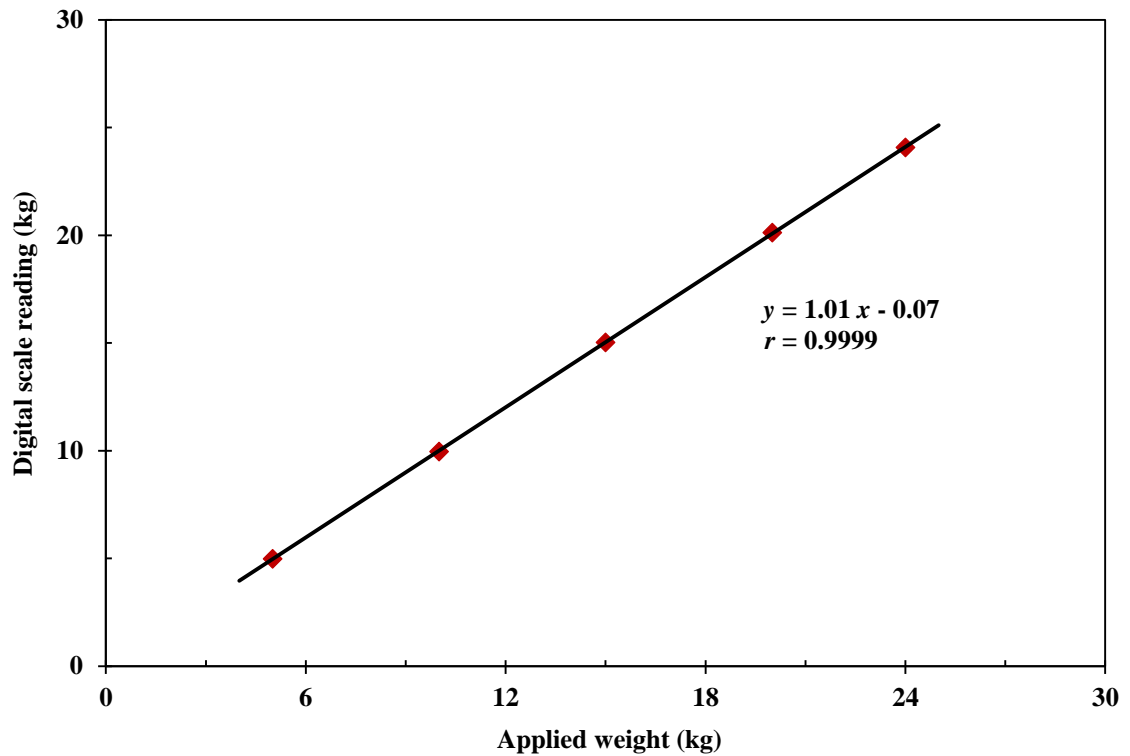


Figure 4-2 Mean calibration results from the small stretching rig. Solid line is from a linear fit, and the corresponding equation is shown. Calibration data are presented in Appendix-A, Table A-1.

4.1.2 Large stretching rig calibration

Calibration of the LSR basically followed the same procedure as the SSR. The LSR was designed to produce a larger loading force from a small applied load through a set of pulleys, the mechanical advantage being around ~8 (Section 3.4.2). Weights up to 6 kg were applied to calibrate the LSR, and Figure 4-3 shows the results. Again, a linear fit gave the calibration equation. Thus, the stress applied to the fibre using the LSR can be determined by the following equation:

$$\sigma_{\text{LSR}} = \frac{(7.41 m_{\text{applied}} + 3.13)g}{A_f} \quad (4-3)$$

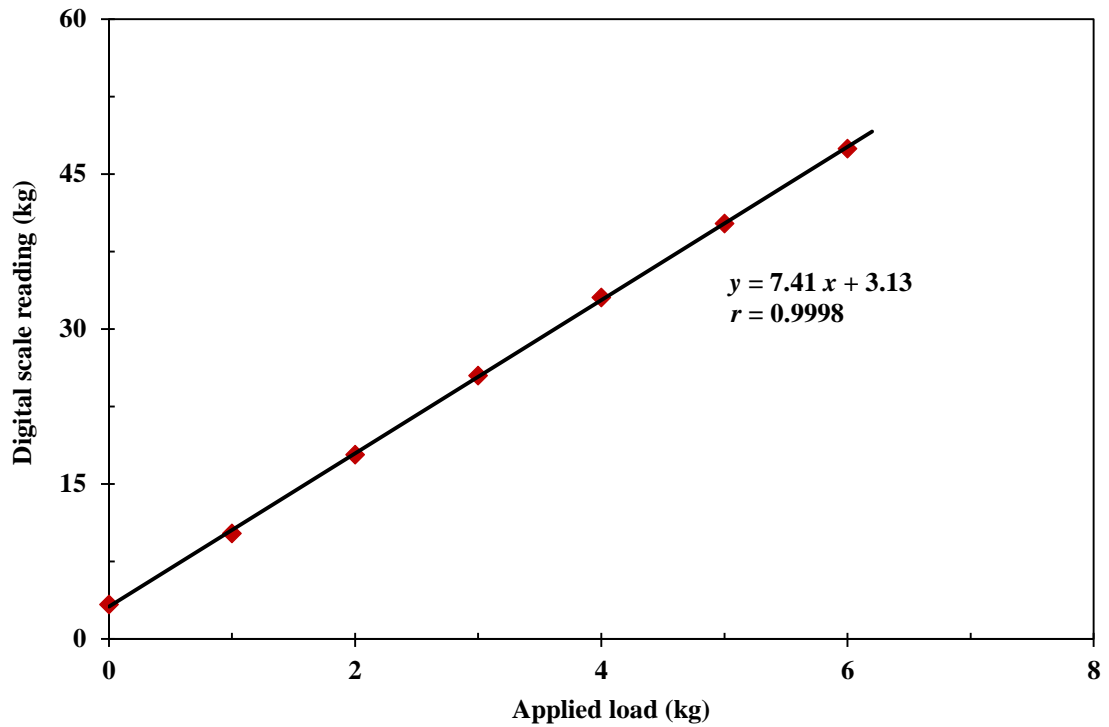


Figure 4-3 Mean calibration data from the large stretching rig. Solid line is from the linear fit, and the corresponding equation is also shown. Calibration data are presented in Appendix-A, Table A-2.

4.1.3 Effectiveness of stress generated from the stretching rigs

Stretching rig calibration makes it possible to apply the same loads to the polymeric fibres using different equipment; i.e. it can be determined from Equations 4-2 and 4-3 that 10.54 kg applied to the SSR is equivalent to a 1.00 kg applied loading using the LSR. Further evaluation, however, had to be considered to verify the effectiveness of the calibrations and explore any other potential system errors from using the two rigs. For example, friction effects could affect the applied stress on the yarn. With the SSR, the effect may vary, depending on position of the counterbalanced platform. Therefore, batches of nylon 6,6 fibre VPPMC samples and their control counterparts with the same creep loading conditions were made using both the SSR and LSR for direct comparison. Since an applied creep stress of ~330 MPa for 24 h and Charpy impact testing have been used for the majority of investigations into the performance of VPPMCs in previous research work [1, 2, 5-7, 10, 98, 99], these procedures were adopted here to evaluate the stretching rig performance.

Table 4-1 Charpy impact test results from VPPMC samples fabricated with different stretching rigs and polyester resins. Tests were performed two weeks after sample moulding; SE is the standard error. Individual sample results are presented in Appendix-A, Tables A-3 and A-4.

Batch	Mean impact energy (kJ m ⁻²)		Increase in energy (%)
	Test ± SE	Control ± SE	
SSR-GPR	39.83 ± 1.72	29.41 ± 3.17	35.45
	43.99 ± 2.15	35.33 ± 3.43	24.51
	49.22 ± 2.53	34.49 ± 0.90	42.72
Mean ± SE	44.35 ± 1.55	33.08 ± 1.62	34.23 ± 5.29
LSR-GPR	42.42 ± 2.10	31.01 ± 1.19	36.77
	45.36 ± 1.80	33.64 ± 1.51	34.81
	42.79 ± 2.00	35.35 ± 1.98	21.06
Mean ± SE	43.52 ± 1.11	33.33 ± 0.98	30.88 ± 4.94
SSR-SLT	38.67 ± 1.03	21.99 ± 0.90	75.89
	36.01 ± 1.94	26.09 ± 0.97	38.01
	39.63 ± 2.54	20.08 ± 0.43	97.32
Mean ± SE	38.10 ± 1.11	22.72 ± 0.80	70.40 ± 17.34
LSR-SLT	37.31 ± 2.67	22.44 ± 0.97	66.22
	35.42 ± 3.41	21.35 ± 0.77	65.9
	35.97 ± 2.06	22.68 ± 0.66	58.63
Mean ± SE	36.23 ± 1.50	22.16 ± 0.46	63.58 ± 2.48

Two polyester resins were used as the matrix material: general purpose resin (GPR), supplied by CFS Fibreglass, UK; DSM Synolite 0382-A-1 resin (SLT), supplied by Polycraft Products, USA. As suggested by the suppliers, 2% of MEKP catalyst was used for both resins. For each resin, three batches of 10 samples (5 prestressed ‘test’ and 5 non-prestressed ‘control’) with 330 MPa for 24 h creep condition were produced using the SSR and LSR separately, with the procedures described in Section 3.5.1. Impact tests were performed two weeks after moulding to enable direct comparison with previous research [7], and Table 4-1 shows the results. For all batches, the prestressed test samples show higher absorbed energy than the control samples. The results indicate that prestressing can enhance the impact performance of the composites, in accordance with the previous findings [2, 5, 7, 11, 12]. For both resin materials, two-sided hypothesis testing has shown no significant difference in the increase in impact energy absorption from VPPMC samples produced with the different rigs at 5% significance level. Therefore, it can be concluded that there is no difference in VPPMC samples (with the same viscoelastic strain level) produced by the SSR or LSR. However, from SE data in Table 4-1, slightly higher fluctuations in the impact results using the SSR are noticed,

which suggests that composites manufactured with the LSR have more consistent mechanical properties. Table 4-1 also shows that both resins demonstrate different Charpy impact test characteristics, the GPR being more brittle: Section 4.3 has further details.

4.2 NYLON FIBRE EVALUATION

From the instigation of VPPMC research following a patent [9], laboratory-grade nylon 6,6 fibre, supplied by Goodfellow Cambridge Ltd., UK, has been the principal reinforcing material used for experimental work. Since a principal aim of this project was to focus on aspects of industrially-based VPPMC production, an alternative supplier of nylon yarn was required, from which larger quantities at a significantly lower cost could be obtained. This was Ogden Fibres Ltd., UK, an industrial textiles supplier. Although both previously used and new fibre materials were continuous untwisted multifilament yarns of ~94 tex, the evaluation of the new and old fibre was necessary to determine potentially structural differences. Hence, direct comparisons with the previous nylon-fibre based research findings [1, 2, 5-7, 10, 98, 99] could be made with the current work.

This evaluation was carried out by considering: (i) fibre topography; (ii) viscoelastic behaviour and (iii) microstructure. For (i), SEM (Section 3.4.4) was adopted to evaluate the sample topography in terms of filament diameter, and the number of filaments per yarn; for (ii), creep and recovery tests were performed to examine the strain-time behaviour, and viscoelastic recovery force was also monitored to determine fibre contraction properties; (iii) was achieved utilising WAXD (Section 3.4.5) to evaluate any differences at a microstructural level.

4.2.1 SEM topography

To produce a VPPMC, annealing is conducted on nylon 6,6 fibre at 150 °C for 0.5 h to remove manufacturing-induced residual stresses [5, 10, 144] (Section 3.2.1). Hence, the topography of the new and old fibre materials was analysed in both as-received (non-

annealed) and annealed form. Here, annealing of the new and old fibres was carried out simultaneously to ensure the same heating treatment. Samples of yarn ~100 mm in length were annealed in the (calibrated) Carbolite fan-assisted oven (Section 3.4.1), and suitable yarn lengths were then cut and mounted onto SEM sample stubs. Similarly, sample stubs of as-received fibre were also prepared. Results are shown in Figure 4-4. Some very minor longitudinal features were observed in the old fibre samples which were considered to be from the original fibre manufacturing process, as reported in Ref [6]. Apart from this, the surfaces of both fibre samples in either as-received or annealed condition, appeared to be clean and smooth. Thus no major differences in fibre topography were found between the new and old yarns.

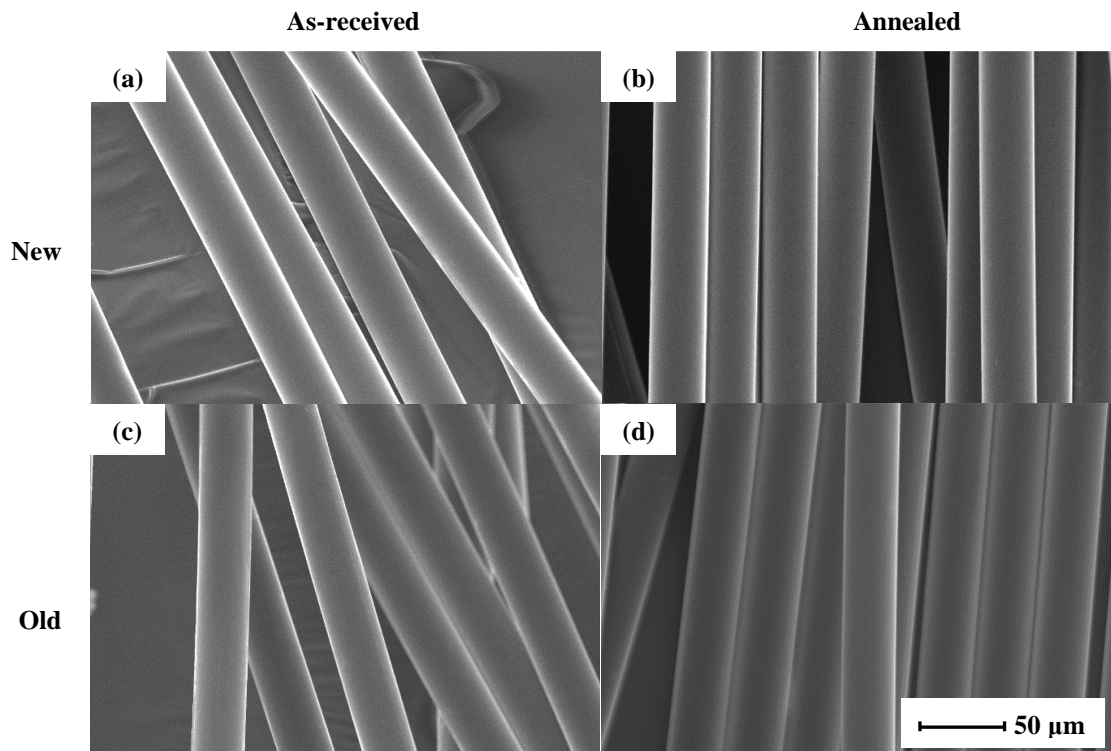


Figure 4-4 SEM micrographs of the nylon 6,6 fibres: (a) as-received new yarn (ARN); (b) annealed new yarn (ANN); (c) as-received old yarn (ARO); (d) annealed old yarn (ANO). Micrographs were taken ~212 h after the annealing.

Both fibre materials were then inspected by SEM in terms of fibre diameters and the number of filaments in one single yarn in both as-received and annealed states. For diameter measurement, five single filaments were chosen randomly, and three readings were taken from three different locations on each filament; thus 45 diameter readings were collected for each sample, and results are shown in Figure 4-5. The diameters of

both new and old fibres before annealing were identical, and gave $26.6 \pm 0.1 \mu\text{m}$. A shrinkage in diameters was found upon annealing for both yarns, i.e. 2.26% for the new yarn, and 0.75% for the old yarn. As discussed in Section 3.2.1, this would suggest that the old yarn had better thermal stability at a microstructural level. Following annealing, there were ~ 140 filaments with diameter of $26.0 \pm 0.1 \mu\text{m}$ in the new fibre material, compared with ~ 135 filaments of $26.4 \pm 0.1 \mu\text{m}$ filament diameter in the old nylon yarn. These small differences resulted in the cross-sectional area of the new yarn being marginally greater ($<1\%$) than the old material, contributing to a slight reduction in applied stress for the laboratory standard creep run.

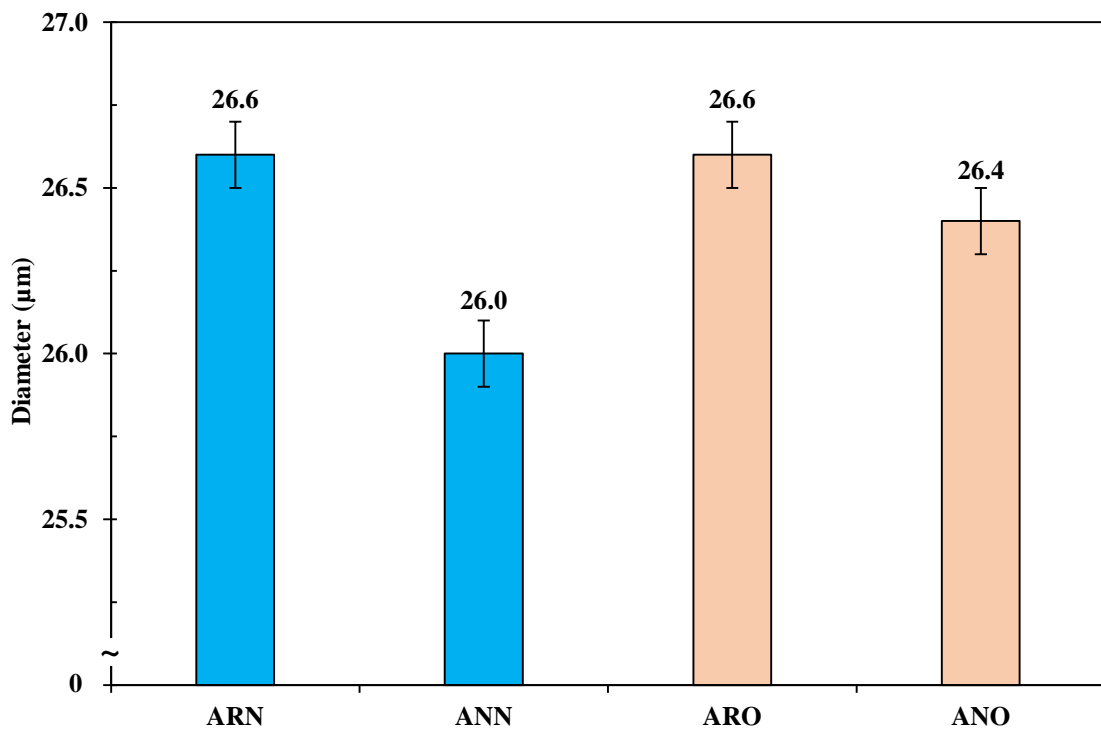


Figure 4-5 Diameters of the nylon 6,6 fibre of both new and old yarn before and after annealing; error bars are standard errors. Measured diameter results are presented in Appendix-A, Table A-5.

4.2.2 X-ray diffraction

Following from Section 4.2.1, the crystalline structure of both yarns was further examined through WAXD analysis in: (i) as-received condition, to determine any initial structural differences; (ii) annealed condition, to evaluate possible micro-structural changes after heating to 150°C for 30 min. All the nylon 6,6 yarn samples were cut at the same time,

to ~1300 mm in length. New and old yarn samples were subjected to simultaneous annealing, while the non-annealed yarns were stored at room temperature (20-22°C) with 30-40% RH. All nylon yarns were then cut, folded into 6 parallel yarns, and brushed into flat ribbons with a length of ~50 mm and ~10 mm in width. WAXD samples were prepared by fitting the flat ribbons into sample holders as described in Section 3.4.5 (Figure 3-18).

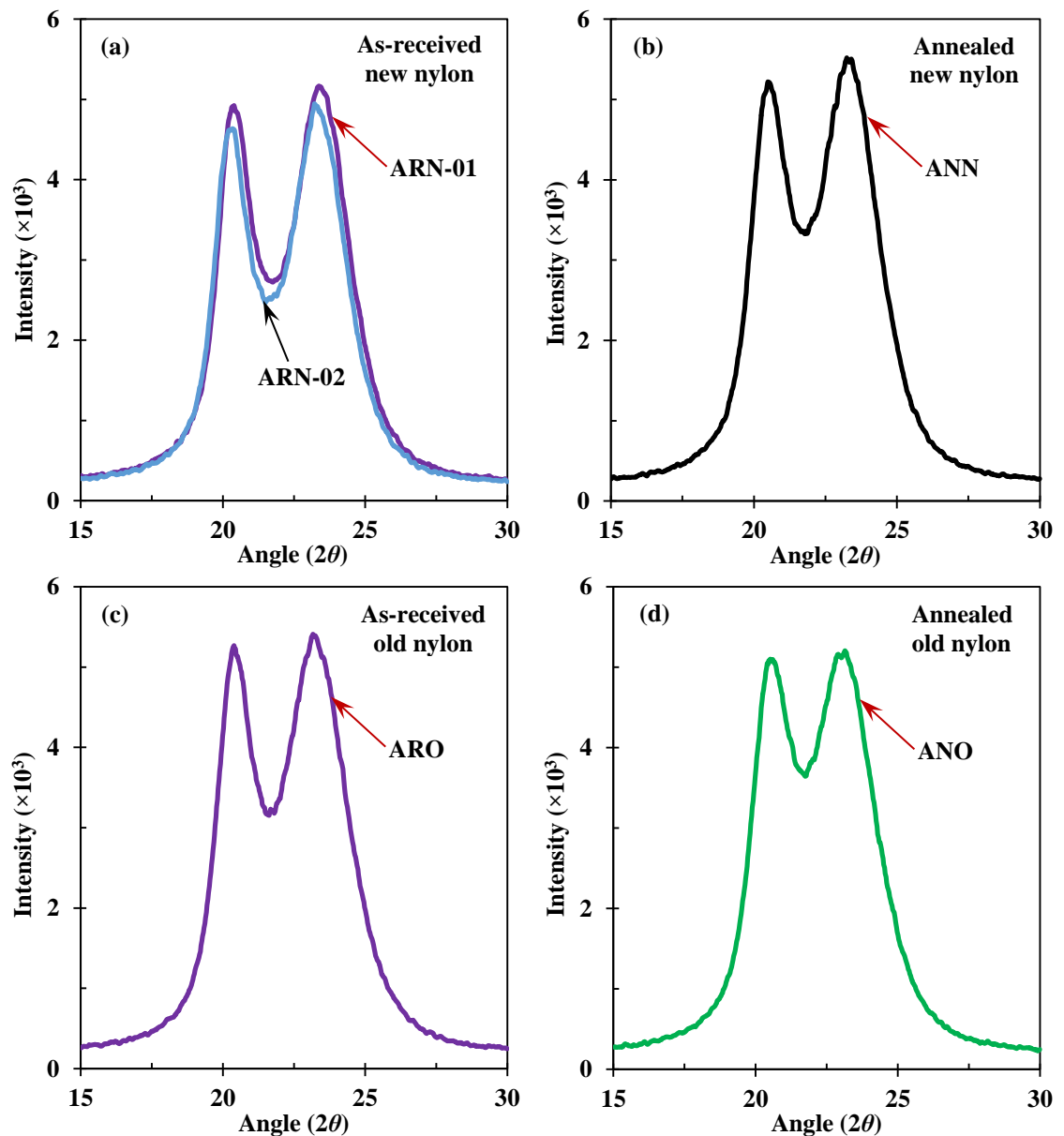


Figure 4-6 X-ray diffraction patterns of both fibre materials before and after annealing. Samples were tested ~45 h after annealing.

WAXD scanning was performed ~45 h after sample preparation. This minimised any availability issues associated with the WAXD equipment, and Figure 4-6 shows the

results. Two peaks were found between 2θ values of 15-30°: (i) the peak at ~20.5° corresponds to the (100) crystal plane, which reveals the inter-chain distance; (ii) the peak at ~23.5° relates to the (010, 110) doublet [185, 186], showing the inter-sheet distance. This is consistent with Section 3.2.4.3. For repeatability, two samples of as-received new yarn were tested under the same scanning conditions. The slight variation in peak position is considered to arise from sample preparation, though the same quantity of yarn had been used for each sample. It was not possible to keep exactly the same fibre surface exposed to the X-rays, and attempts to avoid filaments overlapping would have been unrealistic.

Further profile features could be characterised through profile analysis software (Section 3.2.4.3). Here, the XRD patterns in Figure 4-6 were deconstructed into sharp peaks from crystal planes superimposed on a broad amorphous halo, and results are shown in Table 4-2 in terms of crystal plane position 2θ , spacing d , full-width at half-maximum $FWHM$, and apparent crystal size ACS (Section 3.2.4). The amorphous halo parameters appear to show little or no variation. Despite the slight variations in parameter values from the repeated samples (ARN-01 and ARN-02), the crystalline regions can be characterized through ACS , crystallinity and index of crystalline perfection (ICP) in Table 4-2. For both old and new fibres, the crystallinity has increased slightly after annealing. As discussed in Section 3.2.1, this is caused by the recrystallisation in localized areas when samples are subjected to heating [150, 151, 153]. After recrystallisation, there are narrower distributions of intermolecular bond distances and directions [150], which in turn give the reduction in d of the (100) crystal plane peak. The reduction in ICP values from annealing shows the shift in peak positions (Section 3.2.4.5). It is reported that residual stress within a fibre would shift the peak position [161]. Here, annealing has resulted in molecular relaxation, due to the removal of manufacture-induced residual stresses (Section 3.2.1). Thus the reduction in ICP values is expected to be a result of stress release to give a lower value of enthalpy [154] through annealing. Though the crystal size may be affected by considerable defects and disorder within the crystal structure [172], the ACS of both the (100) and (010, 110) peaks in the new yarn show a decrease after annealing, while the values from the old yarn remain constant. Thus, the old yarn has a more thermally stable microstructure compared with the new yarn. This is supported in Section 4.2.1 that a larger decrease in diameter is found with the new yarn.

Table 4-2 Microstructural parameters of both materials before and after annealing.

	Sample	ARN-01	ARN-02	ANN	ARO	ANO
(100)	2θ ($^{\circ}$)	20.4	20.3	20.5	20.4	20.5
	d (\AA)	4.37	4.39	4.34	4.36	4.34
	$FWHM$	1.29	1.30	1.41	1.40	1.40
	ACS (\AA)	63	62	57	58	58
(010, 110)	2θ ($^{\circ}$)	23.7	23.5	23.6	23.4	23.2
	d (\AA)	3.81	3.82	3.82	3.83	3.85
	$FWHM$	2.05	1.82	2.10	2.19	2.19
	ACS (\AA)	40	45	39	37	37
Amorphous	2θ ($^{\circ}$)	22.8	22.8	22.8	22.8	22.8
	$FWHM$	3.65	3.81	3.52	3.75	3.75
Crystallinity (%)		51.71	50.51	52.97	55.81	58.10
ICP (%)		77	79	73	73	66

Marcellan [111] has demonstrated the applicability of the three-phase ‘Swiss-cheese’ model (Section 2.7.2) on high performance nylon 6,6 fibre. Thus, the same microstructural model can be adopted in this section to provide support to above findings at a molecular level. As proposed by Prevorsek [104, 107], the crystalline microfibrils are surrounded by amorphous domains, the TTMs within the oriented amorphous domains control the mechanical performance of the fibre. Based on findings of the annealing effects on nylon 6,6 fibres, i.e. increased molecular folding [150, 151] in oriented amorphous regions and relaxation of molecules in noncrystalline regions [105], the increase in tensile modulus with annealing time observed by Babatope and Isaac [144] may be caused by either (i) the compensation of TTMs from isotropic amorphous regions near the oriented amorphous domains or (ii) partial loads carried by crystals upon loading. This is further investigated in Chapter 5 through the application of various creep stress levels on nylon 6,6 fibre.

4.2.3 Creep and recovery

As discussed in Sections 4.2.1 and 4.2.2, the new yarn showed slightly lower crystallinity, and more thermally sensitive behaviour. The potential viscoelastic behaviour changes caused by these differences were investigated through creep and recovery tests. Following the fibre annealing (150°C for 30 min), both new and old nylon 6,6 yarn samples were subjected to the lab standard creep condition, 330 MPa for 24 h, and Figure

4-7 shows the strain-time data, associated with the curve-fits using the Weibull based distribution model [96] (Section 3.2.2, Equations 3-1 and 3-2). Four parameters were obtained using commercially available software *CurveExpert 1.4* and are shown in the figure. Each set had three separate yarns for assessing experimental repeatability, and all the readings were taken under ambient conditions of around 20.0-21.5°C and 30-40% RH. Despite the data variations, the creep and recovery behaviour of both yarns can be seen to follow the same trend. Since the same loading condition was applied, the slightly lower creep strain in the old yarn samples might be attributed to their greater crystallinity. Otherwise, the resulting parameters show comparable values from both yarns.

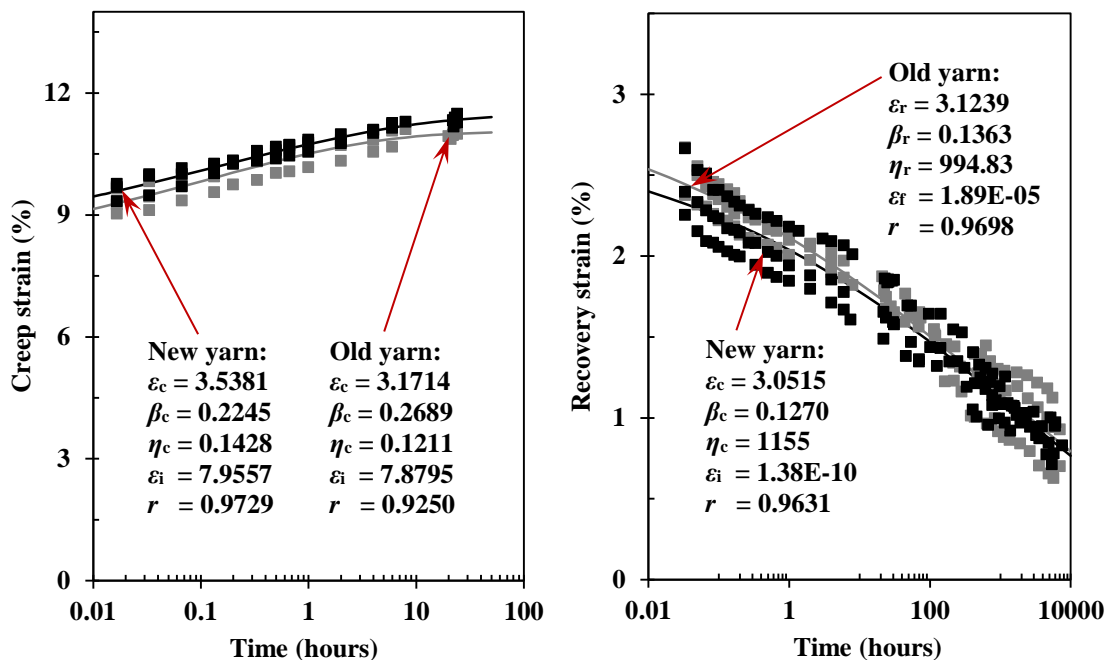


Figure 4-7 Creep and recovery strain-time data for the annealed new and old yarns. Line-fits and parameters were obtained from the Weibull based model [96] using *CurveExpert 1.4*; r is the corresponding correlation coefficient.

4.2.4 Recovery force

The effect of differences in crystallinity on viscoelastic behaviour is further evaluated in terms of viscoelastic recovery force. When a polymeric fibre is subjected to a creep stress, followed creep load removal, the elastic strain recovers instantaneously; the remaining recovery strain, which is viscoelastic (i.e. time-dependent), starts to decrease with time. Thus, if a polymeric material has been fixed at a constant strain when it undergoes

viscoelastic recovery, the contraction of fibre will produce a force [99]. Measurement of the recovery force follows the same procedures described in Section 3.4.3. Briefly, following annealing, two nylon 6,6 yarns were glued together at their ends, and attached to the bobbins which were compatible with both the SSR (Figure 3-15 a) and FMR (Figure 3-16), to form a fibre loop of ~350 mm in length. The loop was then subjected to the 330 MPa, 24 h creep condition using the SSR. On releasing the creep load, the loop was in a loose state, after being allowed to fully recover its elastic strain. The bobbins, with the attached fibre loop, were transferred to the FMR, and the loop was gradually tightened to a fixed strain. Contraction of the fibre loop was detected through a force sensor fitted at the top of the FMR. Since recovery force data from the old yarn has been published in Ref [99], only the new nylon 6,6 fibre was tested and compared to the force output data with the old yarn. For repeatability, two batches of fibre samples were evaluated.

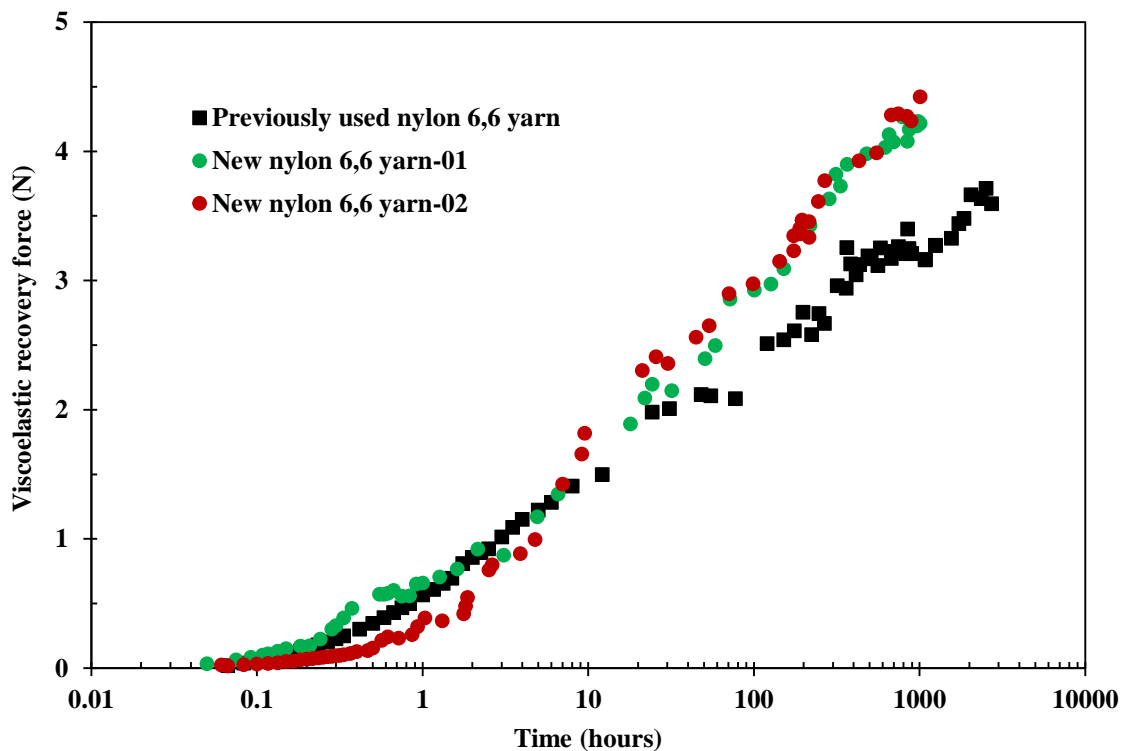


Figure 4-8 Viscoelastic recovery force from both new and old nylon 6,6 yarns. The force output data of the old yarn is from [99].

Figure 4-8 shows recovery force measurement up to 1000 h from new nylon 6,6 fibres, with results from the old yarn [99] for comparison. Though the humidity in the laboratory was controlled to be 30-40% (since nylon fibre is sensitive to humidity), the spread in data below 3 h can be attributed to humidity variations, caused by limitations in the

humidity control method. Beyond 3 h however, there is good repeatability within the new fibre samples (since there were more flexibility in controlling the humidity). Nevertheless, after ~12 h into recovery, Figure 4-8 shows that the new yarn produced a greater recovery force (> 20%) over the same time period. The slightly larger fibre cross-sectional area (<1%) reported in Section 4.2.1 would be expected to have a minimal effect (at the same applied creep load) on force output; clearly, if there was an effect, it would have reduced the recovery force of the new yarn. The lower value of crystallinity, as discussed in Section 4.2.2 however, may be the main factor influencing the force output characteristics of the fibres.

4.3 RESIN SELECTION FOR VPPMC PRODUCTION

The production of viscoelastically prestressed composite samples followed the previously adopted procedure as described in Section 3.2.3. The benefits in mechanical properties from viscoelastically generated prestress have been demonstrated with composites based on polyester resin [1, 5, 10] and epoxy resin [6]. A comparable resin was needed for this research. As polyester resin was the most studied resin, potential resins for evaluation fell into this category. Successful resin candidates would require at least: (i) low viscosity prior to curing; (ii) high transparency; (iii) low curing temperature; (iv) demonstrate the benefits from prestress in terms of impact energy absorption.

4.3.1 Resin curing characteristics

It is known that gel time and curing temperature are important factors that can influence composite material properties. These can differ considerably from resin to resin. To produce a VPPMC, the selected resin should have a suitable curing time; i.e. neither too long (may be detrimental to fibre viscoelastic recovery effect) nor too short (lack of time for preparation). A low curing temperature is also preferred to prevent potential structural changes to the polymeric fibre. Therefore, it is essential that the basic resin properties are known and understood before usage. The curing process of the resins to be evaluated was monitored through exothermic testing, and Figure 4-9 shows the experimental set-up.

To solidify a resin, MEKP catalyst was added to a concentration of 2 wt%, as suggested in the supplier data sheets. The mixed resin was quickly cast into a HDPE mould with 50 mm inner diameter, and 10 mm depth. The resin curing temperature was measured through a TES-303 digital thermometer, with its thermocouple wire inserted inside the HDPE mould, and the tip was located at mid-height in the resin. Ambient temperature and humidity were monitored by a digital thermohygrometer with its sensor positioned close to the mould. The humidity was maintained between 30% -40%.

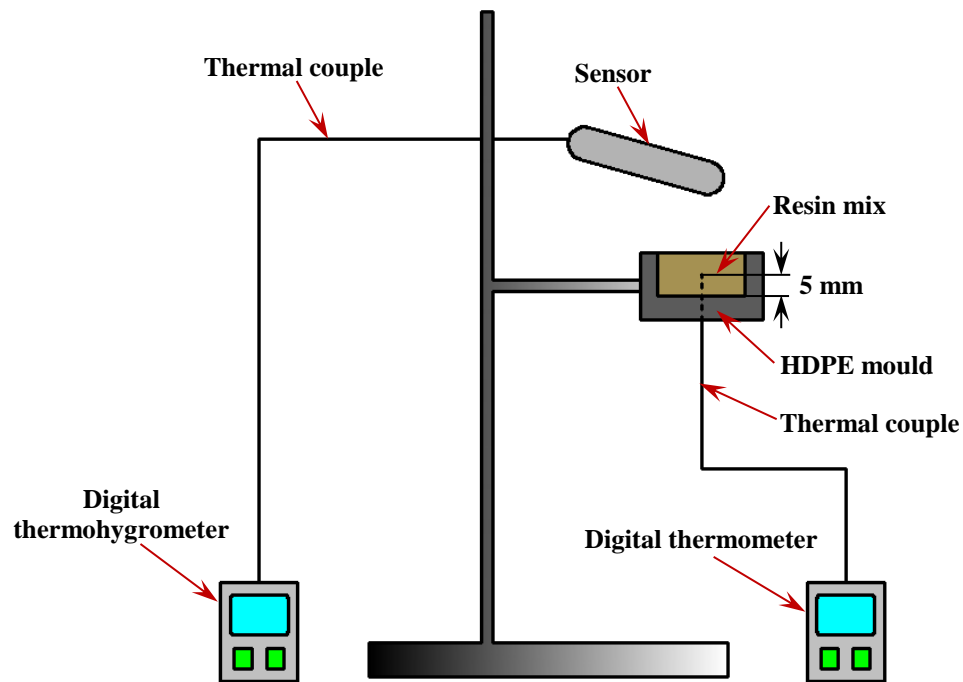


Figure 4-9 Schematic illustration of experimental set-up for resin exothermic tests.

Five different polyester resins were evaluated. These were: GPR and SLT, as described in Section 4.1.3; CFS casting resin (CFS), from CFS Fibreglass, UK; polylite 32032-00 resin (PLT), MB Fibreglass, UK; DSM synolite 0382-A-1 resin (SLT) and S-70361TA-isophthalic polyester laminating resin (STA), both were from Polycraft Products, USA. The exothermic temperature-time test results are shown in Figures 4-10 to 4-14. The curing process of each polyester resin follows similar characteristics: when the resin starts to gel, heat is released, and temperature within the resin increases quickly. At the peak temperature, most of the chemical crosslinking reactions are completed, thus the temperature starts to decrease towards room temperature.

Table 4-3 Summary of the resin exothermic tests, data are from Figures 4-10 to 4-14.

Resin	Peak Tem (°C)	Gel point (min)	Viscous-rubbery (min)	Hard-rubbery (min)
GPR	62.9	18.5	20.0	34.5
PLT	27.9	21.0	25.0	65.0
SLT	33.2	13.0	15.0	27.0
STA	47.4	20.0	24.0	38.0
CFS	35.6	14.5	19.0	31.0

Table 4-3 summarises the peak temperatures, the gel time (A), time to become viscous-rubbery (B), and a hard-rubbery (C) state during the resin curing process. Here, ‘viscous-rubbery’ was a state close to jelly, which had mechanical properties comparable to cold, cooked pasta, and was able to flow very slowly; ‘hard-rubbery’ was more comparable to that of a hard pencil eraser with no flow capability. The graphs and table show that the GPR and STA resins have the highest curing temperatures, which may induce greater thermal residual stresses within the sample and could be detrimental to the prestress effect. The gel time of the SLT and CFS resins are short, which may lead to insufficient time for composite sample preparation. Therefore, the PLT resin is considered to be the most appropriate choice.

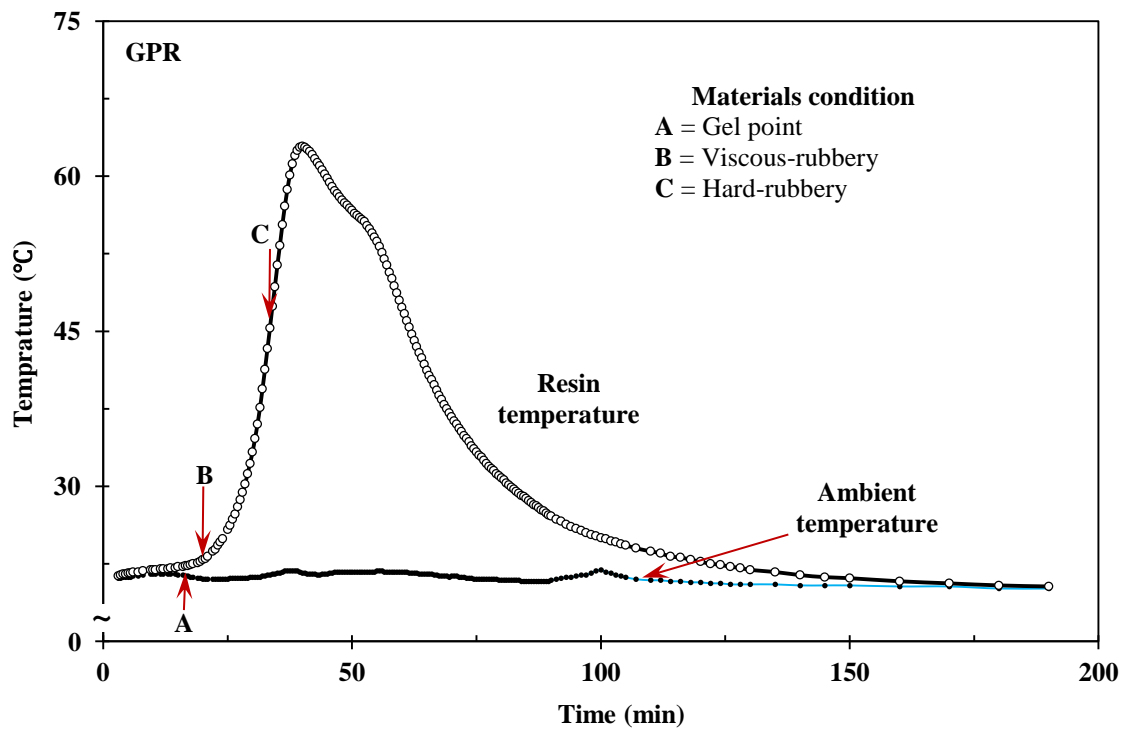


Figure 4-10 Curing process for the general purpose resin, mixed with 2% catalyst. Ambient temperature range was 20.1° to 21.9°C.

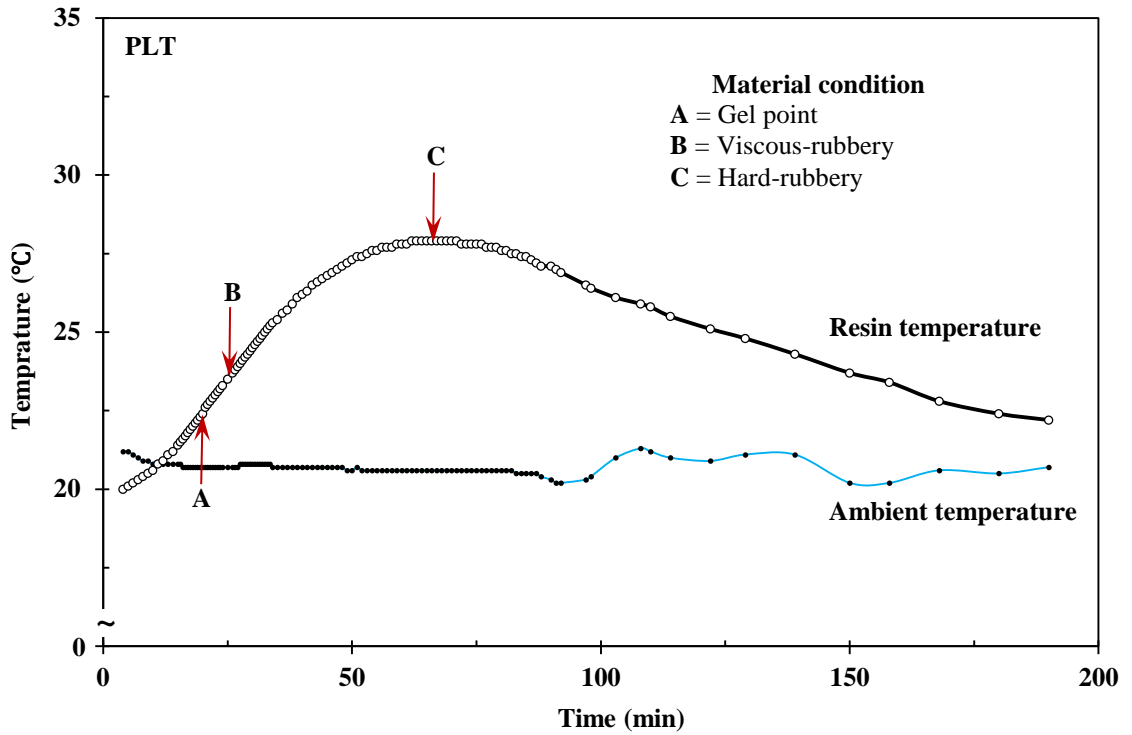


Figure 4-11 Curing process for the polylite 32032-00 resin, mixed with 2% catalyst. Ambient temperature range was 20.2° to 21.3° C.

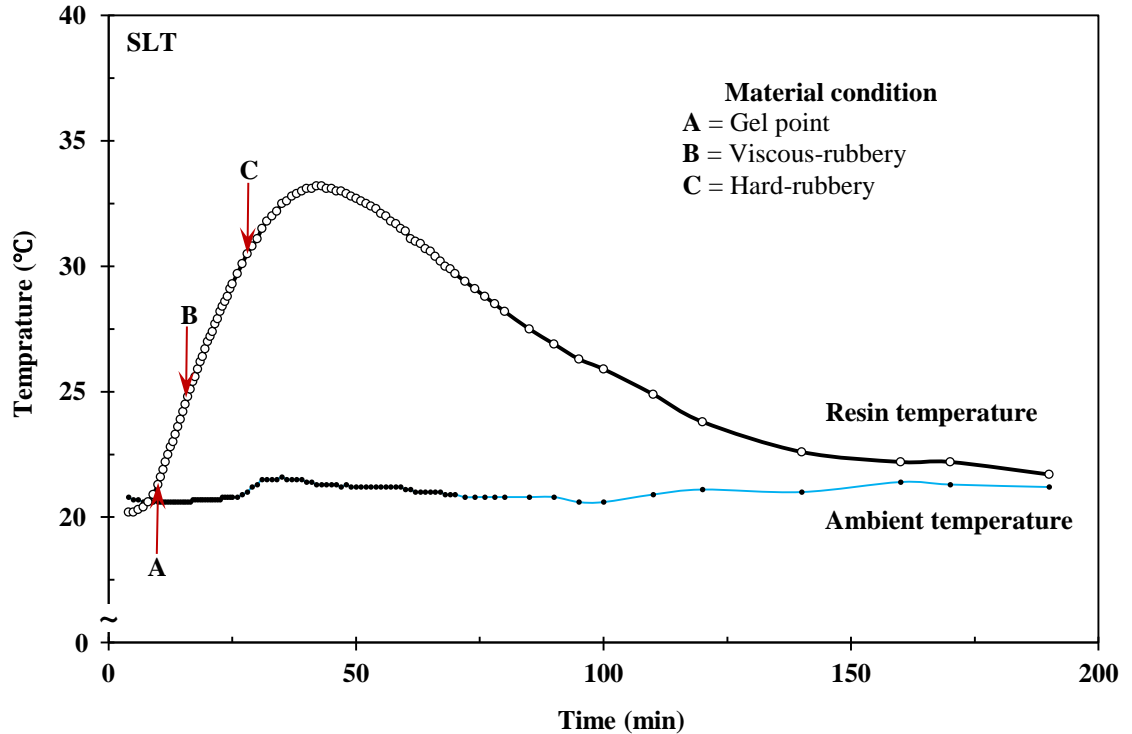


Figure 4-12 Curing process for the DSM synolite 0382-A-1 resin, mixed with 2% catalyst. Ambient temperature range was 20.2° to 21.6° C.

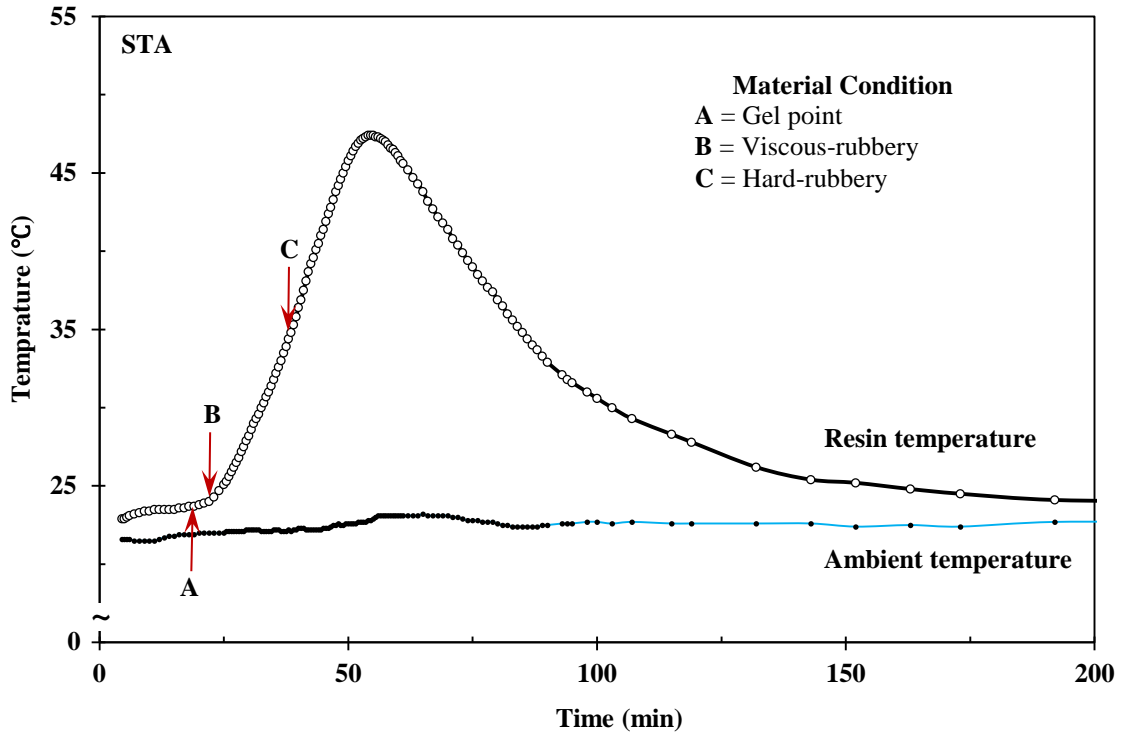


Figure 4-13 Curing process for the S-70361TA-isophthalic polyester laminating resin, mixed with 2% catalyst. Ambient temperature range was 20.6° to 21.6°C.

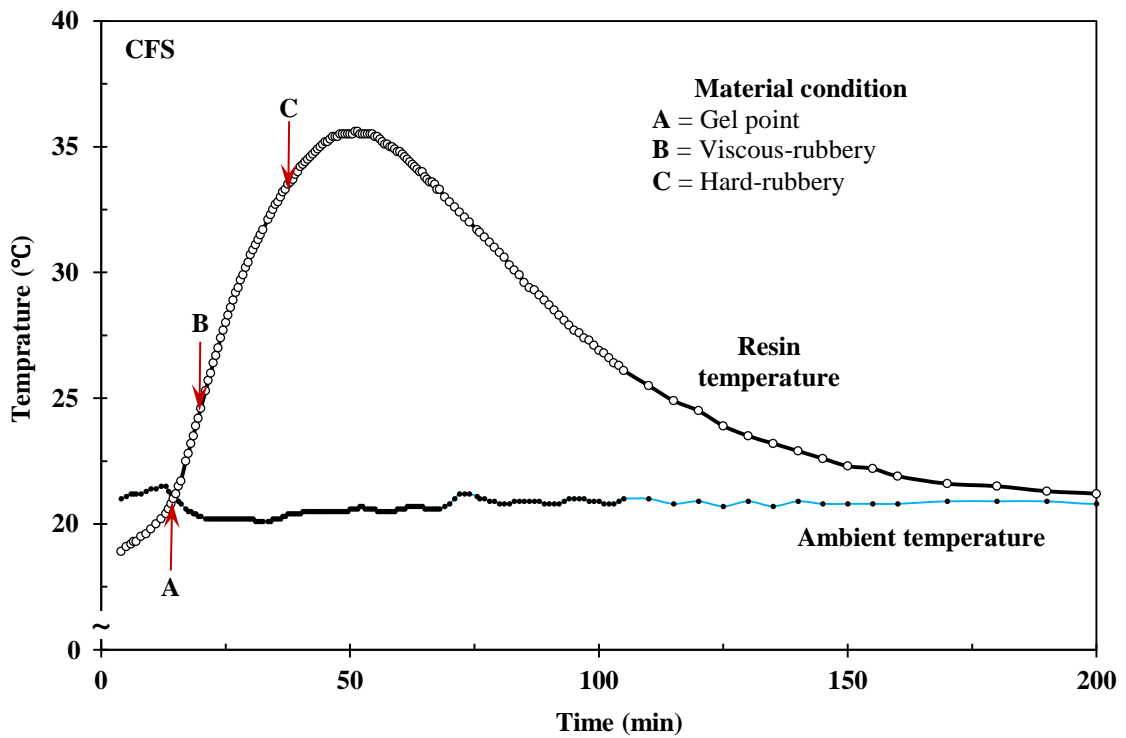


Figure 4-14 Curing process for the CFS casting resin, mixed with 2% catalyst. Ambient temperature range was 20.1° to 21.5°C.

4.3.2 Charpy impact testing

Following from Section 4.3.1, the potential resin candidates were further evaluated through impact testing to assess the potential benefits from prestress effects. Both resin only samples and unidirectional fibre VPPMC samples were produced following the procedures described in Section 3.5.1. A creep condition of 330 MPa for 24 h was adopted for composite production. Two identical aluminium moulds were used for sample fabrication, each could produce five $80 \times 10 \times 3$ mm strip samples. Hence, each resin only batch had 10 individual samples, and each composite batch consisted of 5 prestressed ‘test’ and 5 non-prestressed ‘control’ samples. Three batches of samples were produced for each condition to evaluate repeatability. Impact tests were performed two weeks after sample manufacture, and results are shown in Table 4-4.

Table 4-4 Charpy impact test results for resin only and composite samples produced with various resins. Individual test data are presented in Appendix-A, Tables A-6 and A-7.

Batch	Mean impact energy (kJ m ⁻²)			Increase in energy (%)
	Resin only \pm SE	Test \pm SE	Control \pm SE	
GPR	3.71 \pm 0.30	42.42 \pm 2.10	31.01 \pm 1.19	36.77
	3.56 \pm 0.23	45.36 \pm 1.80	33.64 \pm 1.51	34.81
	3.51 \pm 0.14	42.79 \pm 2.00	35.35 \pm 1.98	21.06
Mean \pm SE	3.59 \pm 0.13	43.52 \pm 1.11	33.33 \pm 0.98	30.88 \pm 4.94
PLT	1.20 \pm 0.10	37.02 \pm 1.78	20.71 \pm 0.63	78.76
	2.62 \pm 0.24	35.36 \pm 1.71	25.03 \pm 0.96	41.26
	1.82 \pm 0.08	35.58 \pm 1.96	21.61 \pm 1.13	64.69
Mean \pm SE	1.88 \pm 0.14	35.99 \pm 0.99	22.45 \pm 0.70	61.57 \pm 10.94
SLT	1.65 \pm 0.15	37.31 \pm 2.67	22.44 \pm 0.97	66.22
	2.87 \pm 0.34	35.42 \pm 3.41	21.35 \pm 0.77	65.9
	2.24 \pm 0.12	35.97 \pm 2.06	22.68 \pm 0.66	58.63
Mean \pm SE	2.25 \pm 0.15	36.23 \pm 1.50	22.16 \pm 0.46	63.58 \pm 2.48
STA	3.54 \pm 0.21	52.14 \pm 2.98	28.24 \pm 1.66	84.60
	3.09 \pm 0.10	54.45 \pm 1.63	32.57 \pm 2.26	67.18
	3.12 \pm 0.08	49.26 \pm 2.75	29.56 \pm 0.83	66.66
Mean \pm SE	3.32 \pm 0.12	51.95 \pm 1.46	30.12 \pm 1.02	72.81 \pm 5.90
CFS	1.47 \pm 0.09	45.23 \pm 1.55	21.93 \pm 0.85	106.23
	1.63 \pm 0.04	43.42 \pm 4.40	21.62 \pm 0.99	100.82
	1.76 \pm 0.13	45.43 \pm 2.87	27.85 \pm 1.24	63.12
Mean \pm SE	1.62 \pm 0.06	44.69 \pm 1.71	23.80 \pm 0.95	90.06 \pm 13.56

Again, the benefits from viscoelastic prestress effects were observed for all the resins used. Figure 4-15 shows the impact test results against the peak curing temperature for each resin used. A linear fit to the data points shows the trend, and the corresponding equations are also presented. It shows that the impact toughness of the matrix is sensitive to the peak curing temperature for both the resin only samples and the composite (control sample) materials. The CFS, PLT and SLT resins have similar low impact toughness properties.

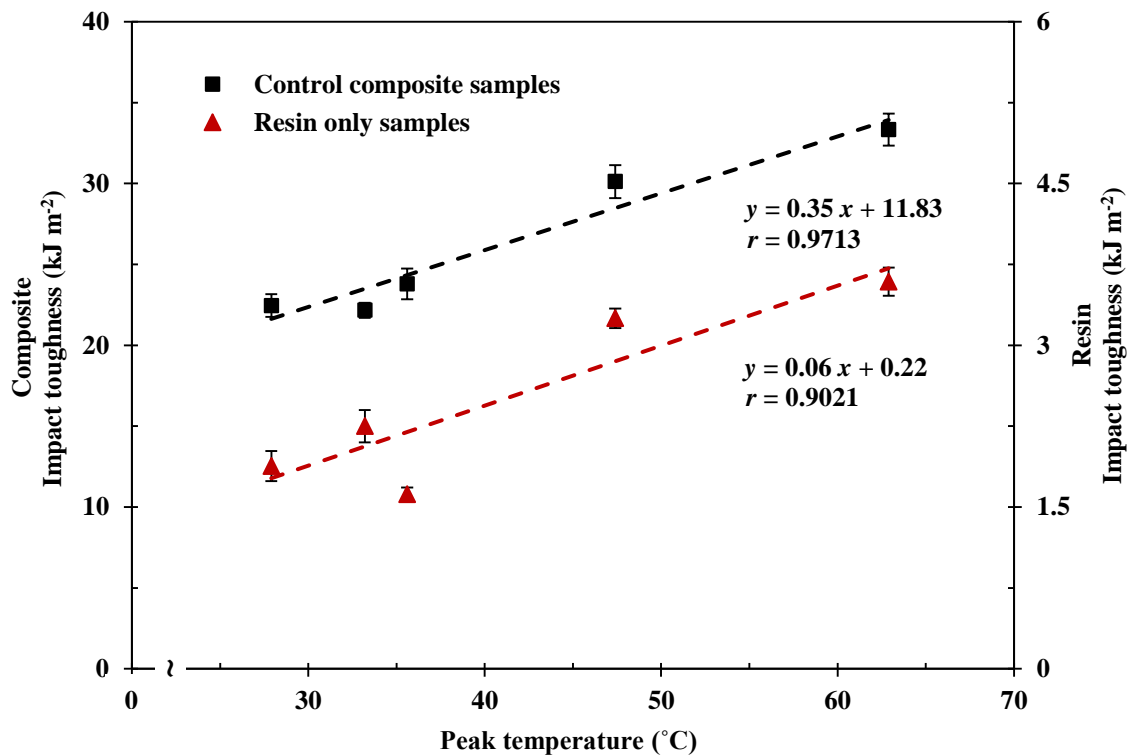


Figure 4-15 Comparison of resin properties with peak curing temperature. Data points are from Tables 4-3 and 4-4. Dashed line is from a linear fit; the corresponding equation is also shown.

As discussed in Section 4.1.3, the VPPMC samples produced with both SSR and LSR are (within the limits of experimental error) identical. Thus direct comparison of the current data can be made with the previous findings [12, 92]. Figure 4-16 shows the impact toughness of the resin only samples against the increase obtained from the prestress effect in VPPMC samples, together with historic data from Refs [12, 92]. A linear fit was applied to the data points. Though the correlation coefficient is relatively weak (i.e. 77%), it shows a trend in that the benefit from viscoelastic prestress appears to decrease with increasing impact toughness of the matrix materials. This may suggest changes in the

load transfer mechanism for different resin based composite materials. It would indicate that the tougher the matrix is, the weaker the stress interaction through the fibre-matrix interface; i.e. lower compressive stresses are generated from the viscoelastically strained fibres at the interface regions due to localised deformation of the matrix. This might give a lower increase in impact toughness. Further investigations into fibre-matrix interface interactions would be required to obtain a better understanding of this phenomenon.

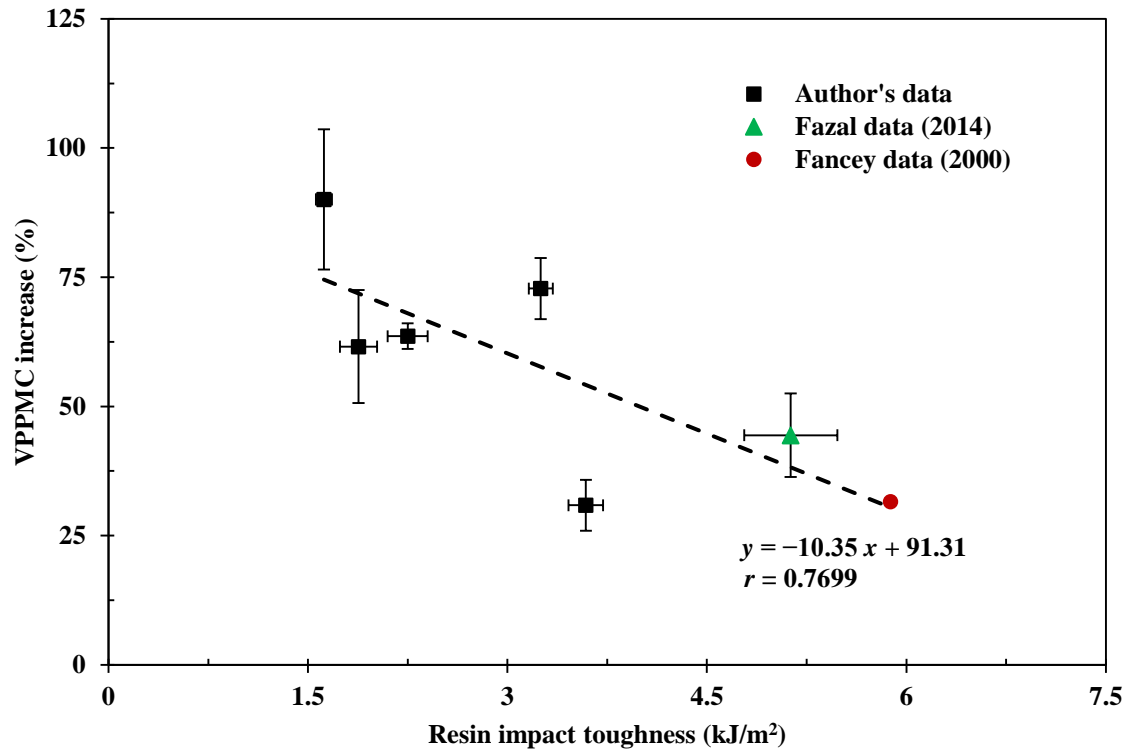


Figure 4-16 Plot of increase in impact energy absorption of VPPMC samples against the impact toughness of resin only samples. The triangle data point is from Ref [92]; the round circle data point is from Ref [12]. Dashed line is from a linear fit, together with the corresponding equation.

4.3.3 Resin selection

The investigation into resins show that matrix properties play an important role in the performance of both resin only and composite materials. Benefits from the viscoelastic prestress effect were observed for all the resin candidates; however, the mechanical benefits from viscoelastic prestress appear to decrease with increasing matrix impact toughness. Though further investigations are required to understand this issue further, it is beyond the scope of this thesis. To select the suitable resin for VPPMC production,

various issues need to be considered. Figure 4-16 suggests that PLT, SLT and CFS resins showed maximised prestress effects and thus would be suitable matrix materials. The exothermic tests of the resin curing process showed that SLT and CFS resin have short gel times, i.e. <15 min (Table 4-3), which may be insufficient for sample preparation. Therefore, the PLT resin was considered to be appropriate for this research. It is comparatively superior in: (i) low viscosity, to facilitate casting of samples with high fibre volume fractions; (ii) moderate gel time for sample preparation; (iii) good transparency after curing, which enables observation of the fibre distribution, porosity and debonding effects after mechanical testing; (iv) benefits from viscoelastic prestressing; (v) lowest peak curing temperature, which minimizes thermal residual stresses.

4.4 CONCLUSIONS

Preliminary investigations into the materials and equipment have been performed in this section to support and prepare for the main research project work. The calibration of the stretching rigs enabled direct comparison with previous research; the viscoelastic behaviour of the new nylon 6,6 fibre has been studied and compared to the previously used nylon yarn [1, 2, 5-7, 10, 98, 99] in various aspects; an appropriate resin has been selected to offer suitable properties for VPPMC production. The main findings from this section are listed as follows:

- (i) Following calibration of the two stretching rigs (SSR and LSR), Charpy impact testing shows that there is no significant difference in the performance of samples produced with either stretching rig. However, slightly stable mechanical behaviour of the composite samples produced from the LSR was observed.
- (ii) The cross-sectional area of the annealed new nylon 6,6 fibre yarn is marginally greater (<1%) than the old (equivalent) material which in turn contributes to a slight reduction in applied stress for the standard creep run (based on specified load).
- (iii) The annealing effect on nylon 6,6 fibre is highlighted in terms of shrinkage in fibre diameter and crystallinity. It is found that the new yarn has a lower crystallinity which is more thermally sensitive compared to the previously used fibre material. Therefore, subjected to the same creep conditions, the new yarn produces higher strain values and gives a slightly greater viscoelastic recovery force.
- (iv) Experimental investigations with various polyester resins show that a higher peak curing temperature may produce a matrix with higher impact toughness; the mechanical benefits from viscoelastic prestress appear to decrease with increased impact toughness of the matrix material.

Therefore, the large stretching rig (LSR) was considered to be the principal equipment for producing viscoelastic creep in polymeric fibres as required in later chapters. The PLT (polylite 32032-00) resin was selected as the appropriate matrix material for this research. The slight difference in the characteristics of the new nylon 6,6 yarn compared with the old material was also noted for later comparison with previous research findings.

Chapter 5

VISCOELASTIC BEHAVIOUR OF NYLON 6,6 FIBRE AND ITS EFFECT ON VPPMCS

SUMMARY

This Chapter investigates the viscoelastic behaviour of nylon 6,6 fibre and its effect on the impact behaviour of VPPMCs. Large creep stresses ranging from 330 MPa to 590 MPa were applied to the fibre yarns to determine creep strain-time performance, corresponding recovery strain was monitored in situ. The yield properties of the fibre were determined from creep rupture tests where a stress of 665 MPa was applied. A latch-based Weibull model, as previously adopted, enabled the prediction of the ‘true’ elastic modulus through elasticity from the creep-recovery data. The time-stress superposition principle (TSSP) was applied to predict the long-term performance of the material. Since nylon fibre showed approximately linear viscoelastic behaviour in both creep and recovery performance, this corresponded with the applicability of TSSP, in that the stress shift factor, $\log \alpha_\sigma$, had a linear relationship with creep stress.

The effect of viscoelastic creep strain level on the impact behaviour of VPPMCs were conducted through Charpy impact tests. Batches of VPPMC samples were prepared with their control counterparts and subjected to impact tests. WAXD and recovery force measurement of the fibre sample subjected various creep strain levels were carried out to provide potential contributions towards further understanding of the viscoelastic mechanisms within a VPPMC.

5.1 INTRODUCTION

Viscoelastic behaviour can have a profound influence on the mechanical performance of polymeric fibres [18]. Clearly, knowledge of the appropriate viscoelastic characteristics of reinforcements is vital for producing VPPMCs. Fibre materials are considered to store mechanical energy during tensile creep, which is progressively released through time-dependent viscoelastic recovery following load removal. When constrained in a matrix, the recovery of polymeric fibre imparts compressive stresses into the matrix, hence improving the mechanical properties of the composites. Research into the morphological structure of semi-crystalline fibres has resulted in models for different fibrous structures, i.e. the microfibrillar model (Section 2.7.1), and the Swiss-cheese model (Section 2.7.2). Though it is still inconclusive on a microstructural scale [146], the behaviour of nylon fibres can be explained by the Swiss-cheese model [111] as proposed by Prevorsek [104, 107]. Briefly, nylon fibre can be considered to consist of three phases, i.e. crystalline regions (anisotropic), isotropic amorphous regions and orientated amorphous domains. The orientation occurs during the drawing process and is associated with re-crystallization [105], i.e. phase transaction (Section 3.2.4.2). Therefore, differences in the fibre forming process could induce discrepancies on the microstructural scale, and further affect mechanical properties. For example, nylon 6,6 as fibre, is shown to exhibit linear viscoelasticity below 50 MPa creep stress [96, 193]; however, as a matrix material, nonlinear viscoelastic performance has been demonstrated under creep conditions of up to 40 MPa [113]. On the other hand, the time-dependent viscoelastic properties of polymeric materials can be represented through a spring-dashpot latch model as proposed by Fancey [97]. The creep, recovery and stress relaxation behaviour of a polymeric material correlate well with the stretched exponential Weibull functions (Sections 3.2.2 and 3.2.3).

Previous work on VPPMCs has shown that viscoelastically generated prestress from polymeric fibres can improve the mechanical properties of the composite materials, these typically being ~15% in tensile strength [6], ~33% in impact toughness [2, 5, 98], and

~50% in flexural stiffness [1]. To date however, a creep condition of ~330 MPa applied for 24 h, has been used for the majority of investigations into the performance of nylon-based VPPMCs in previous research [1, 2, 5-7, 10, 98, 99]. Thus, the effect of viscoelastic strain level on the mechanical properties of VPPMCs is unknown. In this Chapter, the viscoelastic characteristics of nylon 6,6 fibre under various creep conditions were investigated in terms of creep, recovery and recovery force. A latch-based Weibull model as previously developed (Sections 3.2.2) enabled the prediction of the ‘true’ elastic modulus through elasticity from the creep-recovery cycle. The TSSP was applied to predict the long-term performance of the material (Section 5.2.2). Finally, by applying various creep strain levels to nylon 6,6 yarns, batches of VPPMC samples were made with their control counterparts. Charpy impact testing was used to determine the effect of viscoelastic creep strain level on impact properties.

5.2 BACKGROUND

5.2.1 Viscoelastic behaviour

Viscoelastic behaviour exhibits both elastic and plastic characteristics when undergoing deformation. Particular interest in this phenomenon includes creep, relaxation and hysteresis [18]. Polymeric materials exhibit time-dependent plastic deformation when a constant stress (below the yield stress) level is maintained as shown in Figure 5-1 (a) and (b); such deformation is defined as viscoelastic creep [194]. In general, a creep strain curve may consist of three stages. An initial rapid elongation ε_i (mainly elastic deformation, independent of time), is produced once a creep load is applied. In Stage I, the creep rate decreases rapidly with time, which may be attributed to molecular chain slippage and reorientation [195]. After a certain period, Stage II follows, in which the rate reaches a steady-state minimum value, and usually lasts for a relatively long period. Finally, Stage III occurs with a rapid increase in creep rate beyond the yield creep strain, which ultimately leads to creep fracture of the material [18, 195-197]. It should be noted that Figure 5-1 (b) is an idealised curve and some materials may only possess partial stages of the curve. This is depending on the polymer microstructure [18].

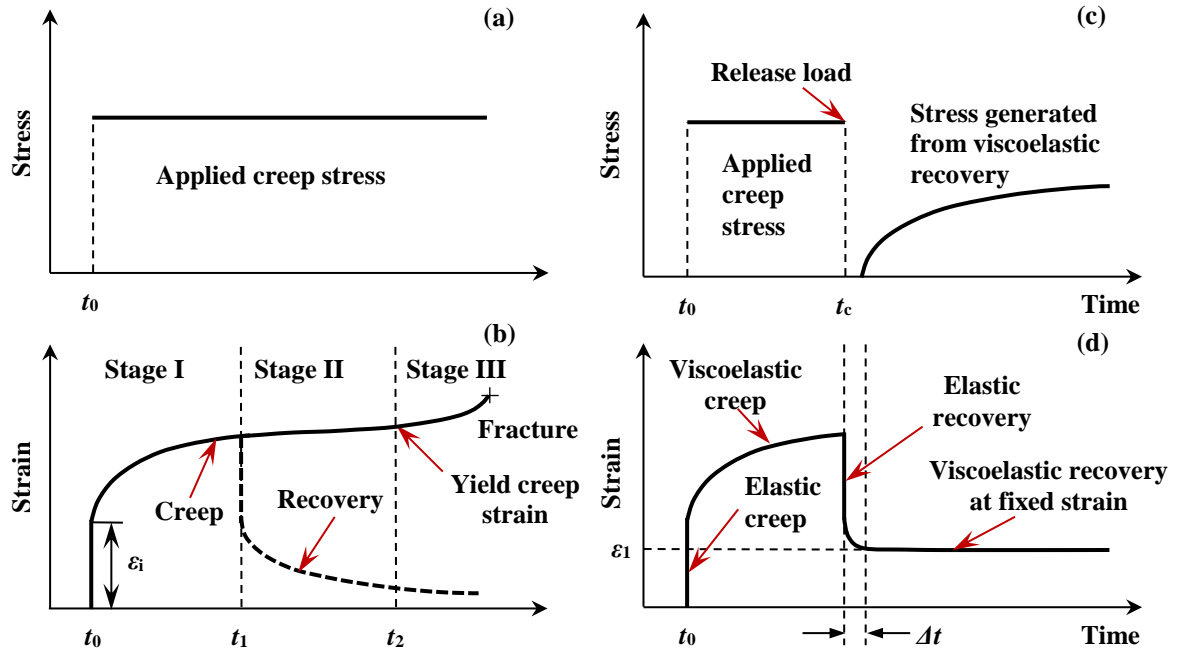


Figure 5-1 Schematic of the creep and recovery characteristics of a polymeric material: (a) creep and recovery behaviour under constant stress; (b) creep and recovery cycle following load removal at t_c , and subsequent recovery (through stress) at a fixed strain.

The viscoelastic recovery strain-time curve after releasing the creep load at t_1 is also shown as a dashed line in Figure 5-1 (b). Following load removal, the polymeric sample undergoes recovery, elastically and viscoelastically. Elastic deformation recovers immediately, while viscoelastic deformation is time-dependent behaviour. Figure 5-1 (c) shows the stress generated from the viscoelastic recovery. On releasing the creep load at t_c , a time window Δt , as illustrated in Figure 5-1 (d), is allowed to elapse to lock the residual strain either on force measurement equipment (Section 3.4.3) or within a polymeric matrix (i.e. in a VPPMC). Assuming ϵ_1 is the level of strain constrained, a time-dependent stress will be generated due to contraction of the viscoelastic component [99]. Equations 3-1 to 3-3, from the latch-based Weibull model developed by Fancey [96] to describe the viscoelastic behaviour of polymeric fibres (Sections 3.2.2 and 3.2.3), were adopted here for curve-fitting purposes.

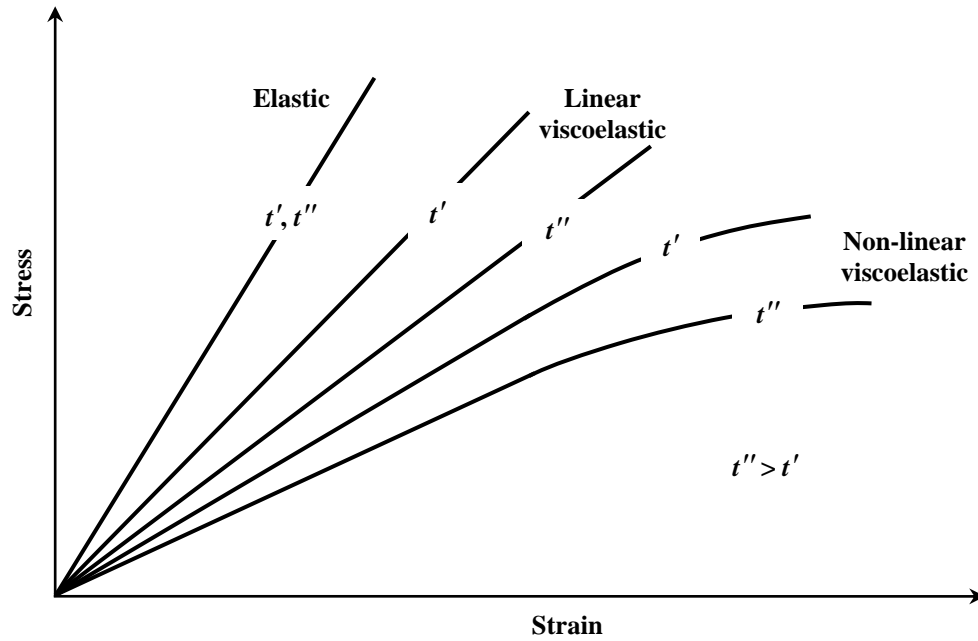


Figure 5-2 Schematic of stress-strain behaviour for elastic and viscoelastic materials at two values of elapsed time t' and t'' . Redrawn from [16].

Figure 5-2 shows schematically, the stress and strain behaviour of elastic and viscoelastic materials at two fixed values of elapsed time t' and t'' during creep tests. For a perfectly elastic material, the stress σ is directly proportional to the strain ϵ , giving a constant gradient referred to as the Young's modulus. For a viscoelastic solid material, the stress is a function of strain and time, and the material is considered to be linear viscoelastic when stress is directly proportional to the strain with different gradients at fixed time values [16]. Nylon 6,6 fibre for example, has shown approximately linear viscoelastic properties up to ~ 50 MPa creep stress over a period exceeding 1000 h using published creep data [193]; however, there is increasing deviation from linear viscoelasticity below 100 h at relatively low creep loads (< 50 MPa) [96].

5.2.2 Time-stress superposition principle

Since the viscoelastic behaviour of polymeric materials is time-dependent, the TSSP is developed to predict the viscoelastic response of the material over a large time scale. The superposition principle is first established for time and temperature, which forms the well-known time-temperature superposition principle (TTSP), as discussed later in Section 6.2.2. TTSP is based on the Doolittle formula, in which the viscosity is shown as a

function of free volume [198]; also, Ferry and Stratton [199] found that the free volume interpretation of the dependence of viscosity can be extended to concentration, pressure, and tensile strain. Thus, for polymers with a Poisson's ratio μ less than 0.5, the increase in fractional free volume f from stress-induced strain ε can be given by [199]:

$$\partial f / \partial \varepsilon = (\beta_f / \beta)(1/v)(\partial v / \partial \varepsilon) \quad (5-1)$$

where, β is the compressibility coefficient; β_f is the compressibility of the free volume; v is the specific volume. For small strain change $\Delta\varepsilon$, the strain shift factor, α_ε , can be defined as:

$$\log \alpha_\varepsilon = - \frac{[1/(2.303f_0)] \Delta\varepsilon}{f_0/(\beta_f/\beta)(1-2\mu) + \Delta\varepsilon} \quad (5-2)$$

where, f_0 is the free volume fraction at reference strain. Since strain $\varepsilon = \sigma/E$, where σ is the stress applied to the polymer and E is the elastic modulus, then assuming α_σ is the stress shift factor:

$$\log \alpha_\sigma = - \frac{[1/(2.303f_0)] (\sigma - \sigma_0)}{Ef_0/(\beta_f/\beta)(1-2\mu) + (\sigma - \sigma_0)} \quad (5-3)$$

Equation 5-3 is identical to the well-known Williams-Landel-Ferry (WLF) equation when $C_3=1/(2.303f_0)$ and $C_4=Ef_0/(\beta_f/\beta)(1-2\mu)$, which is:

$$\log \alpha_{\sigma} = -\frac{C_3(\sigma - \sigma_0)}{C_4 + (\sigma - \sigma_0)} \quad (5-4)$$

The TSSP as described by Equation 5-4 has been reported to fit well to the creep behaviour of unoriented nylon 6,6 monofilaments using low creep stress values (<50 MPa) [200]. Here, the TSSP was applied to the creep behaviour of oriented nylon 6,6 fibres subjected to large creep stresses, i.e. 330 MPa to 590 MPa. A successful transformation of the $\log \alpha_T$ (temperature shift factor) values from creep [193] and stress relaxation [201] have been reported in relation to predicting the long-term behaviour of recovery in nylon 6,6 fibre [10] and the (associated) impact toughness in nylon-based VPPMCs [5, 98]. Therefore, the $\log \alpha_{\sigma}$ parameter values generated from creep characteristics were also applied to the corresponding recovery strain-time data to predict the long-term recovery performance within the context of the free volume theory.

5.2.3 Elastic modulus

Most polymers are viscoelastic materials, tensile testing will produce both elastic and viscoelastic deformation simultaneously. Elastic deformation, like a spring, can be totally recovered after load removal; conversely, viscoelastic deformation acts like a time-dependent dashpot. In order to obtain the ‘true’ elastic modulus of a viscoelastic solid, the stress-strain relationship from pure elasticity is required, which is not possible from routine tests; i.e. no load can be physically applied instantaneously [18]. Moreover, the exact stress-strain characteristics of plastic materials are highly dependent on strain rate and environmental conditions [202]. Therefore, the elastic modulus of a polymer can vary considerably. However, the Weibull distribution equation can fit well to creep strain data [96, 97], which allows the prediction of purely elastic strain under different stress levels. Thus, creep tests of nylon 6,6 fibre, under a range of applied stresses, can provide a pure elastic stress-strain curve, which enables the prediction of the ‘true’ elastic modulus of the viscoelastic material.

5.3 EXPERIMENTAL PROCEDURES

5.3.1 Creep and recovery

Creep and recovery measurements followed previously described procedures as shown in Section 3.4.2. Briefly, following annealing, nylon 6,6 yarns were subjected to creep loading using the SSR. Creep strain was monitored under ambient conditions of 20.0-21.5°C and 30-40% RH. Five creep stress values (330 MPa, 395 MPa, 460 MPa, 525 MPa and 590 MPa) were applied to the annealed nylon 6,6 yarns for a period of 24 h in separate runs. For repeatability purposes, three samples of annealed yarn were subjected to creep at each of the stress values, and recovery strain was subsequently monitored after each 24 h creep run. A commercially available software package (*CurveExpert 1.4*) was used to fit the Weibull-based spring-dashpot latch model (Section 3.2.2) to the creep and recovery strain-time data; all the equation parameters and the correlation coefficients were provided to indicate the curve fit quality. Previous research has demonstrated there were no differences in surface features between the test and control fibres from standard creep conditions, i.e. 330 MPa for 24 h; however, as there may have been potential fibre damage from elevated creep strain levels, this was evaluated further through the Weibull model (Section 3.2.2), SEM (Section 3.4.4) and WAXD (Section 3.4.5).

5.3.2 Viscoelastic recovery force

By subjecting a polymeric fibre to creep stretching, subsequent contraction of the fibre will produce a recovery force (at a constant strain) which enables force monitoring through a force sensor. Measurement of the recovery force followed the procedures outlined in Section 3.4.3. Due to time limitations, recovery force was monitored up to 1000 h, and two yarn samples at each stress condition were tested for assessing repeatability. Again, *CurveExpert 1.4* was used to fit the Weibull-based latch model, i.e. Equation 3-3 (Section 3.2.3), to the recovery force-time data.

5.3.3 Wide-angle X-ray diffraction

WAXD was adopted to evaluate potential microstructural changes within the nylon 6,6 fibre after creep loading. Creep followed the same details outlined in Section 5.3.1. Briefly, to maintain identical conditions with the creep and recovery tests, the same length of fibre, i.e. ~1300 mm was used for WAXD. Following load removal, fibre yarns were cut and folded into 6 parallel yarns, and then brushed into flat ribbons. All the fibre ribbons were trimmed to ~100 mm in length, which ensured appropriate fitting into a sample holder. Ribbon width was maintained at ~10 mm which minimised overlapping effects. The flat fibre ribbons were then mounted on WAXD sample holders, and yarns were adjusted to be as parallel as possible.

WAXD scanning was carried out on an X-ray diffractometer using Cu-K α radiation ($\lambda=1.5406 \text{ \AA}$). Procedures and experimental settings followed Section 3.4.5. Profile analysis was achieved using commercially available software, *MDI Jade 6.0*. The background was maintained as linear. Since the mathematical model based on the Pearson VII function (Equation 3-9) offered the best profile fitting to nylon 6 fibre over the Gaussian, Lorentzian and Logistic functions [175], it was also adopted in this research to provide the profile fitting. A shape factor of 2 ensured adequately stabilised diffraction patterns [111, 146, 179].

5.3.4 Production and evaluation of composite samples

Production of composite samples followed the procedures in previous studies on nylon fibre-based VPPMCs [1, 2, 98] as outlined in Section 3.5.1, the main points are summarised here. As discussed in Section 4.1.3, to produce a batch of composite samples, the LSR (Section 3.4.2) was used to induce viscoelastic creep strain on nylon fibres. A clear-casting polyester resin, i.e. Reichold PolyLite 32032, was used with 2% MEKP catalyst as the matrix material, following careful selection in Section 4.3. A batch of test and control samples was moulded simultaneously with the same resin mix to ensure no differences between samples other than fibre prestressing. Following demoulding, samples were cut and stored in polyethylene bags at room temperature.

Composite samples were evaluated through Charpy impact testing to determine the effect of viscoelastic creep level on impact toughness. This was carried out at 336 h (two weeks) after composite manufacture, and experimental procedures and settings followed Section 3.5.2, operated in accordance with BS EN ISO 179 standard [191].

5.4 RESULTS AND DISCUSSION

5.4.1 Fibre topography

Examination of potential fibre damage from elevated creep strain levels was carried out through SEM (Section 3.4.4). As the five creep stress conditions ranged from 330 MPa to 590 MPa for the creep and recovery tests, fibre topography of the highest stress level (590 MPa) was evaluated and compared to the control (non-stretched) nylon yarn to determine potential fibre damages. Figure 5-3 shows the SEM micrographs, the test fibres being previously subjected to the 590 MPa creep stress for 24 h, compared with the control sample. There appear to be no differences in terms of fibre topography. Thus it may be inferred that there is no damage from the maximum (24 h) exposure to the 590 MPa creep condition.

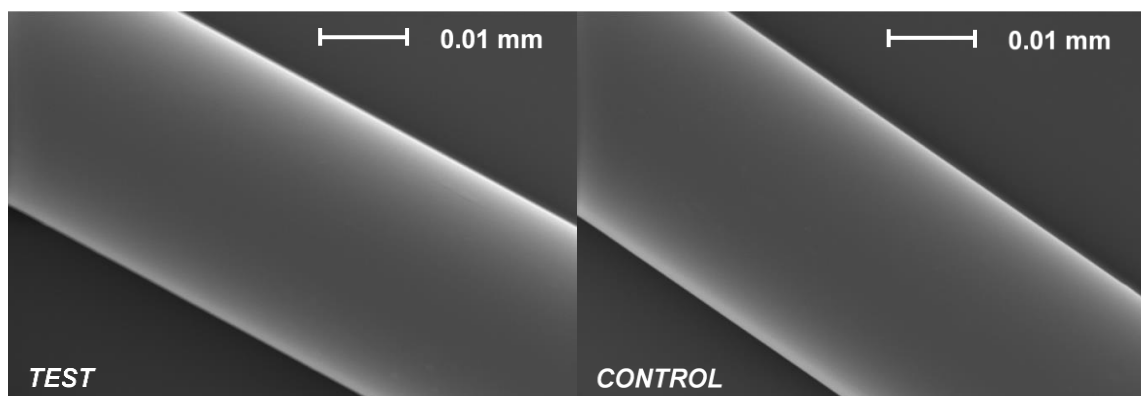


Figure 5-3 SEM micrographs of the nylon 6,6 fibres, showing test (24 h creep at 590 MPa) and control (no creep) samples. Both fibres were annealed simultaneously. While the test sample was subjected to creep, the control sample was positioned nearby to ensure the same ambient conditions. Micrographs were taken 72 h (to allow for sample preparation) after creep load removal for the test sample.

5.4.2 Fibre creep and recovery characteristics

Figure 5-4 (a) shows creep strain-time data under the five creep stress conditions, together with the curve-fits using Equation 3-1 (Section 3.2.2). The corresponding equation parameter values are listed in Table 5-1. Despite data scatter, the three runs at each stress demonstrate good repeatability. As the nylon 6,6 fibre is multifilament yarn (Section 3.1.1), the scatter in data points is primarily due to the inconsistency in manually locating the edges of inked marks during strain measurements. It is apparent that the creep strain increases with applied creep stress, which in terms of a mechanical model for viscoelastic behaviour, may result from more time-dependent latch elements being activated under higher creep stresses [96].

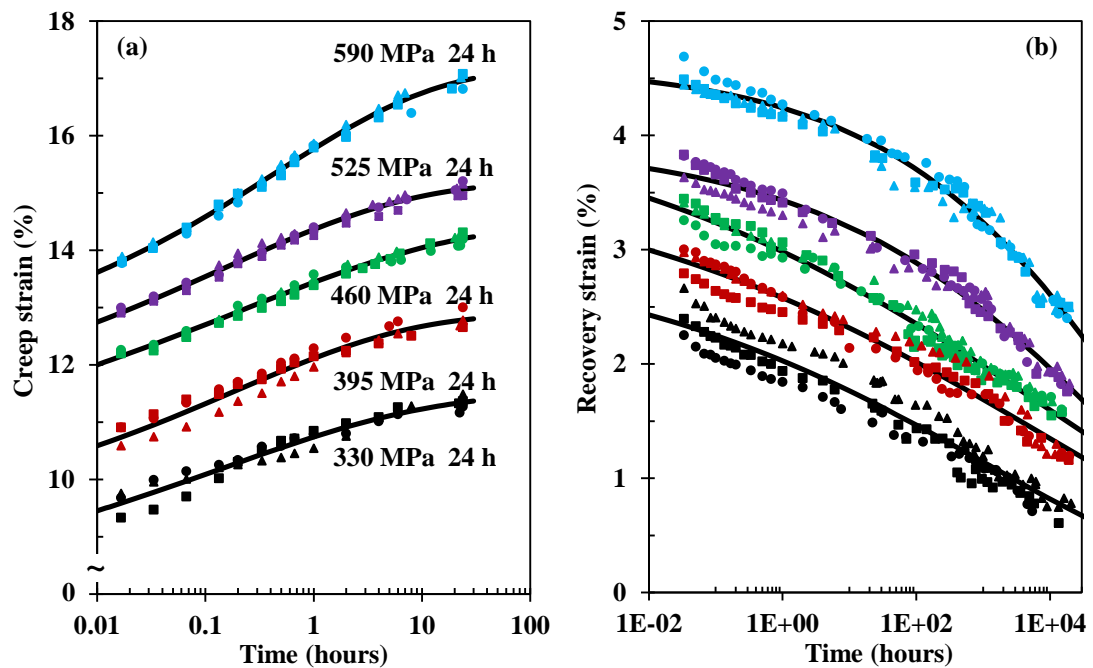


Figure 5-4 Strain-time data for (a) 24 h creep and (b) recovery at the five stress values with curve-fits from Equations 3-1 and 3-2.

The resulting recovery data from the 24 h creep runs in Figure 5-4 (a) are shown in Figure 5-4 (b), in which the strain data were monitored to approximately two years in real time. The corresponding parameter values from Equation 3-2 are shown in Table 5-1. Clearly, there is greater scatter with the recovery strain data in Figure 5-4 (b), compared with the creep strain data in Figure 5-4 (a). This is attributed to the yarns being held in a high state of tension for the latter case, which facilitated measurements. Nevertheless, the recovery

parameters for 24 h creep at 330 MPa in Table 5-1 are comparable to those previously obtained with the old yarn material [10]. Of particular importance is the values for ε_i in Table 5-1: although they have increased with applied creep stress, ε_i from creep at the highest stress (590 MPa) is less than $10^{-4}\%$. Thus, (unwanted) viscous flow effects are predicted by Equation 3-2 to be negligible. This indicates that most of the available recovery is viscoelastic, which implies that the viscoelastic prestressing mechanism would not be limited by an eventual contribution from viscous flow [10, 98].

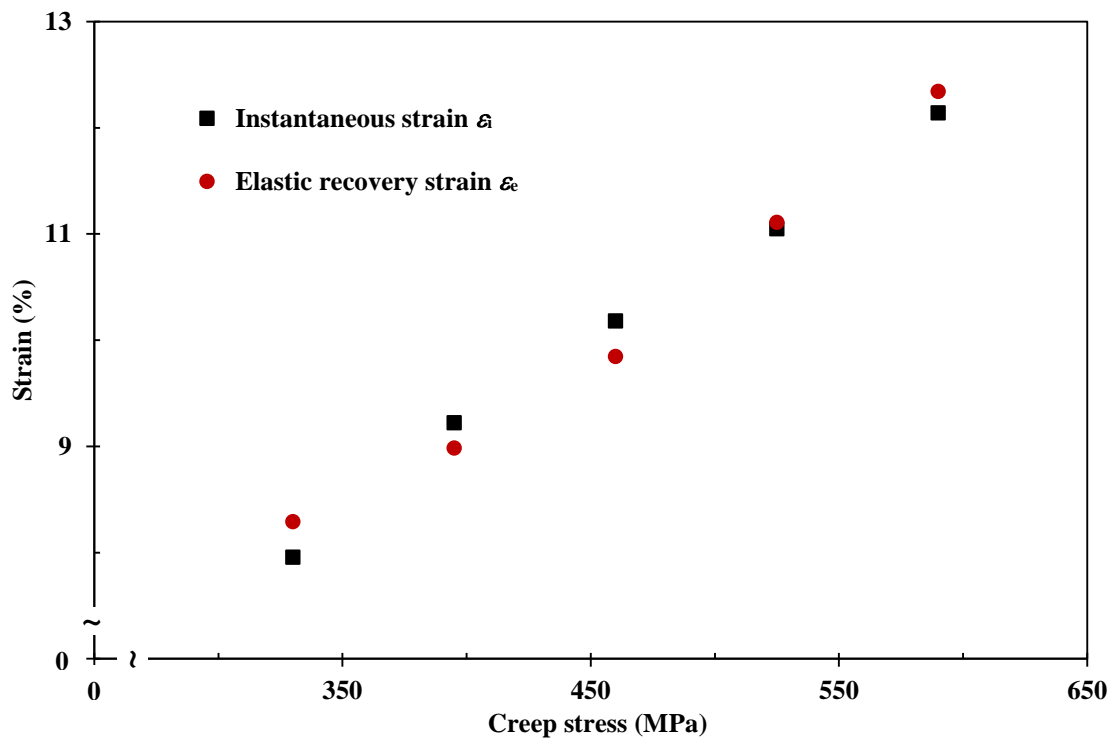


Figure 5-5 Plot of instantaneous strain ε_i and elastic recovery strain ε_e values at each creep condition. These values are obtained from Equations 3-1 and 3-2.

Since the creep and recovery at each stress condition corresponds to the same tests, the instantaneous elastic recovery ε_e , can be determined from the difference between the total strain at the end of a 24 h creep test, and the initial value of recovery strain from viscoelasticity and viscous flow [96] (Figure 3-5). The predicted ε_e values are shown in Figure 5-5, together with associated instantaneous strain ε_i values (creep strain at 0 min) from Table 5-1. It shows that for each creep condition, the instantaneous elastic strain ε_i compares well with the predicted ε_e value (within <1% difference). The scatter in data points is considered to be within the limitations of experimental measurements. This

indicates that the elastic strain was fully recovered upon load removal. Therefore, it may be concluded that there is no creep-induced fracture in the fibres even after being tensioned at 590 MPa for 24 h. This is consistent with the findings in Section 5.4.1.

Table 5-1 Summary of the creep and recovery parameter values from data in Figure 5-4 using Equations 3-1 and 3-2; r is the correlation coefficient.

24 h applied stress (MPa)	ε_c (%)	Creep parameters			r
		β_c	η_c (h)	ε_i (%)	
330	3.538	0.2245	0.1428	7.956	0.9729
395	3.665	0.2614	0.1856	9.223	0.9707
460	4.317	0.2048	0.1889	10.181	0.9939
525	4.148	0.2419	0.1418	11.049	0.9926
590	5.044	0.2830	0.4256	12.141	0.9957
24 h applied stress (MPa)	ε_r (%)	Recovery parameters			r
		β_r	η_r (h)	ε_f (%)	
330	3.052	0.1270	1155	$< 10^{-9}$	0.9651
395	3.800	0.1068	7175	$< 10^{-9}$	0.9795
460	4.361	0.1056	9637	$< 10^{-4}$	0.9865
525	3.956	0.1734	77400	$< 10^{-4}$	0.9878
590	4.621	0.2062	150468	$< 10^{-5}$	0.9853

5.4.3 Stress rupture testing

To determine the fibre failure properties, a higher creep stress was applied to nylon 6,6 yarn with ambient conditions of 20.0-21.5°C and 30-40% RH. Since the breaking strength of nylon 6,6 fibre is 700-900 MPa [10], 665 MPa creep stress (value restricted by the stretching rig) was adopted for the testing. Annealed fibre samples were stretched to break and the results are shown in Figure 5-6. Three fibre samples were tested to assess repeatability. Since yarn samples were approaching fracture points beyond the yield strain, the fracture point was not captured due to the rapid increase in creep rate that occurs in Stage III as characterised in Section 5.2.1. Thus data were available for two runs monitored up to 2 h, and one run up to 3 h. The yield creep strain (Section 5.2.1) was found to be ~18%, and this was reached after 2 h of stretching. Beyond the yield point, the fibre yarn progressed until fracture. Since Equation 3-1 is not applicable to the creep data beyond the yield point, the curve-fit is limited to the strain-time data below 18%, and parameter values are listed in the figure below. This is further discussed in Section 5.4.5.

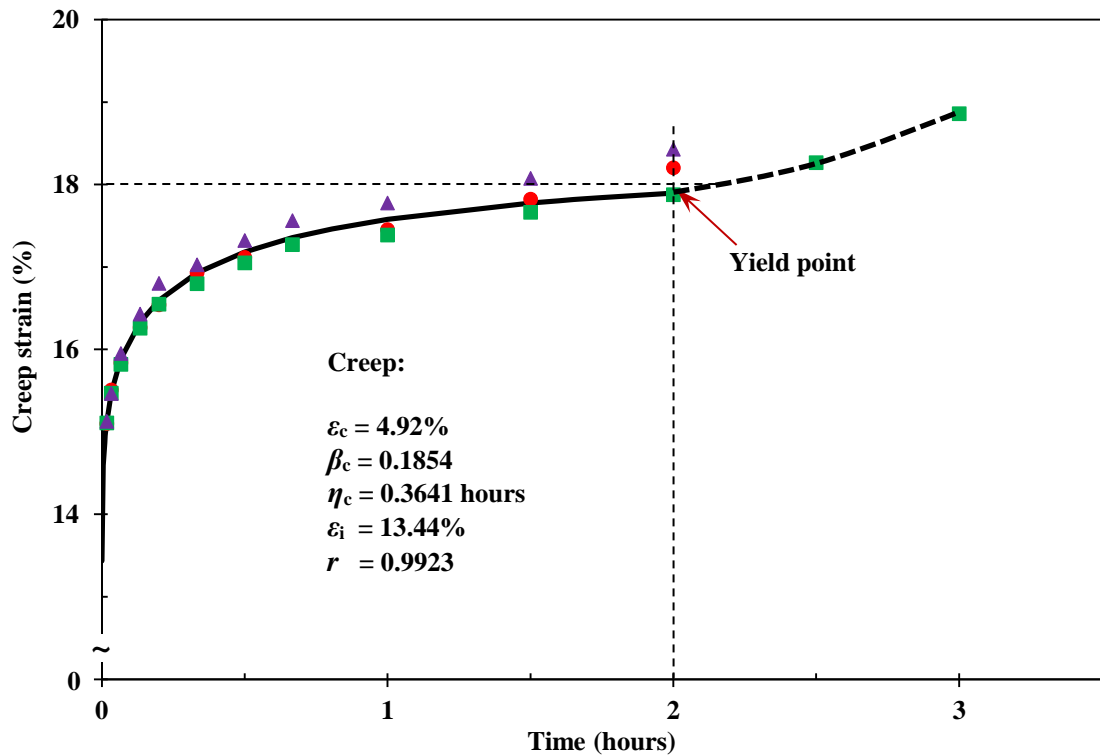


Figure 5-6 Strain-time data from nylon 6,6 fibre under 665 MPa creep stress. Dashed line shows the development of Stage III in creep behaviour, which quickly leads to fibre failure.

5.4.4 Predicting the ‘true’ elastic modulus

Since the Young’s modulus of viscoelastic materials can be strongly influenced by testing conditions, such as strain rate and temperature [203, 204], the modulus of nylon 6,6 can range from 2.8 to 4.9 GPa [205, 206]. The instantaneous elastic strain ε_i from Equation 3-1 is a predicted value which cannot be measured. Therefore, linear regression between ε_i and stress σ could be an approach to evaluate the ‘true’ modulus of nylon 6,6. Howard and Williams [193] investigated the creep of nylon 6,6 fibres at small stresses (10.1 MPa, 35.2 MPa, 50.3 MPa); Fancey [2, 10, 96] examined the creep and recovery behaviour of nylon 6,6 yarns using 282 MPa, 342 MPa and 401 MPa creep stresses. By using the ε_i values from Table 5-1 and Figure 5-6, together with the data from literature, the established relationship between ε_i and σ is shown in Figure 5-6. A linear fit was applied and the gradient value gave a true modulus value of 4.61 GPa. The scatter in data points may, at least in part, be attributed to differences in the microstructural characteristics (i.e. variations in crystallinity) between nylon 6,6 fibres used in the current studied material and previously adopted fibre yarns in Refs [2, 10, 96] (as discussed in Section 4.2.2). The

dashed lines in Figure 5-7 represent a ‘worst case’ gradient on both sides of the best linear fit with intercepts set as 0, and these gave values of 4.91 GPa and 4.07 GPa, respectively. This provides an indication of the uncertainty in the modulus result. Therefore, the true modulus result was found to be 4.6 ± 0.4 GPa.

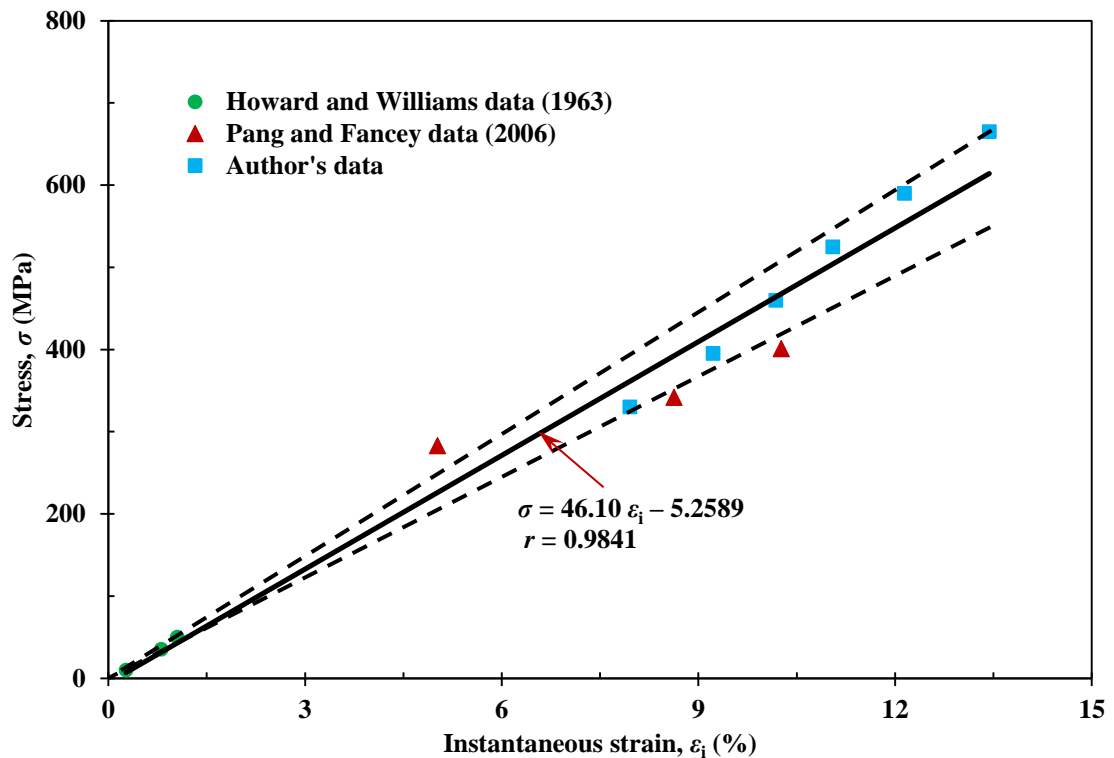


Figure 5-7 Plot of elastic strain ϵ_i , predicted from Equation 3-1, versus creep stress σ values. A linear regression was applied, indicating that the modulus value of nylon 6,6 fibre is 4.61 GPa. Dashed lines show a ‘worst case’ gradient on both sides of the best linear fit with intercepts set as zero, indicating the uncertainty in the modulus result.

5.4.5 Linear viscoelasticity

Following from Sections 5.4.2 and 5.4.4, the linear viscoelasticity of nylon 6,6 fibre was evaluated based on these results. As discussed in Section 5.2.1, the creep strain isochrones at fixed elapsed time periods were produced from the curves in Figure 5-4 (a). The results are shown in Figure 5-8, with linear regression fits to show the trend, and the scatter in data points can be attributed to the discrepancy in strain measurements (Section 5.4.2). It is clear that the linear gradient values decrease with the increase in creep duration, which suggests that nylon 6,6 fibre shows approximate linear viscoelastic

performance under creep deformation at high stress values, i.e. 330-590 MPa. This is in accordance with creep behaviour below 50 MPa stress [96, 193].

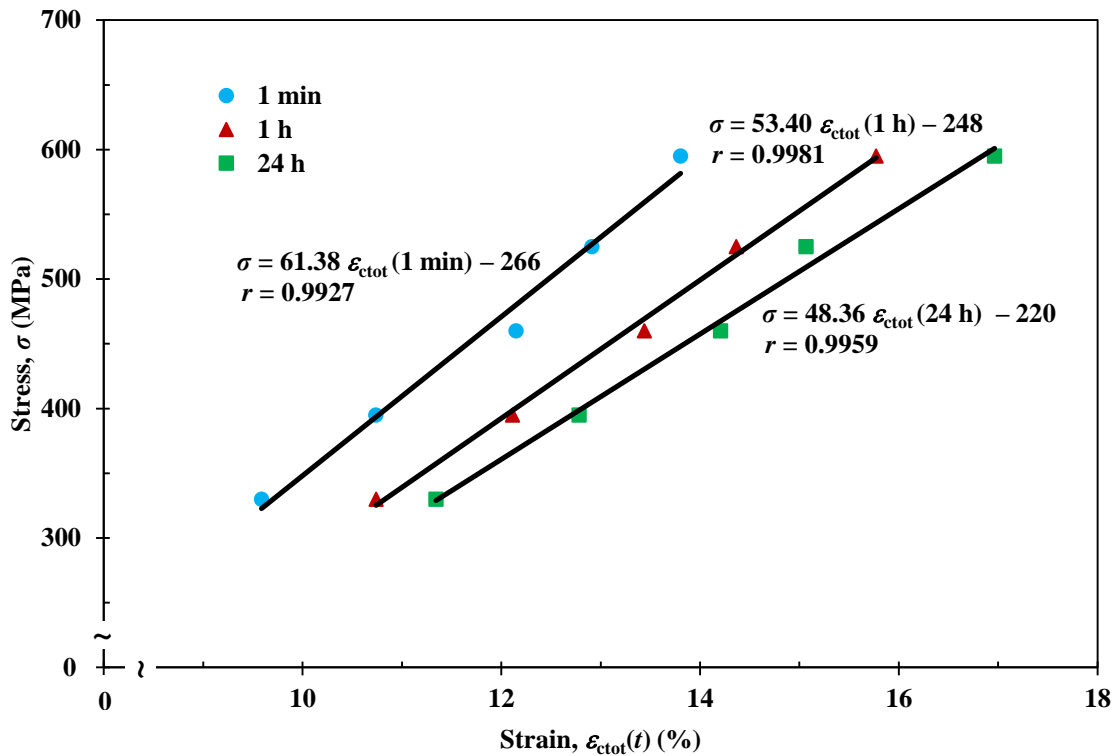


Figure 5-8 Creep strain isochrones of nylon 6,6 fibre at 1 min, 1 h and 24 h respectively. Linear regression shows the trends.

Since creep stress is directly proportional to strain at a fixed value of elapsed time [16, 197] for linear viscoelastic material, a shift factor α_c can be defined mathematically as follows:

$$\alpha_c = \frac{\epsilon_{ctot}(\sigma_0, t)}{\epsilon_{ctot}(\sigma_1, t)} \quad (5-5)$$

where, $\sigma_0 > \sigma_1$. Therefore, a higher creep strain could be shifted to $\epsilon_{ctot}(\sigma_0, t)$ through α_c . By selecting five strain values from the curve-fits using Equation 3-1 as shown in Figures 5-4 (a) and 5-6, the shift factor α_c (for each creep stress value) can be determined. The

330 MPa creep strain data were set as the reference. Resulting data are shown in Table 5-2, and plotted in Figure 5-9. A linear regression fitted well to the data points.

Table 5-2 Shift factor (α_c) values determined from Equation 5-5, as calculated from the average of five selected creep strain values on the fitting curves at each creep condition, relative to 330 MPa. SE is the standard error.

	330 MPa	395 MPa	460 MPa
$\alpha_c \pm \text{SE}$	1	0.8869 ± 0.0004	0.7990 ± 0.0003
	525 MPa	590 MPa	665 MPa
$\alpha_c \pm \text{SE}$	0.7496 ± 0.0011	0.6765 ± 0.0030	0.6135 ± 0.0010

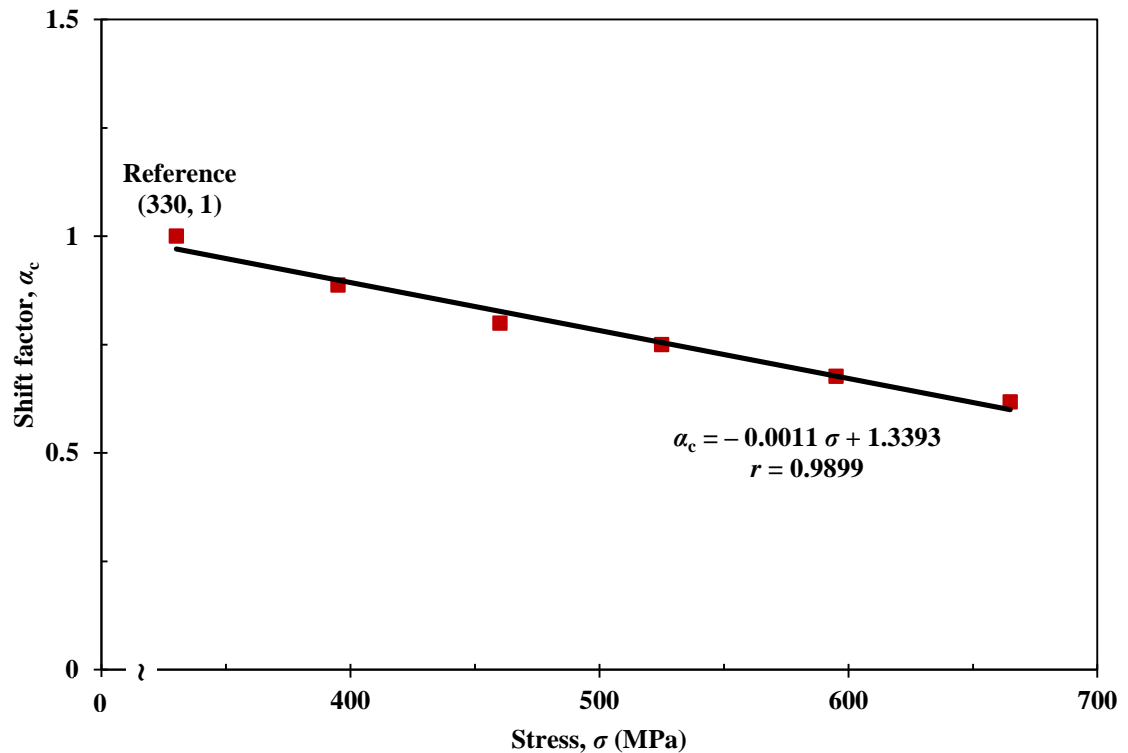


Figure 5-9 Shift factor α_c for each creep stress value; data points are from Table 5-2 (330 MPa creep stress is set as the reference).

Shift parameter α_c values in Table 5-2 were applied to the creep runs from Figures 5-4 (a) and 5-6, and Figure 5-10 shows the normalised results. The normalised creep strain data, from 330 MPa to 590 MPa, show a good fit, as most of the shifted data points fall within the scatter area of the 330 MPa creep condition. This indicates stability in viscoelasticity up to a creep stress of 590 MPa. Of particular interest, is that stable linear viscoelastic behaviour was observed with the 665 MPa creep data as highlighted by the dashed line

below 1 h (Figure 5-10). It is clear that the rapid growth in creep rate, categorized as Stage III (Section 5.2.1), started beyond 1 h of creep loading, thus the yield creep strain as determined in Section 5.4.3 can be considered as being limited to ~17.5%. Therefore, it may be concluded that creep behaviour of nylon 6,6 below the yield strain shows stable linear viscoelastic characteristics, which in turn makes the linear superposition principle applicable [197]. These results are in accordance with previous findings. While the WLF equation (Section 6.2.2) has predicted a non-linear relationship between temperature and temperature-shift factor (Section 6.2.2) for polymer materials, a linear relationship was successfully applied to nylon 6,6 material in terms of long-term creep [193], stress relaxation [201, 207], and dynamic tensile modulus [207] performance. Since TSSP shares the same free volume theory with TTSP (Section 5.2.2), speculation can be made that $\log \alpha_\sigma$ may also show linear behaviour with stress values. This is investigated in Section 5.4.6.

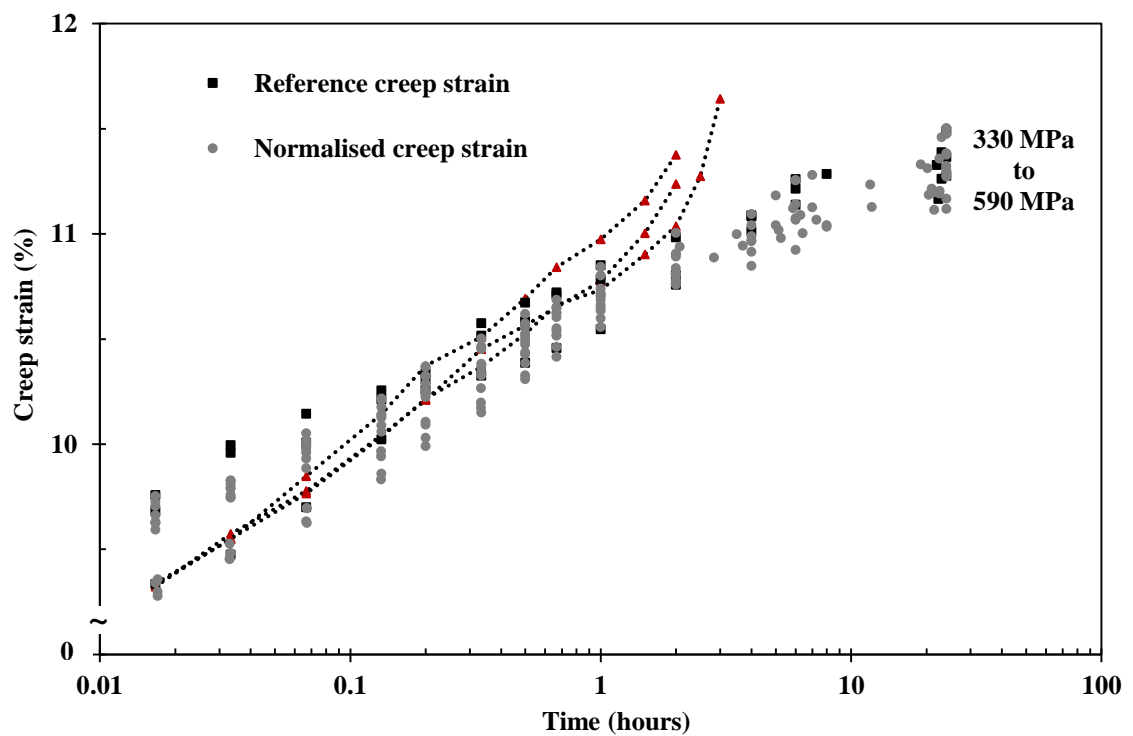


Figure 5-10 Strain-time relationships normalised to the 330 MPa creep condition through shift factors α_c from Table 5-2.

Analogous to the linear viscoelastic behaviour in creep, α_r is defined as the recovery shift factor:

$$\alpha_r = \frac{\varepsilon_{\text{rvis}}(\sigma_0, t)}{\varepsilon_{\text{rvis}}(\sigma_1, t)} \quad (5-6)$$

Again, a higher recovery strain under $\sigma_1 (>\sigma_0)$ can be shifted to $\varepsilon_{\text{rvis}}(\sigma_0, t)$ through α_r for a linear viscoelastic material. Since fibre rupture occurred under 665 MPa stress, recovery runs up to 590 MPa stress were used to study the linear viscoelastic recovery of nylon 6,6 fibre. The same procedures as described earlier were used here to determine the parameter values for each recovery condition, and results are listed in Table 5-3 and shown in Figure 5-11. Regression indicates a linear relationship between α_r and applied stress.

Table 5-3 Shift factor (α_r) values determined from Equation 5-6, as calculated from the average of five selected recovery strain values on the fitting curves at each creep condition, relative to 330 MPa. SE is the standard error.

	330 MPa	395 MPa	460 MPa
$\alpha_r \pm \text{SE}$	1	0.7915 ± 0.0117	0.6850 ± 0.0128
	525 MPa	590 MPa	
$\alpha_r \pm \text{SE}$	0.6031 ± 0.0189	0.4905 ± 0.0167	

Recovery strain-time curves as shown in Figure 5-4 (b), were shifted through α_r , and normalised results are shown in Figure 5-12. The viscoelastic recovery of nylon 6,6 fibre generally aligns with the 330 MPa recovery strain, though a large scatter of data was observed beyond 100 h. This scatter in data points can be attributed to reasons given in Section 5.4.2. Again, despite the data scatter, recovery behaviour of nylon fibre indicates approximate linear viscoelasticity.

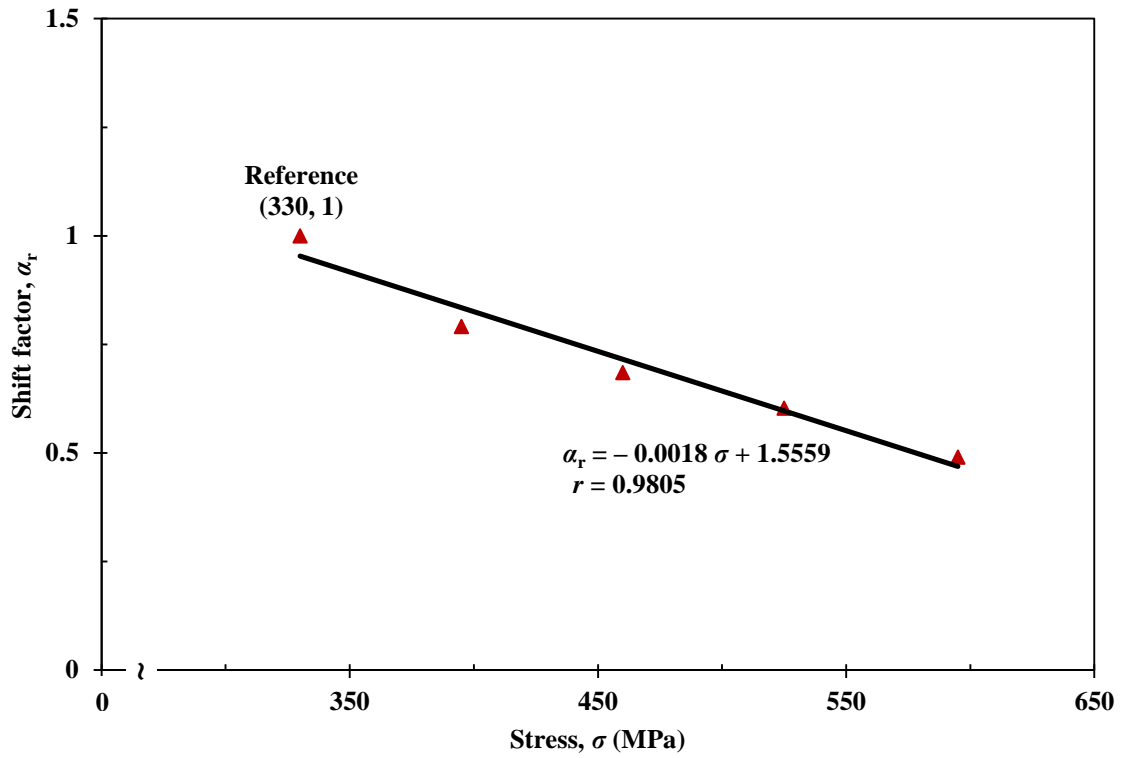


Figure 5-11 Shift factor α_r for each recovery curve; data points are from Table 5-3 (recovery strain from 330 MPa creep is set as the reference).

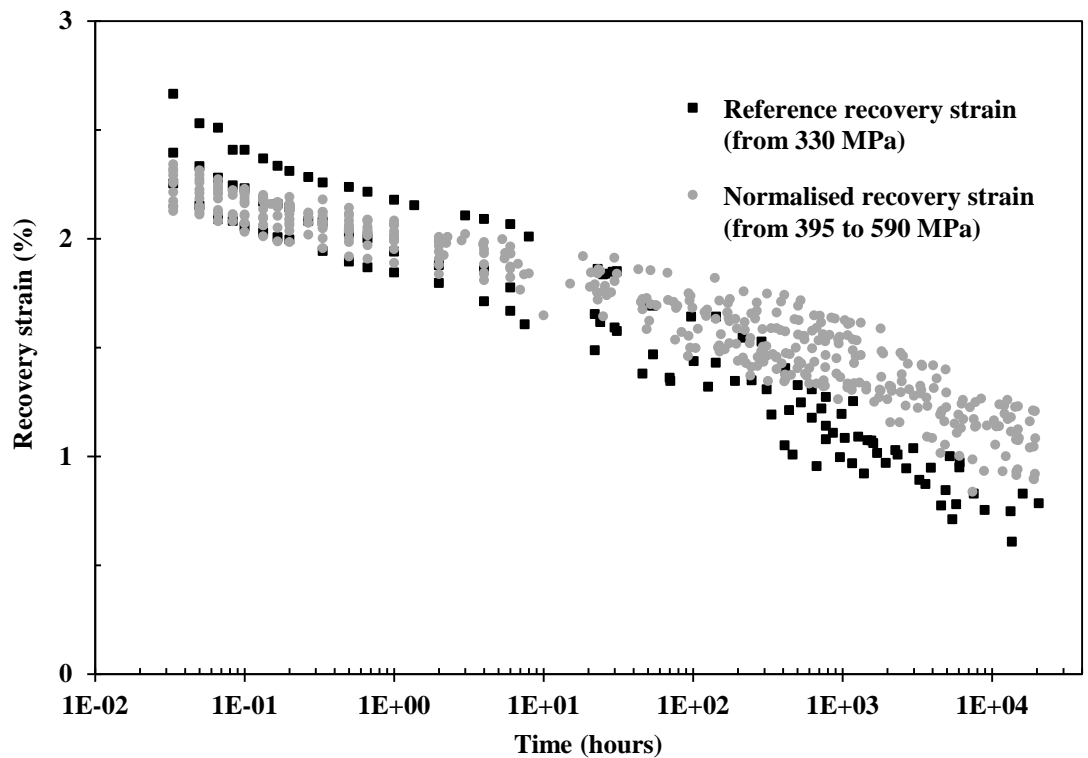


Figure 5-12 Strain-time relationships after normalising to the 330 MPa recovery condition through shift factors α_r , as shown in Table 5-3.

5.4.6 Long-term viscoelastic behaviour

Creep tests were carried out using a maximum value of 665 MPa stress as reported in Section 5.4.3. TSSP was applied to various creep runs below the yield strain, i.e. up to the 590 MPa creep condition. Thus, single step short-term (24 h) creep strain-time data as shown in Figure 5-4 (a) could be superposed, and the resulting master creep curve was obtained through a horizontal shift of creep stress curves, i.e. t to t/a_{σ} . Normalised results are shown in Figure 5-13. Since temperature and humidity for all the creep strain measurements were controlled to be under the same conditions (Section 5.3.1), the 330 MPa creep strain was selected as the reference σ_0 value. Equation 3-1 was used for curve fitting, and corresponding parameter values are also shown in Figure 5-13. Since elastic strain is dependent on stress, the value of ε_i for the 330 MPa reference creep stress as given in Table 5-1 was adopted.

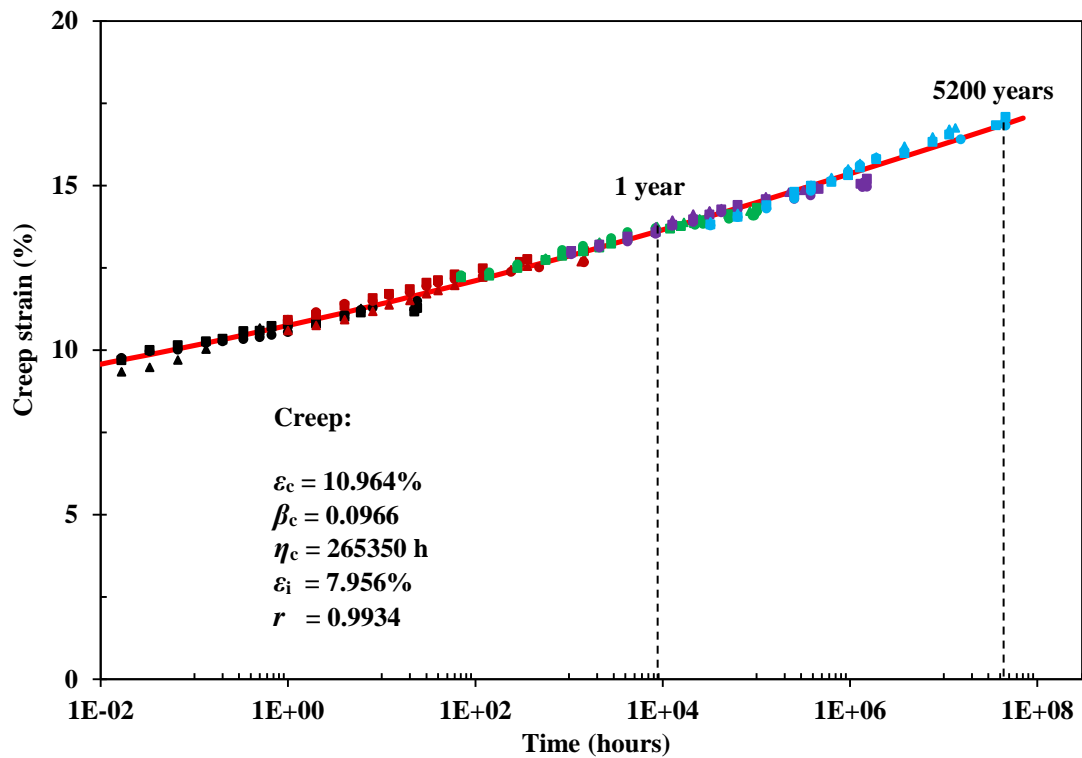


Figure 5-13 Master curve for creep strain versus time in nylon 6,6 fibre, obtained from TSSP, using data from Figure 5-4 (a).

As indicated in Figure 5-13, the master curve is well fitted by Equation 3-1. The curve effectively shows the creep deformation at 330 MPa loading over a vast time scale, and demonstrates the long-term dimensional stability of nylon 6,6 fibre. The stress shift factor

was plotted as $(\log \alpha_\sigma)$ versus $(\sigma - \sigma_0)$ and is shown in Figure 5-14. Instead of an apparent non-linear relationship between $\log \alpha_\sigma$ and stress as predicted by Equation 5-4, a linear regression was well fitted to the data points, giving a gradient of 0.024 MPa^{-1} . This enabled $\log \alpha_\sigma$ to be determined at 590 MPa relative to 330 MPa, and the resulting value was -6.2798. Thus, for shifting strain data from t to t/α_σ , the viscoelastic creep using 590 MPa would be $\sim 1,904,800$ times faster than a creep loading of 330 MPa, i.e. nylon yarns subjected to 590 MPa for 24 h would be equivalent to a 330 MPa creep stress applied for ~ 5200 years.

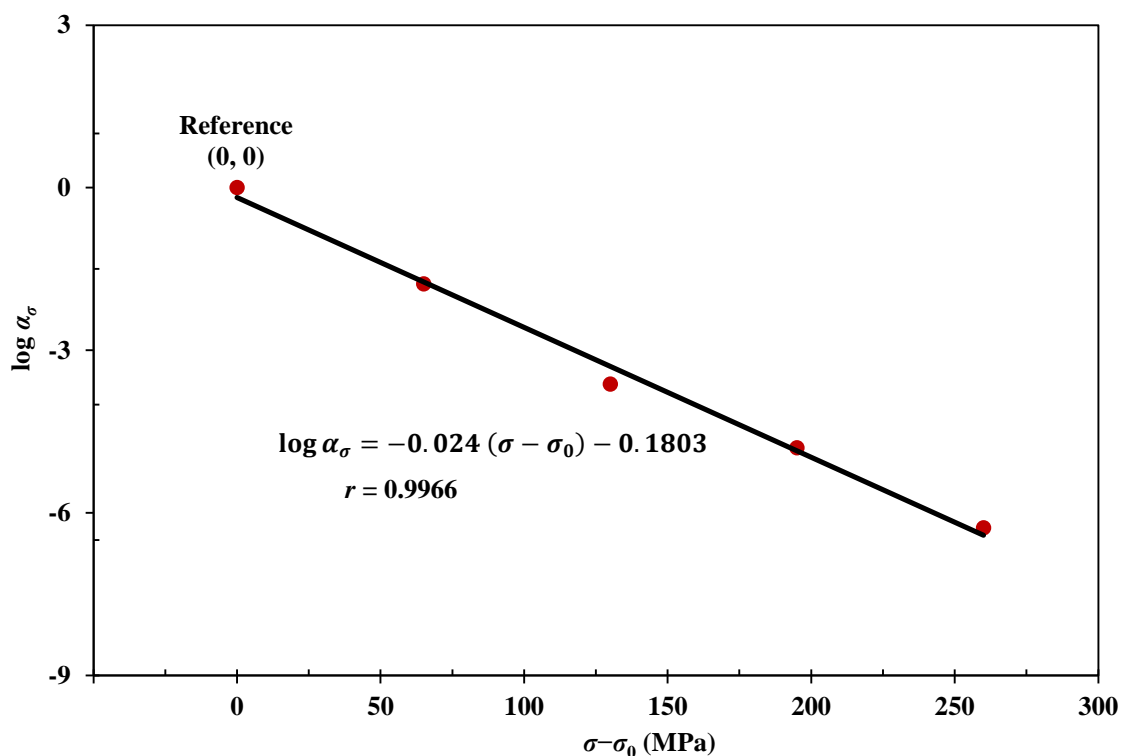


Figure 5-14 Plot of the time-stress shift factor, α_σ , as a function of stress difference. Reference creep stress is 330 MPa. The line and equation are from linear regression, r is the correlation coefficient.

The principle of linear TSSP in creep behaviour as shown above was also applied to the recovery performance of nylon 6,6 fibre. Here, the recovery strain under 590 MPa stress was set as the reference, and the same shift factor values in Figure 5-14 were applied to the recovery data given in Figure 5-4 (b) in a reversed order. The resulting recovery master curve is shown in Figure 5-15. This recovery corresponds to the removal of load on yarns being subjected to 330 MPa creep stress for $\sim 4.56 \times 10^7$ h as represented in Figure 5-13. Equation 3-2 was used for curve-fitting as shown in Figure 5-15, together with the

parameter values. It is worth noting that viscoelastic flow effects are predicted to be negligible (Section 5.4.2).

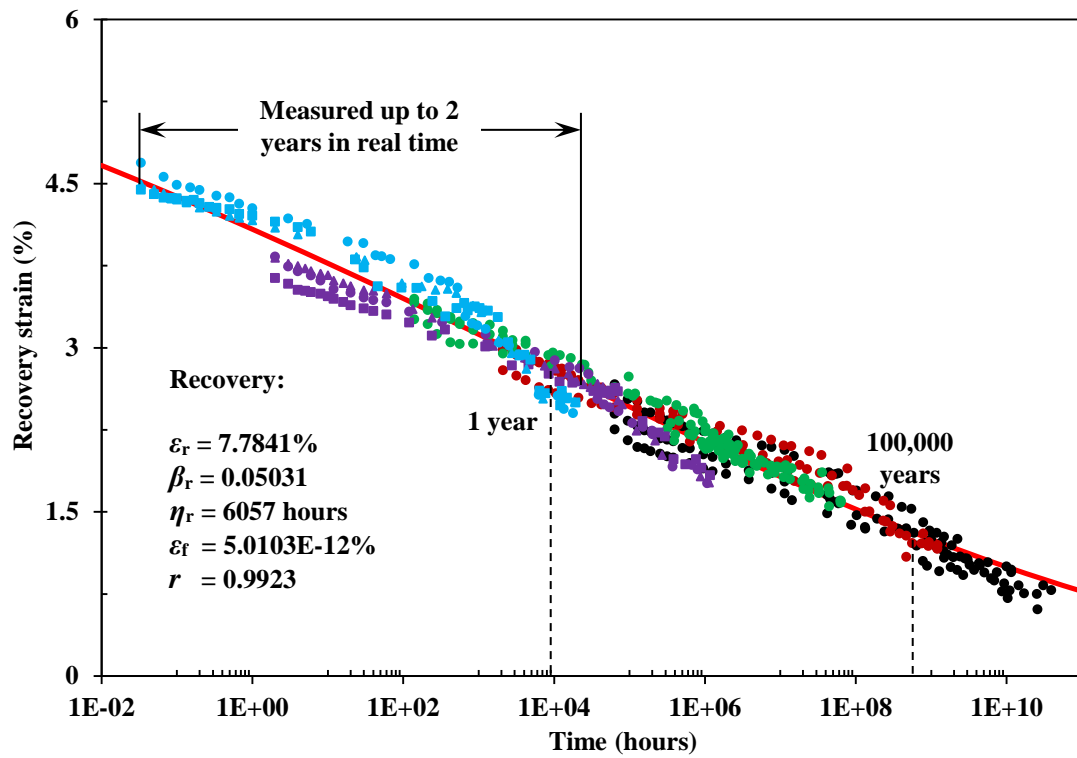


Figure 5-15 Recovery master curve obtained from TSSP using data from Figure 5-4 (b) plotted against time. Applied shift factor values are the same as shown in Figure 5-14, but in a reversed order.

5.4.7 Effect of viscoelastic creep strain on VPPMC performance

Sections 5.4.1 and 5.4.2 demonstrate that there was no creep-induced fracture even when subjected to 590 MPa for 24 h. Thus, VPPMC samples with various viscoelastic creep strain levels can be made through embedding the previously stretched fibres within a matrix. Here, the minimum and maximum creep stress conditions (330 MPa and 590 MPa) and one intermediate creep stress value (460 MPa) were selected to evaluate the effect of viscoelastic creep strain on impact toughness of VPPMCs. The viscoelastic creep strain level can be represented by the $\varepsilon_c(24)$, which is $[\varepsilon_{ctot}(24\text{ h}) - \varepsilon_i]$, i.e. subtract the elastic creep strain from the total creep strain at 24 h. Thus the $\varepsilon_c(24)$ value can be calculated from Figure 5-4 (a) and Table 5-1 using Equation 3-1, and they were found to be 3.39%, 4.03% and 4.82% for 330 MPa, 460 MPa and 590 MPa creep conditions, respectively. Batches of standard impact testing samples were made following the

procedures in Section 5.3.4. For repeatability, each strain level had five batches of test and control samples. Impact tests were performed two weeks after production, and Table 5-4 shows the results. Two-sided hypothesis testing results (at 5% significance level) have shown that the mean of the test samples from 460 MPa are significantly higher than the other two prestressing conditions.

Table 5-4 Charpy impact test results relative to each 24 h creep condition. Samples were tested 336 h after moulding. Individual test data are presented in Appendix-B, Table B-1.

Batch	Mean impact energy (kJ m ⁻²)		Increase in energy (%)
	Test ± SE	Control ± SE	
330 MPa (24 h)	33.93 ± 3.14	23.78 ± 1.48	42.64
	37.02 ± 1.78	20.71 ± 0.63	78.76
	35.36 ± 1.71	25.03 ± 0.96	41.26
	36.71 ± 2.89	25.60 ± 1.15	43.37
	35.58 ± 1.96	21.61 ± 1.13	64.69
Mean ± SE	35.72 ± 0.99	23.35 ± 0.59	54.14 ± 7.52
460 MPa (24 h)	39.63 ± 2.22	24.08 ± 0.74	64.60
	37.30 ± 0.54	22.28 ± 0.88	67.39
	38.57 ± 1.35	19.46 ± 0.15	98.21
	39.36 ± 0.95	22.59 ± 0.66	74.23
	44.81 ± 1.86	23.41 ± 0.59	91.36
Mean ± SE	39.93 ± 0.81	22.36 ± 0.42	79.16 ± 6.66
590 MPa (24 h)	30.08 ± 2.51	21.49 ± 1.25	39.96
	35.77 ± 1.46	21.72 ± 0.44	64.70
	35.62 ± 1.11	22.19 ± 0.63	60.48
	37.64 ± 1.75	23.98 ± 0.82	56.93
	36.59 ± 1.36	24.29 ± 0.37	63.51
Mean ± SE	35.14 ± 0.62	22.74 ± 0.32	57.12 ± 4.49

The influence of creep strain level on impact behaviour is further presented in Figure 5-16. It is clear that the benefit from prestress is greatest at 460 MPa creep for 24 h, and this gives 79.16% increase in impact energy absorption compared to their control counterparts. Increasing the creep stress further to 590 MPa, reduces the impact benefit to 57.12%. This indicates that an optimum viscoelastic fibre prestressing level exists to maximise the prestress effects for VPPMC production. Though approximate linear viscoelastic recovery was demonstrated in Sections 5.4.5 and 5.4.6 (free viscoelastic strain recovery), the recovery of fibre yarn within a VPPMC was constrained (at fixed strain) by the matrix. Hence, the measurement of recovery force at fixed strain was required to understand further the prestress effect, as investigated in the following section.

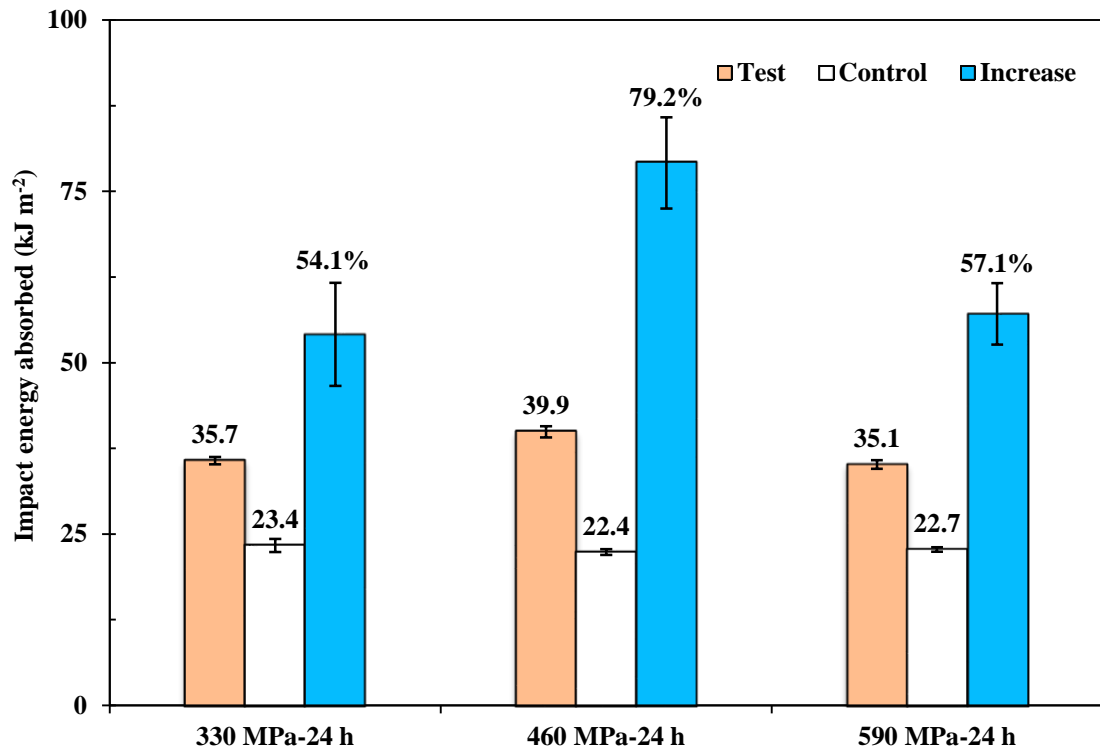


Figure 5-16 Charpy impact test results from Table 5-4; error bars represent the standard error.

5.4.8 Recovery force

Recovery force levels, generated from the three creep settings, were monitored up to 1000 h, and results are shown in Figure 5-17. The recovery force-time data under 330 MPa for 24 h were taken from Section 4.2.4. For repeatability, two runs for each creep condition were evaluated. Data scatter is attributed to effects as discussed in Section 4.2.4. Following creep load removal, the fibre loops subjected to 460 MPa and 590 MPa creep show similar recovery rates, but there is divergence beyond 3 h. At 336 h (the age at which Charpy impact tests were performed in Section 5.4.7), the mean recovery force was found to be 3.76 ± 0.06 N, 4.31 ± 0.08 N and 3.24 ± 0.11 N for 330 MPa, 460 MPa, and 590 MPa creep conditions, respectively. Recovery force measurement is not directly related to the recovery performance within a VPPMC, i.e. there are differences between strain locked by the matrix and the force measurement rig, due to process procedures (Sections 3.4.3 and 3.5.1). The results do demonstrate however, that the 460 MPa creep stress gives the highest recovery force beyond 100 h. This corresponds to the Charpy impact results, in that the highest impact increase was observed with the 460 MPa prestress condition in Section 5.4.7.

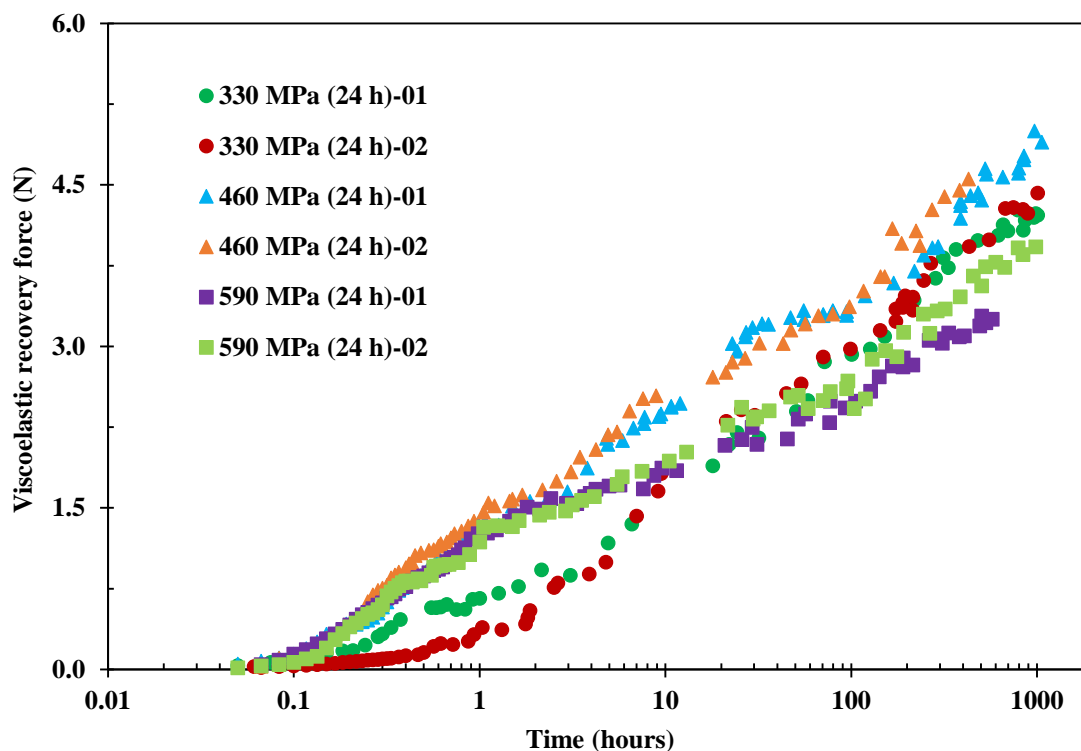


Figure 5-17 Viscoelastic recovery force generated from the three creep conditions. Data for the 330 MPa, 24 h creep condition are from Section 4.2.4.

5.4.9 X-ray diffraction

The creep deformation mechanism within nylon 6,6 fibre was further investigated through WAXD, and resulting WAXD patterns under the three creep conditions are shown in Figure 5-18. As facilities were limited to stretching one yarn at a time, there were slight variations in sample age during WAXD scanning. For each diffraction pattern, the most intense region consists of two crystalline reflections for (i) the peak at $\sim 20.3^\circ$ corresponding to the (100) crystal plane, showing the inter-chain distance and (ii) the peak at $\sim 23.5^\circ$ relating to the (010, 110) doublet, revealing the inter-sheet distance [185, 186]. These two peaks are reflected from the α -crystals oriented in a triclinic unit cell as shown in Figure 3-9 in Section 3.2.4.2. Peak positions in Figure 5-18 show slight variations, which may due to variability in sample preparation (as discussed in Section 4.2.2). There are significant differences in terms of peak intensity from the three creep settings, showing an increase in intensity of both peaks with increasing creep stress. This demonstrates the sensitivity of orientation to the creep loading process.

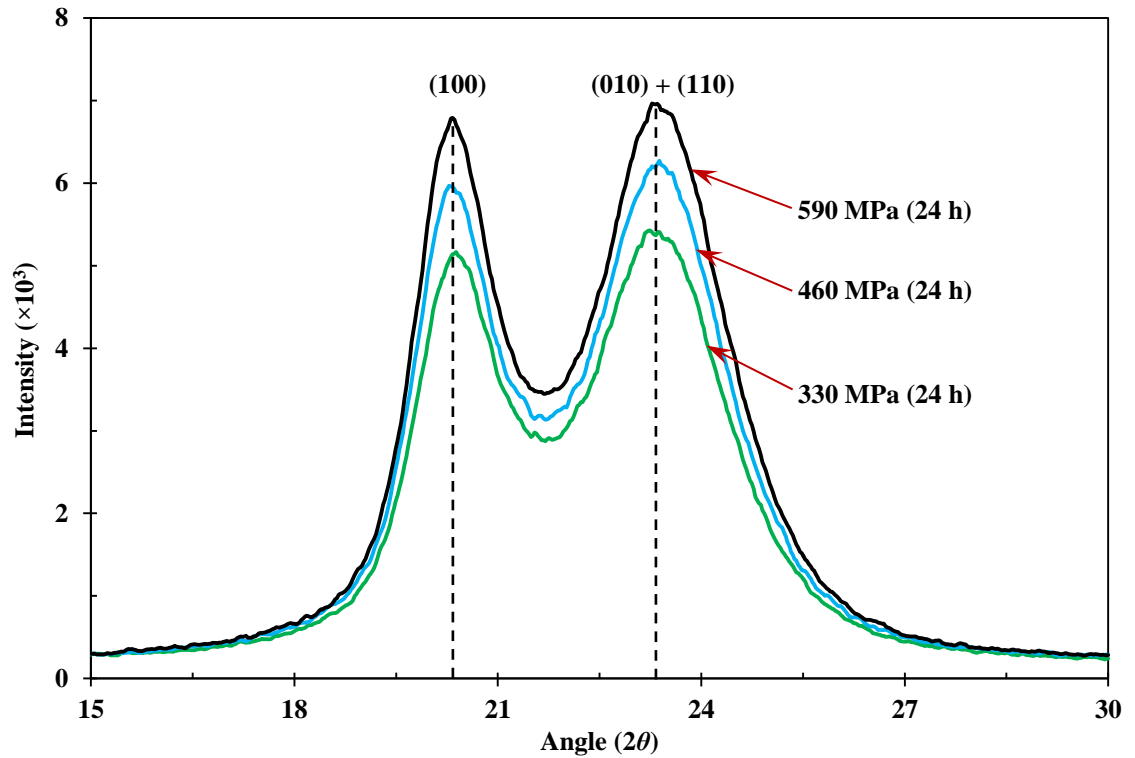


Figure 5-18 Comparison of WAXD patterns for the nylon 6,6 fibre under the three creep conditions. Sample age (following load removal) was 20 h for 330 MPa, 44 h for 460 MPa and 68 h for 590 MPa.

Table 5-5 Microstructural parameters for the nylon 6,6 fibre after creep process.

	Sample	Non-creep	330 MPa (24 h)	460 MPa (24 h)	590 MPa (24 h)
(100)	2θ (°)	20.52	20.37	20.34	20.34
	d (Å)	4.341	4.372	4.378	4.378
	$FWHM$	1.41	1.36	1.32	1.31
	ACS (Å)	57	59	61	62
(010, 110)	2θ (°)	23.55	23.44	23.58	23.58
	d (Å)	3.817	3.813	3.812	3.809
	$FWHM$	2.10	1.92	2.09	2.04
	ACS (Å)	39	42	39	40
Amorphous	2θ (°)	22.77	22.78	22.64	22.69
	$FWHM$	3.52	3.88	3.67	3.70
Crystallinity (%)		52.97	58.15	59.95	60.34
ICP (%)		72.6	77.6	78.5	79.1

Further details of peak features were obtained through deconvolution of the diffraction patterns into sharp peaks with a profile fitting technique as described in Section 5.3.3, and the results are listed in Table 5-5. The details of annealed but non-stretched pattern parameters as shown in Table 4-2 (Section 4.2.2), are also provided in the table for

reference. The crystallinity increased with creep stress. This can be attributed to the recrystallization occurring during the loading process as discussed in Section 3.2.4.2. Despite the annealing effects on nylon 6,6 fibre (Section 4.2.2), similar increases in crystallinity with applied tensile strains were also observed by Marcellan et al [111] on non-annealed nylon 6,6 yarn. Also, they detected a decrease in the reduction of the isotropic amorphous index, and an increase in amorphous orientation [111]. Therefore, the increase in intensity with creep stress (as shown in Figure 5-18), may be caused by molecular orientation occurring in the isotropic amorphous regions.

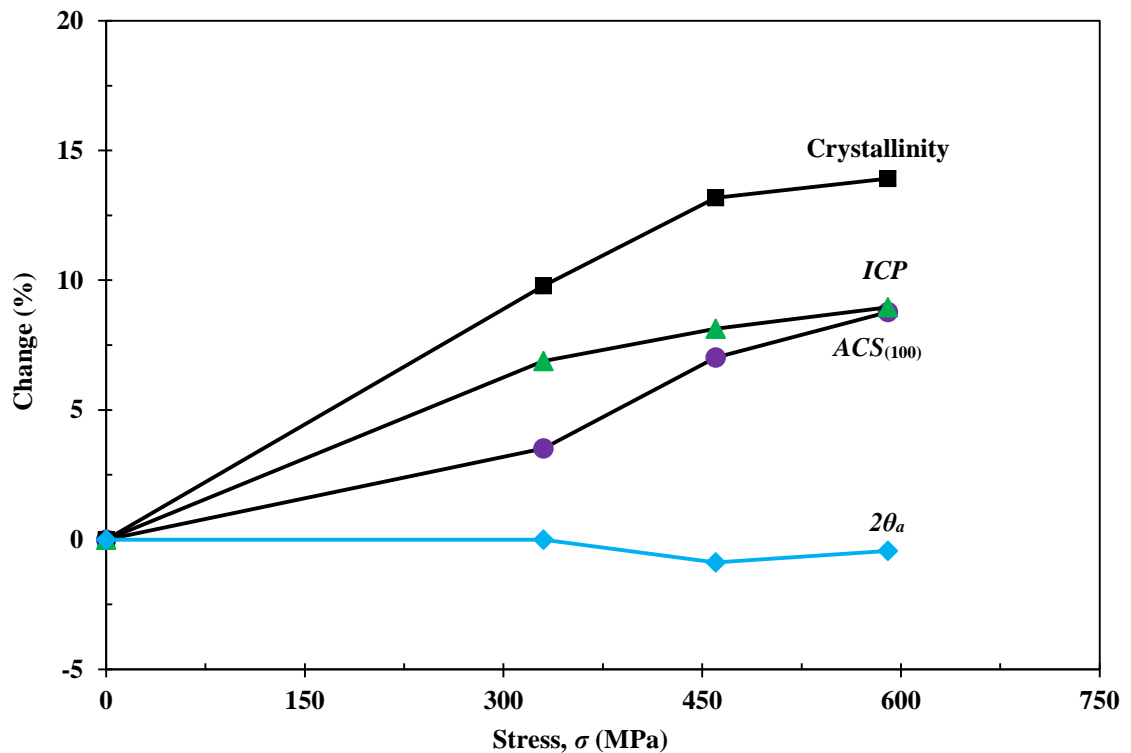


Figure 5-19 Changes (%) in microstructural parameters with creep stress in terms of crystallinity, apparent crystal size (*ACS*), index of crystalline perfection (*ICP*) and amorphous peak position ($2\theta_a$).

The influence of creep processing on fibre microstructure is highlighted in terms of changes in WAXD parameters, as shown in Figure 5-19. The amorphous halo position was found to remain relatively stable with respect to the creep stress. The index of crystalline perfection, *ICP*, is defined for interpreting the shift in crystalline peak positions from (100) and (010, 110) planes, compared to the crystalline characteristics proposed by Bunn and Garner [143] (Section 3.2.4.5), and this showed an increase with creep stress. However, referring to the spacing data from Table 5-5, the perpendicular

chain-to-chain distance within the $d_{(100)}$ plane increased with creep load, to reach a constant value at the 460 MPa and the 590 MPa creep, which is equal to that of the non-annealed yarn (Section 4.2.2). This is also confirmed through apparent crystal size ACS data from the as-received fibre. In contrast, the perpendicular sheet-to-sheet distance $d_{(010, 110)}$ decreased with loading, which could be caused by compaction along the a -axis direction induced from the loading of the molecular chains oriented along the fibre axis. Therefore, it can be concluded that for the increase in creep stress from 0 to 590 MPa, the minimized energy of the structure due to annealing [154] is affected, both crystallinity and *ICP* rates decrease. The inter-chain distance, which is controlled by van der Waals interactions, is stabilised after 460 MPa stress; the inter-sheet distance, controlled by hydrogen bonds, continues to decrease, which indicates the sheets became closer.

5.4.10 Viscoelastic deformation mechanisms in nylon 6,6 fibre

Nylon 6,6 fibre has demonstrated approximately linear viscoelastic characteristics under low creep deformation levels, i.e. up to ~50 MPa creep stress over a period exceeding 1000 h [193]. Here, the creep performance of fibre yarn with large strain deformation (up to 17% creep strain) from 330 MPa to 590 MPa creep stress also demonstrates linear viscoelasticity, as presented in Section 5.4.5. This is further verified through TSSP in Section 5.4.6. While semi-crystalline nylon 6,6 fibre is usually regarded as a two-phase system in X-ray diffraction, i.e. crystalline and amorphous regions as discussed in Section 5.4.9, the amorphous region has been refined into isotropic amorphous and oriented amorphous domains [111, 183]. The oriented amorphous regions can be considered as the bridging area that connects the isotropic and crystalline regions, which occurs during the drawing process of the fibre [105]. As proposed by the ‘Swiss-cheese’ model [104, 107], crystals are surrounded by the oriented amorphous chains, i.e. TTMs (Section 2.7.2). Thus, viscoelastic deformation within nylon 6,6 can be considered to be controlled by the performance of (i) crystalline regions; (ii) isotropic amorphous regions; and (iii) oriented amorphous domains. A model can be proposed to describe the creep deformation of nylon 6,6 fibre, as shown in Figure 5-20.

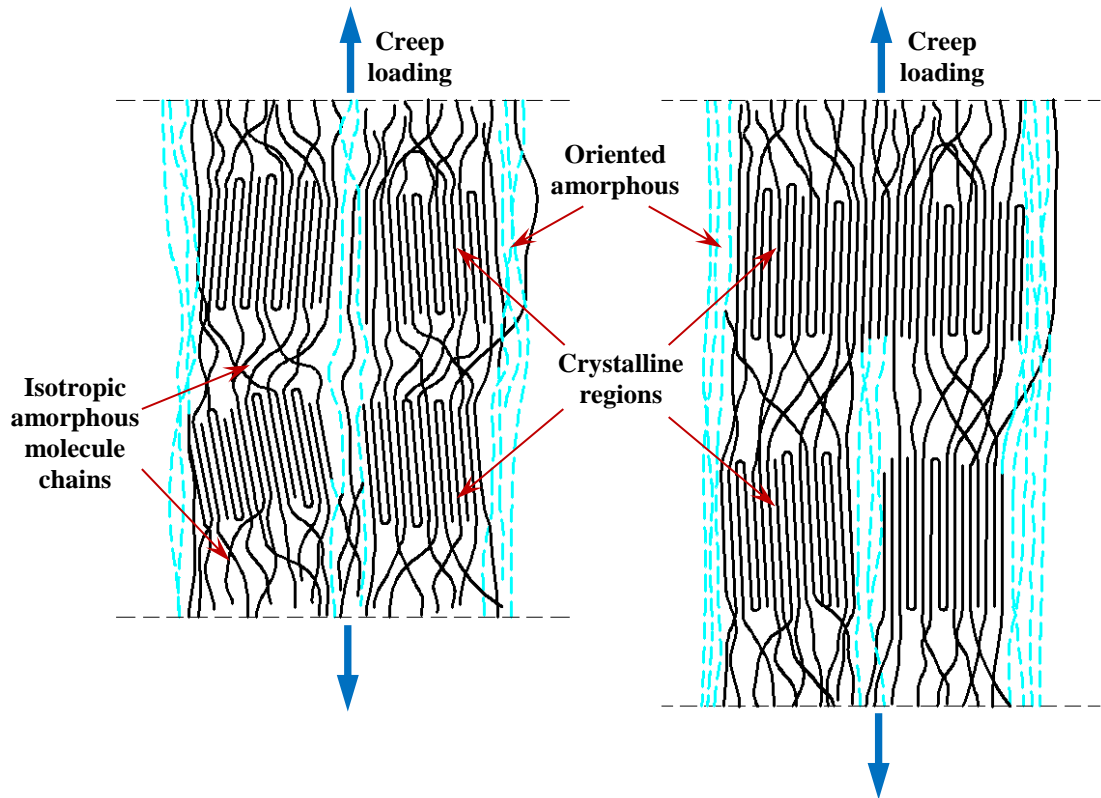


Figure 5-20 Schematic representation of creep deformation within nylon 6,6 fibre. Solid lines in crystalline regions represent both molecular chains and sheets; dashed lines represent TTMs.

Generally, for semi-crystalline polymeric fibre, the instantaneous elastic deformation is mainly determined by the crystalline regions, while the time-dependent viscoelastic deformation is caused by behaviour within the amorphous regions [113, 208]. When nylon 6,6 fibre is subjected to creep stress conditions, both orientation and phase transformation occurs within all three regions, i.e. (i), (ii) and (iii). The increase in crystallinity and $ACS_{(100)}$ from creep stress, as shown in Table 5-5 and Figure 5-19 demonstrates recrystallization; the increase in intensity is attributed to the increase in orientation with creep stress. Since TTMs are considered to control the mechanical properties of polymeric fibres [104, 111], the phase transformation from isotropic amorphous to oriented amorphous ensures the compensation of TTMs through local ordering [151] to provide more potential load carrying molecules when subjected to a higher stress. Following load removal, the full recovery in instantaneous elastic strain infers no creep-induced fracture in the crystalline regions (Section 5.4.2), while the WAXD parameter values show the non-recoverable offset in inter-sheet distances induced by compaction (Section 5.4.9). Since TTMs are in a highly taut state under creep,

the recovery of oriented amorphous regions may dominate the initial recovery stage (< 10 h), i.e. rapid recovery upon load removal. This may explain that as reported in Section 5.4.8, the time-dependent recovery force generated from the 460 MPa and the 590 MPa creep conditions show a relatively higher rate of increase than the 330 MPa for the initial period of ~10 h.

5.4.11 Viscoelastic prestress mechanisms within VPPMCs

The viscoelastic deformation of nylon fibre can be represented by a latch-based mechanical model [97], i.e. time-dependent deformation of fibre may be represented by a number of latches controlled by springs and dashpots connected in series. During creep loading, the latch elements are progressively triggered to store energy, and higher applied stress may result in more sites being activated (Section 5.4.2). This correlates with the impact results as presented in Section 5.4.7 (when up to 460 MPa stress was adopted for a 24 h fibre prestressing). Beyond the 460 MPa however, although stable linear viscoelasticity was observed as shown in Sections 5.4.5 and 5.4.6, there was a decrease in impact benefits from viscoelastic fibre prestressing at the 590 MPa stress condition. This reveals further insights into viscoelastic prestress mechanisms within a VPPMC.

Referring to the microstructural model as presented in Figure 5-20, locations for mechanical energy storage can be considered as consisting of: (i) elastic energy storage sites (EESTs), which determine elastic deformation from the crystalline regions, are fully recovered immediately after load removal up to the 590 MPa creep stress value (Section 5.4.2); (ii) viscoelastic energy storage sites (VESTs), which control the time-dependent viscoelastic deformation in amorphous regions. Hence, as discussed in Section 5.4.9, the increase in crystallinity and $ACS_{(100)}$ with applied creep stress values may be considered to correspond with the increase in the number of EESTs, and reduction in VESTs.

The increase in Charpy impact energy from ~54% to ~79% shows that, though there may be a reduction in the number of VESTs from the 330 MPa to the 460 MPa, more sites are progressively triggered under the higher creep stress of 460 MPa. When subjected to the 590 MPa creep however, since nylon 6,6 yarns are approaching full usage of the energy storage sites under 460 MPa creep, the reduction in prestress benefits (at 590 MPa) may

be caused by: (i) availability of VESTs to store more energy as creep stress increases (a saturation effect) and (ii) VESTs being impeded by interactions caused by increasing molecular orientation (Figure 5-18) and possibly crystallographic changes, i.e. $d_{(010, 110)}$ and other parameters in Table 5-5. Thus (i) and (ii) would also explain the lower value for the viscoelastic recovery force as shown in Figure 5-17. Therefore, there is an optimum creep strain value for VESTs to release the stored energy, to obtain the maximum benefits from viscoelastic fibre prestressing within a VPPMC.

The above discussion also offers a potential explanation to the fact that for the currently used nylon 6,6 fibre, the ~54% increase in impact energy is higher than that from recent published work with nylon-based VPPMCs, i.e. 30-40% [5, 7]. Despite the variation in resin formulation and V_f , the difference in crystallinity between the annealed new and old yarns, i.e. 53% relative to 58% (Section 4.2.2, Table 4-2), may result in fewer VESTs to be available in the old yarn, when subjected to the same creep loading. Moreover, the new yarn has a lower elastic strain value; i.e. 7.96% in ε_i (Table 5-1), as predicted by Equation 3-1, relative to 8.63% for the old yarn [2]. Therefore, the old yarn has more EESTs, providing further evidence for the observed differences in impact energy.

5.5 CONCLUSIONS

To better understand the prestress mechanisms within a VPPMC, the viscoelastic properties of nylon 6,6 fibre under high creep stress values were investigated in this chapter through various testing methods. Charpy impact tests were carried out to determine the effect of viscoelastic creep strain level on impact behaviour of VPPMCs. The main findings include:

- (i) Creep and recovery tests of nylon 6,6 fibre show that elastic strains were fully recovered for the 24 h creep conditions, up to 590 MPa, upon load removal; this indicates there is no creep-induced fracture. Since viscous flow was considered negligible for all the 24 h creep conditions, the viscoelastic prestressing mechanism would not be limited by this.
- (ii) The yield creep strain is determined from creep rupture tests, in which fibre yarns were subjected to 665 MPa creep stress. Yield strain was achieved after 2 h, and quickly led to fracture beyond ~18% creep strain.
- (iii) The ‘true’ modulus of nylon 6,6 fibre is found to be 4.6 ± 0.3 GPa; this was achieved through the use of the Weibull-based function from which the pure elastic strain was predicted.
- (iv) Both creep and corresponding recovery show approximate linear viscoelastic characteristics at large creep deformations, from 330 to 590 MPa creep conditions. From this context, the yield strain of nylon 6,6 is narrowed to ~17.5%, which corresponds to the limit of stable linear viscoelastic behaviour.
- (v) TSSP shows a linear relationship between the stress shift factor, $\log \alpha_\sigma$, and stress, which is applicable to linear viscoelastic solids. Again, stability in long-term linear viscoelastic behaviour is observed; this allows the creep behaviour under 330MPa to be predicted over a large time scale. Thus creep

at 590 MPa for 24 h would be equivalent to 330 MPa creep stress for ~5200 years.

Stress shift factor values are successfully transferred to the recovery strain data, this being equivalent to load removal in the shifted creep master curve; thus yarns would have been stretched with 330 MPa creep stress for $\sim 4.56 \times 10^7$ h. Though this is unrealistic, it does demonstrate a well fitted master curve, from which stable linear viscoelastic recovery behaviour can be inferred.

- (vi) The prestress levels within a VPPMC can be quantitatively represented by the viscoelastic creep strain generated through different creep stress conditions. Charpy impact test results show a limitation in mechanical benefits from prestress effects, when subjected to the highest creep value, i.e. 590 MPa for 24 h. It is suggested that an optimum value exists to maximise the prestress benefits for VPPMC production; this is verified by the recovery force measurements in that, the (intermediate) 460 MPa 24 h creep condition gives the highest recovery force beyond 100 h.
- (vii) Findings from WAXD patterns show that crystallinity increases with creep stress. The deformation in crystalline regions is non-recoverable, i.e. an offset in crystalline spacing is observed; the degree of orientation is also increased.
- (viii) The three-phase microstructural model can be applied to explain the viscoelastic behaviour of nylon fibre; hence a modified creep deformation model is proposed. By considering both the three-phase microstructural model and latch-based mechanical model, a viscoelastic prestress mechanism is proposed. It offers an explanation to the observation that there is an optimum creep strain level to maximise the prestress benefits.

Observation of viscoelastic behaviour of nylon 6,6 fibre shows that the viscoelastic prestressing mechanism would not be limited by viscous flow, and there is no creep-

induced fracture even under the 590 MPa, 24 h creep condition. Charpy impact results demonstrate the effects of viscoelastic creep strain on impact behaviour of VPPMCs. Since the mechanical benefits from viscoelastic prestress is found to be limited by the viscoelastic creep strain level, it is clear that the same strain value can be obtained through higher stresses over shorter time intervals. Therefore, process optimization can be considered to reduce the processing time for VPPMC production, which would benefit potential industrial application. Detailed research of this is covered in Chapter 6.

Chapter 6

TOWARDS OPTIMISATION OF LOAD-TIME CONDITIONS FOR PRODUCING VPPMCS

SUMMARY

This chapter investigates the optimisation of load-time conditions for producing VPPMCs, based on the creep and recovery performance of nylon 6,6 fibre as reported in Chapter 5. The Weibull-based model allows the prediction of viscoelastic creep strain at each creep condition, and this offers opportunities to reduce the processing time for fibre stretching. Since prestress benefits within a VPPMC are determined by the viscoelastic recovery of polymeric fibres, prestress levels can be represented by the viscoelastic creep strain. Therefore, the same prestress level can be attained by employing a higher creep stress over a shorter term, and the standard 24 h creep condition can be reduced to tens of minutes.

The effectiveness of the basic principle was verified through Charpy impact testing. By subjecting the samples to natural aging (up to 0.5 years) or accelerated aging (time-temperature superposition), the short-term and long-term performance of VPPMCs were investigated. Further consideration was given to the optimisation of load-time conditions for VPPMC production.

6.1 INTRODUCTION

VPPMC methodology requires the use of polymeric fibres with appropriate viscoelastic properties. To produce a VPPMC, the fibre stretching and moulding operations are decoupled; i.e. production process involves two stages: (i) polymeric fibres are stretched under a constant load for a period of time so that they undergo viscoelastic creep; (ii) the fibres are released from the load before they are moulded into a resin matrix (e.g. polyester or epoxy resin). This offers great flexibility in VPPMC production. Thus, a creep load can be applied to fibres with relatively simple equipment; then, after the load is released, the fibres can be chopped to any length and placed in any orientation within any mould geometry that is capable of being filled with a matrix resin.

To date however, all VPPMC-based studies at Hull have utilised a creep loading period of 24 h [1-8, 10-12]. This is a convenient period for research purposes, but this length of time would be less practical for VPPMC production in a commercial environment. The purpose of this chapter is to contribute towards process optimisation by significantly reducing the 24 h creep loading period for VPPMC production. Since most of the research to date has involved nylon 6,6 fibres [1, 2, 5-7, 10-12], this is the reinforcing material under investigation. The effect of viscoelastic creep strain levels on the impact behaviour of nylon-based VPPMCs has been investigated in Chapter 5; here, the time required for reaching a specified creep strain was significantly reduced through higher loading conditions. Another potential aspect is longevity. Research has shown there is no deterioration in benefits from prestress in nylon fibre-based VPPMCs under standard (24 h) creep conditions up to the equivalent of 20,000 years at a constant 20°C [98]. However, the long-term performance of optimised creep conditioned samples still needs to be ascertained. This can be achieved by applying the TTSP. A further aspect to be addressed, is to consider optimisation at a creep strain higher than that obtained under the normal 24 h loading conditions, so that fibre prestressing benefits can be maximised.

6.2 PRINCIPLES

6.2.1 Creep time reduction

To reduce the creep time applied to polymeric fibres for VPPMC production, the applied stress must be increased from the ‘standard’ 24 h creep stress of ~ 330 MPa applied to nylon 6,6 fibres [1, 3, 5-8, 10]. Factors to consider are whether a much higher creep stress (i) increases the risk of failure from fibre fracture during the creep cycle and (ii) results in unwanted changes to the fibre properties. It has been demonstrated in Sections 5.4.1 and 5.4.2 that there is no creep-induced fracture in nylon 6,6 fibre even when subjected to 590 MPa for 24 h. Thus, an empirical approach is adopted here to reduce the fibre processing time, and Figure 6-1 illustrates the basic principle.

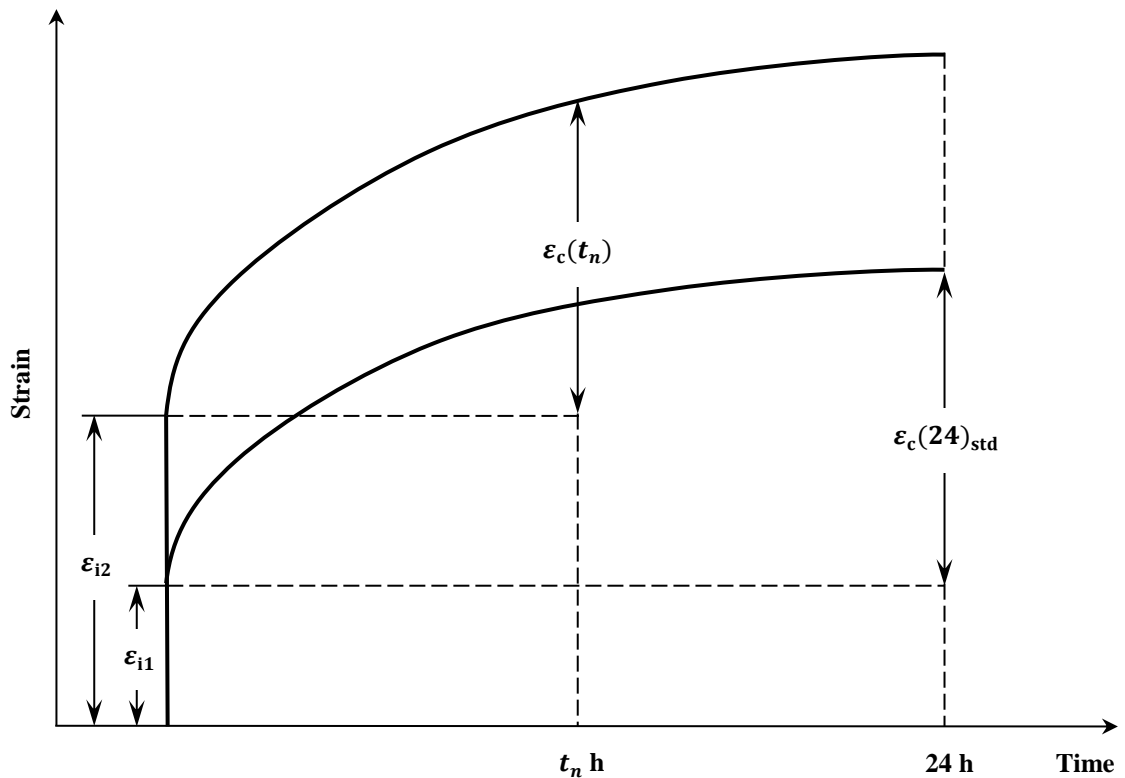


Figure 6-1 Reducing the fibre creep time from 24 h to t_n by equalising the creep strain from a higher stress, $\epsilon_c(t_n)$, with $\epsilon_c(24)_{std}$.

As explained in Section 3.2.2, a creep strain curve can be represented through a Weibull-based equation (Equation 3-1). Therefore, instantaneous strain ϵ_{i1} and the time-dependent strain value $\epsilon_c(24)_{std}$, can be found. Subsequent runs, performed at stress values, σ_n ,

higher than the standard run, are expected to provide strain values by Equation 3-1. The value for $\varepsilon_c(t_n)$ will be equal to $\varepsilon_c(24)_{\text{std}}$, where $t_n < 24$ h; again, $\varepsilon_c(t_n)$ excludes the corresponding instantaneous strain, ε_2 . Therefore, a value for t_n which approaches the shortest practical creep time, t_{min} , can be determined, consistent with other factors (no fibre damage) outlined above. The next step is to compare measurements of recovery strain as a function of time from a run subjected to creep up to t_n , with those obtained from a standard creep run. The expectation is that fitting the data to Equation 3-1 should reveal similar parameter values from both runs.

The final step is to validate the effectiveness of VPPMCs produced under the t_n creep conditions. Since Charpy impact testing has been used for the majority of investigations into the performance of nylon fibre-based VPPMCs [2, 5, 7, 8, 10-12], this is the most appropriate evaluation method. Thus batches of VPPMC samples using t_n can be compared with similar batches produced under standard (24 h) creep conditions, and evaluated through both short-term (natural aging) and long-term (accelerated aging) mechanical performance. Viscoelastic force measurement of nylon 6,6 yarns under t_n creep conditions is also carried out, which may provide useful experimental evidence to support the basic principle.

6.2.2 Time-temperature superposition principle

For long-term mechanical performance, the TTSP concept is utilised. Based on the free volume theory, TTSP is commonly used to generate the master curve for tensile creep [193], flexural creep [209], dynamic tensile modulus [207], stress relaxation [201, 207], or predict the long-term viscoelastic recovery [10] behaviour of polymeric materials. TTSP can be mathematically expressed as:

$$\varepsilon\left(T, \frac{t}{a_T}\right) = \varepsilon(T_0, t_0) \quad (6-1)$$

where, α_T is defined as the temperature shift factor; T_0 is arbitrarily chosen as the reference temperature and T is any other temperature. Each creep strain value $\varepsilon(T, t/\alpha_T)$ has a corresponding value on the master curve $\varepsilon(T_0, t_0)$ at temperature T_0 . According to free volume theory, the viscosity of a material, η , can be related to free-space via the Doolittle equation [198]:

$$\ln \eta = \ln A + B/f \quad (6-2)$$

where, f is the free volume fraction; A and B are material constants. Linear dependence of the free volume fraction on temperature change is addressed with the relation [210]:

$$f = f_0 + a_T(T - T_0) \quad (6-3)$$

where, a_T is the thermal expansion coefficient of the free volume fraction; f_0 is the free volume fraction at reference temperature T_0 . If the time-temperature shift factor is defined as $\alpha_T = \eta(T)/\eta(T_0)$, the ratio of viscosities at two different temperatures, the time-temperature superposition can be given as [210]:

$$\log \frac{\eta(T)}{\eta(T_0)} = \log \alpha_T = -\frac{B}{2.303f_0} \left(\frac{T - T_0}{f_0/a_T + T - T_0} \right) \quad (6-4)$$

This yields the well-known WLF equation when $C_1=B/(2.303f_0)$, $C_2=f_0/a_T$.

The TTSP as shown in Equation 6-4 infers a non-linear relationship between temperature and the shift factor $\log \alpha_T$; however, as discussed in Section 5.4.5, nylon 6,6 fibre shows

approximately linear viscoelasticity within the yield creep strain, so the linear superposition principle holds [197]. This corresponds with the following: (i) Howard and Williams [193] applied the TTSP to the creep of oriented nylon 6,6 fibre under anhydrous conditions when a low range of creep stresses (10-51 MPa) was adopted, and results show that the shift factor $\log \alpha_T$ was linear to temperature; (ii) Murayama et al [201] investigated the applicability of TTSP to the stress relaxation of nylon 6,6 fibre, and a linear relationship between shift factor $\log \alpha_T$ and temperature was obtained; (iii) similarly, a linear curve was also obtained by Dunell et al [207] through the investigation into superposition of stress relaxation and dynamic tensile modulus of nylon 6,6 monofilaments at temperatures between 10° and -100°C; (iv) the linear relationship was also followed with unoriented nylon 6,6 filaments [200] when subjected to small creep strains. Therefore, rather than the non-linear relation as represented in Equation 6-4, a simpler linear TTSP was established for oriented nylon 6,6 fibre, which is based on the published data in terms of creep [193] and stress relaxation [201] as shown in Figure 6-2.

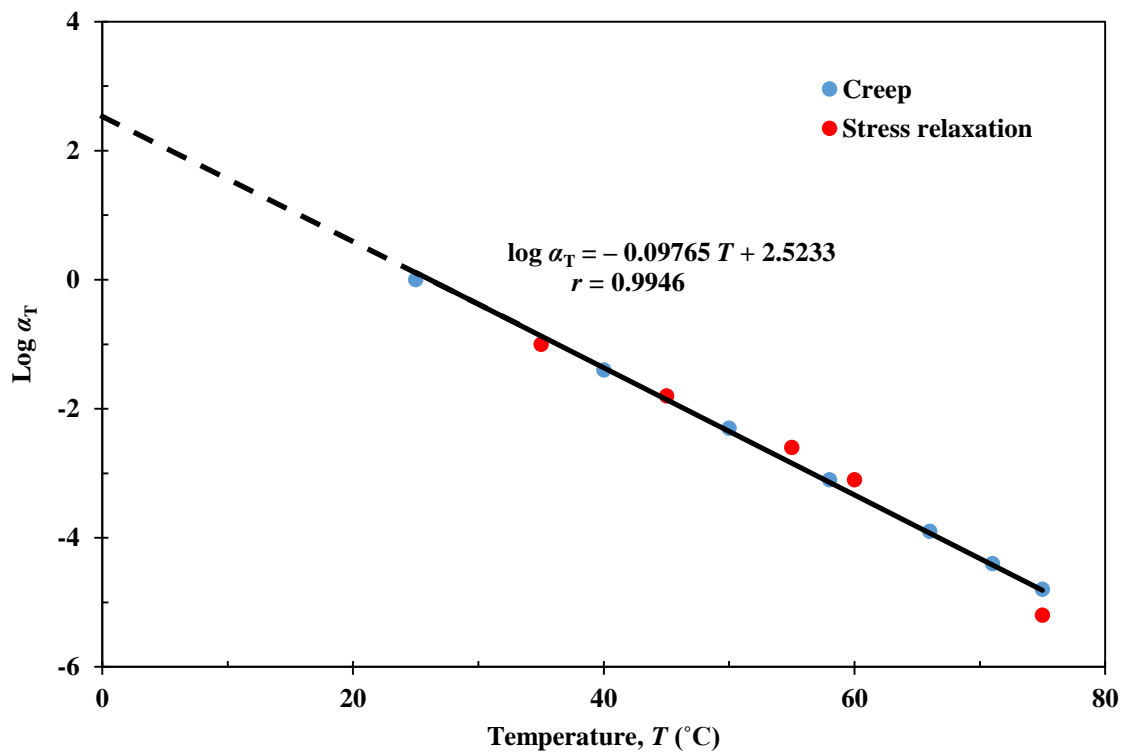


Figure 6-2 Plot to determine the time-temperature shift factor α_T using published data for creep [193] and stress relaxation [201] in nylon 6,6 fibre. Reference temperature was 25°C where $\log \alpha_T = 0$; the solid line and the equation shows the linear regression, and r is the correlation coefficient. Redrawn from [98].

Previous research on nylon 6,6 fibre has shown that viscoelastic recovery is a long-term phenomenon [10]. A further investigation into long-term impact performance through TTSP of standard nylon fibre-based VPPMCs (~330 MPa for 24 h) successfully demonstrated that there is no deterioration in benefits from prestress over an equivalent of 20,000 years at a constant 20°C [98]. Therefore, the TTSP is adopted here to investigate the long-term behaviour of VPPMC samples under t_n creep conditions to determine any potential changes in prestress mechanisms. To transfer an elevated temperature into a time scale shift in terms of free volume, the accelerated aging method from Ref [98] was employed here. Thus, Figure 6-2 shows the relationship between $\log \alpha_T$ and temperature T for nylon 6,6 fibre up to 75°C. A linear regression was fitted to the data points in Ref [98], giving a gradient of $0.09765^\circ\text{C}^{-1}$; this is comparable to 0.093 as determined by Williams and Bender [200] through the investigation of unoriented nylon 6,6 filaments. This enables $\log \alpha_T$ to be determined at 70°C relative to 20°C, and the resulting value is -4.8825. Therefore, viscoelastic activity would be 76,300 times faster at 70°C relative to 20°C; i.e. if samples are subjected to 70°C for 2,298 h, the prestress effect from viscoelastic recovery mechanisms will be aged to an equivalent of 20,000 years at 20°C.

6.3 EXPERIMENTAL PROCEDURES

6.3.1 Creep and recovery

Creep and recovery measurements followed previously described procedures in Section 3.4.2. Here, three 24 h creep loads were selected for detailed assessment, providing stress values of 330, 460 and 590 MPa in which 330 MPa represented the standard creep stress and the highest value (590 MPa) was consistent with avoiding risks of fibre damage as outlined in Sections 5.4.1 and 5.4.2. With these results, $\varepsilon_c(24)_{\text{std}}$ was determined from the 330 MPa creep data and data from the 460 MPa and the 590 MPa enabled the corresponding $\varepsilon_c(t_n)$ values to be obtained using Equation 3-1 and commercially available software, i.e. *CurveExpert 1.4*.

Two further sets of three creep runs were performed, one at the 460 MPa and the other at the 590 MPa, over creep times equal to t_n in each case, to compare the recovery strain-time characteristics with those from the standard 24 h, 330 MPa creep data. Equation 3-2 was used with *CurveExpert 1.4* for this purpose. Since the recovery characteristics might be expected to be similar, any significant deviation between the three data sets may indicate differences in viscoelastic creep-recovery mechanisms.

6.3.2 Preparation and evaluation of composite samples

Composite sample preparation followed the procedures from previous studies [1, 2, 98] as described in Section 3.5.1. A V_f of $\sim 2.0\%$ was adopted for all composite sample production in this chapter. Charpy impact testing of the VPPMC samples followed the procedures as described in Section 3.5.2. Here, impact behaviour was evaluated in terms of: (i) naturally aged short-term impact performance and (ii) long-term impact properties from accelerated aging. For (i), 5 batches of VPPMC samples were produced for each creep condition and were either stored to 336 h (2 weeks) or 4392 h (6 months) at room temperature (19-22°C), and then impact tested. For (ii), samples were stored at room temperature for at least 2 weeks, and then subjected to accelerated aging prior to the impact tests.

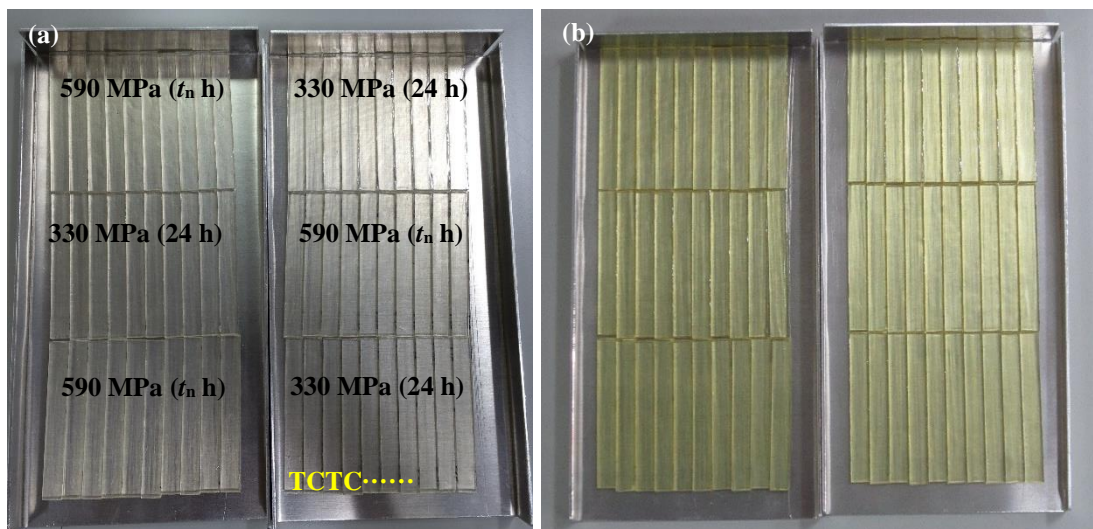


Figure 6-3 Arrangements of samples within a tray (a) before and (b) after being subjected to the accelerated aging. T stands for test sample, and C is the control (non-prestressed) counterpart.

A calibrated fan-assisted oven was used for accelerated aging, with a long-term temperature stability of $\pm 0.3^\circ\text{C}$. Batches of samples with fibres previously subjected to creep at 590 MPa for t_n h were aged, together with the standard VPPMC sample batches for reference. Due to the limitation in capacity of the fan-assisted oven, three batches of VPPMC samples fabricated with each of the two creep conditions were evaluated (i.e. six batches in total). Heating treatment was maintained at a constant 70°C for 2,298 h (3.2 months), which is equivalent to an exposure of 20,000 years at 20°C in terms of viscoelastic recovery within the nylon fibres (Section 6.2.2). Two aluminium trays were used, and each contained three batches (i.e. 15 test and 15 control samples). Samples were placed as a single layer on the tray, and Figure 6-3 (a) shows the arrangements of samples before aging, with individual test and control samples in alternating positions within a batch. This ensured all the batches were subjected to the same heating conditions. After the heating treatment, as shown Figure 6-3 (b), samples were removed from the trays and stored in polythene bags at room temperature for a further 336 h prior to impact tests.

6.3.3 Viscoelastic recovery force

Previous studies into the force output-time characteristics of viscoelastically recovering fibres [3, 4, 99] have provided useful insights into fibre behaviour. In this chapter, recovery force induced by creep loading within the nylon fibre was measured to provide further understanding towards process optimisation of VPPMCs. Procedures followed those previously described, as shown in Section 3.4.3. Here, the generated recovery force from up to t_n creep conditions were evaluated and compared to the standard 24 h creep runs. Since elastic deformation was fully recovered after load removal (Section 5.4.2), the recovery forces induced by the same viscoelastic creep strain, i.e. either from the standard 24 h or t_n h (higher creep stress) runs, were expected to be similar.

6.4 RESULTS AND DISCUSSION

6.4.1 Creep and recovery characteristics

Creep strain-time data from Section 5.4.2 provide a basis for this research. Three creep conditions, i.e. at 330, 460 and 590 MPa creep stress, were selected and their strain-time results are redrawn and shown in Figure 6-4, together with the corresponding recovery data. Using the Weibull-based curve-fits from Equation 3-1, the $\epsilon_c(24)_{std}$ value (330 MPa) was found to be 3.39% (Section 5.4.7). Thus, for $\epsilon_c(t_n)$ to be equal to $\epsilon_c(24)_{std}$ (Section 6.2.1), the t_n values (at ~3.4% strain level) from the 460 MPa and 590 MPa creep data were found to be 92 min and 37 min, respectively.

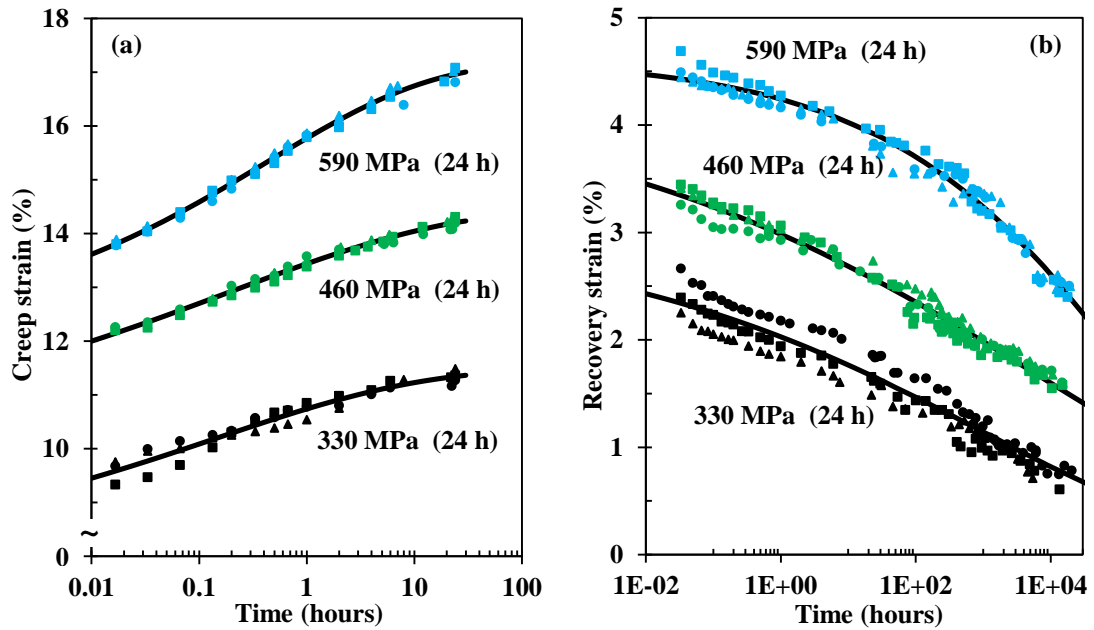


Figure 6-4 Strain-time data for (a) 24 h creep and (b) recovery at the three stress values with curve-fits from Equations 3-1 and 3-2. Redrawn from Figure 5-4.

Creep strain-time data at the 460 MPa and 590 MPa for the corresponding t_n values (92 min and 37 min) are shown in Figure 6-5, with the resulting recovery strain data. The Weibull parameters (Equations 3-1 and 3-2) are also shown in Figure 6-5. Again, it is worth noting that ϵ_f is less than $10^{-4}\%$ in both cases (Section 5.4.2). Subtracting the instantaneous elastic strain, the $\epsilon_c(t_n)$ values for the 460 MPa and 590 MPa were found to be 3.59% and 3.38%, respectively. These values are comparable to the $\epsilon_c(24)_{std}$ value

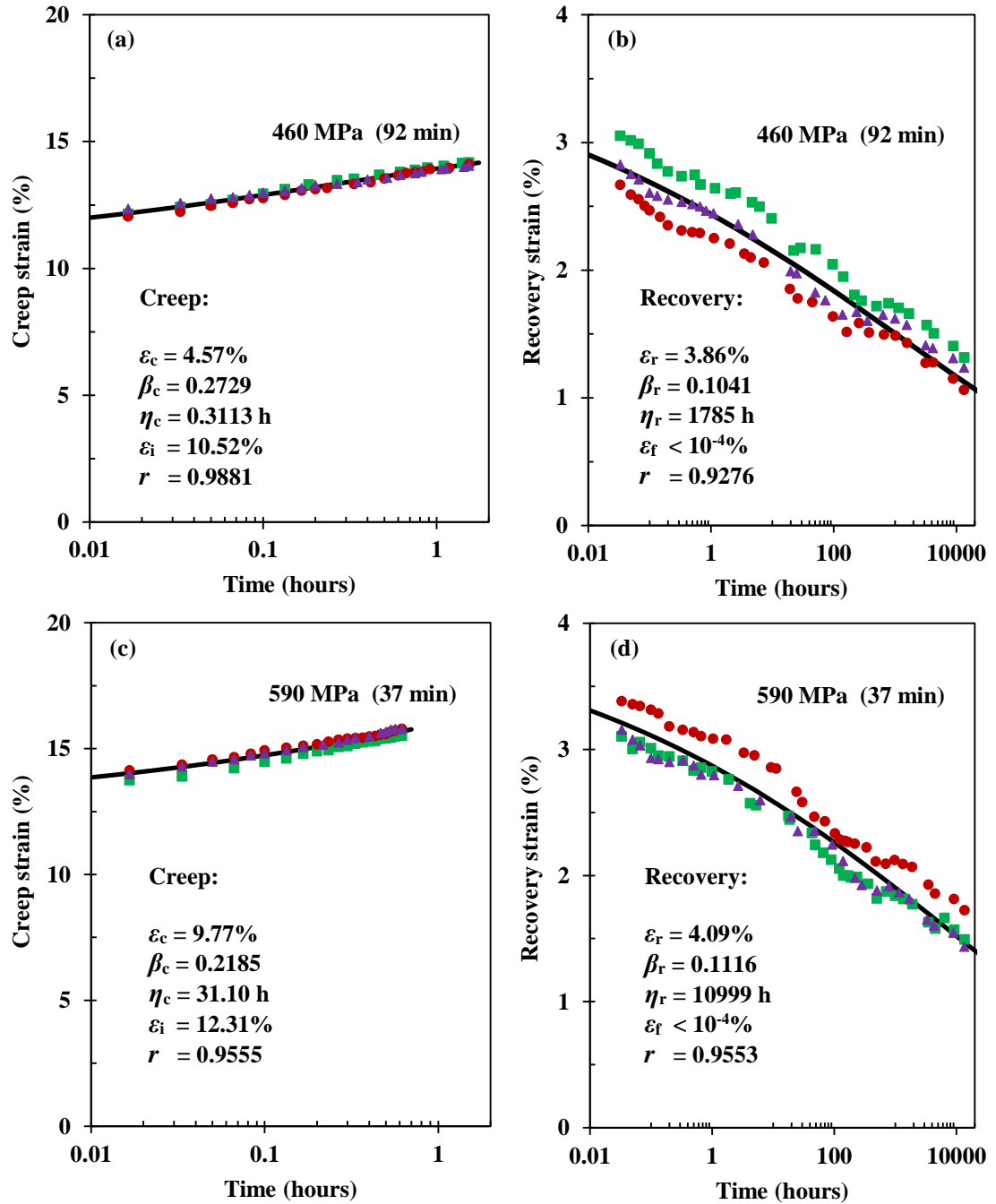


Figure 6-5 Plots of creep strain to values of t_n for 460 MPa and 590 MPa, and the corresponding recovery strain-time data. Curve-fits and associated parameters are from Equations 3-1 and 3-2, as shown in Section 3.2.2.

from 330 MPa (3.39%). The variation can be attributed to experimental uncertainties; in particular, locating the ink marks during measurements on the nylon yarn samples. By comparing the recovery data from 330 MPa in Figure 6-4 (b) with the results in Figure 6-5 (b) and (d), it can be seen that higher creep stress values applied over shorter times increase (slightly) the resulting recovery strain as a function of time. The effect is clarified in Figure 6-6, which shows the fitting curves from Equation 3-2 plotted on common axes, over a much longer timescale. This is in contrast with the suggestion in Section 6.3.1, that the recovery characteristics might be expected to be similar. Since the curves in Figure 6-6 represent recovery data in which viscoelastic creep strain was equalised (Figure 6-1), only the elastic strain components differed between the three creep stress levels. Although ε_i , the elastic strain at the onset of creep, increases with applied stress, the resulting elastic recovery strain, ε_e , should also increase. This is demonstrated by the calculated ε_e values in Figure 6-6 corresponding with the ε_i data in Table 5-1 (Section 5.4.2) and Figure 6-5, to within < 1% strain.

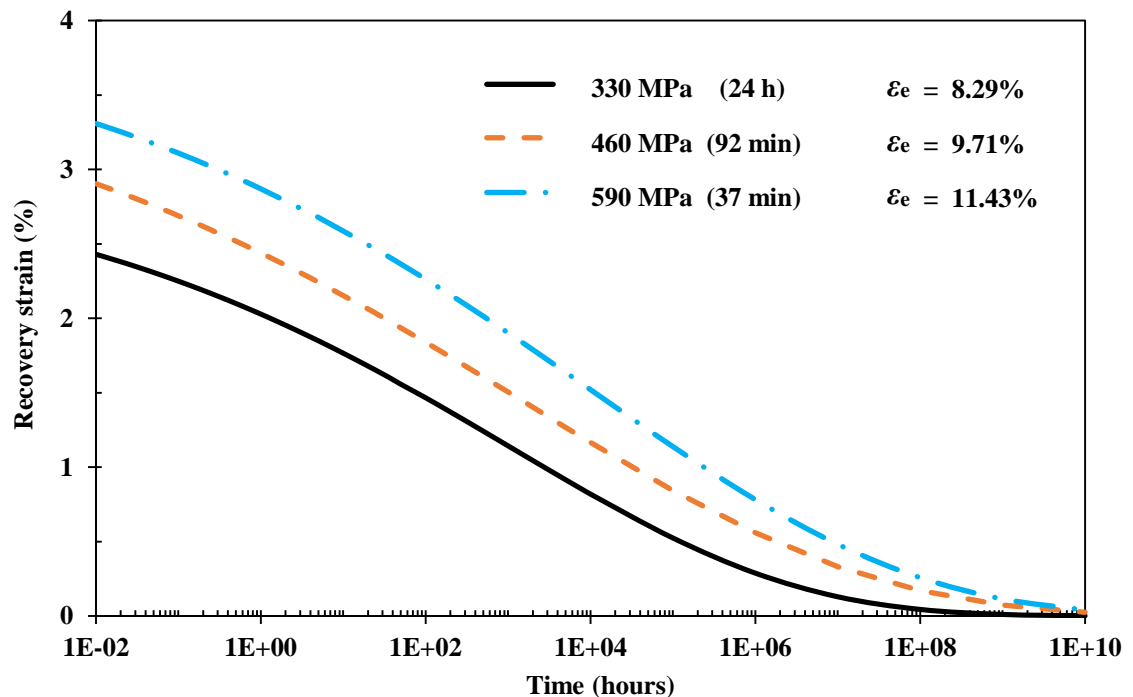


Figure 6-6 Recovery curves from Figures 6-4 and 6-5, using Equation 3-2, plotted on common axes to show their offsets.

The viscoelastic response during creep and recovery can be described by the action of sites triggered, through spring-dashpot time constants, by mechanical latches. On a

molecular level, this can be envisaged as segments of molecules jumping between positions of relative stability [96, 97]. Therefore, when a higher stress is applied, more sites could be triggered earlier during creep, compared with creep applied at 330 MPa over the same timescale, and this allows t_n to be reduced to achieve the same level of viscoelastic creep strain. It also might be expected that some of these sites are only activated at higher creep stress levels (i.e. >330 MPa) and, during recovery, their time-dependent triggering characteristics may be different to those sites activated at 330 MPa. Therefore, this effect may explain the offset between the three recovery curves in Figure 6-6.

6.4.2 Recovery force

As described in Section 6.4.1, to achieve the same $\varepsilon_c(24)_{\text{std}}$ value (330 MPa), the t_n values from the 460 MPa and 590 MPa creep data were found to be 92 min and 37 min respectively. Since both optimised conditions were assumed to provide the same mechanical benefits as VPPMCs (Section 6.2.1), the recovery force with the 590 MPa for 37 min condition was investigated, and compared to the standard creep runs from Figure 4-8 (Section 4.2.4). Two runs were tested for each creep condition (for repeatability), and these were monitored up to 1000 h. The resulting data are shown in Figure 6-7. Although there is variation in the data points, the 590 MPa condition shows a slightly higher recovery rate below 10 h, which corresponds with the findings in Section 5.4.8, i.e. that a higher creep stress would create faster recovery in the initial stages. As discussed in Section 5.4.10, this may be due to the quick response of TTMs upon load removal, which dominates for several hours. Beyond 10 h however, the 590 MPa condition gave slightly lower values of recovery force.

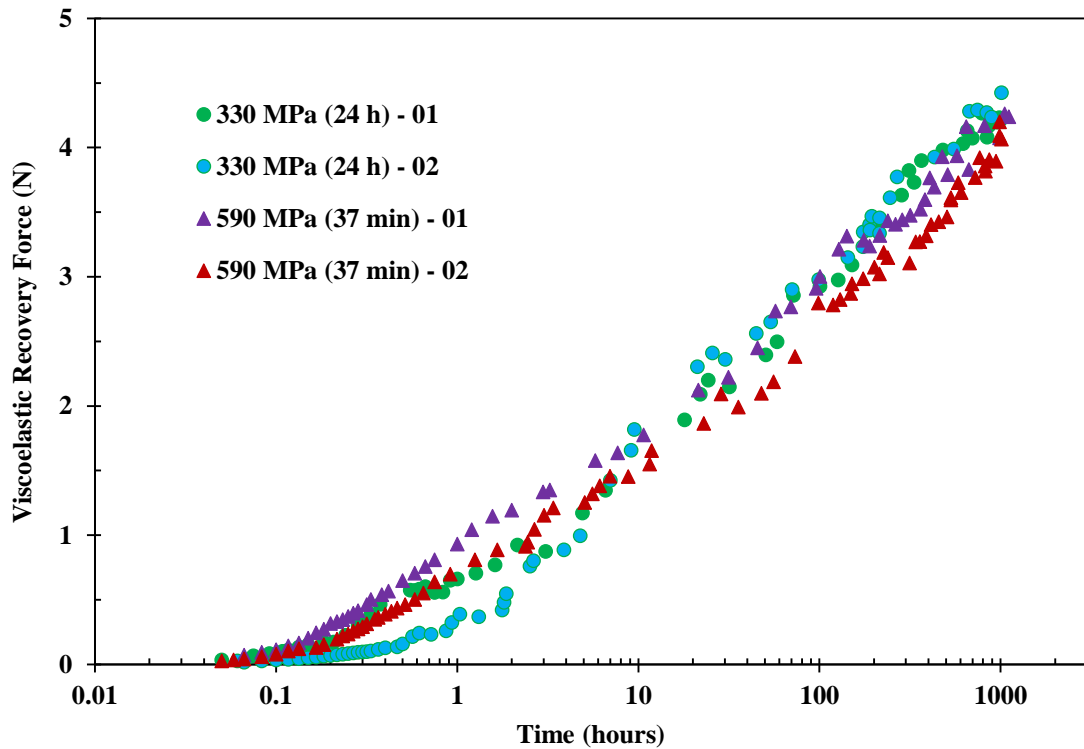


Figure 6-7 Recovery force measurements from nylon 6,6 fibre after being subjected to the standard creep condition (data from Figure 4-16) and the 590 MPa 37 min condition.

The Weibull-based model represented by Equation 3-3 (Section 3.2.3) was fitted to the experimental data as shown in Figure 6-7 and corresponding parameter values are presented in Table 6-1. This enables the prediction of recovery force values at 336 h after creep load removal, which can be expected to directly relate to the absolute value of recovery force within a VPPMC at the same age. The resulting data gives 3.76 ± 0.06 N, and 3.46 ± 0.14 N for 330 MPa and 590 MPa conditions respectively, and two-sided hypothesis testing shows that these two forces are the same at a significance level of 5%. Thus, the recovery force generated from the two creep conditions are equivalent within the limits of experimental error. Therefore, it may be concluded that recovery force from the reduced time creep (up to 590 MPa creep stress) gives a similar value to the standard creep conditions at an equivalent viscoelastic creep strain level.

Table 6-1 Summary of the recovery force parameter values from data in Figure 6-7 using Equation 3-3; r is the correlation coefficient.

Creep condition	Recovery force				r
	σ_v (MPa)	Δt (h)	η (h)	β	
330 MPa-24 h -01	5.2028	0.0414	9.6148	0.3382	0.9989
330 MPa-24 h -02	5.0470	0.1632	59.778	0.3831	0.9968
590 MPa-37 min-01	11.744	0.0676	4135.6	0.1337	0.9989
590 MPa-37 min-02	14.527	0.0751	116460	0.1548	0.9988

6.4.3 Short-term impact performance

Data from the Charpy impact tests are summarised in Table 6-2 and Figure 6-8; also, impact results from the standard batches (330 MPa for 24 h) in Section 5.4.7 are shown for reference. Clearly, there are variations from batch to batch with each creep condition, but the increase in impact energy absorbed is consistent with previous findings from nylon-based VPPMCs [2, 5, 10-12]. The data show little difference in impact energy absorption, either in relative or absolute terms for the three creep conditions. Two-sided hypothesis testing shows no difference between test sample means for the three prestressing conditions at 5% significance level. Therefore, there is no detriment to impact toughness by utilising the 460 MPa or 590 MPa creep stress conditions, compared to the standard 24 h condition. Since the viscoelastic creep strain for the three creep conditions are controlled to be the same (Section 6.4.1), the benefits from prestress can be directly related to the strain levels. This corresponds with Section 5.4.7, in that strain levels affect the mechanical benefits, which can be further explained as: the same strain level in polymeric fibres, i.e. nylon 6,6 fibre within the VPPMC matrix, will generate the same amount of recovery force (Section 6.4.2), to induce a similar amount of stress. Since the VPPMC internal stress is considered to be the main factor that influences the mechanical benefits, the same level of mechanical benefits are therefore obtained.

Table 6-2 Summary of Charpy impact results, tested at 336 h (two weeks) after manufacture. Five sample batches were tested for each prestressing condition (5 test and 5 control samples in each batch); SE is the standard error. Individual test data are presented in Appendix-C, Table C-1.

Batch	Actual age (h)	Mean impact energy (kJ m ⁻²)		Increase in energy (%)
		Test ± SE	Control ± SE	
330 MPa (24 h)	336	33.93 ± 3.14	23.78 ± 1.48	42.64
		37.02 ± 1.78	20.71 ± 0.63	78.76
		35.36 ± 1.71	25.03 ± 0.96	41.26
		36.71 ± 2.89	25.60 ± 1.15	43.37
		35.58 ± 1.96	21.61 ± 1.13	64.69
		Mean ± SE	35.72 ± 0.99	23.35 ± 0.59
460 MPa (92 min)	336	40.35 ± 2.81	25.93 ± 1.16	55.59
		39.42 ± 1.95	24.58 ± 1.05	60.35
		37.82 ± 1.86	23.24 ± 1.13	62.78
		33.87 ± 1.21	21.97 ± 0.85	54.20
		37.37 ± 1.67	22.83 ± 0.42	63.66
		Mean ± SE	37.77 ± 0.92	23.71 ± 0.48
590 MPa (37 min)	336	34.43 ± 3.68	24.62 ± 1.12	39.86
		38.59 ± 2.24	23.31 ± 0.79	65.58
		37.17 ± 4.06	25.00 ± 0.98	48.68
		37.51 ± 1.32	23.56 ± 0.94	59.21
		37.97 ± 2.77	24.27 ± 0.72	56.44
		Mean ± SE	37.14 ± 1.25	24.15 ± 0.40

Figure 6-9 shows typical test and control samples following impact testing. In concurrence with the data, there appear to be no discernible differences in the fracture characteristics between the samples made from the three creep conditions. The greater area of fibre-matrix debonding observed in the test samples is consistent with findings from previous studies of VPPMCs based on nylon 6,6 fibre [2, 5, 7, 10-12]. Although all four mechanisms for mechanical property improvements cited in Section 2.6 may contribute towards increased impact energy absorption in the test samples, mechanism (iv) is the main factor [7]. This mechanism, i.e. residual shear stresses at the fibre–matrix interface regions promoting (energy absorbing) debonding over transverse fracture, explains the larger area of debonding (hence increased energy absorption) seen in the test samples in Figure 6-9.

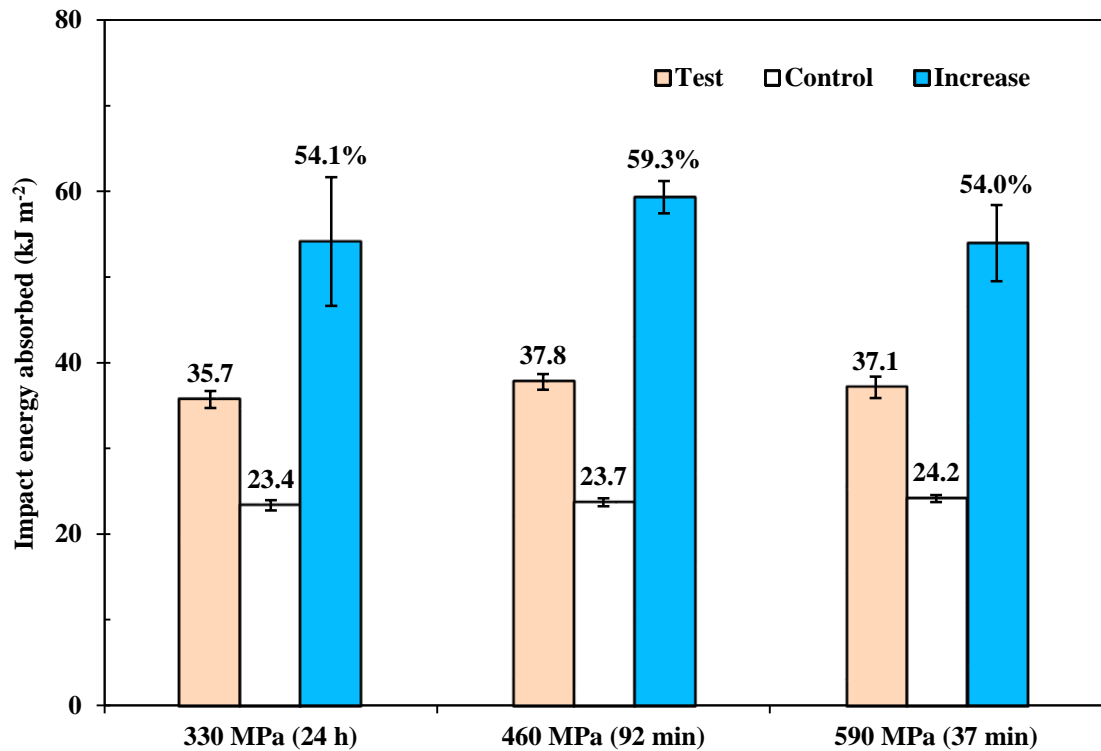


Figure 6-8 Charpy impact test results from Table 6-2; error bars represent the standard error.

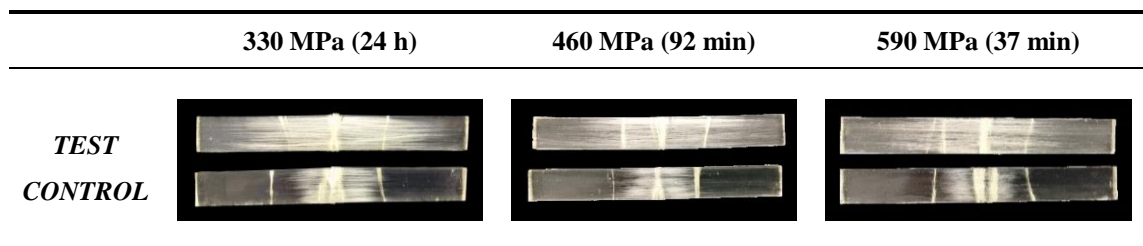


Figure 6-9 Representative test and control samples following Charpy impact testing, showing similar debonding and fracture characteristics from the three creep conditions; note the larger area of fibre-matrix debonding in the test samples.

Since all impact tests were performed on samples at 336 h, the results can be compared with viscoelastic recovery strain data at the same age. From Figure 6-6, the recovery strains at 336 h can be obtained using Equation 3-2, and give approximately 1.3%, 1.7% and 2.1% from recovery at the 330 MPa, 460 MPa and 590 MPa runs respectively. The differences here may be attributed to possible changes in triggering sites during creep (Section 6.4.1). Nevertheless, when these recovery strains are subtracted from their respective ε_r (at $t = 0$) values as shown in Table 5-1 (Section 5.4.2) and Figure 6-5, the resulting elapsed viscoelastic recovery strains (at 336 h) are approximately 1.8% (330

MPa), 2.2% (460 MPa) and 2.0% (590 MPa); i.e. they are similar. As with the similarity in recovery force from the two creep conditions (Figure 6-7), these strain values can be expected to relate directly to viscoelastic creep strain levels in the VPPMC samples at 336 h, and clearly there is concurrence with the Charpy impact test data in Figure 6-8.

Table 6-3 Summary of Charpy impact results, tested at 4392 h (0.5 years) after manufacture. Five sample batches (5 test and 5 control samples in each batch) were tested for each prestressing condition; SE is the standard error. Individual test data are presented in Appendix-C, Table C-2.

Batch	Actual age (h)	Mean impact energy (kJ m ⁻²)		Increase in energy (%)
		Test ± SE	Control ± SE	
330 MPa (24 h)	4392	40.00 ± 2.40	25.77 ± 0.64	55.21
		35.50 ± 3.12	20.32 ± 0.63	74.72
		37.71 ± 1.44	23.43 ± 0.81	60.96
		34.97 ± 3.71	23.13 ± 0.38	51.20
		34.31 ± 3.01	25.05 ± 1.14	36.95
		Mean ± SE	36.50 ± 1.22	23.54 ± 0.47
590 MPa (37 min)	4392	44.14 ± 1.82	25.17 ± 1.27	75.33
		44.26 ± 3.11	24.46 ± 0.50	80.98
		39.76 ± 2.70	25.51 ± 0.69	55.85
		35.34 ± 1.74	23.96 ± 1.78	47.49
		34.06 ± 1.90	22.90 ± 0.35	48.71
		Mean ± SE	39.51 ± 1.24	24.40 ± 0.50

Furthermore, batches of VPPMC samples with their control counterparts were produced and allowed to age in real time to 4392 h (0.5 years). Again, batches corresponding to the 590 MPa, 37 min creep condition were evaluated, together with standard 330 MPa, 24 h batches for reference. Table 6-3 shows the Charpy impact results. Of particular interest, is that the increase in impact energy in both cases is comparable, and this is verified through a two-sided hypothesis test at a significance level of 5%. Therefore, the viscoelastic recovery mechanism from nylon 6,6 fibre within these VPPMCs is still functional, and there is no deterioration in prestress benefits up to 0.5 years in real time, when compared with the data in Table 6-2.

6.4.4 Long-term impact performance

Though viscoelastic recovery force offers an explanation to the internal stress, its long-term behaviour does not necessarily relate to that of a VPPMC, due to possible matrix effects. Thus VPPMC performance was investigated by employing the TTSP. Figure 6-3 (b) shows the samples after accelerated aging. Other than the sample colour, there are no significant differences visually between the batches. Figure 6-4 summarises the Charpy impact results from testing two weeks after the heat treatment. By subjecting the VPPMC samples to accelerated aging, the increase in impact energy absorption shows that viscoelastically generated prestress remains active (at least in terms of time-temperature superposition) for an equivalent of 20,000 years at a constant 20°C with both creep conditions. In concurrence with the previous research on accelerated aging effects on standard VPPMC samples (330 MPa for 24 h) [98], there is no deterioration in increased energy absorption; i.e. as verified through a two-sided hypothesis test (5% level), the mean increase value of $52.81 \pm 3.09\%$ agrees with the impact result ($54.14 \pm 7.52\%$) performed at 336 h after moulding. Compared with the optimised creep condition, i.e. 590 MPa for 37 min, the benefit from prestress is also similar. Again, hypothesis testing shows that the increase of $60.43 \pm 9.52\%$ is not different to $52.81 \pm 3.09\%$ at a 5% significance level.

Table 6-4 Summary of Charpy impact results. Samples were subjected to accelerated aging to an equivalent of 20,000 years at 20°C. Each prestressing condition is represented by three batches, with 5 test and 5 control samples in each batch; SE is the standard error. Individual test data are presented in Appendix-C, Table C-3.

Batch	Exposure to 70°C	Age equivalent @ 20°C	Mean impact energy (kJ m ⁻²)		Increase in energy (%)
			Test ± SE	Control ± SE	
330 MPa (24 h)	2,298	20,000	34.51 ± 2.07	22.30 ± 1.11	54.73
			33.74 ± 1.63	22.99 ± 0.77	46.76
			34.77 ± 2.32	22.15 ± 0.96	56.94
			Mean ± SE	34.34 ± 1.09	22.48 ± 0.52
590 MPa (37 min)	2,298	20,000	31.78 ± 0.81	22.44 ± 0.84	41.64
			32.65 ± 0.20	18.93 ± 0.47	72.47
			35.91 ± 1.74	21.48 ± 0.33	67.18
			Mean ± SE	33.45 ± 0.76	20.95 ± 0.51

6.4.5 Aging effects and the time-temperature boundary

Aging effects on the viscoelastic recovery of nylon fibres within the VPPMCs, in terms of Charpy impact performance, are plotted in Figure 6-10. Here, data is collected from Tables 6-2, 6-3 and 6-4. As verified through hypothesis testing, it is clear that the 590 MPa, 37 min creep condition shows the same increase in absorbed energy as the standard 24 h creep condition (330 MPa), with both natural aging (Section 6.4.3) and accelerated aging (Section 6.4.4). This demonstrates that the same viscoelastic creep level achieved through higher stress (up to 590 MPa) via a shorter term remains active, and there is no deterioration in increased energy absorption in either short-term naturally aged samples to 336 h (2 weeks) and 0.5 years or samples subjected to accelerated aging to an equivalent of 20,000 years at room temperature. Thus, within a VPPMC, nylon fibres pre-tensioned through 590 MPa for 37 min is broadly the same with the 330 MPa, 24 h creep condition, i.e. creep processing time could be reduced from 24 h to tens of minutes by using higher stresses (up to 590 MPa) with no detriment to impact performance.

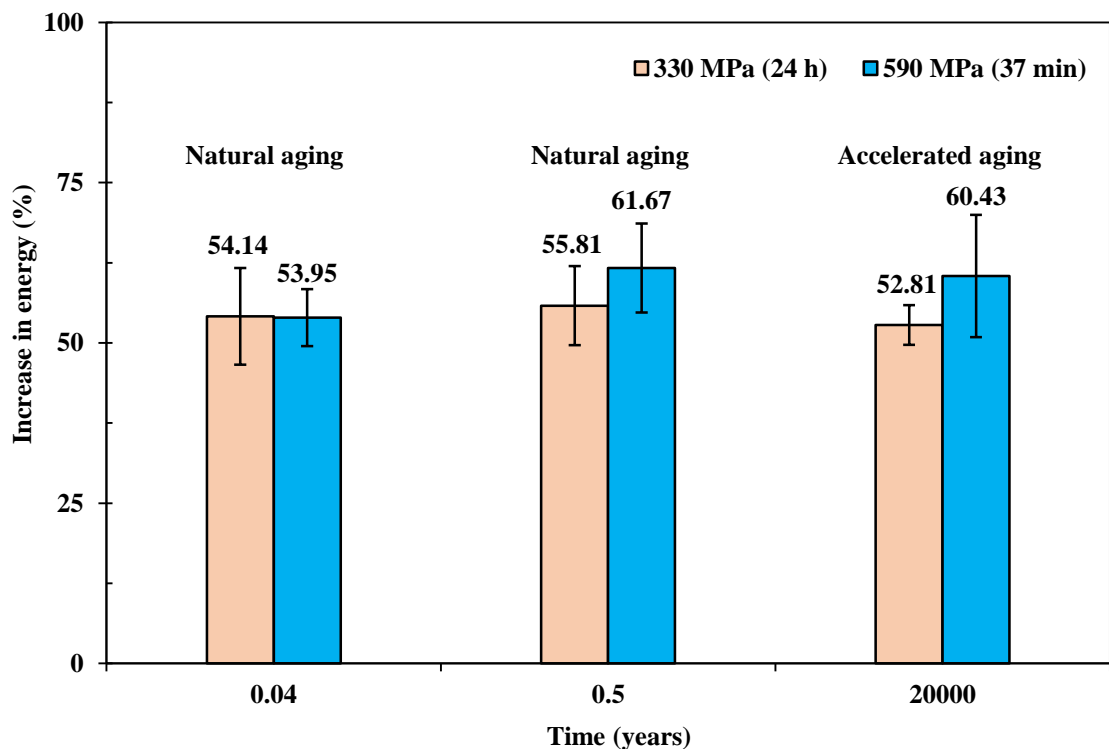


Figure 6-10 Increase in impact energy against time for VPPMC samples produced under the two creep conditions. Data are collected from Tables 6-2, 6-3 and 6-4.

Previous work has shown that recovery effects from subjecting the polymeric fibre to relatively short-term creep (342 MPa for 24 h) can be observed over several decades of time [10]. The above findings demonstrate that the viscoelastic recovery within a VPPMC is a long-term activity. Since viscoelastic activity is temperature-sensitive (so that time-temperature superposition holds) [98], Figure 6-11 shows the time-temperature boundary established in accordance with Figure 6-2 (Section 6.2.2) for nylon 6,6 yarn. Clearly, the increase in ambient temperature will reduce the potential functional life over which VPPMCs are known not to deteriorate. It shows that exposure to 70°C for 2,298 h would be equivalent to ~25 years at 50°C ambient temperature. Hence, for a VPPMC that is produced from creep conditions of 330 MPa for 24 h or 590 MPa for 37 min, the prestress effects can be expected not to deteriorate for at least ~25 years at a constant 50°C. This would lead VPPMCs to many practical industrial applications.

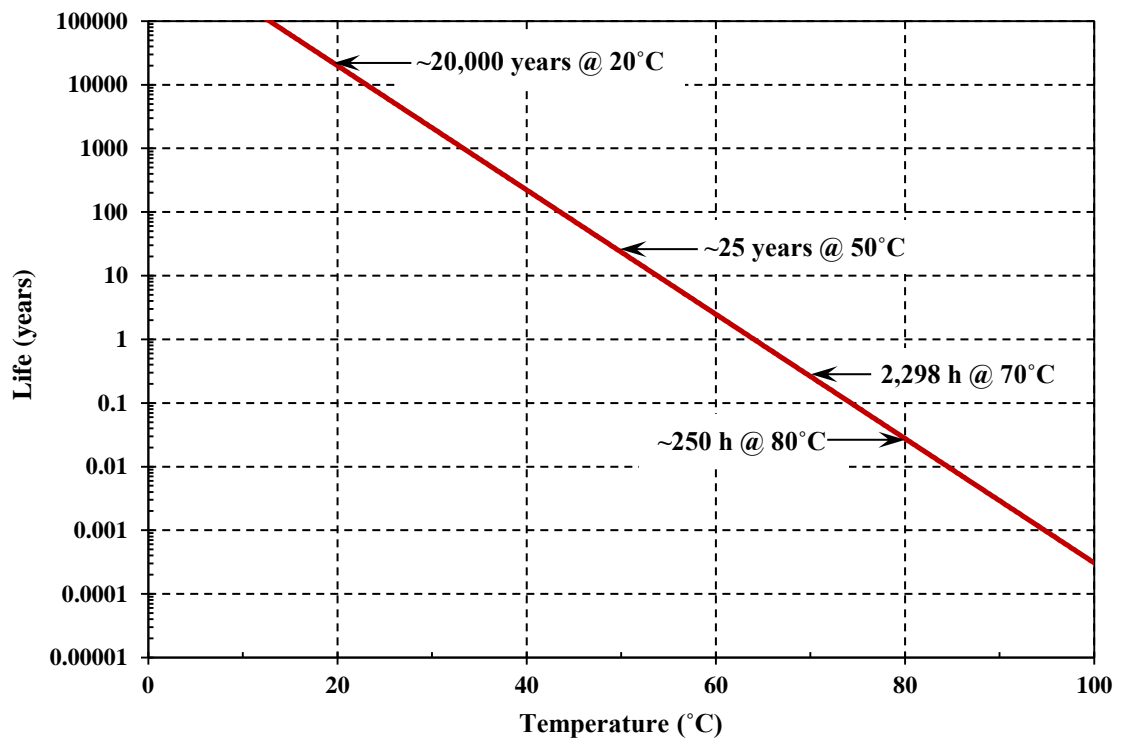


Figure 6-11 Time-temperature boundary established in accordance with Figure 6-2 to an equivalent of 20,000 years at 20°C, showing the reduction in known life with increasing ambient temperature. Redrawn from [98].

6.4.6 Towards optimisation of load-time conditions

As a consequence of the findings from Sections 6.4.3 to 6.4.5, the possibility of a general relationship to obtain the required viscoelastic creep strain level for a range of applied creep stress σ and t_n values can be considered. Though Charpy impact tests were conducted for three creep conditions, the basic principle as illustrated in Figure 6-1 can be applied to the other two creep stress states (395 MPa and 525 MPa) as indicated in Section 5.4.2. Therefore, t_n values from the 395 MPa and 525 MPa creep runs could also be found to provide a more reliable relationship between σ and t_n , and the results are shown in Figure 6-12. Since these load-time conditions are based on subjecting the fibres to 330 MPa for 24 h, all $\epsilon_c(t_n)$ strain values are $\sim 3.4\%$. It indicates a simple logarithmic trend, thus it offers an opportunity to predict the required creep stress for a designated t_n value, i.e. the current line-fit suggests that an increase in applied stress to, for example, 1 GPa, could reduce t_n to within 6 min.

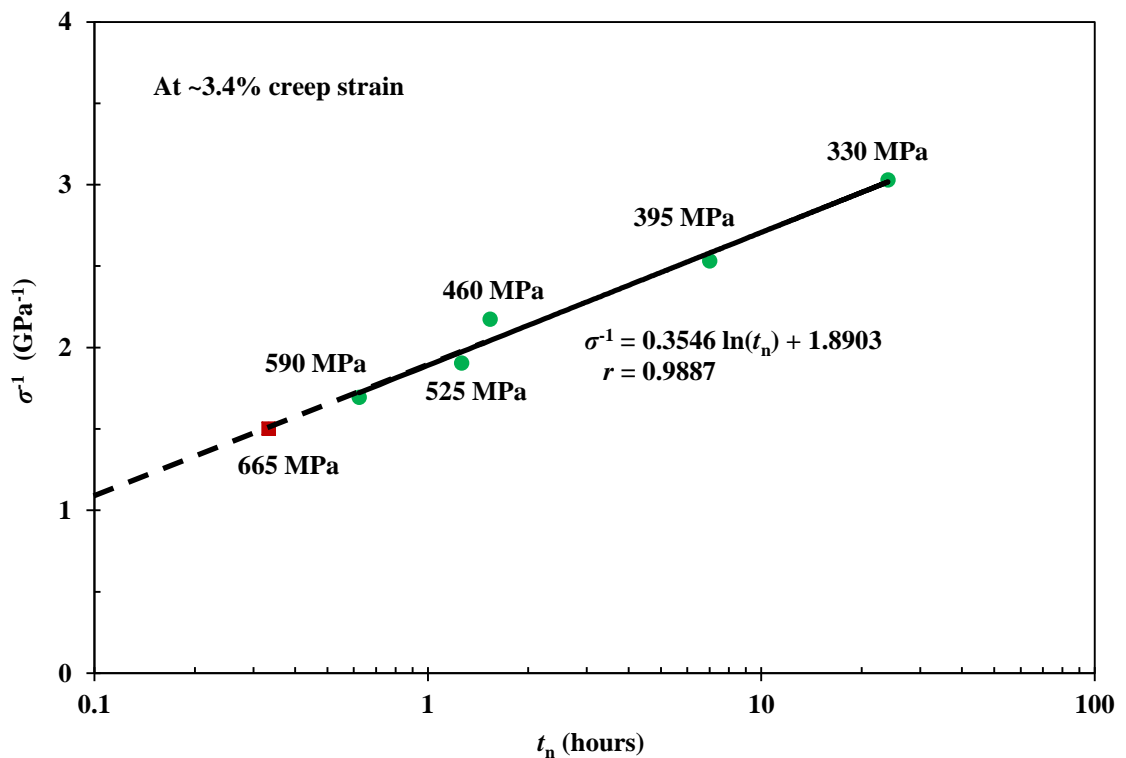


Figure 6-12 Plot showing the relationship between applied creep stress σ and required t_n for loading. Round data points are calculated using the basic principle as shown in Figure 6-1; the square point predicts the creep stress requirement for a stretching period of 20 minutes.

The effectiveness of the trend was experimentally evaluated. This was achieved by selecting a point on the extended dashed line in Figure 6-12. Batches of Charpy impact samples were made with the obtained creep condition, and benefits from prestress were investigated through impact testing. The equation indicates that stress values of 797 MPa and 715 MPa correspond to 10 min and 15 min stretching respectively; however, initial attempts on creep stress under these conditions rapidly led to fibre fracture due to stress concentration effects. Since it is known that nylon fibre could sustain a 665 MPa creep stress for more than 1 h (Section 5.4.3), this value was adopted here, which requires a 20 min stretching time according to the equation shown in Figure 6-12. Thus batches of composite samples were made under these conditions and Table 6-5 shows the impact results, from testing at 336 h (2 weeks) after manufacture. The five batches of samples give an absorbed energy increase of $55.78 \pm 3.77\%$. Two-sided hypothesis testing at 5% significance level shows that the increase is equivalent to the benefits ($54.14 \pm 7.52\%$) from the standard runs (330 MPa for 24 h), as shown in Table 6-2. Referring back to the creep strain-time data with 665 MPa creep stress, as shown in Figure 5-6 (Section 5.4.3), the strain value ϵ_c for $t_n = 20$ min was found to be 3.49%, which is comparable to the $\epsilon_c(24)_{std}$ value at 330 MPa, i.e. 3.39%. Therefore, the results indicate that $\sim 3.4\%$ viscoelastic creep strain would give an increase of $\sim 56\%$ in absorbed impact energy. In terms of industrial application, this improvement in mechanical properties could be achieved within a few minutes of fibre stretching as shown in Figure 6-12, if stress concentration effects can be avoided.

Table 6-5 Charpy impact results for VPPMC samples produced with the creep condition of 665 MPa for 20 min; testing was performed at 336 h after manufacture; SE is the standard error. Individual test data are presented in Appendix-C, Table C-4.

Batch	Actual age (h)	Mean impact energy (kJ m ⁻²)		Increase in energy (%)
		Test \pm SE	Control \pm SE	
665 MPa (20 min)	336	34.74 \pm 1.18	22.54 \pm 1.16	54.14
		37.32 \pm 1.44	24.00 \pm 0.59	55.54
		38.42 \pm 1.78	22.73 \pm 0.45	68.99
		38.74 \pm 2.46	25.03 \pm 0.59	54.79
		34.00 \pm 1.69	23.38 \pm 0.55	45.46
Mean \pm SE		36.65 \pm 0.82	23.53 \pm 0.35	55.78 \pm 3.77

6.4.7 Further optimisation

For the current viscoelastic creep strain levels used in this research, Section 5.4.7 demonstrated that the benefits from viscoelastic prestress was maximised when fibres were subjected to 460 MPa for 24 h, and the $\epsilon_c(24)$ value (460 MPa) was found to be 4.03%. Thus, further optimisation in load-time conditions could be considered, in terms of increasing the prestress benefits by applying the same principle (Section 6.2.1) to a higher viscoelastic creep strain, i.e. $\sim 4.0\%$. Since it is known that nylon 6,6 can sustain a 665 MPa creep stress for more than 1 h (Section 5.4.3), then for $\epsilon_c(t_n)$ equal to $\epsilon_c(24)$ at 460 MPa (Section 6.2.1), the t_n values for creep at 590 MPa and 665 MPa were found to be 134 min and 48 min respectively. Data from corresponding Charpy impact results are summarised in Table 6-6. For reference, batches subjected to 460 MPa for 24 h from Table 5-4 (Section 5.4.7) are also shown.

Table 6-6 Summary of Charpy impact results, tested at 336 h (two weeks) after manufacture. Five sample batches were tested for each prestressing condition with 5 test and 5 control samples in each batch; SE is the standard error. Individual test data are presented in Appendix-C, Table C-4.

Batch	Actual age (h)	Mean impact energy (kJ m ⁻²)		Increase in energy (%)
		Test \pm SE	Control \pm SE	
460 MPa (24 h)	336	39.63 \pm 2.22	24.08 \pm 0.74	64.60
		37.30 \pm 0.54	22.28 \pm 0.88	67.39
		38.57 \pm 1.35	19.46 \pm 0.15	98.21
		39.36 \pm 0.95	22.59 \pm 0.66	74.23
		44.81 \pm 1.86	23.41 \pm 0.59	91.36
		Mean \pm SE	39.93 \pm 0.81	22.36 \pm 0.42
590 MPa (134 min)	336	38.73 \pm 1.76	20.79 \pm 0.62	86.26
		39.38 \pm 1.19	23.18 \pm 0.68	69.90
		38.35 \pm 1.95	23.70 \pm 0.51	61.82
		42.00 \pm 3.15	23.25 \pm 0.74	80.69
		41.75 \pm 3.39	24.06 \pm 1.49	73.53
		Mean \pm SE	40.04 \pm 0.92	22.99 \pm 0.35
665 MPa (48 min)	336	42.07 \pm 4.99	23.91 \pm 0.49	75.95
		43.29 \pm 1.86	23.87 \pm 0.66	81.23
		37.57 \pm 1.53	22.81 \pm 0.60	64.67
		39.29 \pm 2.10	23.66 \pm 0.72	66.05
		44.07 \pm 2.84	25.16 \pm 0.09	75.17
		Mean \pm SE	41.26 \pm 1.30	23.89 \pm 0.28

The resulting mean data from Table 6-6 are shown in Figure 6-13. Again, the optimised conditions are in good agreement with the 24 h creep runs in terms of increase in energy absorption. Although there is a slight reduction in increased impact energy over the three creep conditions, from 79% to 73%, they are not statistically significant; i.e. two-sided hypothesis testing shows that there is no significant difference in absorbed energy increase. Thus, ~4.0% viscoelastic creep strain gives a mean increase in energy absorption of ~75%. Therefore, compared to the strain level at ~3.4% (Section 6.4.3), an 18% increase in viscoelastic creep strain results in a further increase of ~34% in prestress benefits.

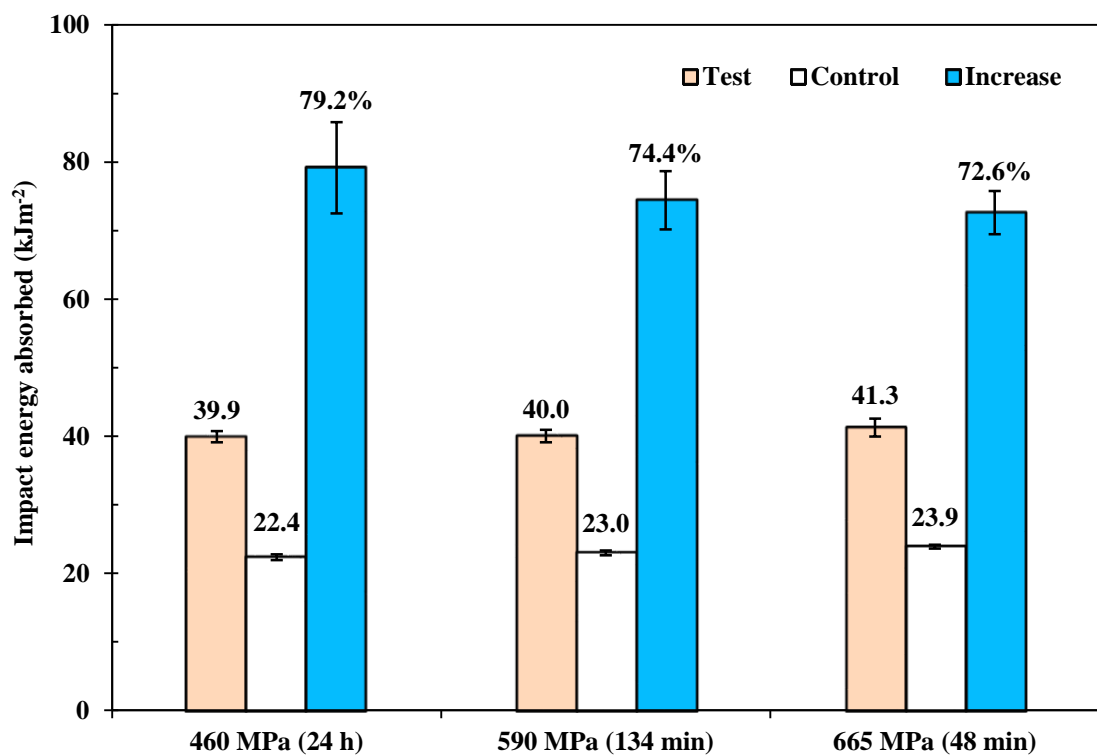


Figure 6-13 Charpy impact test results from Table 6-6; the three creep conditions are equivalent in terms of final viscoelastic creep strain for $\epsilon_c(24)$ at 460 MPa, i.e. ~4.0%; error bars represent the standard error.

A further five batches of VPPMC samples with their control counterparts, produced with the 590 MPa, 134 min creep condition were stored for 4392 h (0.5 years) prior to impact testing to investigate stability in prestress benefits. The results are shown in Table 6-7. Again, all batches show the benefits from viscoelastic prestress. The mean increase of $64.10 \pm 7.66\%$ is statistically the same as the $74.44 \pm 4.24\%$ result in Table 6-6, based on

hypothesis testing at 5% significance level. Therefore, there is no deterioration in impact energy absorption of VPPMC samples at ~4.0% creep strain level for up to 0.5 years in real time.

Table 6-7 Charpy impact results. Fibre yarns were subjected to 590 MPa for 134 min, and tested at 4392 h after fabrication; SE is the standard error. Individual test data are presented in Appendix-C, Table C-2.

Batch	Actual age (h)	Mean impact energy (kJ m ⁻²)		Increase in energy (%)
		Test ± SE	Control ± SE	
590 MPa (134 min)	4392	37.65 ± 2.09	26.05 ± 0.74	44.54
		38.57 ± 2.44	25.14 ± 0.63	53.38
		36.16 ± 3.16	22.82 ± 0.46	58.48
		40.19 ± 3.49	22.09 ± 0.66	81.95
		42.26 ± 4.60	23.20 ± 0.28	82.17
Mean ± SE		38.96 ± 1.21	23.86 ± 0.42	64.10 ± 7.66

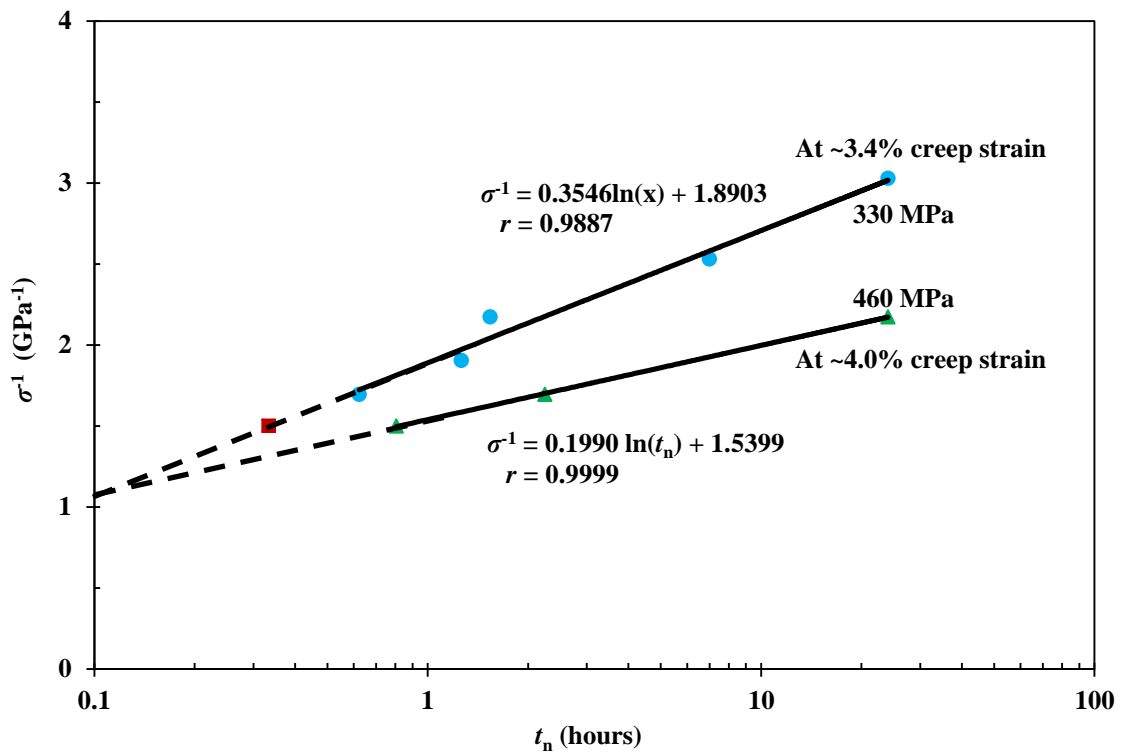


Figure 6-14 Plot showing relationship between applied creep stress σ and required t_n for loading to a level of ~4.0% viscoelastic creep strain ϵ_c , i.e. yarns were stretched under 460 MPa for 24 h. Data points were calculated using the basic principle as shown in Figure 6-1.

Using the principles described in Section 6.4.6, optimisation of load-time conditions at a creep strain level of ~4.0% could be constructed, and the relationship between applied

stress σ and t_n is shown in Figure 6-14, together with the curve at $\sim 3.4\%$ strain level from Figure 6-12. Again, a logarithmic trend is well fitted to the data points. It shows that the two curve-fits meet each other at ~ 0.1 h and, as this is beyond the fibre breaking strength (700-900 MPa [10]), the logarithmic relationships must become invalid.

6.4.8 Prestress mechanisms

The effect of prestress performed in Section 5.4.7 have shown a decrease in benefits when fibres are subjected to 590 MPa for 24 h, i.e. $\sim 4.8\%$ in creep strain. At lower creep strains however, this chapter demonstrates that the same viscoelastic creep strain level would generate equivalent mechanical benefits within a VPPMC, which was verified by exploiting various creep stress (up to 665 MPa) conditions to obtain the same $\varepsilon(t_n)$ value. Here, two creep strain levels were adopted in accordance with the findings from Section 5.4.7. Thus a $\sim 3.4\%$ (Section 6.4.3) strain level represents the standard creep condition (330 MPa for 24 h) and $\sim 4.0\%$ (Section 6.4.7) represents the strain when the greatest mechanical benefits were observed for all the prestress conditions under investigation. For $\sim 3.4\%$, the near optimised creep condition, i.e. 590 MPa for 37 min, impact performance is broadly the same as the standard VPPMC samples (330 MPa for 24 h). Also, there is no detriment to impact behaviour in samples either naturally aged to 0.5 years or artificially aged to an equivalent (in terms of TTSP) of 20,000 years at a constant 20°C ambient temperature. Confirmation of performance at a creep strain level of $\sim 4.0\%$ is obtained, by evaluating the impact performance of VPPMC samples up to 0.5 years in real time.

These findings further promote understanding of the viscoelastic prestress mechanisms within VPPMCs as proposed in Section 5.4.11. For example, the 590 MPa creep conditions in Figure 6-15 show the increase in impact energy from samples tested at 336 h (two weeks), as a function of creep time. Time-dependent viscoelastic deformation is controlled by the amorphous regions [113, 208]. Thus, VESTs (Section 5.4.11) are progressively triggered to store energy through longer exposure to the same creep stress (590 MPa). However, as the creep stretching progresses over longer periods, an optimum level for prestress benefits from stored energy releasing was observed. As discussed in Section 5.4.11, this may be attributed to (i) availability of VESTs to store more energy as

creep time increases under a constant creep stress (a saturation effect) and (ii) VESTs being impeded by interactions caused by increasing molecular orientation and possibly crystallographic changes. Thus effectively, increasing the creep stress or increasing the creep time have similar effects on VESTs, as demonstrated by Section 5.4.7 (stress) and Figure 6-15 (time).

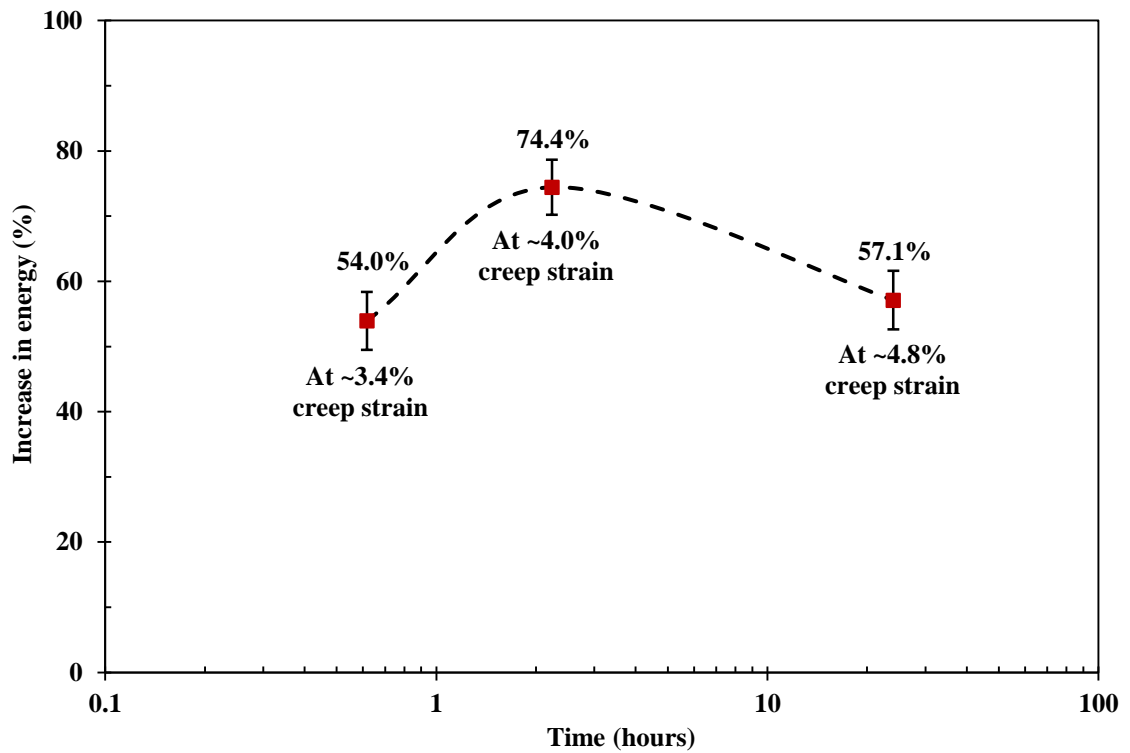


Figure 6-15 Summary of increase in impact energy from samples tested at 336 h (two weeks), a creep stress of 590 MPa was adopted for all runs. Various creep strain levels were achieved through longer exposure to creep loading; i.e. 37 min for ~3.4%, 134 min for ~4.0% and 24 h for 4.8%. Data were collected from Tables 5-4, 6-2, and 6-6.

6.5 CONCLUSIONS

This chapter has taken the first steps towards process optimisation by investigating the feasibility of reducing the creep loading period for VPPMC production. By using nylon 6,6 fibres, the main findings include:

- (i) The previously adopted viscoelastic creep strain, i.e. ~3.4%, which requires a tensile stress of 330 MPa for 24 h, can be achieved over a shorter duration, t_n , using higher stress. Thus t_n is 92 min at 460 MPa and 37 min at 590 MPa.
- (ii) Although there is some offset between viscoelastic recovery strain–time curves from the three creep settings at ~3.4% viscoelastic creep strain level, the elapsed recovery strain values are similar. Recovery force measurements carried out with two creep conditions, i.e. 330 MPa for 24 h and 590 MPa for 37 min, show good agreement in terms of the magnitude of generated recovery force.
- (iii) Charpy impact test data from VPPMC samples corresponding to the three creep settings (at ~3.4% viscoelastic creep strain level) show similar effects in short-term (up to 0.5 years in real time) impact performance; i.e. there is no significant difference in impact energy absorption, giving a mean increase of ~56% compared to their control (non-prestressed) counterparts. This concurs with corresponding recovery force measurements.
- (iv) By using TTSP, the long-term impact performance of VPPMC samples were evaluated through accelerated aging to an equivalent of 20,000 years at a constant 20°C. Results show that the viscoelastic recovery within the composites remains active, and there is no deterioration in impact benefits from fibre prestressing at a viscoelastic creep strain level of ~3.4% for both 330 MPa, 24 h and 590 MPa, 37 min creep conditions.
- (v) A relationship between applied creep stress σ and t_n has been established (at ~3.4% viscoelastic creep strain level), and a logarithmic trend is observed.

This allows prediction of the t_n value required for a given σ . The effectiveness of the trend was verified through Charpy impact tests, i.e. the mean increase in energy absorption of VPPMC samples produced through 665 MPa for 20 min was 55.78% which is comparable with ~56% for the 24 h runs. Subject to avoiding fibre damage however, it may be possible to reduce t_n further.

- (vi) Longer exposure of nylon 6,6 yarns to a higher strain level could increase the viscoelastic prestress-induced mechanical benefits. At ~4.0% viscoelastic creep strain for example, 24 h of creep at 460 MPa can be achieved through 665 MPa for 48 min, and Charpy testing gives a ~75% increase in impact energy. Compared to the ~3.4% strain level, this 18% increase in viscoelastic creep strain results in a ~34% increase in prestress benefits, and there is no deterioration in prestress benefits up to 0.5 years at real time.
- (vii) The increase in impact energy from VPPMC samples is found to be a function of creep time at a constant creep stress (590 MPa). There is an optimum creep processing time (i.e. creep strain level) to maximise the prestress benefits. This is analogous to the influence from increasing the creep stress for a constant (24 h) creep period. Thus, the prestress mechanisms as proposed in Section 5.4.11 are still valid.

Based on these findings, the fibre processing time can be reduced by exploiting a higher fibre creep stress over a shorter term. Charpy impact tests show that at ~3.4% viscoelastic creep strain, fibres subjected to 590 MPa for 37 min give broadly the same VPPMC impact benefits as the standard 24 creep condition, and there is no deterioration in these benefits with long-term performance, i.e. to an equivalent of 20,000 years at a constant 20°C when employing the well-known TTSP. Mechanical benefits from viscoelastic fibre prestressing could be improved through longer exposure of fibres to a higher creep stress level with no detriment to impact toughness, and this has been verified here for up to 0.5 years in real time. Therefore, the full potential from fibre prestressing effects has been approached. This promotes a further step in VPPMC technology towards potential industrial application.

Chapter 7

MORPHING (BISTABLE) COMPOSITES BASED ON VISCOELASTICALLY GENERATED PRESTRESS

SUMMARY

In this chapter, a novel form of shape-changing bistable structure was successfully developed through the use of viscoelastically generated prestress. Bistability was achieved through pairs of deflecting VPPMC strips, orientated to give opposing cylindrical configurations within a thin, flexible resin-impregnated fibreglass sheet. This arrangement enabled the structure to ‘snap through’ between one of two states due to external stimulation. Deflection from the VPPMC strips occurred through compressive stresses generated from the non-uniform spatial distribution of nylon 6,6 fibres undergoing viscoelastic recovery.

Snap-through behaviour of the bistable structure was investigated both experimentally and through modelling. The effects of loading speed, loading geometry, and sample-age on the snap-through properties were presented through experimental investigations. A feasibility study of finite element analysis was carried out to investigate the development of bistability, and the influence of modulus ratio on the snap-through characteristics. Experimental and numerical simulation results showed good agreement with the snap-through behaviour of the bistable structure. From these observations, a possible snap-through mechanism was proposed.

7.1 INTRODUCTION

Morphing structures have received increasing interest in recent years, since they offer opportunities to improve aerodynamic performance and functionality without the need for increased mass and complex construction over a wide range of flight conditions. For example, morphing aerofoils can enable camber and twist changes without conventional actuation mechanisms [211]. Briefly, as reported in Section 2.8, morphing structures can be produced through: (i) thermally induced residual stresses in un-symmetric laminates [69, 120, 121, 125, 126, 128, 132, 133, 212, 213] (Section 2.8.1) and (ii) elastically induced prestress in symmetric laminates [71, 211] or beam structures [72, 73] (Section 2.8.2). However, both methods can be problematic in some aspects. For (i), residual stress generated from thermal expansion mismatch within a non-symmetrical multi-layer laminate is highly susceptible to hygrothermal variability [132], thus it is difficult to exploit thermal effects [211]. For (ii), potential drawbacks arise in terms of complex composite production methods [17, 71], and potential deterioration in prestress levels in a long-term duration [2], as subsequently observed by Mostafa et al [88].

The benefits of VPPMC technology (Section 2.6) could be applied to morphing structures. This chapter provides the details of fabrication and evaluation of a mechanically bistable morphing composite structure, based on the use of fibres for viscoelastically produced prestressing. Snap-through behaviour was investigated through both experimental and numerical simulation.

7.2 PRINCIPLE

To create a simple bistable structure, four identical VPPMC strips can be bonded to a thin, flexible resin-impregnated fibreglass sheet, as shown schematically in Figure 7-1. The cross-sectional spatial density of fibres (such as nylon 6,6) used for producing the prestress in a VPPMC strip is normally non-uniform, due to the use of open casting. This

arises from fibres settling towards the bottom of the mould prior to curing taking place [1, 2, 98]. As described by Timoshenko [192], the critical load P_{cl} for the generation of elastic buckling (beam bending) from an eccentrically compressed column can be calculated through Euler's formula:

$$P_{cl} = \frac{\pi^2 EI}{4L^2} \quad (7-1)$$

where, E is the Young's modulus; I is the second moment of area, which is $(bh^3/12)$ for a rectangular beam of width b and thickness h ; L is the beam length. Therefore, beyond the critical stress, the resulting non-uniform stress distribution created through the thickness of a thin flat strip can be expected to cause bending, to give a mid-span deflection, δ , in Figure 7-1. If a VPPMC strip is considered in isolation, δ can be associated with the prestressed beam relationship [214]:

$$\delta = \frac{PeL^2}{8EI} \quad (7-2)$$

here, P is the force generated from the prestress. The distance between beam and fibre centroids, e , can be estimated from the cross-sectional spatial density of fibres in a composite strip sample. As shown in Figure 7-1, the upper and lower strips are oriented to deflect in opposite directions, giving opposing cylindrical configurations within the structure. Therefore, the whole assembly should be capable of demonstrating bistability.

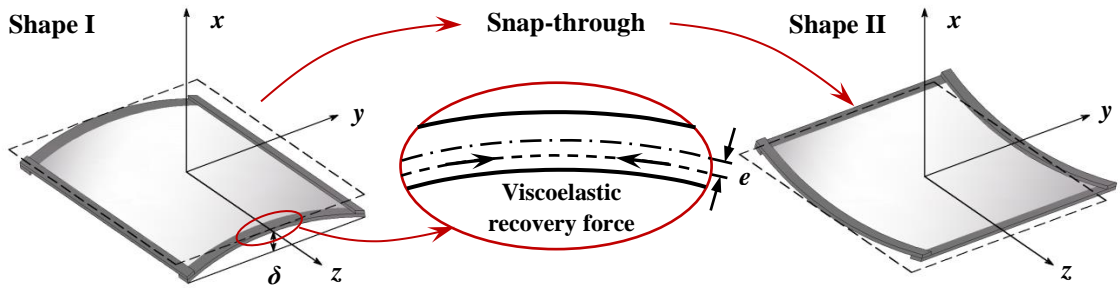


Figure 7-1 Schematic representation of bistable VPPMC principles, showing the VPPMC assembled structure in both states (Shapes I and II) and also the prestress-generated deflection δ in accordance with Equation 7-2.

For a situation where a simple concrete beam is prestressed by steel rods which occupy a relatively small proportion of the total beam volume, Equation 7-2 should be capable of giving realistic predictions [215]. For the current work however, the assumption that E in Equation 7-2 can be represented by the matrix modulus alone may be unrealistic. This arises from (i) the nylon fibres occupying a significant proportion of the total beam volume and (ii) the addition of the resin-impregnated fibreglass sheet. Thus a more appropriate value for E in Equation 7-2 might be obtained by measuring the deflection from a representative composite beam. From the conventional three-point beam-bending relationship [192], the flexural modulus $E(t)$ can be determined from deflection $\delta(t)$ at the centre of the beam at time t using:

$$E(t) = \frac{FL^3}{48\delta(t)I} \quad (7-3)$$

where F is the load applied at the centre of the beam. By measuring $\delta(t)$, when $t = 5$ s, the result for $E(t)$ from a beam, where $h \ll L$, is close to the true elastic modulus [1, 4]. Therefore, Equation 7-3 may be used to obtain a more realistic E value for Equation 7-2.

7.3 EXPERIMENTAL PROCEDURES

7.3.1 Production of VPPMC strips

Production of the VPPMC strips followed the procedures in Section 3.5.1 and the main points are outlined here. The same materials, i.e. nylon 6,6 fibre (Section 3.1.1) and Reichold Polylyte 32032 polyester resin (Section 4.3) were used. As ~ 330 MPa is the most widely used stress to generate the creep preloading [1, 2, 7, 10, 11, 98, 99], annealed fibre yarns were subjected to a 330 MPa tensile creep stress for 24 h under ambient conditions (20-21°C, 30-40% RH). The creep load was subsequently released and the yarn was folded, cut into ~ 500 mm lengths and brushed into flat ribbons ready for moulding.

VPPMC strips were open-cast in two aluminium moulds using the same resin mix, and the process was completed within 0.5 h following the fibre stretching procedure. Each mould had a polished channel that was 10 mm wide and 1 mm deep, for casting a 450 mm strip of composite. Based on the total cross-sectional area of fibres, relative to the strip cross-sectional area, the average (macroscopic) V_f was $\sim 18\%$. The two composite strips were removed from the moulds after ~ 2 h and each strip was cut into two 200 mm lengths to provide the four individual VPPMC strip samples.

7.3.2 Production of the bistable composite structure

To produce a bistable composite assembly, a 200×200 mm square fibreglass tissue, with an areal density of 30 gm⁻² was used. First, the tissue was impregnated, by hand lay-up, with the same resin used in Section 7.3.1. Based on weight measurements, the fibreglass volume fraction (V_{GF}) was 3.2%. Following resin curing, after ~ 24 h, two of the 200 mm VPPMC strips (Section 7.3.1) were bonded to each side of the fibreglass layer. The assembled composite sample was then held under a weighted solid plate for a further ~ 48 h. For repeatability purposes, three of these VPPMC-based ‘test’ samples were produced and stored at $20 \pm 2^\circ\text{C}$ for subsequent evaluation. As facilities were limited to producing one sample at a time, there was some slight variation in sample age on subsequent testing.

During hand lay-up and curing, the fibreglass layer was placed on mould release film. Therefore, the side in contact with the film surface had a smooth finish while the opposite side had a comparatively rough surface. Cylindrical shapes with this smooth resin layer on the outside convex surface are denoted as Shape I, while the smooth layer on the inside concave surface are denoted as Shape II.

A ‘control’ sample of the composite assembly was also required, this being structurally identical to the VPPMC-based test samples, but with the 24 h fibre stretching stage omitted. Instead, the annealed yarn at this stage was stored under the same ambient conditions for 24 h, prior to composite production. Therefore, the control sample provided a reference to determine whether other production-based stresses might be significant.

7.3.3 Evaluation of the bistable composite assembly

The three test assemblies were evaluated in terms of (i) static and (ii) dynamic characteristics. For (i), since the recovery force generated from viscoelasticity is time-dependent [99], this has a direct effect on sample deflection through Equation 7-2. Hence the static (stable) deflection at the centre of each bistable assembly was monitored with time, this being associated with δ in Figure 7-1 and Equation 7-2. Nevertheless, since δ was measured for the assembled structure, i.e. the sum of the VPPMC strip thickness and fibreglass-resin sheet, some caution was required (as discussed in Section 7.2) when considering the applicability of Equation 7-2. This led to the production and evaluation of separate composite strips, as described in Section 7.3.4.

For (ii), a Lloyd Instruments EZ-50 testing machine with a 2.5 N load cell was used for dynamic (snap-through) evaluation of the bistable samples. Each test sample was supported on a rigid three-point bending jig as illustrated in Figure 7-2, and a jig span of 190 mm allowed the supports to be centred on the VPPMC strips at the sample edges. Bending was achieved using two different (solid) indenters as schematically shown in Figure 7-2 (a) and (b).

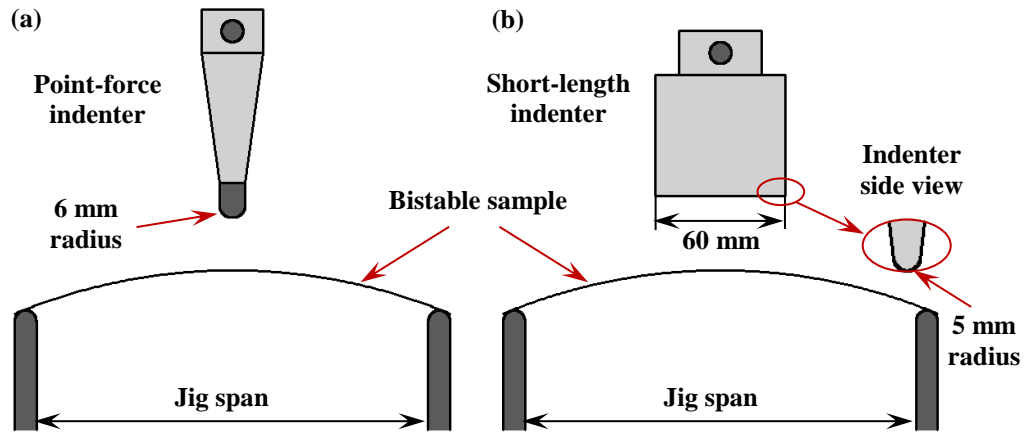


Figure 7-2 Schematic three point bending set-up used to evaluate the snap-through characteristics of the VPPMC-based test samples: (a) is the point-force indenter; (b) is the short-length indenter.

Three bistable samples were each tested three times to give a total of nine readings in each snap-through direction. They were evaluated for: (i) snap-through response from different loading speeds; (ii) snap-through response from different indenter geometry; (iii) short-term aging effects. For (i), two test speeds were used, slow (6 mm/min) and fast (60 mm/min). For (ii), two types of indenter were used to provide point-force and short-length force loading. Point-force loading was achieved by using a round indenter with a 6 mm nose radius; short-length loading was performed with a 60 mm length, 5 mm nose radius indenter as shown in Figure 7-2. To investigate (iii), the same samples were tested at two different ages. The first evaluations were made after the samples had been stored for 350-650 h; these samples were then stored (at $20 \pm 2^\circ\text{C}$) for a longer period and re-evaluated at 3800-4100 h.

7.3.4 Evaluation of beam deflection

To determine a more representative value for E in Equation 7-2, a simple three-point bending test was required, from which Equation 7-3 could be used to evaluate $E(t)$. This was achieved through the open casting of four nylon fibre-resin control strips (i.e. no prestress), each 200 mm in length, followed the experimental procedures described in Section 7.3.1. A 10 mm wide strip of resin-impregnated fibreglass tissue with V_{GF} of 3.2% (Section 7.3.2) was then bonded to the isolated control strips (Section 7.3.1) to produce beam-shaped samples representing the cross-sectional structure of the bistable assemblies. Optical microscopy (Section 3.5.4) was also adopted to evaluate the fibre

spatial distribution to estimate e for Equation 7-2. Following sample storage for ~350 h, three-point bending tests were performed on each beam sample to determine the elastic modulus value.

The three-point bending test followed the procedures and experimental set-up as described in Section 3.5.3. In particular, each beam sample was mounted horizontally, with the fibreglass layer facing downwards, as this represented the bending orientation created through prestress in the main VPPMC-based test (bistable) samples. To achieve deflections comparable to those observed in the bistable samples, a load of 1.2 N was adopted. Deflections were measured at 20-21°C on each sample just once and a video recording of the deflection in progress was made, to improve measurement accuracy.

As a further consideration for beam deflection analysis, prestressed strips were also produced as described above; these consisted of (i) four VPPMC strips, each with a 10 mm wide fibreglass layer, and (ii) four VPPMC strips, with no fibreglass layer. These were stored for ~350 h and δ was measured to enable direct comparison with predictions from Equation 7-2.

7.4 FINITE ELEMENT METHOD

7.4.1 Principle

Finite element (FE) analysis offers an approximate solution to realistic types of structures. To further understand the deformation mechanisms of the VPPMC-based bistable morphing composite structure, it is necessary to apply FE to the nonlinear response from snap-through and determine the equilibrium configurations. Thus, FE modelling was used to supplement the experimental study and offers further insight into the snap-through mechanisms from bistability.

The simulation of viscoelastic prestress was achieved by exploring a predefined temperature change in the fibre material. It is well-known that during cooling down

following high temperature curing in composite production, thermal residual stresses will be generated due to the mismatch in thermal expansion coefficients between the constituent materials [17, 36, 37]. Hence, in a FE model, the force can be generated by employing temperature change on the embedded fibre material with a constant thermal coefficient [71, 85]. Since recovery force inside a VPPMC sample has been measured through experimental procedures [99], the magnitude of the recovery force can be represented by the thermal induced force within a model, to induce deflection, as shown in Figure 7-1.

7.4.2 Material properties

As discussed in Section 7.3.4, isolated composite control strips were made to evaluate the deflection; the dimensions of a typical sample were measured to be 9.89 ± 0.01 mm in width and 1.10 ± 0.02 mm in thickness. A further batch of 4 cured fibreglass strips were made following the procedures described in Section 7.3.2, to determine the thickness of the mid-fibreglass layer within a bistable assembly, which was found to be 0.40 ± 0.03 mm. The mechanical properties of the materials involved here are listed in Table 7-1. The thermal expansion coefficient of nylon fibre was needed to model thermal residual stresses, for representing viscoelastic recovery force, as generated from fibre prestressing (Section 7.4.1).

Table 7-1 Mechanical properties of the materials involved in the bistable assembly.

	Nylon 6,6 fibre [145]	Polyester resin [1, 216]	E-glass fibre fabric [35]
Density, ρ (g/cm ³)	1.14	1.12	2.55
Young's modulus, E (GPa)	3.3	3.3	72
Poisson's ratio, ν	0.41	0.40	0.25
Thermal expansion coefficient, α (°C ⁻¹)	90×10^{-6}	--	--

Since the glass fibre layer was very thin (~0.40 mm), it was not realistic to measure the elastic modulus through three-point bending tests in Section 7.3.4. Thus a predictive model was considered to determine the stiffness. Normally, for randomly oriented two

phase fibre composites, an expression similar to the ‘rule of mixtures’ for the effective modulus E_{RO} can be utilised as follows [194]:

$$E_{RO} = kE_fV_f + E_mV_m \quad (7-4)$$

where, k is a fibre efficiency parameter which depends on V_f and the E_f/E_m ratio; this is usually between 0.1 to 0.6. For a two-dimensional (in plane) random orientation of fibres, it has been demonstrated that k is $3/8$ [194].

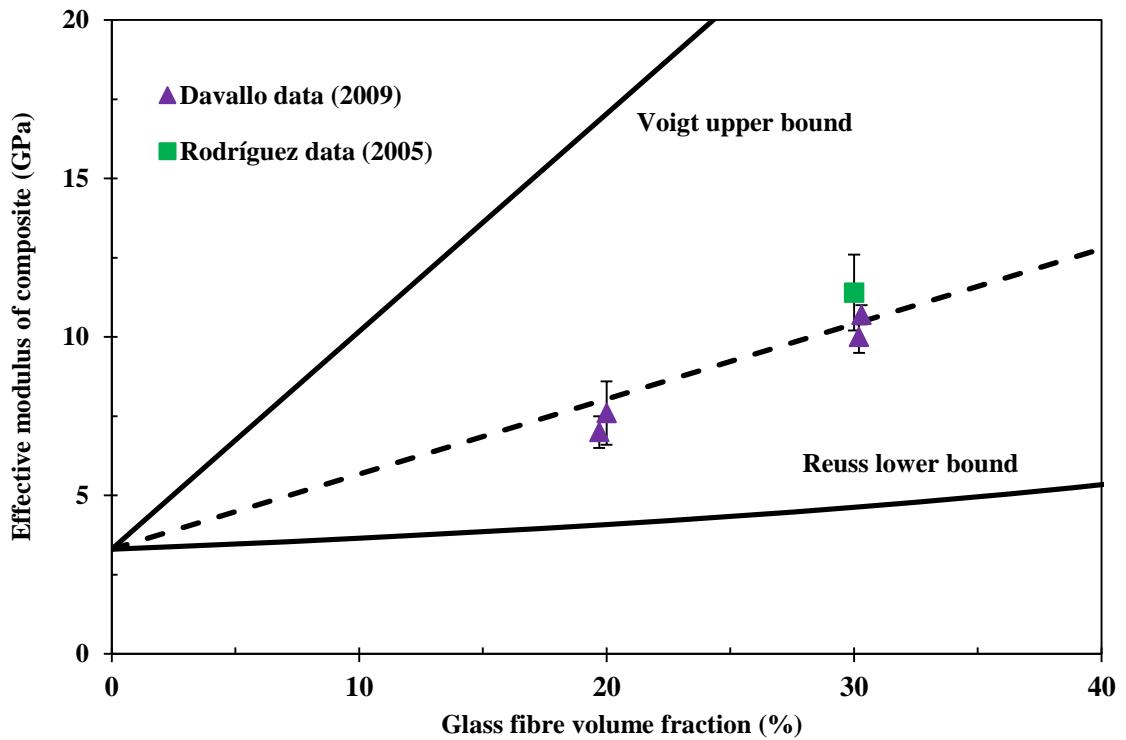


Figure 7-3 Effective modulus of glass fibre mat reinforced polyester resin composite as a function of fibre volume fraction. The dashed line was from Equation 7-4 with $k = 3/8$; the black solid lines were fitted with the ‘rule of mixtures’ relationships (Section 2.2).

To determine the effectiveness of Equation 7-4, it was evaluated for glass fibre mat reinforced PMCs. With the material properties listed in Table 7-1, the effective modulus of glass fibre mat reinforced PMC is plotted in Figure 7-3 as a function of fibre volume fraction, together with the upper and lower bounds from the ‘rule of mixtures’ (Section 2.2), and the experimental data were from Refs [217, 218]. Good agreement was found

between predicted values from Equation 7-4 with $k = 3/8$ and data from the published work. Thus, the effective modulus of the fibreglass layer in the bistable structure was calculated using Equation 7-4 with $k = 3/8$ and found to be 4.06 GPa.

7.4.3 FE model

For the FE study, numerical simulation analysis was developed to identify the structural response of the bistable assembly and the possible effect of various factors on the sample configuration. To simulate the bistable morphing structure as illustrated in Figure 7-1, the model consists of four identical $200 \times 10 \times 1$ mm strips with 18% V_f and a $200 \times 200 \times 0.4$ mm fibreglass layer (Section 7.4.2). As previous research shows that fibres settle towards the bottom of the mould [1, 2, 98], fibres were set to be 0.2 mm away from the beam centroids, and constrained within the matrix utilising the ‘embedded region’ method. This value was also verified through optical microscopy in Section 7.5.2. Strips were bonded on the edges of the fibreglass layer through ‘tie’ constraints and numbered as ‘X1’, ‘X2’, ‘Y1’, ‘Y2’, with strips ‘X1’ and ‘X2’ placed on Z- side of the layer, and strips ‘Y1’, ‘Y2’ on Z+ side as presented in Figure 7-4.

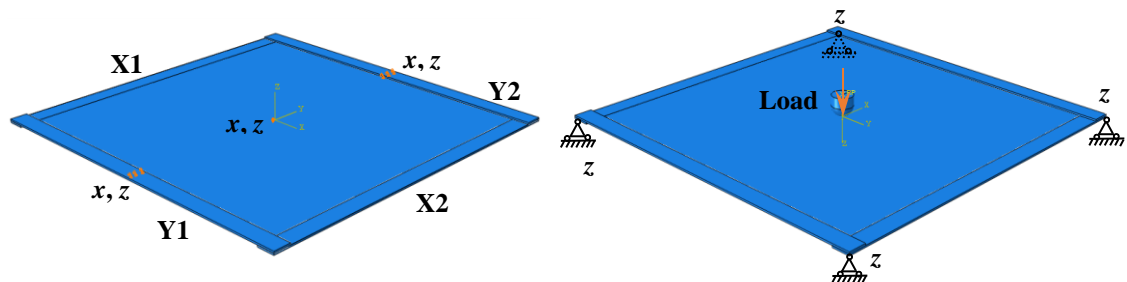


Figure 7-4 Boundary and loading conditions on the plate: (a) constraints applied in Step-1; (b) constraints applied in Step-2.

The analysis was performed using the follows: T3D2 elements (a 2-node linear 3-D truss) on fibres, C3D8R elements (an 8-node linear brick, reduced integration, hourglass control) on VPPMC strips, and S4R elements (4-node general purpose reduced integration shell elements) on mid-shell. Geometrically nonlinear algorithms ‘NLGEOM’ were conducted. The ‘stabilize’ function was used in the model to minimise the instabilities [70, 219] with a damping factor of 1×10^{-6} . Element size used for the shell

was 5×5 mm, and $5 \times 1 \times 0.2$ mm on the strips, which gave a total element number of 9,600. The snap-through model developed in this research consisted of three steps:

Step-1: Generation of the prestress within a composite;

Step-2: Snap-through response of the bistable structure when loaded;

Step-3: Recovery of the structure after snap-through.

In Step-1, since recovery force inside a VPPMC sample was measured through experimental procedures [99], a certain viscoelastic recovery force may be represented through the cooling down of a polymeric fibre with a given thermal expansion coefficient. As fibres are constrained within the composite, compressive stresses in the matrix are generated through the fibre-matrix interface. Since the peak curing temperature of the resin used in this study was monitored to be only 27.9°C (Section 4.4.1), any thermal residual stress induced by resin curing was neglected in the FE analysis. Step-2 was achieved through applying displacement to an indenter with 6 mm radius to simulate the point-force indenter as illustrated in Figure 7-2, at a velocity of 60 mm/min. ‘Analytical rigid’ was employed to simulate the indenter. This does not require meshes, so it can reduce the simulation period and minimize mesh-dependent snap-through load [220]. In Step-3, the loading was removed to enable the model to recover freely.

The constrained translational degrees of freedom applied to the plate in different steps are shown in Figure 7-4. No rotational constraints are applied to the panel. To calibrate the effectiveness of the model solution, the experimental snap-through process of the bistable assembly with sample age of ~ 500 h, loaded with the point-force indenter (Section 7.3.3) at 60 mm/min was chosen as the reference. Numerical simulation results were compared with the experimental data to determine the model significance. Then, development of the snap-through process and effect of modulus ratio on snap-through behaviour were carried out based on the adjusted model solution. The results were subsequently analysed to establish the mechanism of bistability for the proposed bistable structure.

7.5 RESULTS AND DISCUSSION

7.5.1 Static evaluation of the bistable structure

Figure 7-5 shows one of the typical VPPMC-based test (bistable) samples in comparison with the control sample. The test sample with curved surface is shown in one of the two stable shapes, i.e. Shape II as described in Section 7.3.2. It is clear that the control sample is flat, signifying that there were no other production-based residual stresses of any significance. Therefore, it may be concluded that deflection from the test sample is generated entirely through viscoelastic fibre prestressing.

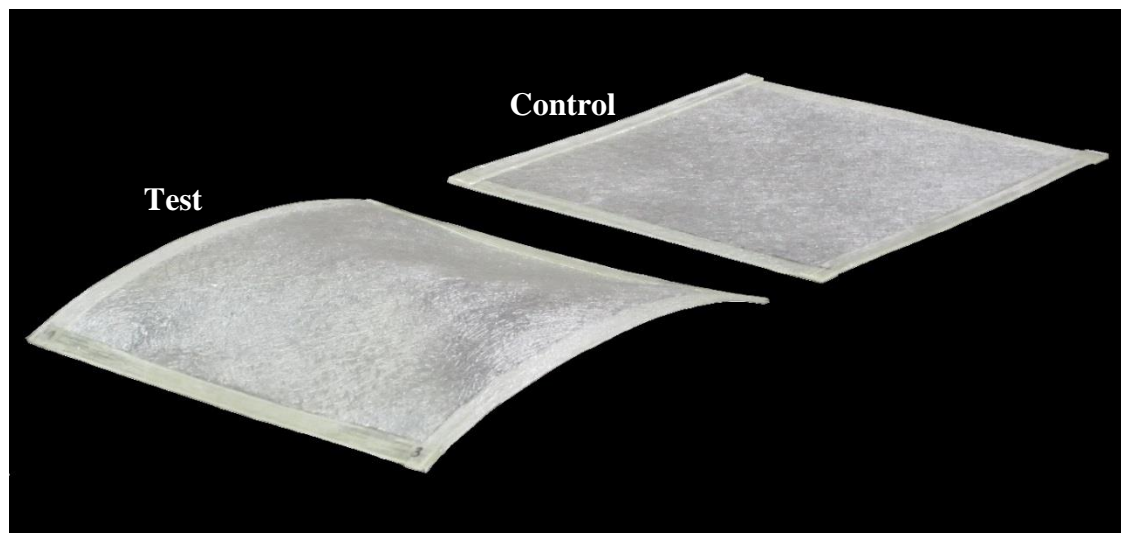


Figure 7-5 An assembled VPPMC-based bistable sample (test), compared with the equivalent control (non-prestressed) sample.

The static deflections were measured with time and the results are shown in Figure 7-6. The dashed curve shows the trend. Each data point is based on two readings, i.e. one reading from each stable state, the data point markers representing the three test samples. The stated deflection δ (\pm standard error) of 11.6 ± 0.4 mm, was the mean from all three samples at ~ 500 h. After a further storage to ~ 4000 h sample age, these measurements were repeated, and the deflection had increased to 15.2 ± 0.5 mm.

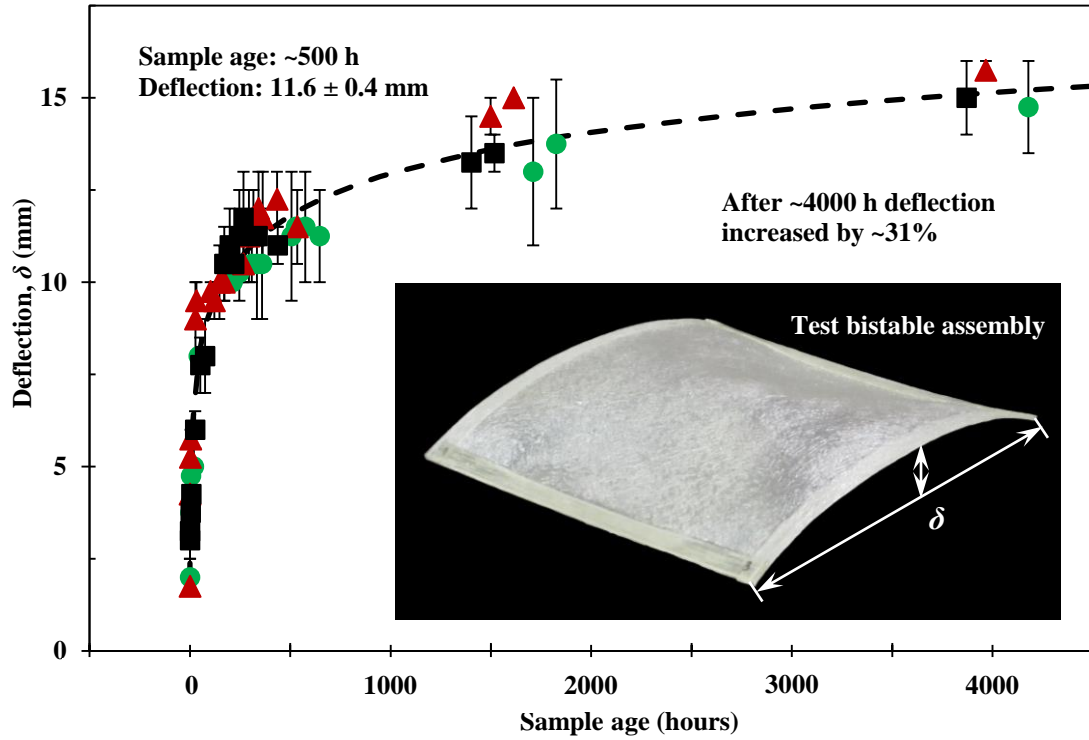


Figure 7-6 Static deflection of the three bistable samples with age. The insert shows the deflection position; the dashed curve shows the trend.

The progressive increase in sample deflection following sample production in Figure 7-6 is consistent with viscoelastic recovery force-time studies [95, 99], i.e. time-dependent behaviour is clearly evident. Although the recovery force generated with the new nylon 6,6 yarn was monitored to 1000 h (Section 4.2.4), the long-term recovery force performance is expected to be comparable to the old (previously used) nylon 6,6 yarn. The later corresponds to the recovery force-time studies monitored to 2700 h [99] and subsequent monitoring to 27000 h [95]. The force produced by viscoelastic recovery of nylon 6,6 yarn at a fixed strain can be estimated from force output-time data in Ref. [99] at 500 h and subsequent work [95] at 4000 h, and the output increased by 29%. Since δ is directly proportional to P in Equation 7-2, it may be expected to correspond with the measured deflection increase from ~500 h to ~4000 h in Figure 7-6. With the latter being ~31%, it is evident that Equation 7-2 may have some applicability when considering the assembled bistable structure.

7.5.2 Static evaluation of the beam structures

Since the four VPPMC strips produced without a fibreglass layer represented an isolated prestressed beam case, the measured deflection may be expected to correspond with the value for δ predicted by Equation 7-2. To assess the applicability of Equation 7-2, a typical cross-sectional view of a VPPMC strip bonded to the fibreglass layer is shown in Figure 7-7. This enables an estimation of e for Equation 7-2 to be made. For an isolated VPPMC strip, the beam thickness, h , was ~ 1.3 mm, which corresponds with the VPPMC strip thickness in Figure 7-7 and e was estimated to be ~ 0.2 mm. For the full beam thickness however, h was ~ 1.7 mm, resulting in e being ~ 0.4 mm. In addition, the recovery force, as represented by P in Equation 7-2, can be determined from Section 4.2.4, which was found to be ~ 22.5 N at ~ 350 h.

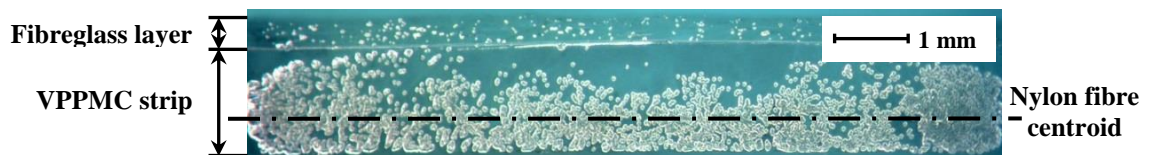


Figure 7-7 Representative cross-sectional view of a VPPMC strip attached to fibreglass-resin sheet, with estimated location of the nylon fibre centroid.

Figure 7-8 shows a typical VPPMC-based test beam (VPPMC strip bonded with a fibreglass layer) with equivalent control sample. Again, the control sample is flat, indicating deflection in the test sample may be generated purely through viscoelastic fibre prestressing. At ~ 350 h, the measured deflection from the four strips (mean \pm standard error) was 19.7 ± 0.8 mm. To predict deflection from Equation 7-2 for this case, three-point bend tests were carried out at ~ 350 h on four identical control sample beams to determine the required value of E using Equation 7-3, which was found to be 1.85 ± 0.07 GPa (mean \pm standard error).

With an isolated VPPMC strip, the matrix modulus E for the polyester resin at 3.3 GPa [1], is (coincidentally) equal to E for the nylon 6,6 fibres [145]. Using these values, Equation 7-2 predicts δ to be ~ 3.7 mm, comparing well with the measured sample deflection, i.e. the mean (\pm standard error) mid-span deflection from the four isolated VPPMC strips at ~ 350 h being 3.6 ± 0.1 mm. For a full beam structure (VPPMC strip

bonded with fibreglass layer) however, the theoretical value of δ determined from Equation 7-2 was ~ 6.0 mm, which is about three times lower than the measured deflection (19.7 ± 0.8 mm). Nevertheless, when the VPPMC strips were constrained in a bistable assembly, it gave a δ value of 11.3 ± 0.4 mm (Figure 7-6) at ~ 350 h. Thus, the deflection value can be significantly influenced by the addition of the fibreglass layer.

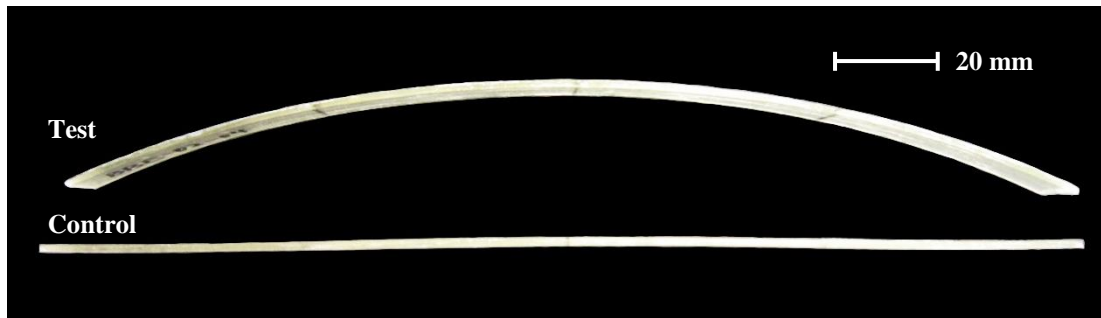


Figure 7-8 Static deflection of VPPMC strip bonded to fibreglass sheet impregnated with the same resin compared with an equivalent control (no prestress) beam sample, ~ 350 h after manufacture.

From all above results, it is evident that although Equation 7-2 may have some applicability (Section 7.5.1), there are significant limitations regarding its use for more detailed analysis involving the full beam structure. These limitations arise from the following: (i) the predicted value for δ is based on an idealised equation that (for example) assumes deflection depending only on elastic behaviour; (ii) uncertainties in estimated parameter values for Equation 7-2, e.g. influence of the non-uniform nylon fibre spatial distribution on e ; (iii) effects of porosity (due to air entrapment within fibres) and interfaces (i.e. fibreglass sheet and fibre-matrix interface regions) on I and E . Thus (iii) may be a major factor contributing to the observed discrepancy between the E value (3.3 GPa) for neat polyester resin [1], and the value (1.85 GPa) determined from the VPPMC-fibreglass beam samples.

7.5.3 Dynamic (snap-through) testing details

Snap-through testing of the bistable structure was first carried out using the point-force indenter, and the experimental arrangement is shown in Figure 7-9, corresponding to Figure 7-2 (a). Shape I indicates the initial cylindrical stable shape and Shape II is the final cylindrical stable shape after the test. Testing was performed at two loading speeds:

6 mm/min to determine slow deformation behaviour and 60 mm/min to obtain fast response characteristics to external loading. For repeatability, the three samples were evaluated at ~500 h, and each sample was tested three times in both snap-through directions. The Effect of test speed on the snap-through characteristic is discussed in Section 7.5.4.

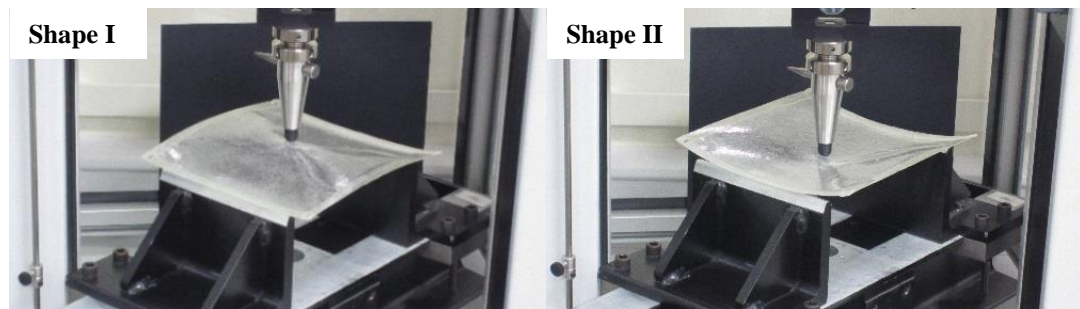


Figure 7-9 Experimental set-up for point-force snap-through tests. Shape I indicates the first cylindrical stable shape before the test; Shape II is the second cylindrical stable shape after the test.

The short-length indenter as illustrated in Figure 7-2 (b) was adopted for the second set of tests, and the experimental set-up is shown in Figure 7-10, together with the two stable shapes (before and after testing). The direction of the short-length indenter is perpendicular to the initial cylindrical shape direction (Shape I) as demonstrated in Figure 7-10. To compare with the point-force snap-through tests in Section 7.5.4, the same experimental arrangement and sample age (~500 h) were used but testing was set at the fast speed (60 mm/min). The results are presented in Section 7.5.5.

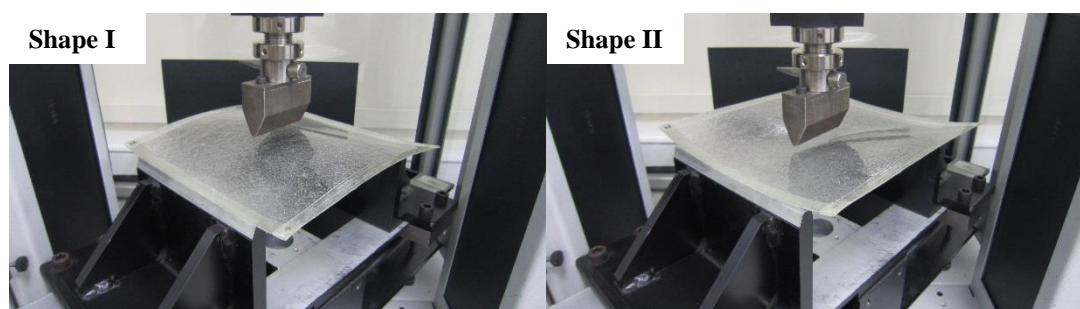


Figure 7-10 Experimental set-up for short-length indenter snap-through tests. The direction of the short-length indenter is perpendicular to the initial cylindrical shape direction (Shape I).

7.5.4 Effect of test speed on the snap-through characteristics

Figure 7-11 shows representative load-displacement curves from one typical bistable sample, for: (a) and (b) tested at 6 mm/min; (c) and (d) tested at 60 mm/min. The snap-through direction for (a) and (c) is from Shape I to Shape II (Section 7.3.2); while (b) and (d) represent the snap-back process from Shape II to Shape I. In Figure 7-11 (a) and (b), the lower test speed appears to produce a longer period of load-displacement ‘vibration’ initially. This vibration can be attributed to the snap-through effect from small ripples on the sample surface as captured in Figure 7-12. Increasing the test speed can reduce the number of ripples, i.e. some ripples may not have enough time to snap-through during quick loading, or ripples may merge to cause a comparatively larger snap-through load and shorter region of vibration as shown in Figure 7-11. A possible explanation for the small ripple effect is that since the whole bistable assembly is produced through hand lay-up (Sections 7.3.1 and 7.3.2), the resin is not evenly distributed throughout the plate, which may result in a variation of snap-through loads to create the ripples. Moreover, although the point-load indenter is positioned at the center of the whole assembly, the sample is not geometrically perfect; thus the point loading force could propagate preferentially in any direction, resulting in unstable load transfer during snap-through.

The results of peak loading force and corresponding displacement from snap-through tests are listed in Table 7-2. At a sample age of ~500 h, the peak force and displacement for the lower test speed were 1.05 ± 0.04 N and 15.1 ± 0.5 mm, respectively; at the higher speed, these values were increased to 1.32 ± 0.04 N and 16.0 ± 0.5 mm. Clearly, these displacement values are larger than the static values (11.6 ± 0.4 mm) reported in Section 7.5.1. Since displacement recorded during snap-through was the maximum value from the centre of each sample, the differences may be explained by flexibility effects within the fibreglass sheet as the static values were measured at the edges of each sample (Figure 7-6). It is also demonstrated in Figure 7-11 that the small ripple effect shown in Figure 7-12 is exacerbated by a lower test speed. Two-sided hypothesis testing shows that the observed peak loads from the two loading speeds are significantly different at 5% significant level. This indicates that for a higher test speed, more energy is stored before snap-through occurs, thus a greater peak load is required.

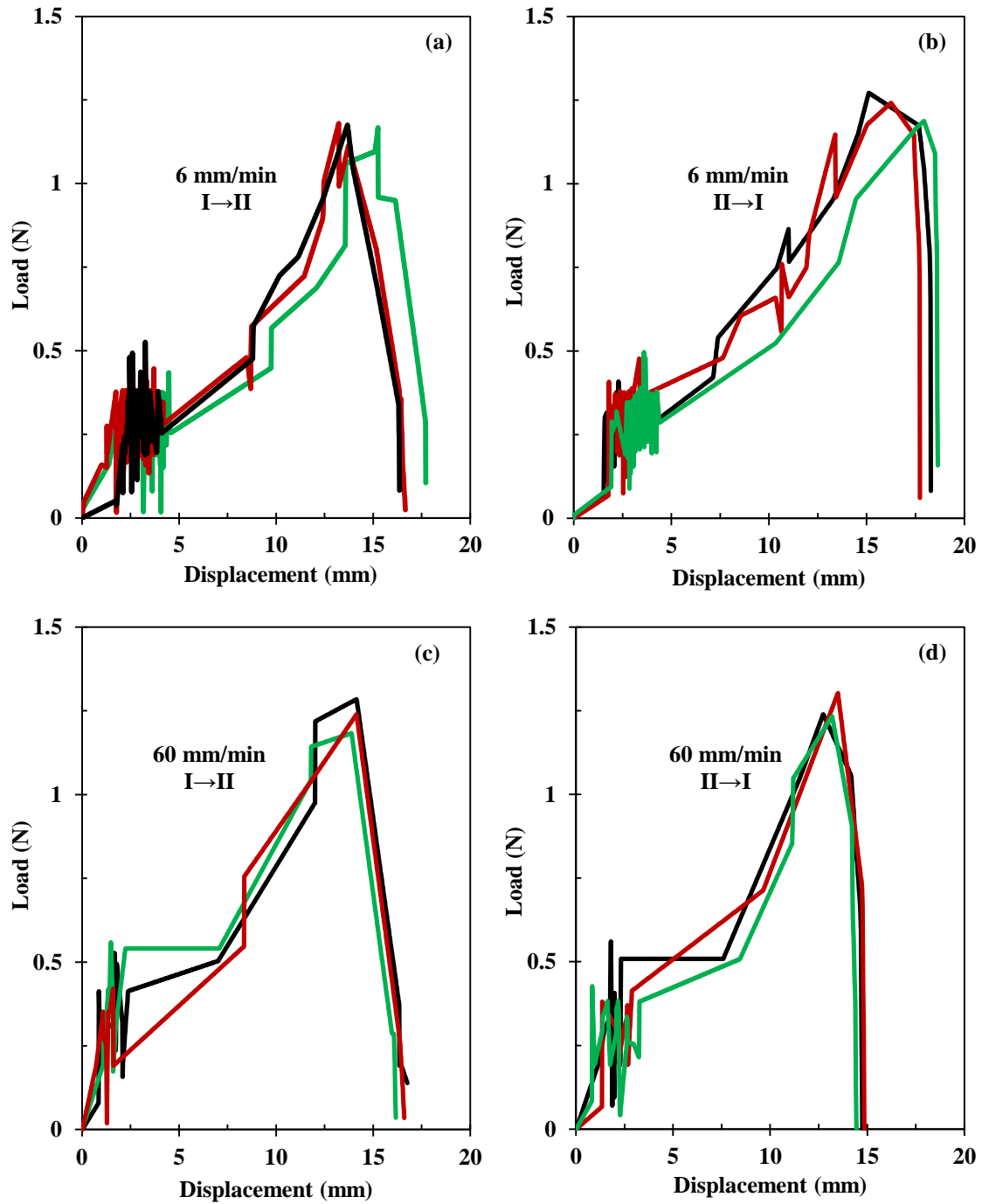


Figure 7-11 Snap-through load response of bistable composite assembly in both directions for 6 mm/min (a, b) and 60 mm/min (c, d).

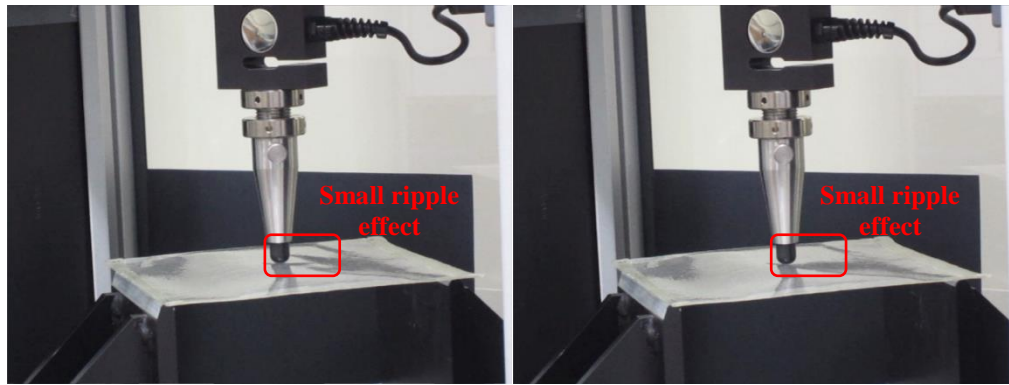


Figure 7-12 Snap-through from small ripple effect at 60 mm/min.

Table 7-2 Point-force loading snap-through test results from two different loading speeds, 6 mm/min and 60 mm/min.

Sample No.	Snap-through direction	Test at 6 mm/min		Test at 60 mm/min	
		Peak load (N)	Displacement at peak load (mm)	Peak load (N)	Displacement at peak load (mm)
1	I→II	1.00 ± 0.05	14.4 ± 0.3	1.32 ± 0.02	16.0 ± 0.4
	II→I	0.92 ± 0.02	12.2 ± 0.4	1.26 ± 0.02	13.1 ± 0.2
2	I→II	0.85 ± 0.04	17.3 ± 0.4	1.10 ± 0.04	17.5 ± 0.8
	II→I	1.12 ± 0.04	16.1 ± 0.7	1.47 ± 0.01	17.6 ± 0.5
3	I→II	1.17 ± 0.01	14.0 ± 0.6	1.24 ± 0.03	14.1 ± 0.1
	II→I	1.23 ± 0.02	16.4 ± 0.8	1.57 ± 0.08	17.7 ± 0.2
Mean ± SE		1.05 ± 0.04	15.1 ± 0.5	1.32 ± 0.04	16.0 ± 0.5

7.5.5 Effect of indenter geometry on the snap-through characteristics

A set of representative load-displacement results using the short-length indenter are shown in Figure 7-13. Compared to the point-force snap-through test with the same test speed (60mm/min) in Figure 7-11 (c) and (d), the short-length loading gives a comparatively stable load transfer to the whole structure. As discussed in Section 7.5.4, point-force loading may promote deformation from different parts of the sample and generate ripples which affect the load transfer. However, for short-length loading, a greater contact area ensured a more stable load transfer in a certain direction to give smoother load-displacement curves during both snap-through and snap-back process, as shown in Figure 7-13.

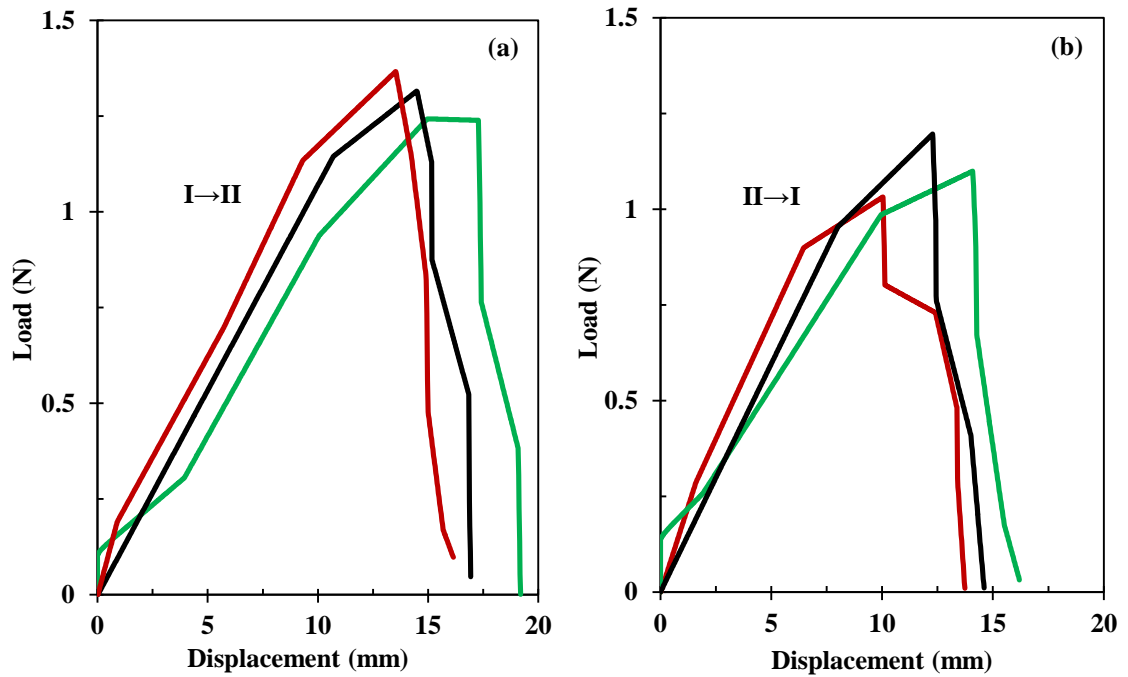


Figure 7-13 Snap-through load response of bistable composite assembly with short-length indenter loading at 60 mm/min test speed.

Figure 7-14 shows a sample at an instant just before and just after snap-through. Unlike the point-force loading, this dynamic behaviour shows one significant ripple generated around the indenter, and after peak loading is reached, the sample quickly jumps to the second stable shape.

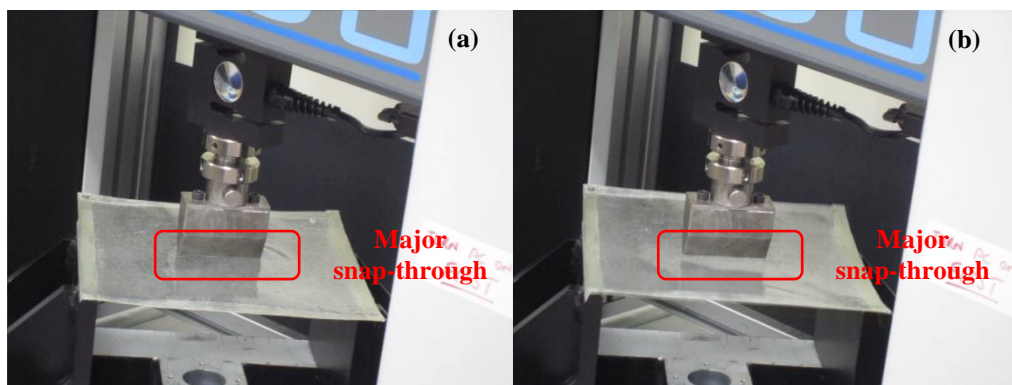


Figure 7-14 Short-length snap-through test and typical sample performance before (a) and after (b) the snap-through moment.

The corresponding results of peak loading force and displacement from short-length snap-through tests are given in Table 7-3, and these can be compared with the point-force loading data from Table 7-2. At a sample age of ~500 h, the peak force and corresponding displacement from point-force loading are 1.32 ± 0.04 N and 16.0 ± 0.5 mm respectively,

compared with 1.32 ± 0.03 N and 12.7 ± 0.5 mm displacement from the short-length indenter. Therefore, the peak loads were the same, but the displacement at peak load was reduced when the short-length indenter is applied. Considering the load-displacement behaviour in Figure 7-13, it can be inferred that short-length loading may reduce the small ripple effect, and the reduction in snap-through displacement can be attributed to the disappearance of small ripples. As test speed is the same, the lower displacement means that the sample needed less time to snap-through to the other stable shape. Thus, the activation of snap-through performance through a greater contact area (a short-length indenter in this case) may promote a faster response in morphing capability.

Table 7-3 Snap-through test results for short-length indenter loading at 60 mm/min.

Sample No.	Snap-through direction	Short-length loading at 60mm/min	
		Peak load (N)	Displacement at peak load (mm)
1	I→II	1.31 ± 0.04	14.3 ± 0.4
	II→I	1.11 ± 0.05	12.1 ± 1.2
2	I→II	1.29 ± 0.06	14.2 ± 0.4
	II→I	1.43 ± 0.02	10.8 ± 0.3
3	I→II	1.36 ± 0.01	14.6 ± 0.5
	II→I	1.42 ± 0.02	10.2 ± 0.8
Mean \pm SE		1.32 ± 0.03	12.7 ± 0.5

7.5.6 Effect of sample age on the snap-through characteristics

To determine the effects of short-term aging, samples were re-tested at ~4000 h. Since the snap-through performance is affected by loading indenter geometry and test speed (Sections 7.5.4 and 7.5.5), the point-force indenter (Figure 7-9) and 60 mm/min were selected as the reference conditions. Following sample storage to ~4000 h, typical snap-through results are shown in Figure 7-15. Compared to the same test conditions with a sample age of ~500 h, i.e. Figure 7-11 (c) and (d), most of the small ripple effects, as demonstrated in Figure 7-12, were no longer observable. As sample age increases, the matrix can be expected to become stiffer. The results presented here indicate that load-displacement behaviour seems to be sensitive to the sample stiffness, i.e. stable load transfer may be promoted by a stiffer structure.

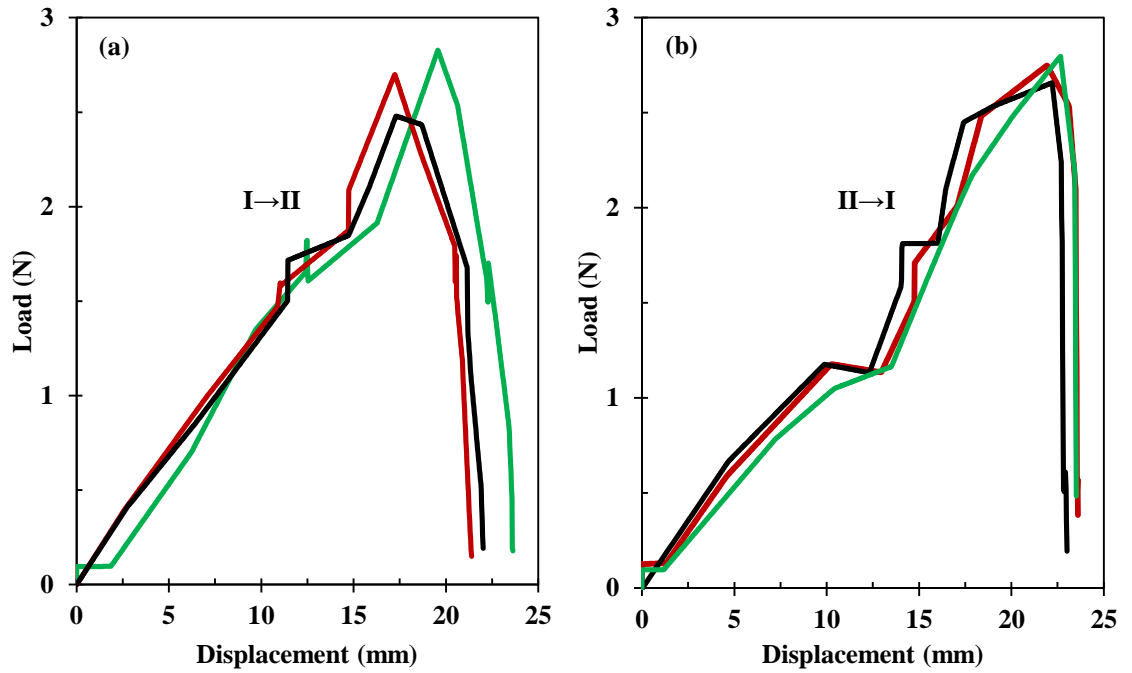


Figure 7-15 Point-force snap-through loading response of bistable composite assembly at 60 mm/min test speed with sample age of ~4000 h.

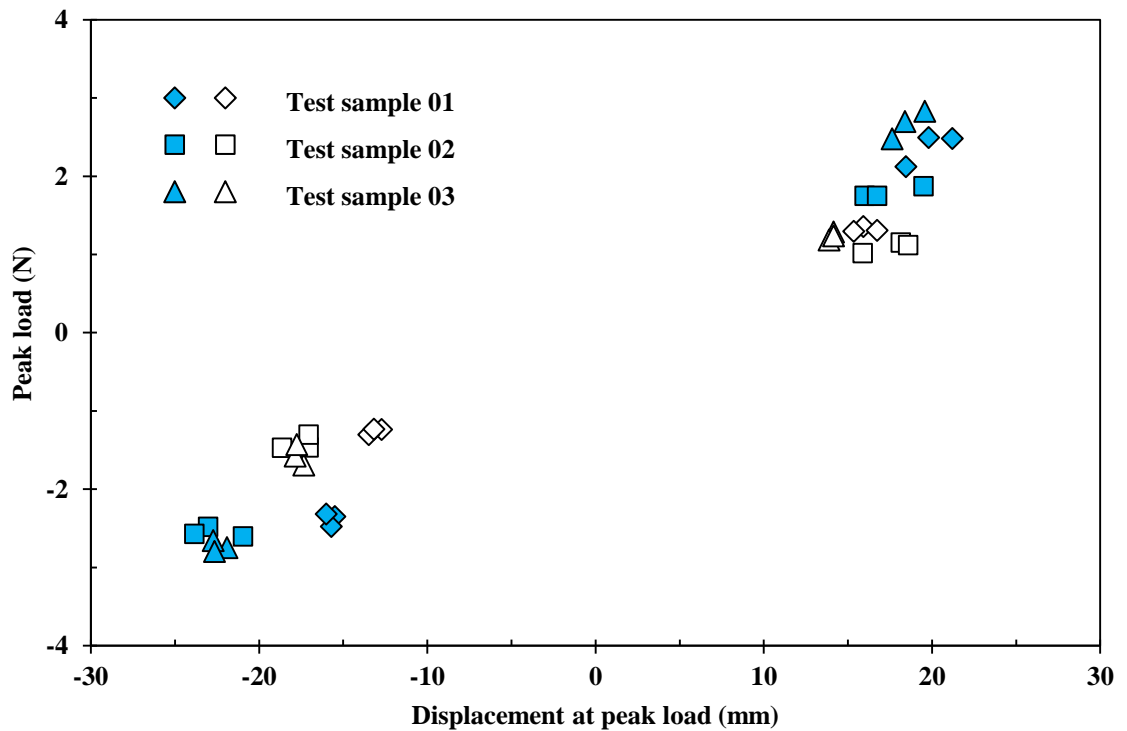


Figure 7-16 Snap-through tests for the three VPPMC-based bistable assemblies using the point-force indenter at 60 mm/min. Hollow symbols represent the tests at ~500 h; filled symbols at ~4000 h.

Figure 7-16 summarises the peak loading force versus displacement results from the point-force snap-through tests at the two sample ages. The close scatter of data points shows good repeatability within the samples. As demonstrated in Table 7-2, with a sample age of ~500 h, results gave a peak force and displacement of 1.32 ± 0.04 N and 16.0 ± 0.5 mm respectively. After further storage to ~4000 h, the peak load increased to 2.42 ± 0.08 N with 19.4 ± 0.7 mm displacement. This increase may be attributed to the following: (i) as sample age increase by 8-fold, the matrix becomes stiffer and needs more energy to deform; (ii) the viscoelastic recovery force within a composite increases with time [95, 99], giving a larger sample deflection, δ (Section 7.5.1), and this would also consume more energy during snap-through.

7.5.7 FE analysis

7.5.7.1 Numerical simulation

The loading history of FE is illustrated in Figure 7-17. As explained in Section 7.4.3, prestress was introduced to the composite through a ‘predefined field’ in Step-1, and only fibres were subjected to the temperature change ΔT . As the amplitude of ΔT determines the generated force which leads to the deflection of samples (Section 7.4.1), the effect of ΔT on the model deflection was considered first and results are shown in Figure 7-18. Since the bistable assembly at a sample age of ~500 h was chosen as the reference (Section 7.4.3), a sample deflection of ~11.6 mm was required. Therefore, the predefined ΔT can be determined from Figure 7-18 as 115°C, and the corresponding model deflection was found to be 11.7 mm as demonstrated in Figure 7-19.

Using the parameters outlined above and information in Section 7.4, the FE model is generated and the first stable shape in the y-direction after Step-1 is shown in Figure 7-19. This is associated with the von Mises stress distribution within the mid-fibreglass layer. For the whole bistable model as illustrated in Figure 7-19 (a), since the stress within the fibres was much higher than the strip and layer, the stress distribution could not be clearly observed. Thus the mid-layer was isolated to demonstrate the stress distribution as presented in Figure 7-19 (b). It shows that the von Mises stress is symmetrical about the centre of the structure, and the maximum von Mises stress is located within the area

influenced by the combined effect of the strips. As the stable cylindrical shape is in the y -direction, any deflection in the y -direction is not constrained, thus a low stress distribution area is formed along this direction. The strip deflection in the x -direction however, is constrained by the structure, which therefore gave a higher concentration of stress.

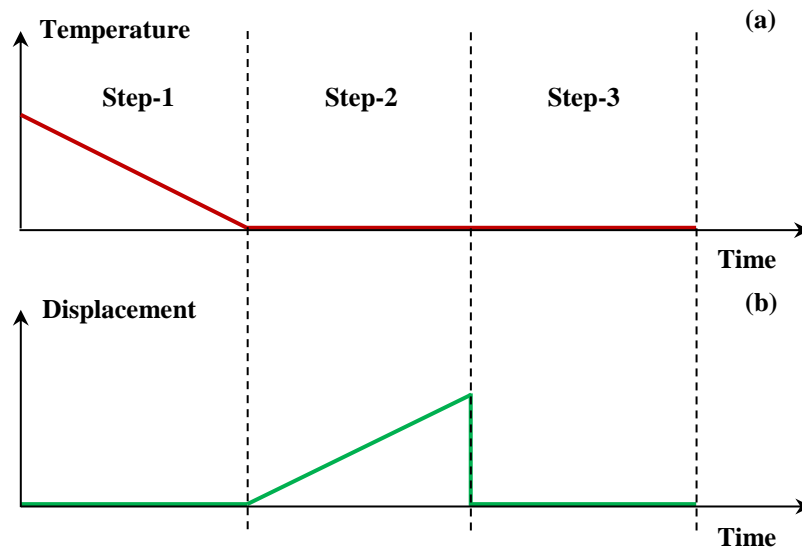


Figure 7-17 Loading history for the FE model: (a) temperature change during the simulation process; (b) displacement change of the indenter throughout the modelling period.

Steps 2 and 3 as described in Section 7.4 and the sequence in Figure 7-17 was then applied to the FE model. In contrast with the experimental investigation, since the model is based on homogeneous materials, the whole structure is perfectly symmetrical, thus the snap-through and snap-back processes (Section 7.5.4) are identical. Therefore, only the snap-through process was investigated and the stable shapes before and after loading are shown in Figure 7-20. Note that the white object is the simulated rigid point-force indenter, and the deflection of the second stable shape in the x -direction was found to be the same as the first stable shape. A loading velocity of 60 mm/min was conducted in Step-2, which allows direct comparison of FE simulation to the experimental snap-through process in Section 7.5.4. Therefore, the results plotted in Figure 7-21 can be associated with a set of typical experimental results.

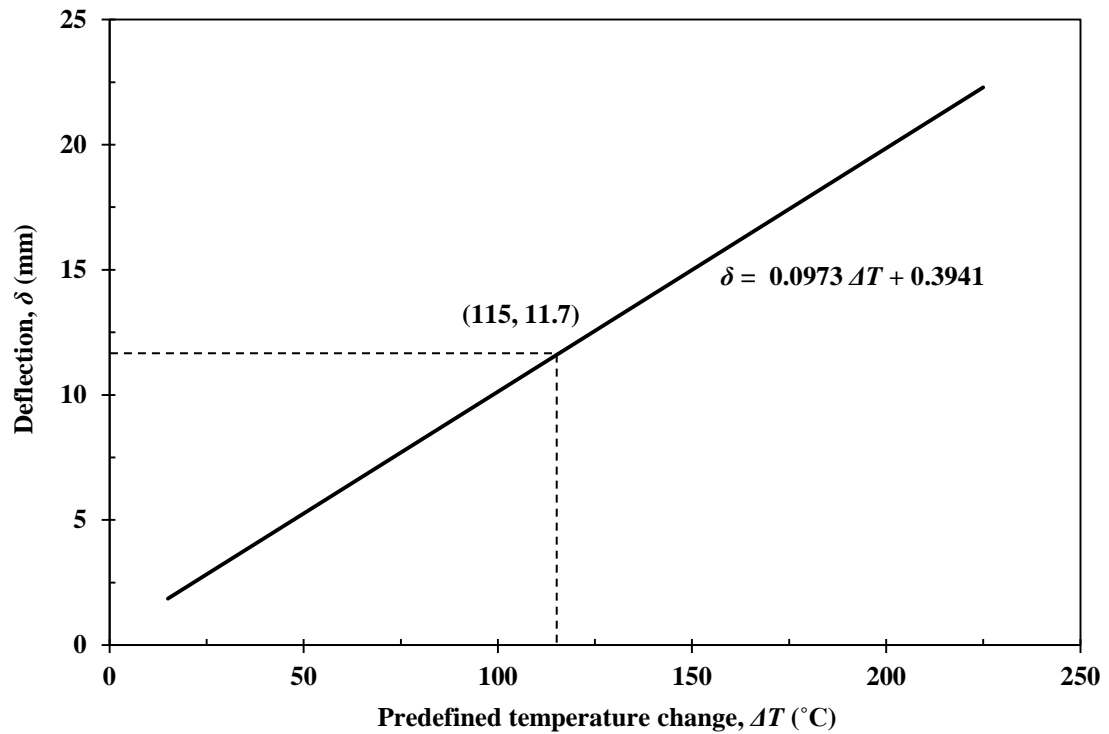


Figure 7-18 Relationship between predefined temperature change ΔT and deflection of the bistable structure from the FE model during Step-1.

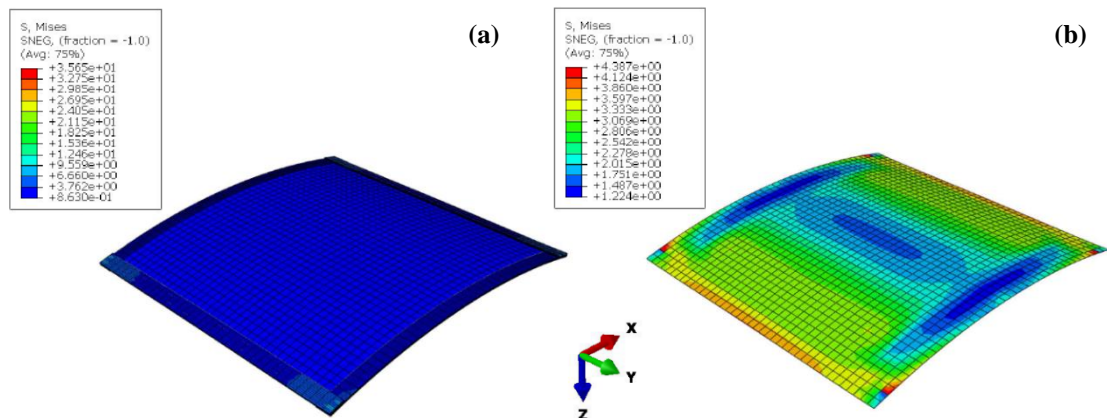


Figure 7-19 Simulated stable shape in y-direction generated after Step-1: (a) stress distribution within the whole bistable structure; (b) stress distribution within the mid-fiberglass layer.

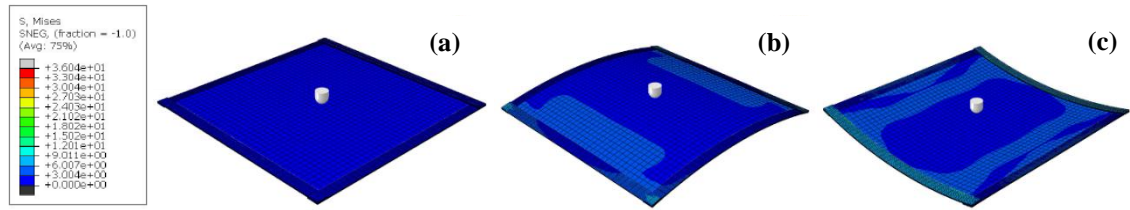


Figure 7-20 Snap-through process of the bistable structure through FEA: (a) original plate; (b) first stable cylindrical shape in y -direction; (c) second stable cylindrical shape in x -direction.

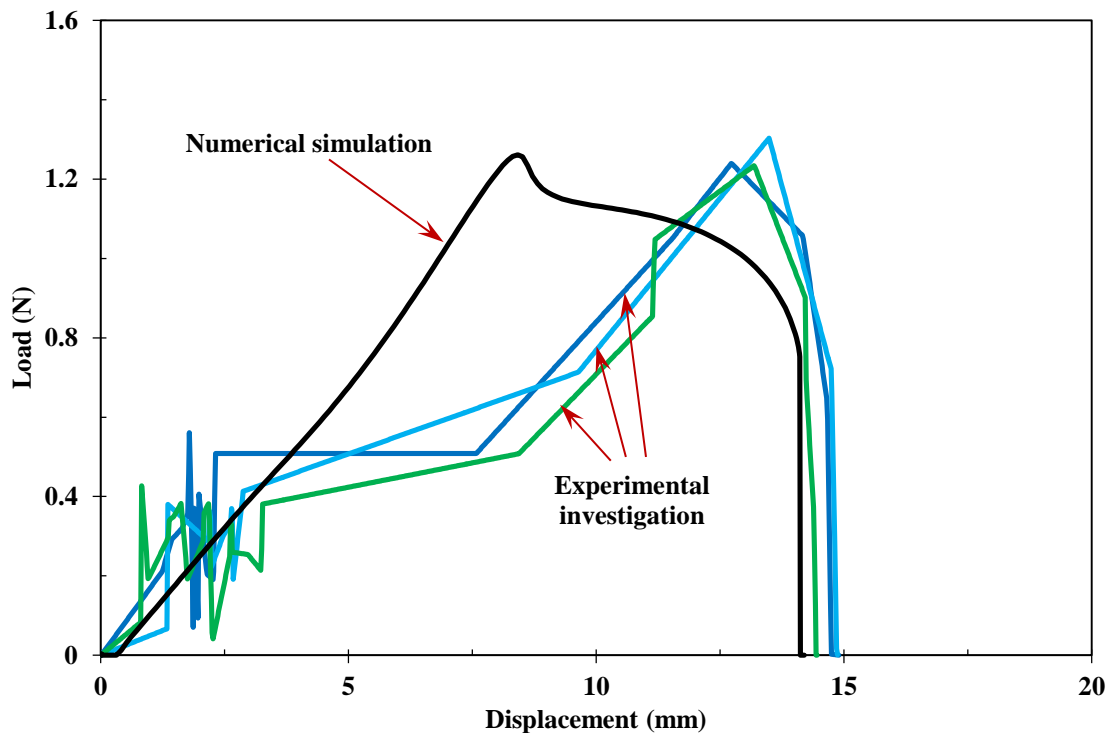


Figure 7-21 Reaction force versus indenter displacement within the snap-through process for FE simulation, compared to the experimental curves from Section 7.5.4.

As discussed in Section 7.5.4, the vibration area at the beginning of the experimental loading process was thought to be caused by variations in fibre distribution, while the FE model was established with homogenous materials. Therefore, the FE load has a linear relationship with loading displacement, as demonstrated in Figure 7-21. The FE gave a peak load of 1.26 N which is comparable to the experimental data of 1.32 ± 0.04 N, and the variation could be attributed to optimisation of model geometry (Section 7.4.3); however, the displacement at peak load was 8.42 mm, i.e. only half that obtained from experimental data (16.0 ± 0.5 mm). Considering that the gradient of the experimental curve near the snap-through area is similar to the FE curve, this discrepancy may be

attributed to energy losses in the vibration area through the rippling effect as represented in Figure 7-12 (Section 7.5.4); hence shift the peak load position. This has been also verified in Section 7.5.5 when the short-length indenter was adopted, i.e. a stable load-transfer gave lower displacement at peak load (Section 7.5.5). It can also be seen that the load-displacement process of the numerical simulation differed from the experimental characteristic in terms of snap-through behaviour: in the experimental process, the snap-through occurred quickly when peak force was reached; in the FE simulation however, there was some delay after the peak load was reached. However, it is found that the critical displacement set in Step-2 for the snap-through phenomenon to occur in the model was 14.2 mm, i.e. similar to the displacement at peak load from the experimental results. When this value was achieved, the panel deformed quickly to the second stable shape. Thus, it can be concluded that since the actual sample is not perfectly symmetrical, the snap through occurs when it has reached the peak load, while the FE results show that the peak load and indenter displacement are both essential for the snap-through behaviour. Since the same loading condition was adopted for both methods, the loading period for the snap-through phenomenon to occur is in good agreement, when optimisation of the model solution and experimental errors are considered.

The FE model of the morphing bistable structure demonstrates validity in terms of peak load and critical displacement. Despite the differences outlined above, it is both a time saving and economical tool to address the model to investigate factors that could affect bistable snap-through behaviour. These include prestress level P , fibre volume fraction V_f , edge length L , and modulus of mid-layer E_{ML} . However, since P and V_f both influence model deflection, the same effect on snap-through performance could be assumed. Of particular interest are the effects of sample deflection and material modulus values on the development of bistable behaviour and understanding of the bistability mechanism. To investigate the effects of various factors, the basic model parameters were maintained constant, and the chosen factor was then set as the variable. However, exploring new VPPMC-based structural designs is not limited to the factors listed above. Other aspects could include, for example, the effects of commingled fibres within this new technology.

7.5.7.2 Development of bistable behaviour

As discussed in Section 7.5.1, although Equation 7-2 may not be directly applicable to predicting deflection in a bistable structure, some applicability has been experimentally demonstrated that the bistable sample deflection δ is directly proportional to the prestress force P , as shown in Equation 7-2. Moreover, Figure 7-18 shows that deflection δ is proportional to ΔT . Thus FE analysis can be used to investigate the development of snap-through behaviour in terms of model deflection; i.e. realistic deflections can be achieved through adjusting the viscoelastic strain levels and fibre volume fraction within a composite. The snap-through responses of the panel with δ ranging from 1.6 to 11.7 mm were investigated using the FE method and results are shown in Figure 7-22. Here, the dashed lines represent the trends in maximum load and critical indenter displacement. The inserted figures show the corresponding deformation moment during different snap-through stages.

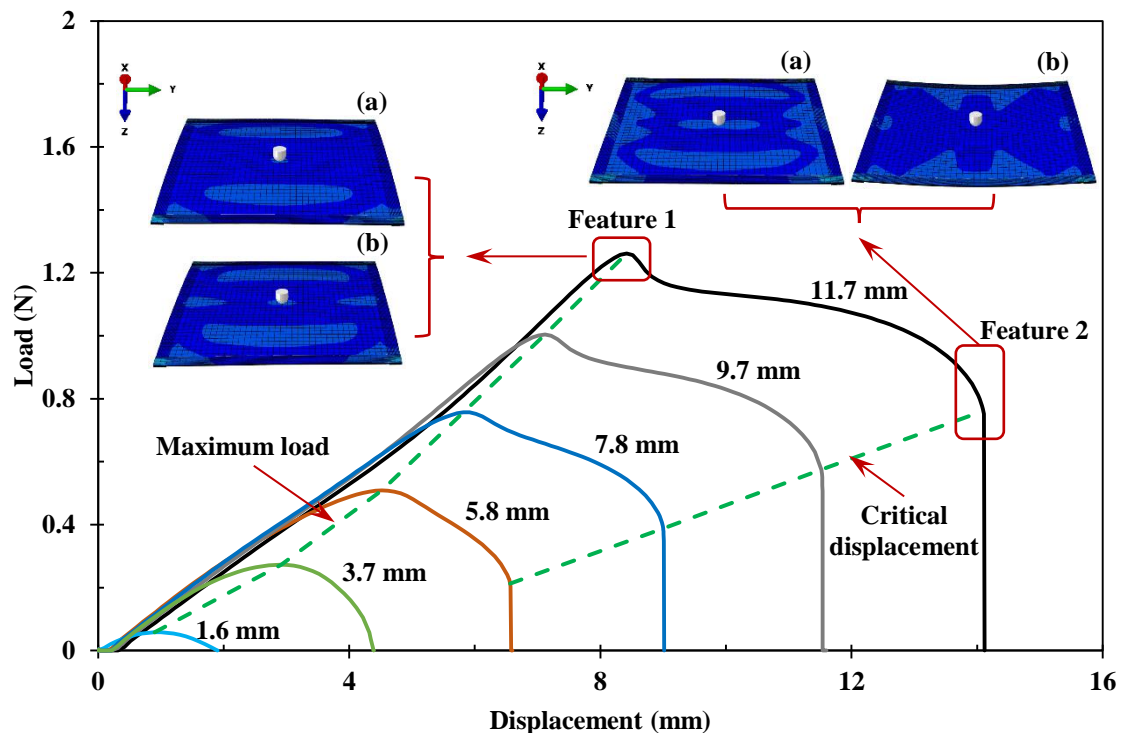


Figure 7-22 Development of the snap-through process for a bistable structure panel with pre-defined deflections. Dashed lines show the change in maximum load and critical displacement for snap-through behaviour; inserted figures show the corresponding deformation before (a) and after (b) the critical moment of each feature.

As shown in Figure 7-22, pre-snap-through behaviour basically follows the same characteristic, and the maximum load increases with sample deflection. No clear critical snap-through indenter displacement was observed with sample deflections less than 3.7 mm. Beyond 5.8 mm, the load at critical displacement increases linearly with deflection. Furthermore, with increasing deflection, peak load and critical displacement diverge from each other, and gradually form two snap-through features as highlighted in Figure 7-22. Feature 1 is formed through the snap of accumulated ripples in the y -direction and gives a peak load to the curve; feature 2 corresponds to the snap of ripples in the x -direction and occurs when the loading indenter reaches the critical displacement; the structure then jumps quickly into the second stable shape.

7.5.7.3 Effect of modulus ratio

Section 7.5.7.2 demonstrates that the snap-through behaviour of the proposed bistable structure depends on the movement of ripples (localised contours) in both x - and y -directions, while two peaks gradually diverge as model deflections increase, generally reducing the quick response ability of morphing structures. This section looks into the feasibility of improving this capability. It is demonstrated in Section 7.5.6 that increasing the sample stiffness can improve the stability in load transfer. Since the mid-layer and VPPMC strips were made from different reinforcements, the possible factor considered in FE to improve the situation is the modulus ratio R_E , defined as the ratio of elastic modulus between the mid-layer and prestressed strips. Thus, $R_E = E_{\text{layer}}/E_{\text{strip}}$. Therefore, the model developed in Section 7.5.7.1 and 7.5.7.2 is denoted with an R_E value of 1.23.

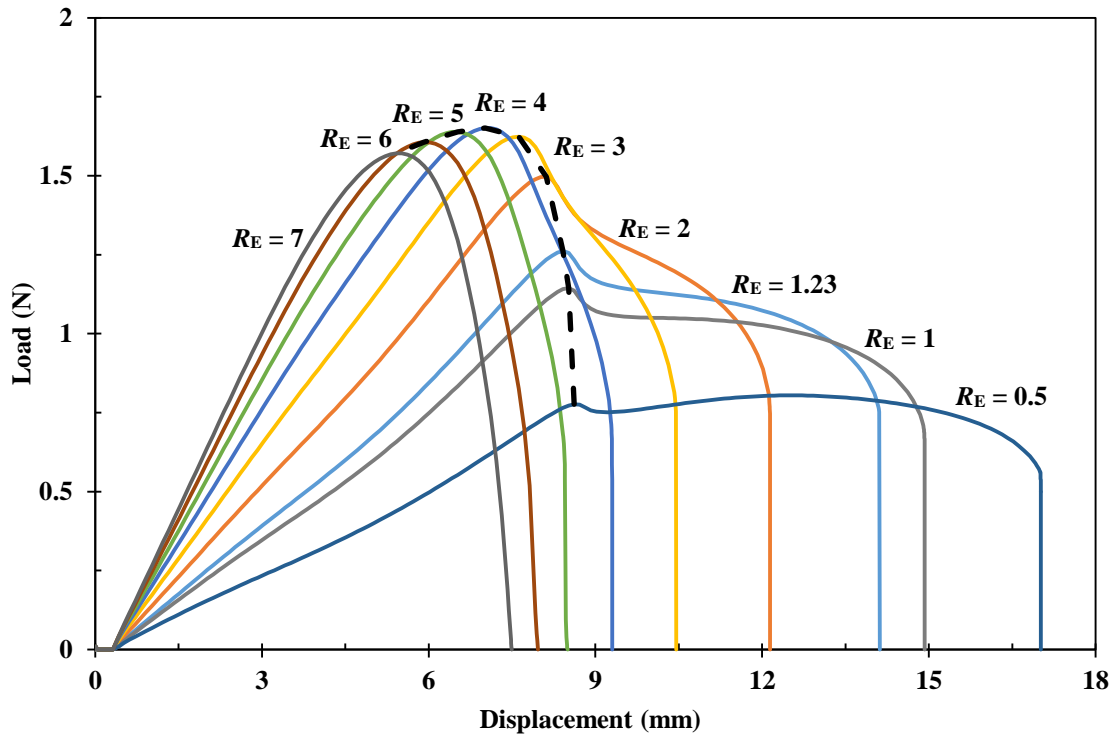


Figure 7-23 FE results for load-displacement curves of bistable structures with different modulus ratios; dashed line shows trend in maximum load.

To investigate the modulus ratio effect, the model parameters were taken from Section 7.5.7.1 and with R_E as the variable, the corresponding snap-through responses are plotted in Figure 7-23. The figure shows that when the mid-layer is more flexible than the VPPMC strips, a larger snap-through region is developed; conversely, as R_E increases, (i.e. the layer becomes stiffer), the two features as demonstrated in Section 7.5.7.2, gradually merge into one peak. The dashed line represents the maximum load during the snap-through process, which grows quickly at the beginning, reaches a peak at the R_E value of 4, and then starts to decrease. Therefore, the quick response ability of the bistable structure can be enhanced through adjustment of the R_E value, i.e. tailored materials can be used to produce the bistable structures for various objectives.

Figure 7-24 shows how the maximum load, critical displacement and model deflection depend on modulus ratio. The critical displacement for snap-through and model deflection generated from the same viscoelastic creep strain levels both decrease as the mid-layer stiffness increases, becoming closer and more stabilised.

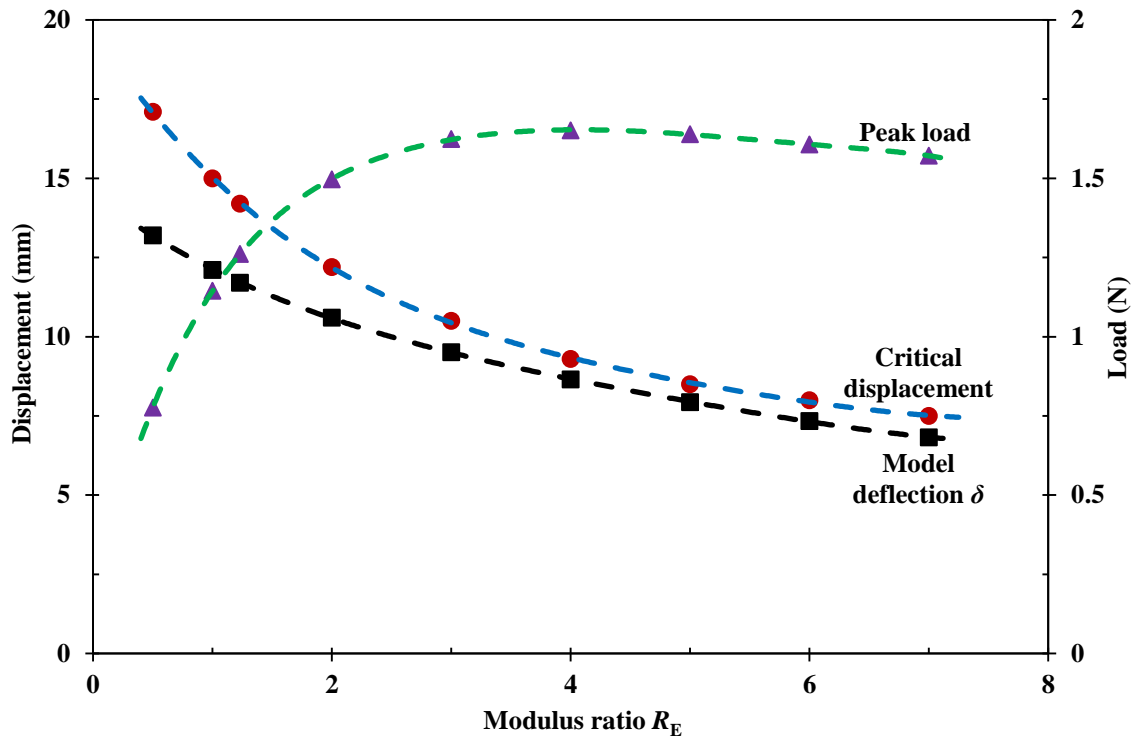


Figure 7-24 FE results of the modulus ratio effect on peak load, critical displacement and model deflection; dashed lines show the trends.

7.5.8 Bistability mechanisms

The snap-through behaviour of a bistable structure utilising VPPMC technology has been investigated through both experimental and numerical methods. For a symmetrical model consisting of homogeneous materials, the snap-through performance is dependent on the ripples accumulated in two directions during the loading process, which leads to two snap-through features (Section 7.5.7.2): (i) the first snap of the ripples generates a peak in the load-displacement curves; (ii) the following snap of ripples determines the value of critical indenter displacement. As the structure is based on two composite materials, a critical value of modulus ratio exists, where the two features merge into one snap-through peak (Section 7.5.7.3). The differences between numerical and experimental results illustrated in Figure 7-21 can be further explained: since the real sample not being perfectly homogeneous as demonstrated in Figure 7-12, the potential energy stored in the first featured ripples is dispersed into small ripples during loading, which leads to the disappearance of the first feature. The snap of small ripples occurs at an early stage of loading to create the vibration area as represented in Figure 7-11, and this shifts the critical snap-through displacement as demonstrated in Section 7.5.5. As the peak

diminishes, some of the energy stored in the first feature may merge into the second featured ripples in the x -direction, hence increase the load needed for snap-through behaviour. Therefore, experimental results possess a greater snap-through load than the numerical simulation, as illustrated in Figure 7-21.

7.6 CONCLUSIONS

This chapter reports on the experimental and numerical investigations of a novel shape-changing bistable structure, using viscoelastically generated prestress. An FE model is successfully developed to simulate the bistability, and the viscoelastically fibre prestressing effect within a VPPMC is achieved by exploiting thermal changes in the fibre material. The main findings are summarised below:

- (i) Viscoelastically generated prestress can be utilised to produce a bistable structure. Bistability is achieved by bonding pairs of deflecting VPPMC strips on each side of a thin, flexible resin-impregnated fibreglass sheet. This enables the structure to snap-through between one of two stable shapes.
- (ii) The beam bending equation that is widely used to predict deflection in prestressed concrete has some applicability in terms of isolated VPPMC strips and the bistable structure; however, there are significant limitations regarding its use for more detailed analysis involving the full beam structure.
- (iii) A small ripple effect is observed during point-force snap-through testing of the bistable structure, and it is exacerbated with a smaller test speed; this discrepancy contributes to the non-uniform distribution of resin within the mid-fibreglass layer, resulting in unstable load transfer.
- (iv) By adopting a short-length indenter, it is found that the small ripple effect can be reduced through a greater contact area; this ensures a more stable load transfer through the whole structure. The reduction in displacement at peak load indicates that the activation of snap-through performance through a greater contact area may promote a faster response in morphing ability.
- (v) The unstable snap-through load transfer from the small ripple effect observed at ~500 h is improved by storing the samples further to ~4000 h. Since the matrix can be expected to become stiffer with aging effects, the snap-through load and displacement are increased.

- (vi) Numerical simulation results of the snap-through behaviour show good agreement with the experimental work in terms of peak load and critical displacement. Investigation into the development of bistable behaviour shows the ripples accumulated in both x - and y -directions give two features which determine the snap-through performance of the bistable structure. These two features gradually diverge as model deflections increase.

By considering the modulus ratio effect, the model solution demonstrates that the fast-response ability of the bistable structure can be significantly increased through adjustment of R_E value; in practice, this can be achieved by employing materials tailored to suit various objectives.

- (vii) Based on the experimental and numerical simulation results, a mechanism for bistability is proposed to offer further insight into the snap-through performance of morphing structures.

VPPMC technology offers an alternative solution to produce morphing composite structures. It offers great flexibility in terms of product geometry and benefits from longevity aspects. Moreover, the influence of sample deflection and modulus ratio shows that VPPMC-based morphing composite structures could be tailored to adopt various industrial applications. Therefore, it opens new opportunities for VPPMC research.

Chapter 8

OVERALL FINDINGS, FUTURE WORK AND CONCLUSIONS

SUMMARY

This chapter summarises the overall findings, potential directions of future work and conclusions. Research has been carried out in Chapters 4 to 7, hence the main findings and contributions are principally from these chapters. Preliminary studies (Chapter 4) involved evaluations of the stretching rigs, and new nylon fibre and matrix resin required for the research. Viscoelastic behaviour of nylon 6,6 fibre and its effect on the impact performance of VPPMCs were carried out in Chapter 5. This enabled the research to progress towards process optimisation in VPPMC production as covered in Chapter 6. Research on the application of VPPMCs to morphing structures was presented in Chapter 7, based on both experimental and numerical investigations. Suggestions for directions of future work are discussed to develop VPPMC technology in terms of scientific understanding and engineering application. Finally, conclusions of the thesis are provided.

8.1 OVERALL FINDINGS

In this research, experimental and numerical simulation work has been carried out to facilitate the understanding of viscoelastic fibre prestressing mechanisms within a VPPMC, and to further promote the application of VPPMCs for industrial applications, i.e. morphing composite structures. Briefly, Chapter 1 gave a brief introduction to the thesis, covering aims, objectives, motivation and thesis structure; Chapter 2 provided a general review of literature work that related to this research; Chapter 3 specified the materials, evaluation principles and experimental procedures involved in subsequent research chapters; Chapters 4-7 presented the detailed research investigations. The main findings and contributions from individual chapters are summarised below:

8.1.1 Preliminary investigations

Preliminary studies required for the main research work have been presented in Chapter 4. These include: (a) stretching rig calibration; (b) nylon fibre evaluation; (c) selection of the matrix material. By considering the above points, the main findings were:

- (i) Calibration of the large and small stretching rigs enabled the same fibre creep strain level to be achieved through the two different rigs, and allowed direct comparison with previous published work; Charpy impact results indicated that VPPMC samples produced with the large stretching rig gave slightly more stable mechanical performance, hence it was the principal equipment used for viscoelastic fibre prestressing in later chapters.
- (ii) Investigation of nylon 6.6 fibre showed that the new yarns used in this research had a slightly lower value in crystallinity compared to the previously adopted fibre yarns. This was considered to be the explanation for the slight differences in creep-recovery strain values (under same creep loading) and viscoelastic recovery force values.

- (iii) A suitable thermoset resin was selected as the main matrix material to produce VPPMCs; it had superior properties over other resin candidates in terms of low viscosity, low curing temperature, good transparency after curing and demonstrating prestress benefits. The increase in impact energy absorption from fibre prestressing was found to decrease with increasing impact toughness of the matrix materials, and further investigations into fibre-matrix interface effects (e.g. microhardness testing, SEM mirror effect technique) would be required to address this issue.

8.1.2 Viscoelasticity of nylon 6,6 fibre and its effect on VPPMCs

The viscoelastic behaviour of nylon 6,6 fibre and the effect of viscoelastic creep strain level on impact performance of VPPMCs were investigated in Chapter 5. By adopting various creep conditions, the viscoelasticity and yield properties of fibre yarns were studied. The time-stress superposition principle was conducted to predict long-term fibre performance, and stress-shift factors were determined. The effect of viscoelastic creep strain level on VPPMCs was evaluated through Charpy impact testing. Therefore, the main findings and contributions were:

- (i) By applying, under 24 h creep conditions, up to 590 MPa stress on the nylon yarns, the creep and recovery strain-time data showed that there was no creep-induced fracture of the fibre material; there was also recovery of elastic strains and the viscoelastic fibre prestressing mechanism would not be limited by the eventual start of viscous flow.
- (ii) The yield creep strain of the nylon fibre material was found to be ~17.5% when subjected to 665 MPa creep stress, and this was achieved after 2 h of creep loading. This determined the maximum creep stress used in Chapter 6.
- (iii) The Weibull-based function was used to determine the pure elastic strain (which cannot be measured through experiment), giving the ‘true’ modulus of nylon 6,6 fibre as 4.6 ± 0.4 GPa.

- (iii) Approximately linear viscoelasticity was observed in nylon 6,6 fibre over a range of 330 MPa to 590 MPa for 24 h creep conditions. This was further verified through application of the linear time-stress superposition principle on the strain-time data; i.e. a linear relationship was obtained between the stress shift factor, $\log \alpha_\sigma$, and the applied creep stress.

- (iv) Charpy impact testing and recovery force measurements demonstrated that an optimum value exists to maximise the mechanical benefits from viscoelastic fibre prestressing. A prestress mechanism has been proposed to explain the above observations at a microstructural level, which is based on the three-phase polymeric microstructural model and latch-based mechanical model.

8.1.3 Towards process optimisation for VPPMC production

Since mechanical benefits from viscoelastic fibre prestressing were found to be limited by creep strain levels as presented in Chapter 5, it was clear that the same viscoelastic creep strain values could be achieved through higher creep stress values over a shorter period. Hence the optimisation of load-time conditions for producing VPPMCs was performed in Chapter 6, with the aim of approaching maximum exploitation of the fibre materials, and to facilitate the industrial production of VPPMCs. The same viscoelastic strain level under different creep stress values was achieved by using the four-parameter Weibull-based function, and the effectiveness of this principle was verified through Charpy impact testing. The main findings are summarised below:

- (i) By employing a higher creep stress value, the creep loading period to induce the same viscoelastic fibre prestressing level within a VPPMC can be significantly reduced from 24 h to tens of minutes. For example, the previously adopted viscoelastic creep strain, i.e. ~3.4%, which requires a tensile stress of 330 MPa for 24 h, could be achieved over a shorter duration, e.g. 590 MPa for 37 min, with no detriment to the impact performance of the VPPMC samples.

- (ii) By adopting the time-temperature superposition principle, the long-term impact performance of VPPMC samples were evaluated through accelerated aging to an equivalent of 20,000 years at a constant 20°C. Results showed that the viscoelastic recovery within the composites remained active, and there was no deterioration in impact benefits from viscoelastic prestress at a creep strain level of ~3.4% for both the 330 MPa for 24 h and 590 MPa for 37 min creep conditions.

- (iii) Longer exposure of nylon 6,6 yarns to a higher creep strain level could increase the viscoelastic prestress-induced mechanical benefits further: at ~4.0% viscoelastic strain level, 24 h creep at 460 MPa was found to be equivalent to creep conditions at 590 MPa for 134 min or 665 MPa for 48 min. Here, a mean increase of ~75% in impact energy absorption was obtained. Again, no deterioration in impact performance was observed up to 0.5 years at real time. Therefore, an 18% increase in viscoelastic strain level, results in a further increase in impact benefits of ~34% from fibre prestressing (compared to the ~3.4% creep strain level).

- (iv) Relationships between the applied creep stress σ and the corresponding fibre processing time t_n were established for the two investigated viscoelastic creep strain levels (i.e. ~3.4% and ~4.0%), and they both followed a logarithmic trend. Thus subject to avoiding fibre damage, it may be possible to reduce t_n further.

- (v) At a constant creep stress value, i.e. 590 MPa, it was found that the increase in impact energy from VPPMC samples was dependent on creep time. This behaviour was comparable to the increasing creep stress (at a constant creep period) effect in terms of VPPMC impact performance; i.e. there was an optimum creep strain level to maximise the prestress benefits in both cases. This follows the prestress mechanism as proposed in Chapter 5.

8.1.4 Application of VPPMCs to morphing structures

Investigation into the application of VPPMCs to morphing structures, i.e. bistable composite structures, was covered in Chapter 7. Both (a) experimental and (b) numerical investigations were carried out to study the snap-through behaviour of the bistable structures obtained. For (a), the effect of loading speed, loading geometry, and sample age were evaluated; for (b), a finite element model was constructed by employing a predefined temperature change in the fibre material; this enabled the development of bistability and influence of the modulus ratio to be subsequently evaluated. From these investigations, the main findings were:

- (i) A bistable morphing structure was successfully produced, based on the principles of viscoelastically generated prestress; it could snap from one stable shape to another due to external loading. The bistable structure consisted of prestressed strips bonded to the sides of a thin, flexible resin impregnated fibre-glass sheet, and bistability was achieved through pairs of strips orientated to give opposing cylindrical configurations within the sheet.
- (ii) Limited applicability of the widely used beam bending equation (as used for prestressed concrete) was observed in terms of the VPPMC-based samples; it was considered that the effective modulus of the structure was significantly influenced by the addition of the fibreglass layer.
- (iii) A small ripple effect (unstable load transition) was observed during snap-through loading; since this was not detected with numerical simulation results, it may have been attributable to the hand lay-up process used during production of the bistable structure, i.e. non-uniform distribution of resin. This effect could be reduced by employing a greater contact area of loading.
- (iv) Numerical simulation results showed good agreement with experimental work in terms of peak load and critical displacement; bistability was developed through the accumulation of localised contours in two directions, and it depended on the modulus ratio of the constituent materials. A snap-

through mechanism for the bistable structure was proposed, based on these observations.

8.2 FUTURE WORK

Following the above findings and observations, directions for future work are proposed below to facilitate the understanding of viscoelastic prestress mechanisms. Some of the questions raised are direct results of the current study. Further investigations could be made to expand the research into VPPMC technology.

8.2.1 Investigation into fibre-matrix interfaces

As reported in Section 4.3.3, the mechanical benefits from viscoelastic fibre prestressing have been found to decrease with increasing impact toughness of the matrix materials. It may be important to study the effects of matrix toughness on the fibre-matrix interface regions within a VPPMC, to promote understanding of the load transfer mechanisms. Viscoelastically generated prestress can induce compressive stresses into a matrix (Section 2.5.1), which can impede crack propagation when VPPMCs are subjected to mechanical testing. A feasibility study of fibre-matrix interface effects within a VPPMC has been reported by Ge et al [221], using (a) microhardness testing and (b) scanning electron microscope mirror effect (SEMME) techniques. For (a), prestressed polymeric fibres within a VPPMC are undergoing viscoelastic recovery, which in turn changes the microhardness indentation geometry; by comparing the changes in prestressed composite samples with their non-prestressed counterparts, the effects of matrix toughness may be obtained. For (b), since the fibre-matrix interfaces have been observed to play a major role in the trapping or diffusion of charges, which is associated with interface strength [222, 223], providing information relating to matrix toughness effects. Therefore, these may also provide useful information towards the further understanding of the fibre-matrix interactions.

8.2.2 Fibre stretching apparatus

It has been demonstrated in Section 6.4.5 that viscoelastic fibre prestressing under 330 MPa for 24 h is broadly the same as 590 MPa, 37 min creep conditions. By subjecting the fibre to a higher creep stress however, it may be possible to reduce the processing time further. In addition, longer exposure of fibres towards the optimum creep strain levels would approach the maximum available viscoelastic energy storage capabilities for the fibre materials. Further investigations into these aspects would require a more suitable fibre stretching method to avoid stress concentrations, which may cause premature fracture of the fibre materials. In addition, previous research into VPPMC technology has extensively focused on unidirectional fibres within small VPPMC strip samples, using low-velocity impact testing as the main investigative method. On-going research includes VPPMCs as continuous or discontinuous prestressed fibre reinforced composite laminates or plates. Therefore, future research may look into the development of fibre processing apparatus for larger amounts of fibre prestressing purposes.

8.2.3 Morphing composite structures

There has been increasing interest in recent years in using composites to produce morphing structures, the simplest being those can snap between one of two stable states. The present research has produced a bistable structure utilising viscoelastic fibre prestressing (Chapter 7); however, multistable structures may also be achievable. For example, based on the same principle, a number of the single bistable structures could be combined to produce a multistable assembly. Moreover, it has been reported that elastic fibre prestressing can be used to create bistable composite laminates [70, 71], the out-of-plane deflections being induced from independent control of elastic prestress levels. Thus, viscoelastic fibre prestressing may also be applicable to the production of bistable or multistable laminates, and deflections could be expected to be controlled by manipulation of the viscoelastic creep strain levels. For example, semi-crystalline fibre, i.e. nylon 6,6 or UHMWPE fibres, used for generating viscoelastically prestress, could be commingled (either within the same layer or impregnated as different layers) with common reinforcing fibres (such as glass or carbon fibre) to produce morphing laminates.

An initial study of prestressed nylon 6,6 fibre commingled with Kevlar fibre hybrid composites has been recently reported [8].

8.3 CONCLUSIONS

In this research, comprehensive experimental and numerical investigations have been carried out to facilitate the industrial application of VPPMCs. The processing time for viscoelastic fibre prestressing is significantly reduced from 24 h to tens of minutes by employing higher creep stress values, with no detriment to impact performance. Longer exposure of nylon fibre to a higher creep strain level increases the prestress benefits. However, there is an optimum viscoelastic creep strain level to obtain maximum prestress effects. The increase in creep stress (at constant creep time) and creep time (at constant creep stress) have similar influence on prestress benefits. Thus the optimum creep strain level can be achieved either through lower creep stress over a longer period, or higher creep stress within a shorter term. This relates to the time-stress superposition principle. A morphing (shape-changing) structure has been produced by the use of viscoelastically generated prestress. This can be modelled (using the finite element method) to investigate the influence of various factors.

REFERENCES

1. Pang, J.W.C. and K.S. Fancey, *The flexural stiffness characteristics of viscoelastically prestressed polymeric matrix composites*. Composites Part A: Applied Science and Manufacturing, 2009. **40**(6-7): p. 784-790.
2. Fancey, K.S., *Fiber-reinforced polymeric composites with viscoelastically induced prestress*. Journal of Advanced Materials, 2005. **37**(2): p. 21-29.
3. Fazal, A. and K.S. Fancey, *UHMWPE fibre-based composites: Prestress-induced enhancement of impact properties*. Composites Part B: Engineering, 2014. **66**: p. 1-6.
4. Fazal, A. and K.S. Fancey, *Viscoelastically generated prestress from ultra-high molecular weight polyethylene fibres*. Journal of Materials Science, 2013. **48**(16): p. 5559-5570.
5. Fancey, K.S., *Viscoelastically prestressed polymeric matrix composites - Potential for useful life and impact protection*. Composites Part B-Engineering, 2010. **41**(6): p. 454-461.
6. Pang, J.W.C. and K.S. Fancey, *Analysis of the tensile behaviour of viscoelastically prestressed polymeric matrix composites*. Composites Science and Technology, 2008. **68**(7-8): p. 1903-1910.
7. Fazal, A. and K.S. Fancey, *Viscoelastically prestressed polymeric matrix composites – Effects of test span and fibre volume fraction on Charpy impact characteristics*. Composites Part B: Engineering, 2013. **44**(1): p. 472-479.
8. Fazal, A. and K.S. Fancey, *Performance enhancement of nylon/kevlar fiber composites through viscoelastically generated pre-stress*. Polymer Composites, 2014. **35**(5): p. 931-938.
9. Fancey, K.S., *Composite fibre-containing materials*. 1997: UK (Patent Number: 2281299B).
10. Pang, J.W.C. and K.S. Fancey, *An investigation into the long-term viscoelastic recovery of Nylon 6,6 fibres through accelerated ageing*. Materials Science and Engineering: A, 2006. **431**(1-2): p. 100-105.
11. Fancey, K.S., *Prestressed polymeric composites produced by viscoelastically strained nylon 6,6 fibre reinforcement*. Journal of Reinforced Plastics and Composites, 2000. **19**(15): p. 1251-1266.
12. Fancey, K.S., *Investigation into the feasibility of viscoelastically generated pre-stress in polymeric matrix composites*. Materials Science and Engineering A-

- Structural Materials Properties Microstructure and Processing, 2000. **279**(1-2): p. 36-41.
13. Jose, J.P. and K. Joseph, *Advances in Polymer Composites: Macro- and Microcomposites – State of the Art, New Challenges, and Opportunities*, in *Polymer Composites*. 2012, Wiley-VCH Verlag GmbH & Co. KGaA. p. 1-16.
 14. Hull, D. and T. Clyne, *An introduction to composite materials*. 1996: Cambridge university press.
 15. Mallick, P.K., *Fiber-reinforced composites: materials, manufacturing, and design*. 2010: CRC press.
 16. Crawford, R.J., *Plastics engineering*. 1998: Butterworth-Heinemann.
 17. Krishnamurthy, S., *Pre-stressed advanced fibre reinforced composites fabrication and mechanical performance*. 2006, Cranfield University: United Kingdom (PhD Thesis).
 18. Lakes, R.S., *Viscoelastic solids*. Vol. 9. 1998: CRC press.
 19. Voigt, W., *Ueber die Beziehung zwischen den beiden Elasticitätsconstanten isotroper Körper*. *Annalen der Physik*, 1889. **274**(12): p. 573-587.
 20. Reuss, A., *Berechnung der Fließgrenze von Mischkristallen auf Grund der Plastizitätsbedingung für Einkristalle*. *ZAMM - Journal of Applied Mathematics and Mechanics / Zeitschrift für Angewandte Mathematik und Mechanik*, 1929. **9**(1): p. 49-58.
 21. Bergstrom, J.S. and M.C. Boyce, *Mechanical behavior of particle filled elastomers*. *Rubber chemistry and technology*, 1999. **72**(4): p. 633-656.
 22. Wang, M. and N. Pan, *Elastic property of multiphase composites with random microstructures*. *Journal of Computational Physics*, 2009. **228**(16): p. 5978-5988.
 23. Jones, R.M., *Mechanics of Composite Materials*. 1975, New York: McGraw-Hill Book Co.
 24. Hill, R., *Elastic properties of reinforced solids: some theoretical principles*. *Journal of the Mechanics and Physics of Solids*, 1963. **11**(5): p. 357-372.
 25. Upadhyay, A. and R. Singh, *Prediction of Effective Elastic Modulus of Biphase Composite Materials*. *Modern Mechanical Engineering*, 2012. **2**(01): p. 6-13.
 26. Hsieh, C.L., W.H. Tuan, and T.T. Wu, *Elastic behaviour of a model two-phase material*. *Journal of the European Ceramic Society*, 2004. **24**(15-16): p. 3789-3793.
 27. Dai, L.H., Z.P. Huang, and R. Wang, *Explicit expressions for bounds for the effective moduli of multi-phased composites by the generalized self-consistent method*. *Composites Science and Technology*, 1999. **59**(11): p. 1691-1699.

28. Hashin, Z. and S. Shtrikman, *A variational approach to the theory of the elastic behaviour of multiphase materials*. Journal of the Mechanics and Physics of Solids, 1963. **11**(2): p. 127-140.
29. Te Wu, T., *On the parametrization of the elastic moduli of two-phase materials*. Journal of Applied Mechanics, 1965. **32**(1): p. 211-214.
30. Hashin, Z., *Analysis of composite materials—a survey*. Journal of Applied Mechanics, 1983. **50**(3): p. 481-505.
31. Shen, Y.L., et al., *Effective elastic response of two-phase composites*. Acta Metallurgica et Materialia, 1994. **42**(1): p. 77-97.
32. Ravichandran, K.S., *Elastic properties of two-phase composites*. Journal of the American Ceramic Society, 1994. **77**(5): p. 1178-1184.
33. Wang, J.A., J. Lubliner, and P.J.M. Monteiro, *A modified direct method for the calculation of elastic moduli of composite materials*, in *Conference: 1. international conference on composites in infrastructure, Tucson, AZ (United States)*. 15-17 Jan 1996: p. 1-15.
34. Mansfield, E.H., *On the elastic moduli of unidirectional fibre reinforced composites*. 1976, Her Majesty's Stationery Office: London. p. 1-18.
35. Materials, A. *E-glass fibre properties*. 2015 [Accessed 2015 November 21, 2015]; Available from: <http://www.azom.com/properties.aspx?ArticleID=764>.
36. Benedikt, B., et al., *An analysis of residual thermal stresses in a unidirectional graphite/PMR-15 composite based on X-ray diffraction measurements*. Composites Science and Technology, 2001. **61**(14): p. 1977-1994.
37. Parlevliet, P.P., H.E. Bersee, and A. Beukers, *Residual stresses in thermoplastic composites—A study of the literature—Part I: Formation of residual stresses*. Composites Part A: Applied Science and Manufacturing, 2006. **37**(11): p. 1847-1857.
38. Jang, B.Z., *Advanced polymer composites: principles and applications*, ed. A. International. 1994, USA: Taylor & Francis.
39. Parlevliet, P.P., H.E. Bersee, and A. Beukers, *Residual stresses in thermoplastic composites—a study of the literature. Part III: Effects of thermal residual stresses*. Composites Part A: Applied Science and Manufacturing, 2007. **38**(6): p. 1581-1596.
40. Tuttle, M.E., R.T. Koehler, and D. Keren, *Controlling Thermal Stresses in Composites by Means of Fiber Prestress*. Journal of Composite Materials, 1996. **30**(4): p. 486-502.
41. Wisnom, M.R., et al., *Mechanisms generating residual stresses and distortion during manufacture of polymer–matrix composite structures*. Composites Part A: Applied Science and Manufacturing, 2006. **37**(4): p. 522-529.

42. Hahn, H.T., *Residual stresses in polymer matrix composite laminates*. Journal of Composite Materials, 1976. **10**(4): p. 266-278.
43. Morozov, V.N., et al., *Effect of heat treatment on the distribution of residual stresses and the properties of epoxy polymers*. Mechanics of Composite Materials, 1987. **22**(5): p. 535-538.
44. Shokrieh, M.M., A. Daneshvar, and S. Akbari, *Reduction of thermal residual stresses of laminated polymer composites by addition of carbon nanotubes*. Materials & Design, 2014. **53**: p. 209-216.
45. Shokrieh, M.M., et al., *The use of carbon nanofibers for thermal residual stress reduction in carbon fiber/epoxy laminated composites*. Carbon, 2013. **59**: p. 255-263.
46. White, S. and H. Hahn, *Mechanical property and residual stress development during cure of a graphite/BMI composite*. Polymer Engineering & Science, 1990. **30**(22): p. 1465-1473.
47. Zhigun, I.G., *Experimental evaluation of the effect of prestressing the fibers in two directions on certain elastic characteristic of woven-glass reinforced plastics*. Mechanics of Composite Materials, 1968. **4**(4-6): p. 691-695.
48. Tuttle, M.E., *A Mechanical/thermal analysis of prestressed composite laminates*. Journal of Composite Materials, 1988. **22**(8): p. 780-792.
49. Fancey, K.S., *Viscoelastically prestressed polymeric matrix composites*, in *Polymer Composites*. 2012, Wiley-VCH Verlag GmbH & Co. KGaA. p. 715-746.
50. Mills, G.J. and R.J. Dauksys, *Effects of prestressing boron/epoxy prepreg on composite strength properties*. AIAA Journal, 1973. **11**(11): p. 1459-1460.
51. Brown, G., *Development of prestressed graphite processing techniques*. 1976, DTIC Document: p. 1-30.
52. Zhifan Chi and T.-W. Chou, *An experimental study of the effect of prestressed loose carbon strands on composite strength*. Journal of Composite Materials, 1983. **17**(3): p. 196-209.
53. Manders, P.W. and T.W. Chou, *Enhancement of strength in composites reinforced with previously stressed fibers*. Journal of Composite Materials, 1983. **17**(1): p. 26-44.
54. Zweben, C. and B.W. Rosen, *A statistical theory of material strength with application to composite materials*. Journal of the Mechanics and Physics of Solids, 1970. **18**(3): p. 189-206.
55. Hedgepeth, J.M., *Stress concentrations in filamentary structures*. NASA Technical Report, 1961: p. 1-36.
56. Motahhari, S. and J. Cameron, *Impact strength of fiber pre-stressed composites*. Journal of Reinforced Plastics and Composites, 1998. **17**(2): p. 123-130.

57. Motahhari, S. and J. Cameron, *Fibre prestressed composites: improvement of flexural properties through fibre prestressing*. Journal of Reinforced Plastics and Composites, 1999. **18**(3): p. 279-288.
58. Zhao, J. and J. Cameron, *Polypropylene matrix composites reinforced with prestressed glass fibers*. Polymer Composites, 1998. **19**(3): p. 218-224.
59. Jorge, L.D.A., A.T. Marques, and P.M.S.T. De Castro, *The influence of prestressing on the mechanical behaviour of uni-directional composites*, in *Developments in the Science and Technology of Composite Materials: Fourth European Conference on Composite Materials September 25–28, 1990 Stuttgart-Germany*, J. Füller, et al., Editors. 1990, Springer Netherlands: Dordrecht. p. 897-902.
60. Cao, Y. and J. Cameron, *Flexural and shear properties of silica particle modified glass fiber reinforced epoxy composite*. Journal of reinforced plastics and composites, 2006. **25**(4): p. 347-359.
61. Hassan, A.K.F. and O.A. Abdullah, *New methodology for prestressing fiber composites*. Universal Journal of Mechanical Engineering, 2015. **3**(6): p. 252-261.
62. Mostafa, N.H., et al., *Effect of equi-biaxially fabric prestressing on the tensile performance of woven E-glass/polyester reinforced composites*. Journal of Reinforced Plastics and Composites, 2016 (In press).
63. Hadi, A.S. and J.N. Ashton, *On the influence of pre-stress on the mechanical properties of a unidirectional GRE composite*. Composite Structures, 1998. **40**(3–4): p. 305-311.
64. Schulte, K. and R. Marissen, *Influence of artificial pre-stressing during curing of CFRP laminates on interfibre transverse cracking*. Composites science and technology, 1992. **44**(4): p. 361-367.
65. Rose, D.H. and J.M. Whitney. *Effect of prestressed fibers upon the response of composite materials*. 1993. Technomic Publishing Company Inc.
66. Hashin, Z. and B.W. Rosen, *The elastic moduli of fiber-reinforced materials*. Journal of applied mechanics, 1964. **31**(2): p. 223-232.
67. Sui, G.X., G. Yao, and B.L. Zhou, *Influence of artificial pre-stressing during the curing of VIRALL on its mechanical properties*. Composites Science and Technology, 1995. **53**(4): p. 361-364.
68. Guo-xin, S., Y. Ge, and Z. Ben-lian, *Effects of prestrain on the fatigue properties of VIRALL laminate*. Composites Science and Technology, 1996. **56**(8): p. 929-932.
69. Hyer, M.W., *Calculation of the room-temperature shapes of unsymmetric laminates*. Journal of Composite Materials, 1981. **15**(1981): p. 296-310.
70. Daynes, S., K.D. Potter, and P.M. Weaver, *Bistable prestressed buckled laminates*. Composites Science and Technology, 2008. **68**(15-16): p. 3431-3437.

71. Daynes, S., et al., *Bistable prestressed symmetric laminates*. Journal of Composite Materials, 2010. **44**(9): p. 1119-1137.
72. Lachenal, X., S. Daynes, and P.M. Weaver, *A non-linear stiffness composite twisting I-beam*. Journal of Intelligent Material Systems and Structures, 2013. **25**: p. 744-754.
73. Lachenal, X., P.M. Weaver, and S. Daynes, *Multi-stable composite twisting structure for morphing applications*. Proceedings of the Royal Society A: Mathematical, Physical and Engineering Sciences, 2012. **468**(2141): p. 1230-1251.
74. BEKAMPIENĖ, P., J. DOMSKIENĖ, and A. ŠIRVAITIENĖ, *The effect of pre-tension on deformation behaviour of natural fabric reinforced composite*. Materials Science, 2011. **17**(1): p. 56-61.
75. Širvaitienė, A., et al., *Vegetable fiber pre-tensioning influence on the composites reinforcement*. Polymer Composites, 2013. **34**(9): p. 1533-1537.
76. Zaidi, B.M., K. Magniez, and M. Miao, *Prestressed natural fibre spun yarn reinforced polymer-matrix composites*. Composites Part A: Applied Science and Manufacturing, 2015. **75**: p. 68-76.
77. Scherf, J. and H.D. Wagner, *Interpretation of fiber fragmentation in carbon/epoxy single fiber composites: Possible fiber pre-tension effects*. Polymer Engineering & Science, 1992. **32**(4): p. 298-304.
78. Motahhari, S. and J. Cameron, *Measurement of micro-residual stresses in fiber-prestressed composites*. Journal of reinforced plastics and composites, 1997. **16**(12): p. 1129-1137.
79. Dvorak, G.J. and A.P. Suvorov, *The effect of fiber pre-stress on residual stresses and the onset of damage in symmetric laminates*. Composites Science and Technology, 2000. **60**(8): p. 1129-1139.
80. Suvorov, A.P. and G.J. Dvorak, *Optimal design of prestressed laminate/ceramic plate assemblies*. Meccanica, 2001. **36**(1): p. 87-109.
81. Suvorov, A.P. and G.J. Dvorak, *Optimized fiber prestress for reduction of free edge stresses in composite laminates*. International journal of solids and structures, 2001. **38**(38): p. 6751-6786.
82. Jevons, M.P., *The effects of fibre pre-stressing on the impact performance of composite laminates*. 2004, Cranfield University: United Kingdom (PhD Thesis).
83. Cao, Y. and J. Cameron, *Impact properties of silica particle modified glass fiber reinforced epoxy composite*. Journal of reinforced plastics and composites, 2006. **25**(7): p. 761-769.
84. Schlichting, L.H., et al., *Composite resin reinforced with pre-tensioned glass fibers. Influence of prestressing on flexural properties*. Dental Materials, 2010. **26**(2): p. 118-125.

85. Jie, L., et al., *Composite resin reinforced with pre-tensioned fibers: a three-dimensional finite element study on stress distribution*. *Odontology*, 2013. **101**(1): p. 29-33.
86. Graczykowski, C., A. Orlowska, and R. Venkat. *The concept of smart prestressed composites. Numerical modelling and experimental evaluation*. in *6th ECCOMAS thematic conference on smart structures and materials*. 2013: Torino, Italy. p. 1-22.
87. Nishi, Y., et al., *Effects of tensile prestress level on impact value of 50 vol% continuous unidirectional 0 degree oriented carbon fiber reinforced epoxy polymer (CFRP)*. *Materials Transactions*, 2014. **55**(2): p. 318-322.
88. Mostafa, N.H., et al., *The influence of equi-biaxially fabric prestressing on the flexural performance of woven E-glass/polyester-reinforced composites*. *Journal of Composite Materials*, 2015. **50**(24): p. 3385-3393.
89. Graczykowski, C., A. Orlowska, and J. Holnicki-Szulc, *Prestressed composite structures – Modeling, manufacturing, design*. *Composite Structures*, 2016. **151**: p. 172-182.
90. Mostafa, N.H., et al., *Effect of fabric biaxial prestress on the fatigue of woven E-glass/polyester composites*. *Materials & Design*, 2016. **92**: p. 579-589.
91. Krishnamurthy, S., et al., *Monitoring pre-stressed composites using optical fibre sensors*. *Sensors*, 2016. **16**(6): p. 1-24.
92. Fazal, A., *Polymer fibre composites: investigation into performance enhancement through viscoelastically generated pre-stress*. 2014, University of Hull: United Kingdom (PhD Thesis).
93. Mostafa, N.H., et al., *Fibre prestressed polymer-matrix composites: a review*. *Journal of Composite Materials*, 2016 (In press).
94. Cui, H., et al., *The flexural characteristics of prestressed bamboo slivers reinforced parallel strand lumber (PSL)*. *Key Engineering Materials*, 2012. **517**: p. 96-100.
95. Fancey, K.S., *Viscoelastically prestressed polymeric matrix composites: An overview*. *Journal of Reinforced Plastics and Composites*, 2016 (In press).
96. Fancey, K.S., *A latch-based weibull model for polymeric creep and recovery*. *Journal of Polymer Engineering*, 2001. **21**(6): p. 489-509.
97. Fancey, K.S., *A mechanical model for creep, recovery and stress relaxation in polymeric materials*. *Journal of Materials Science*, 2005. **40**(18): p. 4827-4831.
98. Fancey, K.S. and A. Fazal, *Prestressed polymeric matrix composites: Longevity aspects*. *Polymer Composites*, 2015. **37**(7): p. 2092-2097.

99. Pang, J.W.C., B.M. Lamin, and K.S. Fancey, *Force measurement from viscoelastically recovering Nylon 6,6 fibres*. *Materials Letters*, 2008. **62**(10-11): p. 1693-1696.
100. Lin, L. and A.S. Argon, *Structure and plastic deformation of polyethylene*. *Journal of Materials Science*, 1994. **29**(2): p. 294-323.
101. Hiss, R., et al., *Network stretching, slip processes, and fragmentation of crystallites during uniaxial drawing of polyethylene and related copolymers. A comparative study*. *Macromolecules*, 1999. **32**(13): p. 4390-4403.
102. Butler, M.F., A.M. Donald, and A.J. Ryan, *Time resolved simultaneous small- and wide-angle X-ray scattering during polyethylene deformation—II. Cold drawing of linear polyethylene*. *Polymer*, 1998. **39**(1): p. 39-52.
103. Bartczak, Z., A.S. Argon, and R.E. Cohen, *Texture evolution in large strain simple shear deformation of high density polyethylene*. *Polymer*, 1994. **35**(16): p. 3427-3441.
104. Bukošek, V. and D.C. Prevorsek, *Model of nylon 6 fibers microstructure microfibrillar Model or “swiss-cheese” model?* *International Journal of Polymeric Materials*, 2000. **47**(4): p. 569-592.
105. Peterlin, A., *Drawing and annealing of fibrous material*. *Journal of Applied Physics*, 1977. **48**(10): p. 4099-4108.
106. Peterlin, A., *Plastic deformation of polymers with fibrous structure*. *Colloid and Polymer Science*, 1975. **253**(10): p. 809-823.
107. Prevorsek, D., et al., *Nylon 6 fibers: changes in structure between moderate and high draw ratios*. *Journal of Macromolecular Science, Part B: Physics*, 1973. **8**(1-2): p. 127-156.
108. Peterlin, A., *Molecular model of drawing polyethylene and polypropylene*. *Journal of Materials Science*, 1971. **6**(6): p. 490-508.
109. Oudet, C. and A. Bunsell, *Effects of structure on the tensile, creep and fatigue properties of polyester fibres*. *Journal of Materials Science*, 1987. **22**(12): p. 4292-4298.
110. Shermatov, M., et al., *Instability of the crystallites in oriented polymers under load*. *Polymer Mechanics*, 1976. **12**(3): p. 468-472.
111. Marcellan, A., et al., *A multi-scale analysis of the microstructure and the tensile mechanical behaviour of polyamide 66 fibre*. *Polymer*, 2006. **47**(1): p. 367-378.
112. Peterlin, A., *Morphology and fracture of drawn crystalline polymers*. *Journal of Macromolecular Science, Part B: Physics*, 1973. **8**(1-2): p. 83-100.
113. Starkova, O., J. Yang, and Z. Zhang, *Application of time–stress superposition to nonlinear creep of polyamide 66 filled with nanoparticles of various sizes*. *Composites Science and Technology*, 2007. **67**(13): p. 2691-2698.

-
114. O'Shaughnessy, M.T., *An experimental study of the creep of rayon*. Textile Research Journal, 1948. **18**(5): p. 263-280.
115. Barbarino, S., et al., *A review of morphing aircraft*. Journal of Intelligent Material Systems and Structures, 2011. **22**(9): p. 823-877.
116. Thill, C., et al., *Morphing skins*. The Aeronautical Journal, 2008. **112**(1129): p. 117-139.
117. Sofla, A., et al., *Shape morphing of aircraft wing: Status and challenges*. Materials & Design, 2010. **31**(3): p. 1284-1292.
118. Daynes, S. and P.M. Weaver, *Review of shape-morphing automobile structures: concepts and outlook*. Proceedings of the Institution of Mechanical Engineers, Part D: Journal of Automobile Engineering, 2013. **227**(11): p. 1603-1622.
119. Lachenal, X., S. Daynes, and P.M. Weaver, *Review of morphing concepts and materials for wind turbine blade applications*. Wind Energy, 2013. **16**(2): p. 283-307.
120. Hyer, M.W., *The room-temperature shapes of four-layer unsymmetric cross-ply laminates*. Journal of Composite Materials, 1982. **16**(4): p. 318-340.
121. Hyer, M.W., *Some observations on the cured shape of thin unsymmetric laminates*. Journal of Composite Materials, 1981. **15**(2): p. 175-194.
122. Portela, P., et al., *Analysis of morphing, multi stable structures actuated by piezoelectric patches*. Computers & Structures, 2008. **86**(3-5): p. 347-356.
123. M.R. Schultz, *A new concept for active bistable twisting structures*. Proceeding SPIE: Smart Structures and Materials 2005. **5764**: p. 241-252.
124. Daynes, S. and P. Weaver, *Analysis of unsymmetric CFRP-metal hybrid laminates for use in adaptive structures*. Composites Part A: Applied Science and Manufacturing, 2010. **41**(11): p. 1712-1718.
125. Betts, D., *Modelling and optimisation of bistable composite laminates*. 2012, University of Bath: United Kingdom (PhD Thesis).
126. Dano, M.-L. and M.W. Hyer, *Thermally-induced deformation behavior of unsymmetric laminates*. International Journal of Solids and Structures, 1998. **35**(17): p. 2101-2120.
127. Dano, M.L. and M.W. Hyer, *Snap-through of unsymmetric fiber-reinforced composite laminates*. International Journal of Solids and Structures, 2002. **39**(1): p. 175-198.
128. Akira, H. and M.W. Hye, *Non-linear temperature-curvature relationships for unsymmetric graphite-epoxy laminates*. International Journal of Solids and Structures, 1987. **23**(7): p. 919-935.

129. Kim, K.S. and H.T. Hahn, *Residual stress development during processing of graphite/epoxy composites*. Composites Science and Technology, 1989. **36**(2): p. 121-132.
130. Diaconu, C.G., P.M. Weaver, and F. Mattioni, *Concepts for morphing airfoil sections using bi-stable laminated composite structures*. Thin-Walled Structures, 2008. **46**(6): p. 689-701.
131. Potter, K.D. and P.M. Weaver, *A concept for the generation of out-of-plane distortion from tailored FRP laminates*. Composites Part A: Applied Science and Manufacturing, 2004. **35**(12): p. 1353-1361.
132. Hufenbach, W. and M. Gude, *Analysis and optimisation of multistable composites under residual stresses*. Composite Structures, 2002. **55**(3): p. 319-327.
133. Gigliotti, M., M.R. Wisnom, and K.D. Potter, *Loss of bifurcation and multiple shapes of thin [0/90] unsymmetric composite plates subject to thermal stress*. Composites Science and Technology, 2004. **64**(1): p. 109-128.
134. Whitney, J.M. and N.J. Pagano, *Shear deformation in heterogeneous anisotropic plates*. Journal of Applied Mechanics, 1970. **37**(4): p. 1031-1036.
135. Whitney, J.M., *Shear correction factors for orthotropic laminates under static load*. Journal of Applied Mechanics, 1973. **40**(1): p. 302-304.
136. Mittelstedt, C. and W. Becker, *Free-edge effects in composite laminates*. Applied Mechanics Reviews, 2007. **60**(5): p. 217-245.
137. Mittelstedt, C. and W. Becker, *Interlaminar stress concentrations in layered structures: part I - a selective literature survey on the free-edge effect since 1967*. Journal of Composite Materials, 2004. **38**(12): p. 1037-1062.
138. Kant, T. and K. Swaminathan, *Estimation of transverse/interlaminar stresses in laminated composites—a selective review and survey of current developments*. Composite structures, 2000. **49**(1): p. 65-75.
139. Gigliotti, M., M.R. Wisnom, and K.D. Potter, *Development of curvature during the cure of AS4/8552 [0/90] unsymmetric composite plates*. Composites Science and Technology, 2003. **63**(2): p. 187-197.
140. Etches, J., et al., *Environmental effects on thermally induced multistability in unsymmetric composite laminates*. Composites Part A: Applied Science and Manufacturing, 2009. **40**(8): p. 1240-1247.
141. Gigliotti, M., et al., *Predicting loss of bifurcation behaviour of 0/90 unsymmetric composite plates subjected to environmental loads*. Composite Structures, 2012. **94**(9): p. 2793-2808.
142. Seymour, R.B., *Polymers for engineering applications*. 1987, United States: American Society for Metals. 65-66.

143. Bunn, C. and E. Garner. *The crystal structures of two polyamides ('nylons')*. in *Proceedings of the Royal Society of London A: Mathematical, Physical and Engineering Sciences*. 1947. **189**(2): 39-68.
144. Babatope, B. and D.H. Isaac, *Annealing of isotropic nylon-6,6*. *Polymer*, 1992. **33**(8): p. 1664-1668.
145. Ltd., G.C. *Polyamide - Nylon 6,6 PA 6,6 data sheet*. [Accessed July 2015]; Available from: <http://www.goodfellow.com>.
146. Lewin, M., *Handbook of fiber chemistry*. 2006: CRC Press.
147. Dholakiya, B., *Unsaturated polyester resin for specialty applications*, in *polyester*, D.H.E.-D. Saleh, Editor. 2012, In Tech.
148. Carothers, W.H., *Studies on polymerization and ring formation. i. an introduction to the general theory of condensation polymers*. *Journal of the American Chemical Society*, 1929. **51**(8): p. 2548-2559.
149. Jones, F.R., *Handbook of polymer-fibre composites*. 1994: Longman.
150. Dismore, P.F. and W. Statton. *Chain folding in oriented nylon 66 fibers*. in *Journal of Polymer Science Part C: Polymer Symposia*. 1966. Wiley Online Library.
151. Statton, W., *High-temperature annealing of drawn nylon 66 fibers*. *Journal of Polymer Science Part A-2: Polymer Physics*, 1972. **10**(8): p. 1587-1592.
152. Sakaoku, K., N. Morosoff, and A. Peterlin, *Drawing of nylon 6 fibers (bristles)*. *Journal of Polymer Science: Polymer Physics Edition*, 1973. **11**(1): p. 31-42.
153. Dumbleton, J. and D. Buchanan, *Annealing experiments on drawn nylon 66 fibers*. *Journal of Polymer Science Part A-2: Polymer Physics*, 1968. **6**(8): p. 1527-1533.
154. Matsuoka, S., *Structural relationship between thermomechanical history and strength of polymeric solids*. *Polymer Engineering & Science*, 1974. **14**(3): p. 162-166.
155. Founda, I., et al., *Optothermal properties of fibers. III. Optical anisotropy in nylon 66 fibers as a function of annealing process*. *Journal of applied polymer science*, 1996. **60**(9): p. 1247-1267.
156. Fouda, I., *Optothermal properties of fiber morphology on nylon 66 fibers due to annealing and drawing processes*. *Journal of applied polymer science*, 2002. **84**(5): p. 916-928.
157. Meinel, G. and A. Peterlin, *Changes in noncrystalline regions of polyethylene during annealing*. *Journal of Polymer Science Part B: Polymer Letters*, 1967. **5**(8): p. 613-618.
158. Bragg, W.L., *The specular reflection of X-rays*. *Nature*, 1912. **90**: p. 410-410.

159. Bragg, W.L. *The diffraction of short electromagnetic waves by a crystal*. in *Proceedings of the Cambridge Philosophical Society*. 1913. **17**: 43-57.
160. Ooi, L.-I., *Principles of X-ray crystallography*. 2010: Oxford University Press.
161. Zhang, S., L. Li, and A. Kumar, *Materials characterization techniques*. 2008: CRC Press.
162. Starkweather, H.W., J.F. Whitney, and D.R. Johnson, *Crystalline order in nylon 66*. *Journal of Polymer Science Part A: General Papers*, 1963. **1**(2): p. 715-723.
163. Brill, R., *über das Verhalten von Polyamiden beim Erhitzen*. *Journal für Praktische Chemie*, 1942. **161**(1-3): p. 49-64.
164. Takashi, I., *Change with temperature in crystal structures of nylons 6, 66 and 610*. *Japanese Journal of Applied Physics*, 1976. **15**(12): p. 2295.
165. Colclough, M. and R. Baker, *Polymorphism in nylon 66*. *Journal of materials science*, 1978. **13**(12): p. 2531-2540.
166. Starkweather, H.W. and G.A. Jones, *Crystalline transitions in powders of nylon 66 crystallized from solution*. *Journal of Polymer Science: Polymer Physics Edition*, 1981. **19**(3): p. 467-477.
167. Liu, X., et al., *Phase transition in polyamide-66/montmorillonite nanocomposites on annealing*. *Journal of Polymer Science Part B: Polymer Physics*, 2003. **41**(1): p. 63-67.
168. Lu, Y., et al., *Influence of thermal processing on the perfection of crystals in polyamide 66 and polyamide 66/clay nanocomposites*. *Polymer*, 2004. **45**(26): p. 8999-9009.
169. Starkweather, H.W., P. Zoller, and G.A. Jones, *The heat of fusion of 66 nylon*. *Journal of Polymer Science: Polymer Physics Edition*, 1984. **22**(9): p. 1615-1621.
170. Murthy, N., S. Aharoni, and A. Szollosi, *Stability of the γ form and the development of the α form in nylon 6*. *Journal of Polymer Science: Polymer Physics Edition*, 1985. **23**(12): p. 2549-2565.
171. Murthy, N., *Metastable crystalline phases in nylon 6*. *Polymer communications*, 1991. **32**(10): p. 301-305.
172. Kohan, M.I., *Nylon plastics handbook*. Vol. 378. 1995: Hanser New York.
173. Lin, D.-J., et al., *Fine structure and crystallinity of porous Nylon 66 membranes prepared by phase inversion in the water/formic acid/Nylon 66 system*. *European Polymer Journal*, 2006. **42**(2): p. 356-367.
174. Segerman, E. and P. Stern, *Two-phase model for structure of polymers*. *Nature*, 1966. **210**: p. 1258-1259.

175. Heuvel, H., R. Huisman, and K. Lind, *Quantitative information from x-ray diffraction of nylon-6 yarns. I. Development of a model for the analytical description of equatorial x-ray profiles*. Journal of Polymer Science: Polymer Physics Edition, 1976. **14**(5): p. 921-940.
176. Hindeleh, A. and D. Johnson, *The resolution of multipeak data in fibre science*. Journal of Physics D: Applied Physics, 1971. **4**(2): p. 259.
177. Riekkel, C., et al., *Aspects of X-ray diffraction on single spider fibers*. International Journal of Biological Macromolecules, 1999. **24**(2): p. 179-186.
178. Murthy, N.S., et al., *Structure of the amorphous phase in oriented polymers*. Macromolecules, 1993. **26**(7): p. 1712-1721.
179. Murthy, N., et al., *Drawing and annealing of nylon-6 fibres: studies of crystal growth, orientation of amorphous and crystalline domains and their influence on properties*. Polymer, 1995. **36**(20): p. 3863-3873.
180. Huisman, R. and H. Heuvel, *Quantitative information from x-ray diffraction of nylon-6 yarns. II. Physical aspects of some quantitative parameters*. Journal of Polymer Science: Polymer Physics Edition, 1976. **14**(5): p. 941-954.
181. Dumbleton, J., D. Buchanan, and B. Bowles, *Characterization of nylon 66 structure from x-ray diffraction*. Journal of Applied Polymer Science, 1968. **12**(9): p. 2067-2078.
182. Hsiao, B.S., R. Barton, and J. Quintana, *Simple on-line X-ray setup to monitor structural changes during fiber processing*. Journal of Applied Polymer Science, 1996. **62**(12): p. 2061-2068.
183. Marcellan, A., et al., *Micro-mechanisms, mechanical behaviour and probabilistic fracture analysis of PA 66 fibres*. Journal of Materials Science, 2003. **38**(10): p. 2117-2141.
184. Feldman, A., et al., *The brill transition in transcrystalline nylon-66*. Macromolecules, 2006. **39**(13): p. 4455-4459.
185. Suzuki, A., Y. Chen, and T. Kunugi, *Application of a continuous zone-drawing method to nylon 66 fibres*. Polymer, 1998. **39**(22): p. 5335-5341.
186. Navarro-Pardo, F., et al., *Effects on the thermo-mechanical and crystallinity properties of nylon 6, 6 electrospun fibres reinforced with one dimensional (1D) and two dimensional (2D) carbon*. Materials, 2013. **6**(8): p. 3494-3513.
187. Murthy, N., H. Minor, and R. Latif, *Effect of annealing on the structure and morphology of nylon 6 fibers*. Journal of Macromolecular Science, Part B: Physics, 1987. **26**(4): p. 427-446.
188. Haberkorn, H., K. Illers, and P. Simak, *Calorimetric, X-ray and infra-red investigations on poly (hexamethylene adipamide)*. Polymer Bulletin, 1979. **1**(7): p. 485-490.

189. Starkweather, H.W. and R.E. Moynihan, *Density, infrared absorption, and crystallinity in 66 and 610 nylons*. Journal of Polymer Science, 1956. **22**(102): p. 363-368.
190. Kessler, M.R., *Advanced topics in characterization of composites*. 2004: Trafford Publishing.
191. BSI, *Plastics-Determination of Charpy impact properties BS EN ISO 179-1 (Part 1: Non-instrumented impact test)*. 2010.
192. Timoshenko, S., *Strength of materials*. 1976, New York: Robert E. Krieger Publishing Company. 258-280.
193. Howard, W.H. and M.L. Williams, *The viscoelastic properties of oriented nylon 66 fibers: part I: creep at low loads and anhydrous conditions*. Textile Research Journal, 1963. **33**(9): p. 689-696.
194. Callister, W.D. and D.G. Rethwisch, *Materials science and engineering: an introduction*. Vol. 7. 2007: Wiley New York.
195. Zhang, Z., J.-L. Yang, and K. Friedrich, *Creep resistant polymeric nanocomposites*. Polymer, 2004. **45**(10): p. 3481-3485.
196. ASTM, *Standard test methods for tensile, compressive, and flexural creep and creep-rupture of plastics [D 2990-01]*. 2001, ASTM International: West Conshohocken.
197. Findley, W.N. and F.A. Davis, *Creep and relaxation of nonlinear viscoelastic materials*. 2013: Courier Corporation.
198. Doolittle, A.K., *Studies in newtonian flow. II. The dependence of the viscosity of liquids on free-space*. Journal of Applied Physics, 1951. **22**(12): p. 1471-1475.
199. Ferry, J.D. and R.A. Stratton, *The free volume interpretation of the dependence of viscosities and viscoelastic relaxation times on concentration, pressure, and tensile strain*. Kolloid-Zeitschrift, 1960. **171**(2): p. 107-111.
200. Williams, M.L. and M.F. Bender, *Extension of unoriented nylon 66 filaments. III. Superposition of data*. Journal of Applied Physics, 1965. **36**(10): p. 3044-3049.
201. Murayama, T., J.H. Dumbleton, and M.L. Williams, *The viscoelastic properties of oriented nylon 66 fibers. Part III: Stress relaxation and dynamic mechanical properties*. Journal of Macromolecular Science, Part B, 1967. **1**(1): p. 1-14.
202. D638-02a, A., *Standard test method for tensile properties of plastics*. 2002, ASTM Standards.
203. Raisch, S.R. and B. Möglinger, *High rate tensile tests – measuring equipment and evaluation*. Polymer Testing, 2010. **29**(2): p. 265-272.

-
204. Richeton, J., et al., *A unified model for stiffness modulus of amorphous polymers across transition temperatures and strain rates*. Polymer, 2005. **46**(19): p. 8194-8201.
205. MatWeb. *materials information database*. [Accessed February 20, 2015]; Available from: <http://www.matweb.com/>.
206. Courtney, T.H., *Mechanical behaviour of materials*. 1990: McGraw-Hill Publishing Company. 224.
207. Dunell, B., A.A. Joanes, and R. Rye, *Viscoelastic behavior of nylon 6-6 monofilaments below room temperature*. Journal of colloid science, 1960. **15**(3): p. 193-204.
208. Bower, A.F., *Applied mechanics of solids*. 2009: CRC press.
209. Chevali, V.S., D.R. Dean, and G.M. Janowski, *Flexural creep behavior of discontinuous thermoplastic composites: Non-linear viscoelastic modeling and time-temperature-stress superposition*. Composites Part A: Applied Science and Manufacturing, 2009. **40**(6-7): p. 870-877.
210. Ferry, J.D., *Viscoelastic properties of polymers*. 1980: John Wiley & Sons.
211. Daynes, S. and P.M. Weaver, *Stiffness tailoring using prestress in adaptive composite structures*. Composite Structures, 2013. **106**: p. 282-287.
212. Bowen, C.R., et al., *A study of bistable laminates of generic lay-up for adaptive structures*. Strain, 2012. **48**(3): p. 235-240.
213. Gude, M., W. Hufenbach, and C. Kirvel, *Piezoelectrically driven morphing structures based on bistable unsymmetric laminates*. Composite Structures, 2011. **93**(2): p. 377-382.
214. Precast/Prestressed Concrete Institute, *PCI design handbook: precast and prestressed concrete, 7th Edition*. 2008: PCI, Chicago.
215. Chen, W., H. Hao, and S. Chen, *Numerical analysis of prestressed reinforced concrete beam subjected to blast loading*. Materials & Design, 2015. **65**: p. 662-674.
216. Aly, M.F., I. Goda, and G.A. Hassan, *Experimental investigation of the dynamic characteristics of laminated composite beams*. International Journal of Mechanical & Mechatronics, 2010. **10**: p. 59-67.
217. Davallo, M. and H. Pasdar, *Comparison of mechanical properties of glass-polyester composites formed by resin transfer molding and hand lay-up technique*. International Journal of Chem Tech Research CODEN (USA): IJCRGG, 2009. **1**(3): p. 470-475.
218. Rodríguez, E., et al., *Characterization of composites based on natural and glass fibers obtained by vacuum infusion*. Journal of Composite Materials, 2005. **39**(3): p. 265-282.

-
219. Dai, F., H. Li, and S. Du, *A multi-stable lattice structure and its snap-through behavior among multiple states*. *Composite Structures*, 2013. **97**: p. 56-63.
 220. Lee, J.-G., et al., *Effect of initial tool-plate curvature on snap-through load of unsymmetric laminated cross-ply bistable composites*. *Composite Structures*, 2015. **122**: p. 82-91.
 221. Ge, C., B. Wang, and K.S. Fancey. *Techniques to investigate viscoelastically generated prestress in polymeric composites*. in *10th International Conference on Composite Science and Technology (ICCST/10)*. 2015. Lisbon, Portugal. p. 1-11.
 222. Kchaou, B., et al., *Role of fibre–matrix interface and fibre direction on dielectric behaviour of epoxy composites*. *Composites Science and Technology*, 2004. **64**(10–11): p. 1467-1475.
 223. Kchaou, B., et al., *Dielectric and friction behaviour of unidirectional glass fibre reinforced epoxy (GFRE)*. *Wear*, 2008. **265**(5-6): p. 763-771.

APPENDIX

SUMMARY

This section summarises the raw experimental data relating to specific chapters presented in order of appearance in the thesis:

Appendix-A provides the data on stretching rig calibration, fibre diameter measurement and impact test results.

Appendices-B and C present impact test data corresponding to Chapter 5 and Chapter 6, respectively.

APPENDIX-A EXPERIMENTAL DATA FOR CHAPTER 4

Table A-1 Stretching rig calibration data for the SSR as shown in Figure 4-2. SE is the standard error.

Reading from digital scale (kg)	Applied weight (kg)				
	5	10	15	20	24
1	5.05	9.88	15.08	20.20	24.05
2	4.98	9.98	15.05	20.10	24.08
3	5.03	9.90	14.98	20.13	24.05
4	4.98	10.03	15.00	20.18	24.05
5	4.98	9.93	15.03	20.13	24.13
6	4.98	10.00	15.05	20.15	24.08
7	4.98	10.03	15.00	20.10	24.08
8	5.00	9.93	14.95	20.13	24.15
9	4.93	9.93	15.10	20.13	24.03
10	5.00	10.03	15.03	20.13	24.08
Mean \pm SE	4.99 \pm 0.01	9.96 \pm 0.02	15.03 \pm 0.01	20.14 \pm 0.01	24.08 \pm 0.01

Table A-2 Stretching rig calibration data for the LSR as shown in Figure 4-3. SE is the standard error.

Reading from digital scale (kg)	Applied weight (kg)						
	0	1	2	3	4	5	6
1	3.25	10.15	17.65	25.30	33.20	40.00	47.50
2	3.45	10.20	17.70	25.65	33.20	40.15	47.50
3	3.30	10.25	17.70	25.55	33.15	40.15	47.45
4	3.25	10.30	17.75	25.65	33.15	40.20	47.40
5	3.40	10.10	17.95	25.55	33.25	40.35	47.45
6	3.50	10.35	17.90	25.50	32.85	40.30	47.55
7	3.20	10.20	18.00	25.50	32.90	40.25	47.50
8	3.15	10.15	17.90	25.40	32.90	40.25	47.45
9	3.50	10.30	17.85	25.45	32.95	40.15	47.40
10	3.35	10.25	18.00	25.45	32.95	40.30	47.50
Mean ± SE	3.34 ± 0.04	10.23 ± 0.03	17.84 ± 0.05	25.50 ± 0.04	33.05 ± 0.06	40.21 ± 0.04	47.47 ± 0.02

Table A-3 Charpy impact test data to evaluate the effectiveness of prestress generated from the stretching rigs, with GPR as the matrix, as presented in Table 4-1. T and C represent prestressed (test) and non-prestressed (control) counterparts, respectively; SE is the standard error.

	Batch	Type	Impact energy absorption (kJ m ⁻²)					Mean ± SE
			1	2	3	4	5	
SSR-GPR	1	T	41.95	33.74	42.24	42.93	38.31	39.83 ± 1.72
		C	33.50	25.57	23.15	24.92	39.89	29.41 ± 3.17
	2	T	50.87	42.85	44.66	37.41	44.16	43.99 ± 2.15
		C	33.76	28.02	39.37	46.44	29.05	35.33 ± 3.43
	3	T	44.95	53.52	41.39	53.12	53.11	49.22 ± 2.53
		C	34.02	32.26	37.45	33.30	35.41	34.49 ± 0.90
LSR-GPR	1	T	44.86	47.73	36.64	38.37	44.49	42.42 ± 2.10
		C	35.44	28.95	30.81	31.00	28.87	31.01 ± 1.19
	2	T	47.76	49.43	39.60	42.89	47.10	45.36 ± 1.80
		C	36.68	30.18	35.62	29.77	35.97	33.64 ± 1.51
	3	T	41.87	44.37	39.51	49.69	38.53	42.79 ± 2.00
		C	30.26	39.55	40.08	34.97	31.88	35.35 ± 1.98

Table A-4 Charpy impact test data to evaluate the effectiveness of prestress generated from the stretching rigs, with SLT as the matrix, presented in Table 4-1. T and C represent prestressed (test) and non-prestressed (control) counterparts, respectively; SE is the standard error.

	Batch	Type	Impact energy absorption (kJ m ⁻²)					Mean ± SE
			1	2	3	4	5	
SSR-SLT	1	T	40.27	41.30	35.93	36.71	39.16	38.67 ± 1.03
		C	23.44	19.31	20.85	22.01	24.32	21.99 ± 0.90
	2	T	38.87	37.72	30.59	32.30	40.58	36.01 ± 1.94
		C	29.31	26.41	25.71	23.25	25.79	26.09 ± 0.97
	3	T	47.88	37.01	34.18	36.05	43.02	39.63 ± 2.54
		C	21.28	19.98	20.51	18.62	20.02	20.08 ± 0.43
LSR-SLT	1	T	38.71	39.04	41.72	26.82	40.24	37.31 ± 2.67
		C	23.82	20.17	22.80	20.33	25.11	22.44 ± 0.97
	2	T	37.07	39.42	23.47	33.50	43.66	35.42 ± 3.41
		C	23.91	20.04	21.18	22.05	19.59	21.35 ± 0.77
	3	T	33.31	43.19	32.40	38.00	32.97	35.97 ± 2.06
		C	21.57	23.58	21.11	22.45	24.68	22.68 ± 0.66

Table A-5 Diameter measurement data for fibre yarn samples. Fibre single filaments were selected from each yarn sample, and three readings were taken from three different locations on each filament. Mean results are presented in Figure 4-5; SE is the standard error.

Sample	Location	Measurement of diameters (μm)															Mean \pm SE
		Filament 1			Filament 2			Filament 3			Filament 4			Filament 5			
ARN	1	27.0	26.9	27.1	26.4	26.3	26.4	26.6	26.6	26.6	26.3	26.3	26.4	26.6	26.6	26.6	26.6 \pm 0.1
	2	27.1	27.1	27.1	26.4	26.3	26.5	26.6	26.7	26.6	26.2	26.3	26.2	26.5	26.6	26.5	
	3	27.0	27.2	27.0	26.3	26.3	26.3	26.5	26.6	26.6	26.4	26.4	26.4	26.6	26.6	26.5	
ARO	1	27.3	27.4	27.4	27.4	27.4	27.4	26.5	26.5	26.4	25.0	25.1	25.1	26.6	26.6	26.6	26.6 \pm 0.1
	2	27.4	27.4	27.4	27.3	27.4	27.4	26.4	26.4	26.4	25.0	25.0	25.0	26.6	26.5	26.6	
	3	27.4	27.4	27.4	27.4	27.4	27.4	26.3	26.3	26.3	25.0	24.9	25.0	26.6	26.5	26.6	
ANN	1	25.7	25.6	25.7	26.0	26.0	26.0	25.3	25.3	25.5	26.4	26.4	26.3	26.4	26.4	26.3	26.0 \pm 0.1
	2	25.5	25.7	25.7	26.1	26.0	26.0	25.6	25.5	25.5	26.6	26.4	26.4	26.3	26.3	26.3	
	3	25.7	25.7	25.8	26.0	26.0	26.0	25.5	25.5	25.5	26.4	26.4	26.4	26.3	26.3	26.3	
ANO	1	26.0	26.0	25.9	27.2	27.2	27.2	26.2	26.2	26.2	26.2	26.2	26.2	26.3	26.2	26.3	26.4 \pm 0.1
	2	25.9	25.9	26.0	27.2	27.2	27.3	26.3	26.3	26.3	26.3	26.3	26.3	26.2	26.3	26.4	
	3	26.0	26.0	26.1	27.1	27.2	27.2	26.2	26.3	26.3	26.3	26.3	26.2	26.2	26.2	26.3	

Table A-6 Charpy impact test data for resin only samples, tested at 336 h (two weeks) after moulding. Mean results are shown in Table 4-4; SE is the standard error.

Matrix	Batch	Impact energy absorption (kJ m ⁻²)										Mean ± SE
		1	2	3	4	5	6	7	8	9	10	
GPR	1	3.55	4.79	4.67	1.66	3.49	3.58	3.84	4.43	2.84	4.27	3.71 ± 0.30
	2	3.60	3.00	2.96	2.97	3.60	4.27	2.54	4.53	4.64	3.45	3.56 ± 0.23
	3	3.46	2.87	4.65	3.44	3.50	3.33	3.75	3.36	3.37	3.42	3.51 ± 0.14
PLT	1	1.58	1.59	0.95	0.95	0.97	1.50	0.92	1.56	0.95	0.98	1.20 ± 0.10
	2	2.80	2.87	0.97	2.97	2.69	3.19	1.77	3.58	2.45	2.87	2.62 ± 0.24
	3	1.65	1.64	1.62	1.92	1.91	1.58	1.84	1.82	2.40	1.81	1.82 ± 0.08
SLT	1	1.57	0.95	1.58	1.60	2.88	1.49	1.76	1.46	1.76	1.48	1.65 ± 0.15
	2	2.36	1.79	1.52	2.49	1.90	3.34	3.09	4.85	4.07	3.28	2.87 ± 0.34
	3	2.48	1.87	2.48	1.88	2.53	1.80	1.77	2.37	2.41	2.78	2.24 ± 0.12
STA	1	2.95	3.61	2.90	2.94	2.99	4.34	3.35	4.63	3.40	4.33	3.54 ± 0.21
	2	2.93	2.89	2.87	2.83	3.47	3.52	2.83	2.77	3.38	3.38	3.09 ± 0.10
	3	3.08	3.01	3.30	2.93	2.88	3.00	3.59	3.51	3.13	2.82	3.12 ± 0.08
CFS	1	1.62	0.98	1.64	1.63	1.64	1.55	0.92	1.55	1.57	1.57	1.47 ± 0.09
	2	1.64	1.63	1.93	1.61	1.64	1.54	1.54	1.54	1.57	1.61	1.63 ± 0.04
	3	1.52	1.55	1.60	0.98	2.04	2.30	2.33	1.50	1.84	1.90	1.76 ± 0.13

Table A-7 Charpy impact test data for nylon-based composite samples (2% V_f), tested at 336 h (two weeks) after moulding. Mean results are shown in Table 4-4; SE is the standard error.

Matrix	Batch	Impact energy absorption (kJ m ⁻²)											
		Test						Control					
		1	2	3	4	5	Mean ± SE	1	2	3	4	5	Mean ± SE
GPR	1	44.86	47.73	36.64	38.37	44.49	42.42 ± 2.10	35.44	28.95	30.81	31.00	28.87	31.01 ± 1.19
	2	47.76	49.43	39.60	42.89	47.10	45.36 ± 1.80	36.68	30.18	35.62	29.77	35.97	33.64 ± 1.51
	3	41.87	44.37	39.51	49.69	38.53	42.79 ± 2.00	30.26	39.55	40.08	34.97	31.88	35.35 ± 1.98
PLT	1	39.03	40.28	30.25	36.92	38.64	37.02 ± 1.78	18.55	21.10	20.22	22.22	21.46	20.71 ± 0.63
	2	36.01	37.93	28.63	36.50	37.68	35.36 ± 1.71	23.42	22.20	26.50	27.33	25.70	25.03 ± 0.96
	3	38.25	35.10	29.01	34.87	40.69	35.58 ± 1.96	21.58	17.99	25.10	21.65	21.72	21.61 ± 1.13
SLT	1	38.71	39.04	41.72	26.82	40.24	37.31 ± 2.67	23.82	20.17	22.80	20.33	25.11	22.44 ± 0.97
	2	37.07	39.42	23.47	33.50	43.66	35.42 ± 3.41	23.91	20.04	21.18	22.05	19.59	21.35 ± 0.77
	3	33.31	43.19	32.40	38.00	32.97	35.97 ± 2.06	21.57	23.58	21.11	22.45	24.68	22.68 ± 0.66
STA	1	59.91	54.17	42.97	48.02	55.63	52.14 ± 2.98	28.52	29.36	25.23	24.41	33.71	28.24 ± 1.66
	2	55.67	56.63	48.21	54.41	57.33	54.45 ± 1.63	37.58	24.06	33.40	33.59	34.22	32.57 ± 2.26
	3	59.12	47.60	42.17	48.49	48.94	49.26 ± 2.75	30.58	27.17	28.92	29.01	32.11	29.56 ± 0.83
CFS	1	45.04	47.31	39.45	46.04	48.29	45.23 ± 1.55	23.47	19.51	20.65	24.05	21.96	21.93 ± 0.85
	2	54.64	39.75	29.05	43.89	49.78	43.42 ± 4.40	23.63	23.28	18.29	20.51	22.41	21.62 ± 0.99
	3	51.56	36.51	51.25	46.01	41.83	45.43 ± 2.87	30.51	25.06	30.72	25.09	27.87	27.85 ± 1.24

APPENDIX-B EXPERIMENTAL DATA FOR CHAPTER 5

Table B-1 Charpy impact test data for nylon-based composite samples, produced under 24 h creep conditions (2% V_f). Samples were tested 336 h (two weeks) after moulding. Mean results are shown in Table 5-4; SE is the standard error.

Prestress condition	Batch	Impact energy absorption (kJ m^{-2})											
		Test						Control					
		1	2	3	4	5	Mean \pm SE	1	2	3	4	5	Mean \pm SE
330 MPa (24 h)	1	37.29	40.24	22.98	38.15	30.97	33.93 ± 3.14	21.18	23.55	23.05	29.45	21.68	23.78 ± 1.48
	2	39.03	40.28	30.25	36.92	38.64	37.02 ± 1.78	18.55	21.10	20.22	22.22	21.46	20.71 ± 0.63
	3	36.01	37.93	28.66	36.50	37.68	35.36 ± 1.71	23.42	22.20	26.50	27.33	25.70	25.03 ± 0.96
	4	38.04	36.34	25.92	42.08	41.14	36.71 ± 2.89	22.44	28.64	27.59	25.52	23.82	25.60 ± 1.15
	5	38.25	35.10	29.01	34.87	40.69	35.58 ± 1.96	21.58	17.98	25.10	21.65	21.72	21.61 ± 1.13
460 MPa (24 h)	1	40.03	41.35	37.17	37.02	41.25	39.63 ± 2.22	22.25	21.22	21.52	24.90	23.07	24.08 ± 0.74
	2	38.50	46.84	45.52	49.60	43.58	37.30 ± 0.54	21.10	23.98	23.56	24.42	24.01	22.28 ± 0.88
	3	46.16	40.47	32.33	38.70	40.47	38.57 ± 1.35	22.31	22.84	26.13	25.42	23.70	19.46 ± 0.15
	4	38.53	36.12	36.08	38.48	37.27	39.36 ± 0.95	24.39	22.38	19.69	21.03	23.92	22.59 ± 0.66
	5	42.39	40.46	34.53	38.21	37.25	44.81 ± 1.86	19.57	18.87	19.54	19.73	19.59	23.41 ± 0.59
590 MPa (24 h)	1	32.43	33.95	20.23	31.02	32.76	30.08 ± 2.51	21.84	21.58	25.23	17.35	21.46	21.49 ± 1.25
	2	37.23	34.44	30.64	38.33	38.23	35.77 ± 1.46	21.50	23.27	21.38	20.59	21.88	21.72 ± 0.44
	3	32.63	38.14	33.89	38.16	35.27	35.62 ± 1.11	24.44	21.55	22.65	21.40	20.94	22.19 ± 0.63
	4	41.45	38.55	33.03	41.07	34.09	37.64 ± 1.75	23.01	23.77	21.97	26.83	24.33	23.98 ± 0.82
	5	38.94	39.71	32.03	35.54	36.75	36.59 ± 1.36	24.98	24.01	24.15	25.19	23.12	24.29 ± 0.37

APPENDIX-C EXPERIMENTAL DATA FOR CHAPTER 6

Table C-1 Charpy impact test data for nylon-based composite samples, produced under two creep conditions (2% V_f). Samples were tested 336 h (two weeks) after moulding. Mean results are shown in Table 6-2; SE is the standard error.

Prestress condition	Batch	Impact energy absorption (kJ m^{-2})											
		Test						Control					
		1	2	3	4	5	Mean \pm SE	1	2	3	4	5	Mean \pm SE
460 MPa (92 min)	1	41.73	40.29	30.42	41.47	47.83	40.35 \pm 2.81	29.59	24.99	22.46	26.75	25.86	25.93 \pm 1.16
	2	37.29	45.66	39.17	41.02	33.95	39.42 \pm 1.95	28.03	23.37	24.65	21.70	25.16	24.58 \pm 1.05
	3	33.98	44.94	37.01	36.61	36.58	37.82 \pm 1.86	22.38	22.23	21.47	22.39	27.70	23.24 \pm 1.13
	4	35.81	34.38	29.38	36.09	33.70	33.87 \pm 1.21	22.29	20.84	20.37	21.21	25.11	21.97 \pm 0.85
	5	31.21	36.63	40.54	39.46	39.02	37.37 \pm 1.67	23.53	23.27	23.74	21.88	21.74	22.83 \pm 0.42
590 MPa (37 min)	1	36.31	47.60	25.86	31.33	31.05	34.43 \pm 3.68	20.63	25.11	26.55	26.84	23.96	24.62 \pm 1.12
	2	36.43	31.57	45.11	39.92	39.95	38.59 \pm 2.24	23.59	20.51	23.76	23.26	25.42	23.31 \pm 0.79
	3	51.36	39.25	27.98	36.29	30.95	37.17 \pm 4.06	26.48	24.03	21.56	26.61	26.31	25.00 \pm 0.98
	4	38.13	32.95	37.07	41.14	38.26	37.51 \pm 1.32	23.07	22.74	22.29	22.42	27.28	23.56 \pm 0.94
	5	42.53	27.18	41.15	38.64	40.37	37.97 \pm 2.77	26.90	24.17	24.30	23.37	22.62	24.27 \pm 0.72

Table C-2 Charpy impact test data for nylon-based composite samples, produced under various creep conditions (2% V_f). Samples were tested at 4392 h (0.5 years). Mean results are shown in Tables 6-3 and 6-7; SE is the standard error.

Prestress condition	Batch	Impact energy absorption (kJ m^{-2})											
		Test						Control					
		1	2	3	4	5	Mean \pm SE	1	2	3	4	5	Mean \pm SE
330 MPa (24 h)	1	37.41	40.12	35.35	49.12	38.01	40.00 \pm 2.40	24.98	24.59	28.17	25.15	25.97	25.77 \pm 0.64
	2	36.01	31.04	26.71	39.01	44.74	35.50 \pm 3.12	21.55	28.38	21.00	19.29	21.38	20.32 \pm 0.63
	3	35.94	43.26	37.67	36.22	35.44	37.71 \pm 1.44	22.79	24.55	23.22	25.69	20.89	23.43 \pm 0.81
	4	34.08	29.97	24.57	40.88	45.32	34.97 \pm 3.71	24.24	21.97	22.69	23.27	23.46	23.13 \pm 0.38
	5	41.25	30.27	26.42	41.42	32.20	34.31 \pm 3.01	24.36	27.76	26.93	21.21	25.01	25.05 \pm 1.14
590 MPa (37 min)	1	48.77	42.47	39.10	47.85	42.51	44.14 \pm 1.82	22.21	24.37	27.91	22.96	28.42	25.17 \pm 1.27
	2	45.73	45.89	32.39	50.76	46.53	44.26 \pm 3.11	23.95	23.61	26.31	24.72	23.71	24.46 \pm 0.50
	3	41.03	47.84	31.48	36.99	41.44	39.76 \pm 2.70	25.39	25.61	24.60	27.99	23.95	25.51 \pm 0.69
	4	35.85	41.76	34.39	32.84	31.88	35.34 \pm 1.74	20.59	22.32	25.31	30.31	21.29	23.96 \pm 1.78
	5	29.76	38.41	29.41	35.17	37.53	34.06 \pm 1.90	22.00	23.21	23.78	23.34	22.18	22.90 \pm 0.35
590 MPa (134 min)	1	36.00	41.21	32.28	43.70	35.07	37.65 \pm 2.09	25.92	26.09	28.51	25.88	23.84	26.05 \pm 0.74
	2	45.60	38.19	31.78	35.20	42.06	38.57 \pm 2.44	22.94	25.55	26.57	25.96	24.66	25.14 \pm 0.63
	3	43.91	40.50	26.27	38.24	31.86	36.16 \pm 3.16	23.77	22.39	23.91	22.54	21.47	22.82 \pm 0.46
	4	50.59	40.76	28.96	42.39	38.25	40.19 \pm 3.49	20.31	23.57	23.47	20.90	22.20	22.09 \pm 0.66
	5	38.95	55.25	27.26	43.32	46.50	42.26 \pm 4.60	23.15	23.40	24.15	22.75	22.53	23.20 \pm 0.28

Table C-3 Charpy impact test data for nylon-based composite samples, produced under two creep conditions (2% V_f). Samples were subjected to accelerated aging to an equivalent of 20,000 years at 20°C before testing. Mean results are shown in Table 6-4; SE is the standard error.

Prestress condition	Impact energy absorption (kJ m ⁻²)												
	Batch	Test						Control					
		1	2	3	4	5	Mean ± SE	1	2	3	4	5	Mean ± SE
330 MPa (24 h)	1	30.85	38.64	28.35	38.09	36.61	34.51 ± 2.07	23.01	22.01	21.23	19.26	25.99	22.30 ± 1.11
	2	37.52	33.40	28.02	36.16	33.61	33.74 ± 1.63	21.13	22.17	24.32	25.23	22.10	22.99 ± 0.77
	3	36.62	41.34	28.52	36.49	30.59	34.77 ± 2.32	22.02	22.43	25.41	19.52	21.40	22.15 ± 0.96
590 MPa (37 min)	1	33.99	30.60	29.66	31.39	33.27	31.78 ± 0.81	21.17	20.99	25.60	22.69	21.74	22.44 ± 0.84
	2	32.34	32.46	33.29	32.22	32.94	32.65 ± 0.20	19.61	19.19	19.64	17.43	19.79	18.93 ± 0.47
	3	40.49	36.44	29.73	37.01	35.89	35.91 ± 1.74	21.99	21.09	21.08	20.75	22.50	21.48 ± 0.33

Table C-4 Charpy impact test data for nylon-based composite samples, produced under different creep conditions (2% V_f). Samples were tested at 336 h (two weeks) after moulding. Mean results are shown in Tables 6-5 and 6-6; SE is the standard error.

Prestress condition	Batch	Impact energy absorption (kJ m^{-2})											
		Test						Control					
		1	2	3	4	5	Mean \pm SE	1	2	3	4	5	Mean \pm SE
590 MPa (134 min)	1	41.38	36.18	42.07	40.98	33.03	38.73 ± 1.76	21.11	18.90	22.55	20.06	21.33	20.79 ± 0.62
	2	38.79	39.16	42.30	35.39	41.24	39.38 ± 1.19	21.14	24.22	21.98	24.62	23.93	23.18 ± 0.68
	3	35.42	44.11	41.13	37.91	33.19	38.35 ± 1.95	23.51	22.31	23.51	23.70	25.47	23.70 ± 0.51
	4	44.19	48.11	31.95	48.05	37.71	42.00 ± 3.15	26.01	22.01	22.85	21.98	23.38	23.25 ± 0.74
	5	40.33	42.45	30.89	42.89	52.17	41.75 ± 3.39	27.33	21.22	22.77	27.93	21.03	24.06 ± 1.49
665 MPa (20 min)	1	36.01	35.49	30.12	35.34	36.74	34.74 ± 1.18	20.39	21.50	20.37	26.20	24.24	22.54 ± 1.16
	2	34.05	41.60	35.32	39.83	35.82	37.32 ± 1.44	24.30	25.35	24.91	23.36	22.06	24.00 ± 0.59
	3	32.58	39.75	41.41	42.10	36.25	38.42 ± 1.78	22.38	22.40	24.00	21.32	23.59	22.73 ± 0.45
	4	40.81	41.81	33.33	45.11	32.63	38.74 ± 2.46	26.10	24.44	26.02	22.98	25.59	25.03 ± 0.59
	5	33.59	34.32	28.05	38.32	35.73	34.00 ± 1.69	21.40	23.59	23.72	24.79	23.38	23.38 ± 0.55
665 MPa (48 min)	1	30.03	41.06	34.52	45.88	58.85	42.07 ± 4.99	23.10	25.31	22.74	24.81	23.58	23.91 ± 0.49
	2	45.39	46.58	41.55	46.19	36.74	43.29 ± 1.86	24.30	22.94	25.29	21.81	25.10	23.87 ± 0.66
	3	37.04	33.53	36.22	38.21	42.83	37.57 ± 1.53	24.11	24.09	21.79	21.11	22.97	22.81 ± 0.60
	4	34.54	35.14	40.89	46.06	39.85	39.29 ± 2.10	22.14	24.15	25.99	23.93	22.12	23.66 ± 0.72
	5	41.90	50.47	36.26	40.98	50.76	44.07 ± 2.84	24.89	25.18	25.45	25.08	25.21	25.16 ± 0.09